Physics of the Ultrafast Dynamics of Excitons in GaN Nanostructures

THÈSE N° 5094 (2011)

ÉCOLE POLYTECHNIQUE FÉDÉRALE DE LAUSANNE

PAR

Pierre Michel CORFDIR

EPFL

ÉCOLE POLYTECHNIQUE
FÉDÉRALE DE LAUSANNE

Suisse
2011

Résumé

Depuis maintenant plus de quinze ans, les nitrures d'éléments III sont devenus la famille de matériaux de choix pour la réalisation de composants optoélectroniques opérant dans le domaine visible et ultraviolet du spectre électromagnétique. Paradoxalement, malgré l'explosion des technologies basées sur les nitrures, la maîtrise de la qualité structurale de ces matériaux n'est pas encore arrivée à maturité, et de nombreux axes de recherche restent ouverts, dans l'optique d'améliorer encore l'efficacité radiative des hétérostructures nitrurées. Mentionnons, en particulier, la réduction de la densité de dislocations, ou encore l'élimination des champs de polarisations internes. Parallèlement aux efforts menés sur le front de la qualité du matériau, il est essentiel de comprendre les mécanismes régissant l'émission de lumière dans les structures à base de nitrure de gallium, ainsi que d'analyser le rôle que peuvent jouer les défauts structuraux sur l'efficacité radiative des dispositifs. S'inscrivant dans cette logique, ce travail de thèse porte sur la dynamique de relaxation et de recombinaison de l'exciton, l'excitation élémentaire du cristal, dans des nanostructures à base de nitrures d'éléments III. Cette étude expérimentale est menée principalement au travers d'expériences de photoluminescence et de cathodoluminescence résolues en temps.

Dans une première partie, nous étudions les propriétés d'émission de nanocolonnes de GaN, nano-objets aujourd'hui particulièrement intéressants puisqu'ils sont totalement dépourvus de dislocation. Pourtant, à basse température, les transitions excitoniques de ces nano-objets sont relativement larges, contrastant a priori avec leur perfection structurale. De plus, la photoluminescence des nanocolonnes de GaN présente une intense transition centrée à 3.45 eV, raie en général absente des spectres enregistrés pour des couches épaisses de GaN de haute qualité. Nous démontrons tout d'abord que l'élargissement des raies excitoniques et, par extension, la luminescence à 3.45 eV, résultent de la distribution statistique des noyaux donneurs au sein de la nanocolonne, la surface de la nanocolonne entraînant une déformation significative des fonctions d'ondes des excitons liés aux atomes donneurs. A l'aide d'un

modèle qualitatif, nous estimons alors à 8 nm l'épaisseur de la couronne de surface où la recombinaison des excitons liés aux donneurs est affectée par la surface.

Nous nous consacrons ensuite à la capture des excitons par les défauts cristallins étendus. En particulier, nous étudions le rôle des fautes d'empilements dans le plan basal, un défaut cristallin radiatif, planaire, fréquemment rencontré dans les couches hétéroépitaxiales de GaN non-polaire. Nous décrivons tout d'abord la diffusion des excitons vers ces défauts, et leur capture par les fautes d'empilements, puis démontrons la localisation des excitons à l'intérieur même des fautes d'empilements. Nos expériences, soutenues par des calculs effectués dans le formalisme de la fonction enveloppe, nous permettent de prouver l'existence de complexes excitoniques liés simultanément aux fautes d'empilements et aux noyaux donneurs. Dans le cas des hétérostructures telles que les puits quantiques (Al,Ga)N/GaN, nous montrons que la dynamique des excitons confinés est dominée par leur capture par les fautes d'empilements. Nos expériences suggèrent enfin que l'intersection entre une faute d'empilements et un puits quantique peut être modélisée par un fil quantique.

Dans la dernière partie de ce travail, nous nous penchons sur la dynamique des excitons dans des hétérostructures (Al,Ga)N/GaN non-polaires, déposées sur des cristaux massifs de GaN. Grâce à cette technique de croissance particulière, les échantillons obtenus présentent des densités de dislocations quatre ordres de grandeur plus faibles que celles observées pour des couches de GaN non-polaire ayant crû sur saphir. Il nous est alors possible d'étudier les mécanismes intrinsèques de relaxation et de recombinaison des excitons, que ce soit dans le régime de confinement quantique faible ou fort. Dans ce dernier cas, nous observons que la recombinaison des excitons confinés est purement radiative jusqu'à 200 K, une première pour des puits quantiques de GaN. Nous proposons enfin que la chute d'efficacité radiative des puits quantiques à plus haute température provient de l'échappement thermique des porteurs du puits vers les barrières, suivi de leur recombinaison non-radiative.

Mots-clefs: nitrure de gallium, nitrures d'éléments III, excitons, puits quantique, nanostructures, photoluminescence, cathodoluminescence, défauts

4

Abstract

For more than fifteen years, III-nitrides have become the materials of choice for the realization of optoelectronics devices operating in the visible-UV spectral range. Yet, while nitride-based technology has truly exploded, the structural quality of this material-class is still low, which is a key issue regarding the radiative efficiency of light-emitting devices. A lot of work is thus devoted to improve the crystal quality of GaN and related materials. As current developments, we mention the reduction of threading dislocations, or the growth of III-nitrides heterostructures along non-polar crystal orientation. In parallel to the efforts dedicated to improve the quality of nitride-based epilayers, it is mandatory to grasp the mechanisms ruling the light-matter interaction, and, in particular, to detail the impact of defects on the radiative efficiency of optoelectronic devices. As a part of this research, the present thesis work is dedicated to the understanding of exciton relaxation and recombination phenomena in nitride-based nanostructures. This experimental study is carried out by time-resolved photo- and cathodoluminescence.

We first focus on the emission properties of GaN nanocolumns, nanostructures that raise currently a huge interest, as they are free of any extended defect. Still, contrasting with their perfect structural quality, the low-temperature photoluminescence spectra of these nano-objects exhibit broad excitonic emission lines. In addition, one observes an intense emission line centered at 3.45 eV, a line absent from the luminescence spectra of high-quality GaN thick layers. We first demonstrate that these two features arise from the statistical distribution of donor atoms across the nanocolum: when a donor nucleus is located in the vicinity of the surface, its wave function is perturbed and the emission properties of donor bound excitons is profoundly altered. Based on a qualitative model, we estimate to 8 nm the thickness of the surface shell layer where the radiative properties of donor bound excitons are affected by the surface.

We then address the capture processes of excitons by extended structural defects. We focus in particular on basal plane stacking faults, planar radiative defects generally encountered in heteroepitaxial non-polar GaN layers. We first describe the diffusion of excitons and their capture by basal stacking faults, and we show that excitons are localized along the stacking fault planes themselves. Supported by envelope function calculations, our experiments demonstrate that donor atoms distributed in the vicinity of the basal stacking faults efficiently localize excitons along the planar defects. Concerning non-polar (Al,Ga)N/GaN quantum wells grown on sapphire, we show that the dynamics of excitons is dominated by their capture by stacking faults. Finally, we attest that the intersection between basal plane stacking faults and a quantum well can be modeled as a quantum wire.

In the last part of this work, we investigate the dynamics of excitons in non-polar (Al,Ga)N/GaN heterostructures grown on bulk GaN crystals. Such layers present dislocation densities four orders of magnitude smaller than those deposited on lattice-mismatched susbtrates, making possible the study of intrinsic relaxation and recombination mechanisms of excitons in the weak as well as in the strong confinement regimes. In the latter case, thanks to the drastic reduction in threading dislocation density, it is possible to observe purely radiative recombination of quantum well free excitons up to 200 K. We attribute the drop in internal quantum efficiency observed at higher temperatures to the escape of quantum well excitons towards the disordered (Al,Ga)N barriers and to their subsequent non-radiative recombination.

Table of Contents

Generalities

Recombination mechanisms of impurity-bound excitons

Exciton capture by radiative and non-radiative extended defects

Intrinsic dynamics of excitons in the weak and strong confinement regimes

Conclusions and perspectives

Miscellaneous

Introduction

Since the proposal by [Esaki1970], thirty years ago, of the possible interest in preparing semiconducting heterostructures, followed by the first observation of electronic confined states in a GaAs quantum well [Dingle1974], semiconductors with reduced dimensionality have excited a huge interest from the scientific community. The fascination attracted to low-dimensional semiconductors arises indeed from the possibility to tune the electronic properties of confined electrons and holes. In parallel, huge progress in the growth processes, mainly molecular beam epitaxy (MBE) and metal-organic vapor phase epitaxy (MOVPE), has made all the expectations -and even more- put in two-dimensional structures become a reality. For instance, the realizations of heterostructures with high electron mobility and density [Dingle1978], or the achievement of lasers with quantum-well based active medium [VanDerZiel1975], have been demonstrated. In addition, the availability of semiconductor heterostructures with high structural quality has allowed for a better understanding of the phenomena ruling light-matter interaction in systems of reduced dimensionality [Deveaud1991,Weisbuch1992].

III-nitrides form a particular class of material among semiconductors. Their energy bandgap ranges from 0.7 to 6.2 eV, which makes them attractive towards the realization of light-emitting devices covering the full near-infrared-UV spectrum. Moreover, compared to III-arsenides, excitons in GaN quantum wells present a large binding energy. Excitons are therefore stable up to room temperature, paving the way for the extension at 300 K of quantum devices demonstrated so far at cryogenic temperatures [Christopoulos2007].

The interest in III-nitrides has been started at the beginning of the seventies by the pioneering work of [Dingle1971], who demonstrated the achievement of a GaN thick layer with well-resolved excitonic reflectance and emission lines at 2 K. However, the impossibility, at that time, to *p*-dope efficiently GaN layers drastically limited the interest in nitrides. The real breakthrough in that field occurred in 1994, when [Nakamura1994] demonstrated the

realization of a working nitride-based blue light-emitting diode (LED). From then, the research in this field has truly exploded. Above all, we refer to the achievement of green LEDs [Nakamura1995] and blue laser diodes [Nakamura1996]. The former has indeed lead to a revolution in solid-state lighting [Ponce1997,Steigerwald2002]: only 17 years after the realization of the first green LED, the classical incandescent bulb invented in 1879 by Swan has been definitely forbidden by the whole European Community. Regarding blue-violet laser diodes, they have not only allowed for more compact data storage with the Blu-Ray discs, but are also widely used for medical applications. Although it would not be possible to quote here all the technological achievements made possible with nitrides, we also mention the realization of ultraviolet detectors [Razeghi1996] and high electron mobility transistors [Khan1993,Ambacher1999]. Later on, the research on nitrides was extended to deep-UV applications [Taniyasu2006], nanotechnology [Duan2000,Johnson2002,Goldberger2003] or even spintronics [Reed2001].

In parallel to the technological realizations listed above, major fundamentals advances were also realized with nitrides. The internal polarization fields in GaN-based heterostructures were studied theoretically [Bernardini1997] and experimentally [Leroux1998]. Overcoming the quantum confined Stark effect then motivated the growth of GaN along non-polar directions [Waltereit2000]. Progresses in the growth and patterning processes made possible the observation of strong light-matter coupling in bulk and quantum well microcavities [Semond2005,Butté2006] and the realization of (In,Ga)N LEDs with high extraction efficiencies [David2005].

What is really striking with nitrides, compared to other classes of semiconductors, is their wide use for technological applications despite their rather low structural quality, when this would be a major problem in other material systems. Due to the absence of substrate lattice-matched to GaN, the dislocation density in the best epilayers is indeed of the order of 10^6 cm^{-2}, a density more than four orders of magnitude higher than what reported for high-quality GaAs layers! At the beginning of this project, in 2007, many mechanisms were already proposed to explain the rather high radiative efficiency of blue and green light-emitting (In,Ga)N/GaN quantum wells. Among them, one can cite spatial fluctuations in Indium incorporation along the quantum well plane [Nakamura1998], the decoration of dislocations by V-shaped pits [Hangleiter2005] or meandering behavior of the (In,Ga)N quantum well layers [Sonderegger2006]. In any case, it is now admitted that free charge

carriers - or excitons- confined in (In,Ga)N are prevented from reaching the dislocations thanks to strong potential fluctuations along the quantum well plane.

The situation is however different in GaN quantum wells, where the localization of excitons is not as strong as in (In,Ga)N. At room temperature, excitons are delocalized along the whole quantum plane and therefore suffer from efficient non-radiative recombinations. Conversely, the absence of localization makes GaN more suitable than (In,Ga)N regarding the investigation of the intrinsic dynamics of excitons, as well as their interaction with point and extended defects. The latter is indeed an important subject of study, since the profound knowledge of the dynamics of charge carriers may lead to a better understanding of the physics underlying many photonic devices. In this context, we aim at investigating the dynamics of excitons in various GaN based systems by picosecond time-resolved photo- and cathodoluminescence. With these techniques, we can indeed generate a population of hot excitons and monitor their energy relaxation as well as their spatial diffusion. In this work, conducted between 2007 and 2011 at the Laboratoire d'Opto-Electronique Quantique at EPFL, we have paid a particular attention to the interactions of the generated excitons with donor impurities as well as with two- and one-dimensional radiative extended defects. We have concentrated too on the intrinsic radiative properties of charge carriers confined in GaN quantum wells, and on the evolution of the recombination processes when going from cryogenic to room temperature. As this work is also part of the current research aiming at the achievement of GaN systems with high radiative efficiency, our experiments will focus on the emission properties of singular low-dimensional GaN systems, such as defect-free GaN nanocolumns or polarization-free quantum wells.

The present manuscript is divided in five main parts. The first one is devoted to the presentation of basic concepts needed for this thesis.

- In Chapter I, we present the structural and optical properties of III-nitrides semiconductors. We focus in particular on the consequences of strain on the symmetry of GaN valence band. After introducing what is an exciton, we give a basic description of the energy relaxation of the first excited state of the crystal in bulk and quantum well structures. We finally put a particular emphasis on the effect of internal polarization fields on the dynamics of excitons, as their elimination motivates the growth of GaN quantum wells along non-polar directions.

- In Chapter II, we describe the experimental tools used to characterize nitride-based nanostructures in this thesis, namely continuous-wave cathodoluminescence and picosecond time-resolved photo- and cathodoluminescence.

The core of this thesis work is divided within the three following parts. First, we discuss the recombination properties of excitons bound to point defects.

- We show in Chapter III that GaN nanocolumns are ideal subjects for such experiments, as they are free of any extended defect. We detail in particular the influence of surface on the wave functions of donor bound excitons and its consequences on the emission spectrum of the nano-objects. This study has been subjected to publication in:

P. Corfdir, P. Lefebvre, J. Ristić, P. Valvin, E. Calleja, A. Trampert, J.-D. Ganière, and B. Deveaud-Plédran, *Time-resolved spectroscopy on GaN nanocolumns grown by plasma assisted molecular beam epitaxy on Si substrates*, J. Appl. Phys. **105**, 013113 (2009).

Then, in the third part, we detail the interaction of excitons with basal plane stacking faults, a radiative kind of planar defect usually modeled as a three monolayers thick type-II quantum well.

- In Chapter IV, we first describe the distribution of stacking faults in *a*-plane GaN thick layers grown on sapphire. We then detail the diffusion mechanisms of excitons from fault-free material to the stacking faults. Particularly, we demonstrate that, at low-temperature, the diffusion of exciton towards stacking faults occur through successive capture / de-trapping mechanisms on donor atoms. We finally show how the local density in basal stacking faults affects the recombination rate of excitons. These results have been reported in:

P. Corfdir, P. Lefebvre, J. Levrat, A. Dussaigne, J.-D. Ganière, D. Martin, J. Ristić, T. Zhu, N. Grandjean, and B. Deveaud-Plédran, *Exciton localization on basal stacking faults in a-plane epitaxial lateral overgrown GaN grown by hydride vapor phase epitaxy*, Journal of Applied Physics **105**, 043102 (2009).

P. Corfdir, J. Ristić, P. Lefebvre, T. Zhu, D. Martin, A. Dussaigne, J.-D. Ganière, N. Grandjean, and B. Deveaud-Plédran, *Low-temperature time-resolved cathodoluminescence study of exciton dynamics involving basal stacking faults in a-plane GaN*, Applied Physics Letters **94**, 201115 (2009).

- In Chapter V, we detail the relaxation of excitons once they have been captured in stacking faults. We first present experimental evidences for the localization of excitons along the stacking fault plane. We then propose this localization to arise from the extrinsic donor atoms distributed in the vicinity of the stacking faults. Finally, we support our proposal with a calculation of the emission energy of donor - stacking fault bound exciton complexes. Specific sections of this Chapter have been published in:

P. Corfdir, P. Lefebvre, J. Ristić, J.-D. Ganière, and B. Deveaud-Plédran, *Electron localization by a donor in the vicinity of a basal stacking fault in GaN*, Physical Review B **80**, 153309 (2009).

- In Chapter VI, we switch to the study of *a*-plane (Al,Ga)N/GaN quantum wells grown on the non-polar GaN templates studied in the two previous chapters. After evidencing the absence of built-in electric fields in the heterostructures, we show by time-resolved cathodoluminescence that the dynamics of excitons is dominated by the capture on stacking faults. Then, we perform temperature- and polarization-resolved photoluminescence experiments to demonstrate that the intersection of stacking faults with an (Al,Ga)N/GaN quantum well results in the formation of quantum wires. These results were first presented in:

P. Corfdir, P. Lefebvre, L. Balet, S. Sonderegger, A. Dussaigne, T. Zhu, D. Martin, J.-D. Ganière, N. Grandjean, and B. Deveaud-Plédran, *Exciton recombination dynamics in a-plane (Al,Ga)N/GaN quantum wells probed by picosecond photo and cathodoluminescence*, Journal of Applied Physics **107**, 043524 (2010).

A. Dussaigne, P. Corfdir, J. Levrat, T. Zhu, D. Martin, P. Lefebvre, L. Balet, J.-D. Ganière, R. Butté, N. Grandjean, and B. Deveaud-Plédran, *One dimensional exciton*

luminescence induced by extended defects in GaN/(Al,Ga)N quantum wells, Semiconductor Science and Technology **26**, 025012 (2011).

The fourth part of this thesis is devoted to the study of non-polar (Al,Ga)N/GaN heterostructures grown on bulk GaN crystals. Thanks to the elimination of polarization fields and stacking faults, combined with the low-dislocation density of the layers, we are able to study the intrinsic dynamics of excitons in both the weak and strong confinement regimes.

- In Chapter VII, we first show that in photoluminescence experiments, the generated charge carriers are almost not affected by extended defects. We then evidence experimentally the quantization of exciton center-of-mass motion in a 200 nm thick GaN layers, and we detail why the energy relaxation of these quantized modes is so inefficient.

- In Chapter VIII, we study the temperature-dependence of excitons strongly confined in *a*-plane (Al,Ga)N/GaN quantum wells. We observe for the first time in nitrides -and up to 200 K- purely radiative recombinations for free excitons in a quantum well. We finally demonstrate that the efficiency drop observed at higher temperatures is due to the thermal escape of carriers out of the quantum well and to their subsequent non-radiative recombination in the disordered (Al,Ga)N barriers. This work has been accepted recently for publication:

P. Corfdir, J. Levrat, A. Dussaigne, P. Lefebvre, H. Teisseyre, I. Grzegory, T. Suski, J.-D. Ganière, N. Grandjean, and B. Deveaud-Plédran, *Intrinsic dynamics of weakly and strongly confined excitons in nonpolar nitride-based heterostructures*, accepted for publication in Physical Review B (2011).

In the last part of this manuscript, we finally provide a summary of our results, as well as perspectives for further investigations.

REFERENCES

[Ambacher1999] O. Ambacher, J. Smart, J. R. Shealy, N. G. Weimann, K. Chu, M. Murphy, W. J. Schaff, L. F. Eastmann, R. Dimitrov, L. Wittmer, M. Stutzmann, W. Rieger, and J. Hilsenbeck, J. Appl. Phys. **85**, 3222 (1999).

[Bernardini1997] F. Bernardini, V. Fiorentini, and D. Vanderbilt, Phys. Rev. B **56**, R10024 (1997).

[Butté2006] R. Butté, G. Christmann, E. Feltin, J. F. Carlin, M. Mosca, M. Ilegems, and N. Grandjean, Phys. Rev. B **78**, 033315 (2006).

[Christopoulos2007] S. Christopoulos, G. Baldassari Höger von Högersthal, A. J. D. Grundy, P. G. Lagoudakis, A. V. Kavokin, J. J. Baumberg, G. Christmann, R. Butté, J.-F. Carlin, and N. Grandjean, Phys. Rev. Lett. **98**, 126405 (2007).

[David2005] A. David, C. Meier, R. Sharma, F. S. Diana, S. P. DenBaars, E. Hu, S. Nakamura, C. Weisbuch, and H. Benisty, Appl. Phys. Lett. **87**, 101107 (2005).

[Deveaud1991] B. Deveaud, F. Clérot, N. roy, K. Satzke, B. Sermage, and D. S. Katzer, Phys. Rev. Lett. **67**, 2355 (1991).

[Dingle1971] R. Dingle, D. D. Sell, S. E. Stokowski, and M. Ilegems, Phys. Rev. B **4**, 1211 (1971).

[Dingle1974] R. Dingle, W. Wiegmann, and C. H. Henry, Phys. Rev. Lett. **33**, 827 (1974).

[Dingle1978] R. Dingle, H. L. Strörmer, A. C. Gossard, and W. Wiegmann, Appl. Phys. Lett. **33**, 665 (1978).

[Duan2000] X. F. Duan, and C. M. Lieber, J. Am. Chem. Soc. **122**, 188 (2000).

[Esaki1970] L. Esaki, and R. Tsu, IBM Journal of Research and Development **14**, 61 (1970).

[Goldberger2003] J. Goldberger, R. R. He, Y. F. Zhang, S. W. Lee, H. Q. Yan, H. J. Choi, and P. D. Yang, Nature **422**, 599 (2003).

[Hangleiter2005] A. Hangleiter, F. Hitzel, C. Netzel, D. Fuhrmann, U. Rossow, G. Ade, and P. Hinze, Phys. Rev. Lett. 95, 127402 (2005).

[Johnson2002] J. C. Johnson, H. J. Choi, K. P. Knutsen, R. D. Schaller, P. D. Yang, and R. J. Saykally, Nature Materials **1**, 106 (2002).

[Khan1993] M. A. Khan, A. Bhattarai, J. N. Kuznia, and D. T. Olson, Appl. Phys. Lett. **63**, 1214 (1993).

[Leroux1998] M. Leroux, N. Grandjean, M. Laügt, J. Massies, B. Gil, P. Lefebvre, and P. Bigenwald, Phys. Rev. B **58**, R13371 (1998).

[Nakamura1994] S. Nakamura, T. Mukai, and M. Senoh, Appl. Phys. Lett. **64**, 1687 (1994).

[Nakamura1995] S. Nakamura, M. Senoh, N. Iwasa, S. Nagahama, T. Yamada, and T. Mukai, Jpn. J. Appl. Phys. **34**, L1332 (1995).

[Nakamura1996] S. Nakamura, M. Senoh, S. Nagahama, N. Iwasa, T. Yamada, T. Matsushita, H. Kiyoku, and Y. Sugimoto, Jpn. J. Appl. Phys. **35**, L74 (1996).

[Nakamura1998] S. Nakamura, Science **281**, 956 (1998).

[Ponce1997] F. A. Ponce, and D. P. Bour, Nature **386**, 351 (1997).

[Razeghi1996] M. Razeghi, and A. Rogalski, J. Appl. Phys. 79, 7433 (1996).

[Reed2001] M. L. Reed, N. A. El-Masry, H. H. Stadelmaier, M. K. Ritums, M. J. Reed, C. A. Parker, J. C. Roberts, and S. M. Bedair, Appl. Phys. Lett. **79**, 3473 (2001).

[Semond2005] F. Semond, I. R. Sellers, F. Natali, D. Byrne, M. Leroux, J. Massies, N. Ollier, J. Leymarie, P. Disseix, A. Vasson, Appl. Phys. Lett. **87**, 021102 (2005).

[Sonderegger2006] S. Sonderegger, E. Feltin, M. Merano, A. Crottini, J. F. Carlin, R. Sachot, B. Deveaud, N. Grandjean, and J. D. Ganière, Appl. Phys. Lett. **89**, 232109 (2006).

[Steigerwald2002] D. A. Steigerwald, J. C. Bhat, D. Collins, R. M. Fletcher, M. O. Holcomb, M. J. Ludowise, P. S. Martin, and S. L. Rudaz, IEEE Journal on Selected Topics in Quantum Electronics **8**, 310 (2002).

[Taniyasu2006] Y. Taniyasu, M. Kasu, and T. Makimoto, Nature **441**, 325 (2006).

[VanDerZiel1975] J. P. van der Ziel, R. Dingle, R. C. Miller, W. Wiegmann, and J. W. A. Nordland, Appl. Phys. Lett. **26**, 463 (1975).

[Waltereit2000] P. Waltereit, O. Brandt, A. Trampert, H. T. Grahn, J. Menniger, M. Ramsteiner, M. Reiche, and K. H. Ploog, Nature **406**, 865 (2005).

[Weisbuch1992] C. Weisbuch, M. Nishioka, A. Ishikawa, and Y. Arakawa, Phys. Rev. Lett. **69**, 3314 (1992).

Part I

Generalities

Chapter I - Structural and optical properties of III-nitrides

The III-nitrides form a particular class of material among the semiconductors. Their emission can indeed been tuned continuously between infrared to deep UV. Even if our work is mainly devoted to the emission properties of GaN, it is important to understand its structural properties, as the electronic and emission properties of a semiconductor rely profoundly on the periodical arrangement of its atoms in the crystal. We thus describe, in this first Chapter, the wurtzite lattice structure, the stable crystal phase for all III-nitrides, and its ensuing electronic band structure. Although we do not detail the growth procedure for the various samples studied in this manuscript, we briefly discuss the major challenges related to the absence of substrate lattice-matched to GaN and to the internal polarizations of III-nitrides. Consequently, rather than a full description of the electronic properties of III-nitrides, this Chapter should be regarded as a summary of the basics elements needed for the understanding of the experimental work discussed in the next Chapters.

I.1. CRYSTAL STRUCTURE

I.1.1. Lattice parameters of binary and ternary III-nitride alloys

Although for specific growth conditions, GaN can crystallize in the metastable cubic zinc-blende phase [Lei1991], the stable phase for III-nitrides is the wurtzite. As shown in Figure 1.1, the wurtzite cell is characterized by the a and c lattice parameters, which give the extension of the cell along the [1000] and [0001] directions, respectively. In this structure, cations and N atoms are arranged in two hexagonal close-pack lattices shifted by $u.c$ along the [0001] direction, where u is the internal displacement parameter. While for the ideal wurtzite structure, ions are located in tetrahedral sites that verify $c / a = 1.633$ and $u = 0.375$, slight

deviations are observed for III-nitrides compounds due to the strong ionicity of the bonds (Table 1.1).
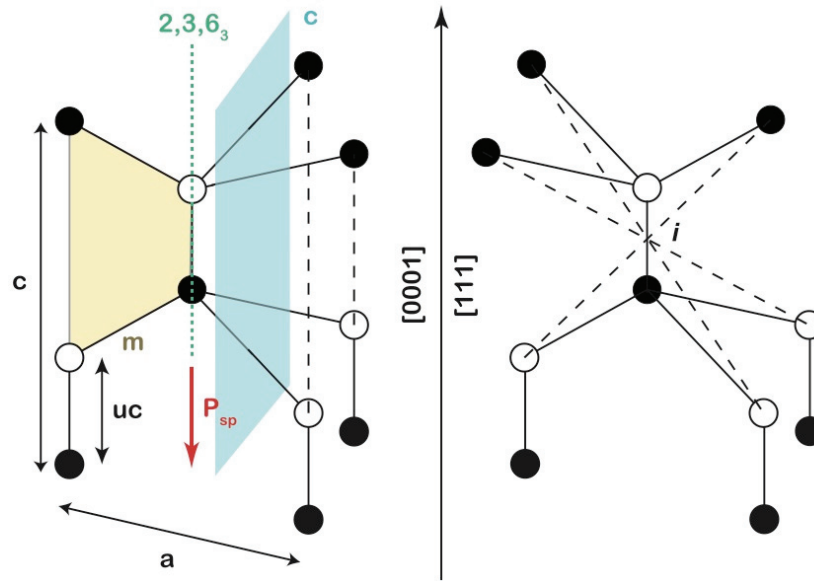
Figure 1.1: Wurtzite (left) and zinc-blende (right) structures. The positions of N and Ga atoms are displayed by open and full circles, respectively, and the bonds between atoms are shown with solid lines. Note that for both structures, the first and second neighbors of a given atom occupy the same sites. Contrary to the zinc-blende, the wurtzite has no inversion center (i), giving rise for GaN to a spontaneous polarization along [000-1]. Reflection and gliding planes (m,c), rotation (2,3) and helicoidal (6_3) axes are also shown.

Concerning the lattice constants of $Al_xGa_{1-x}N$ and $In_xGa_{1-x}N$ ternary alloys, they are given by the Vegard's law, *i.e.* a linear interpolation of the lattice parameters of their respective binary constituents [Ambacher2002].

Materials	GaN	InN	AlN	Ideal wurtzite
a	3.189	3.545	3.112	-
c	5.185	5.703	4.982	-
c / a	1.6259	1.6087	1.6009	1.633
u	0.3769	0.3787	0.3814	0.375

Table 1.1: Lattice parameters for wurtzite GaN, InN and AlN at 300 K. The deviation of the c / a and u parameters with respect to the ideal wurtzite cell is due to the ionicity of the bonds [Butté2007].

I.1.2. Polar and non-polar plane of the wurtzite

The most usual growth direction for III-nitrides is [0001], also referred as *c*-plane, (0001), or polar orientation. However, as shown below, GaN crystals grown perpendicularly to [0001] also raise a lot of interest from the scientific community. They are the so-called non-polar orientations, which gather the [11-20] *a*-planes and the [1-100] *m*-planes (Fig. 1.2).
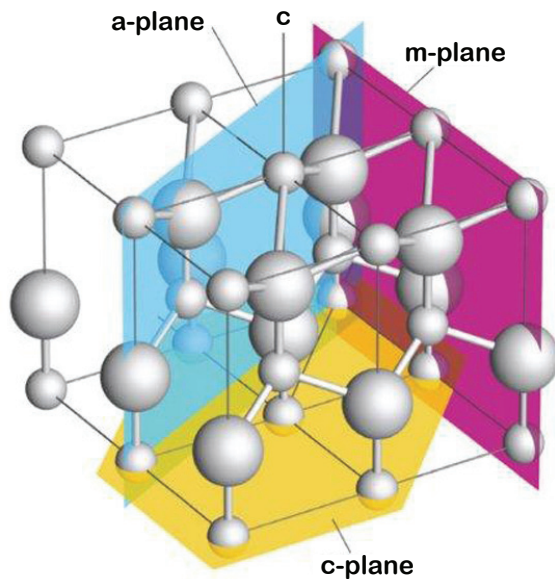
Figure 1.2: Structure of GaN in the wurtzite phase. The yellow plane is perpendicular to the polar, [0001] c-axis, along which most of the nitride-based heterostructures are grown. The non-polar a- (11-20) and m- (1-100) planes are also shown in blue and magenta, respectively (taken from [Ref1]).

I.1.3. Available substrates for the growth of polar and non-polar plane GaN

One of the major weaknesses of III-nitrides is the lack of lattice-matched substrates combined with the fact that the growth of GaN single crystals is complicated and expensive. In most cases, polar GaN is grown on sapphire, SiC or Si. While Si is at first sight the most attractive substrate regarding costs and integration of nitride-based devices into opto-electronics circuits, the mismatch of its lattice parameter and thermal expansion coefficient with those of GaN engender large densities of extended defects (dislocations, stacking faults) in the layers. From the defect-generation point-of-view, SiC seems more suitable for the heteroepitaxy of GaN. However, large SiC wafers are expensive and therefore not appropriate for mass-production. Despite its lattice mismatch of -14 % with GaN, sapphire is relatively cheap and 2 and 6 inches diameter wafers are available. It is therefore the most used substrate for the large-scale production of GaN layers.

Waltereit *et al.* were the first to prepare a heterostructure grown along a non-polar axis. They reported in 2000 the growth by MBE of a *m*-plane (Al,Ga)N/GaN QW grown on [100] γ-LiAlO$_2$ [Waltereit2000]. However, the instability of γ-LiAlO$_2$ at high temperature make it not suited for MOVPE growth. In 2002 and 2003, Craven *et al.* and Haskell *et al.* reported the growth of *a*-plane GaN layers on *r*-plane sapphire by MOVPE and HVPE, respectively [Craven2002,Haskell2003]. From then, the research focused on reducing the extended defect densities and improving the surface roughness (*see* [Haskell2007] *for a review*). In addition to LiAlO$_2$ and sapphire, other substrates such as ZnO, Si and SiC are available for the growth of non-polar layers.

In addition to the lattice mismatch between III-nitride and their substrates, one must also pay attention to the difference between their thermal expansion coefficients [Ambacher1998], as strain can be generated when cooling down the sample from growth to room temperature. Here again, sapphire present the most attractive properties for both the growth of polar and non-polar GaN (*see discussion in* [Zhu2009])

I.1.4. Reduction of defect densities of III-nitride structures

The lattice and thermal coefficient mismatches between III-nitrides and their substrates induce strain that relaxes through the generation of defects. Point and extended defects are imperfections in the regular arrangement of atoms in the crystal and have an extremely negative impact on the emission properties of the material. Vacancies as well as dislocations indeed induce dangling bonds, which act as non-radiative recombination centers for charge carriers [Nolte1990]. The heat generation resulting from such non-radiative recombinations is detrimental regarding the electronic performances of devices, and it is therefore mandatory to reduce the density of defects in the layers.

The most usual technique used for that purpose is the epitaxial lateral overgrowth (ELO), which has first been applied to the growth of polar GaN layers [Beaumont2001] and later to non-polar GaN [Imer2006,Ni2006]. Basically, this technique consists in patterning a GaN substrate with a dielectric mask (SiO$_2$, SiN$_x$) to filter the propagation of extended defects [Beaumont2001]. The growth conditions are first set to seed the growth only in the openings of the mask (the windows). Once the windows areas are filled by material, the growth occurs

vertically and laterally until coalescence of the successive ELO-wings. In the case of *c*-plane GaN, one can also take advantage of the bending of dislocations into the (0001) plane to further reduce the defect density [Gradecak2004]. In Chapters IV, V and VI, we will study *a*-plane III-nitride layers grown by HVPE on sapphire and processed by ELO. For further details on the growth and processing steps of these layers, we refer the reader to [Zhu2009].

An alternative growth technique has been proposed to drastically reduce the density of defect in GaN. The MBE growth of GaN under N-rich conditions results indeed in self-assembled defect-free nanocolumns aligned along [0001] with diameter of the order of 30-100 nm (*see* [Ristic2006]). The recombination properties of charge carriers in such nanostructures will be detailed in Chapter III.

Finally, bulk GaN crystal can also be realized by the high-pressure solution method [Grzegory2001]. Although GaN heterostructures deposited on the polar or non-polar facets of bulk GaN exhibit dislocation densities of the order of 10^5 cm^{-2}, the achievement of GaN single crystals is complicated. Due to the peculiar thermodynamics properties of the GaN-Ga-N_2 system, one indeed requires high temperature and N_2 pressure conditions (of the order of 20 kbar) to grow perfect single GaN crystals. Charge carrier dynamics in *a*-plane GaN quantum wells and thick layers will be described in Chapters VII and VIII.

I.2. BAND STRUCTURE OF III-NITRIDES

In order to describe correctly the light-matter interaction in semiconductors, one has first to understand the microscopic behavior of electrons in solids. Contrary to atoms physics, where electrons occupy discrete energy levels, the binding between atoms in solids leads to a degeneracy lifting for each energy level and to the formation of energy bands. In semiconductors and insulators, the intervals of forbidden energies between the energy bands are called bandgaps. At 0 K, the highest energy fully occupied band is called the valence band, while the lowest-energy empty band is called the conduction band. The particularity of semiconductors compared to insulators relies in the fact that the density of electrons occupying the conduction band (and thus the conductivity of the material) can be tuned by changing the temperature as well as by incorporation of impurities in the crystal. Concerning

light emission, it results from the recombination of a conduction electron with an empty state of the valence band, a hole.

In order to model a system with so many particles (electron density of the order of 10^{23} cm^{-3}), one first adopts the mean-field approximation, which states that all electrons experience the same potential $V(r)$ that respects the periodicity of the crystal. The Schrödinger equation for an electron with wave vector k and occupying the nth energy band is thus:

$$\left(\frac{p^2}{2m}+V(\vec{r})\right)\Psi_{n,\vec{k}}(\vec{r})=E_{n,\vec{k}}\Psi_{n,k}(\vec{r})$$

Eq.(1.1).

From the Bloch theorem, one writes the eigenstates $\Psi_{n,k}(r)$ as a product of a plane-wave $e^{i\vec{k}.\vec{r}}$ with a periodic function $u_{n,\vec{k}}(\vec{r})$ that has the periodicity of $V(r)$. Then, one only needs to solve [Yu2005]:

$$\left(\frac{p^2}{2m}+\hbar\frac{\vec{k}.\vec{p}}{m}+\frac{\hbar^2k^2}{2m}+V(r)\right)u_{n,\vec{k}}(r)=E_{n,\vec{k}}u_{n,\vec{k}}(r)$$

Eq.(1.2).

In order deduce the eigenstates and eigenergies of Eq.(1.2), one treats the second and third terms in the left-hand side of Eq.(1.2) as a perturbation: this is the so-called $k.p$ method. Practically, the $u_{n,\vec{k}}$ and $E_{n,\vec{k}}$ are expressed, for small k, through the coupling between the unperturbed wave functions and energies at $k = 0$:

$$u_{n,\vec{k}}=u_{n,0}+\frac{\hbar}{m}\sum_{n'\neq n}\frac{\left\langle u_{n,0}\left|\vec{k}.\vec{p}\right|u_{n',0}\right\rangle}{E_{n,0}-E_{n',0}}u_{n',0}$$

Eq.(1.3)

and

$$E_{n,\vec{k}}=E_{n,0}+\frac{\hbar^2k^2}{2m}+\frac{\hbar^2}{m^2}\sum_{n'\neq n}\frac{\left|\left\langle u_{n,0}\left|\vec{k}.\vec{p}\right|u_{n',0}\right\rangle\right|^2}{E_{n,0}-E_{n',0}}=E_{n,0}+\frac{\hbar^2k^2}{2m_{eff}}$$

Eq.(1.4),

where m_{eff} is the effective mass. Two major consequences arise from Eq.(1.4). First, the shape of the dispersion of the different energy bands for small wave vectors will be treated as elliptic paraboloids. Second, the larger the energy separation between two bands, the smaller their coupling. We note already that, when the energy maximum of the valence band corresponds to the same wave vector as the energy minimum of the conduction band, the bandgap is direct. In such a case, the radiative recombination of an electron-hole pair at quasi thermal equilibrium is an efficient process (*see* Eq.(1.10) in Section I.2.4). When the conduction and valence band edges do not correspond to the same wave vector, the bandgap is indirect and the recombination of conduction electrons occurs through non-radiative mechanisms.

In this section, we will first specify the amplitude of the bandgap for binary and ternary III-nitride alloys. We will then describe the consequences of the anisotropy of the wurtzite structure on the symmetry of the valence band. We will show, in particular, that the valence band is split in three distinct subbands called A, B and C and we will give analytical expressions for their respective energy band edges in strain free GaN. Next, we will give key indications to apply the *k.p* method when aiming at describing the energy dispersion of the three valence bands in the vicinity of the center of the first Brillouin zone.

We will then address the consequences of strain on the band structure of GaN grown on lattice-mismatched substrates along a polar or non-polar direction. Finally, supported by symmetry considerations, we will discuss the selection rules for an electron recombining from the conduction to the valence bands.

I.2.1 Energy bandgap

In a semiconductor, the energy bandgap E_g is defined as the energy difference between the conduction and valence band edges. III-nitrides always present a direct bandgap, which covers a large range of energy that goes from the mid-infrared for InN to the deep UV for AlN. As a general trend, the shorter the bond length, the larger E_g. At 10 K, the energy bandgap of unstrained GaN is 3.504 eV [Gil1995], while it is 6.089 eV for AlN [Feneberg2010]. Concerning InN, despite the amplitude of its energy band gap has been controversial for many years, it is now admitted that it is of the order of 0.7 eV [Wu2002].

Contrary to the lattice parameters, the bandgap of III-nitride ternary alloys do not exhibit a linear dependence with the composition x. This is mostly due to the fact that the lattice of a $Y_xZ_{1-x}N$ ternary alloy is distorted compared to the lattices of the YN and ZN binary alloys. The deviation from the linear dependence of $E_g(Y_xZ_{1-x}N)$ with x is characterized with the so-called bowing parameter b:

$$E_g(Y_xZ_{1-x}N) = xE_g(YN) + (1-x)E_g(ZN) - bx(1-x)$$ Eq.(1.5).

After a thorough review on experiments and modeling aiming at the determination of b for (Al,Ga)N, Vurgaftman *et al.* recommend to use $b = 0.7$ eV [Vurgaftman2003]. In the case of (In,Ga)N, we note large discrepancies in the values reported for b, which certainly arise from the uncertainties lying on the energy band gap of InN [Wu2002] as well as from the segregation of In atoms in the ternary alloy. Nevertheless, it is suggested that b should be of the order of 1.4 eV [Vurgaftman2003].

When temperature (T) is increased, the dilatation of the crystal leads to a decrease of $E_g(T)$. Usually, this behavior is described by the semi-empirical Varshni's law [Varshni1962]:

$$E_g(T) = E_g(0) - \frac{\alpha T^2}{\beta + T}$$ Eq.(1.6),

where α and β are adjustable fitting parameters. For GaN, α and β are typically equal to 0.8 meV / K and 800 K, respectively [Vurgaftman2003].

I.2.2 Energy edges of the conduction and valence bands

The wurtzite structure belongs to the point group $P6_3mc$, also called C$_{6v}$. As shown in Figure 1.1, the main symmetry operations consist of a 6_3 helicoidal rotation axis and of symmetry planes, all parallel to [0001]. The structure is anisotropic, which leads to a separation of the valence band into two distinct subbands. The energy splitting between the two valence band edges is the crystal field splitting Δ_{cr}. While in the case of GaN, Δ_{cr} is positive and of the order of 10-20 meV [Gil1997,Kumagai1998], it is negative for AlN. When

accounting for the spin-orbit interaction, the higher-energy valence subband of GaN is further split with an amplitude Δ_{so} of approximately 18 meV. One has consequently to deal with three distinct valence bands, which can be seen, when going from high to low energy, as the heavy hole, light hole and split-off bands. As a matter of fact, as heavy and light hole bands in strain free GaN present similar effective masses along k_z (Fig. 1.3), one rather denotes the three valence bands of GaN as A, B and C.
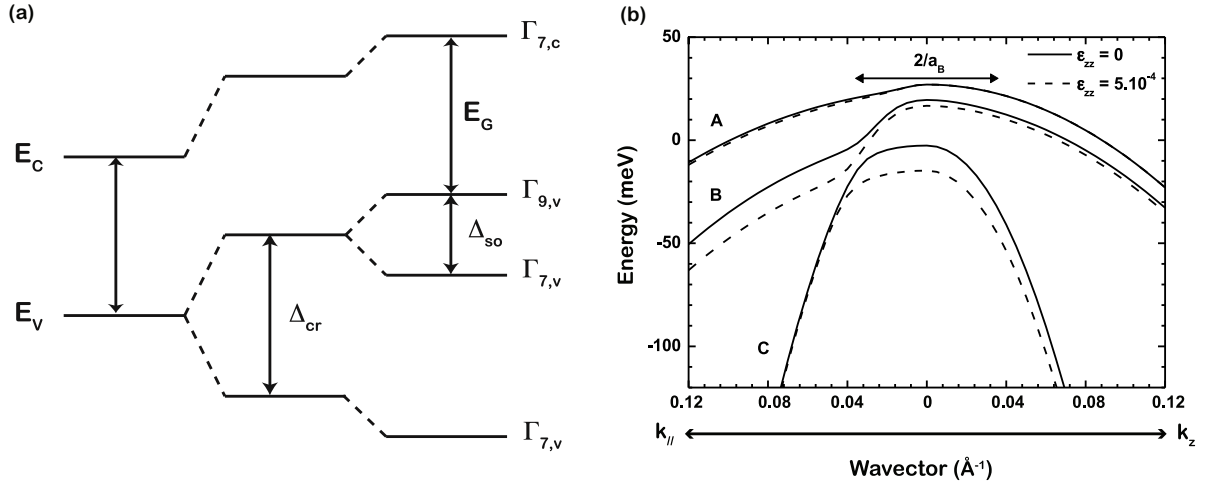
Figure 1.3: (a) Degeneracy lifting of GaN valence band edge by the crystal symmetry (Δ_{cr}) and the spin-orbit interaction (Δ_{so}) (b) A, B and C valence bands dispersions at the center of the Brillouin for strain-free GaN ($\varepsilon_{zz} = 0$) and GaN under biaxial strain in the (0001) plane ($\varepsilon_{zz} = 5.10^{-4}$). $2/a_B$ gives the extension in reciprocal space of the exciton wave function (taken from [Gallart2001]).

When modeling the valence band of GaN, the most common approximation is the quasi-cubic description. In this framework, the [0001] axis of the wurtzite corresponds to the [111] axis of the zinc-blende (sphalerite) structure. The first and second closest neighbors occupy indeed the same positions in both structures, justifying the analogy between the wurtzite and the zinc-blende. In order to account for the anisotropy of the hexagonal symmetry, one introduces an uniaxial deformation along the [111] axis. This allows reproducing the observed splitting of A and B valence band edges in strain free GaN. As described in detail in [Gallart2001,Winkelnkemper2008], it is possible to obtain analytically the conduction and valence energy band edges with respect to Δ_{cr} and Δ_{so}:

$$E_C = E_g + \Delta_{cr} + \frac{\Delta_{so}}{3} \qquad\qquad \text{Eq.(1.7)}$$

and

$$
\begin{cases}
E_{V,A} = \Delta_{cr} + \dfrac{\Delta_{so}}{3} \\[2mm]
E_{V,B} = \dfrac{1}{2}\left(\Delta_{cr} + \dfrac{\Delta_{so}}{3}\right) + \sqrt{\dfrac{1}{4}\left(\Delta_{cr} + \dfrac{\Delta_{so}}{3}\right)^2 + \dfrac{2\Delta_{so}^2}{9}} \\[2mm]
E_{V,C} = \dfrac{1}{2}\left(\Delta_{cr} + \dfrac{\Delta_{so}}{3}\right) - \sqrt{\dfrac{1}{4}\left(\Delta_{cr} + \dfrac{\Delta_{so}}{3}\right)^2 + \dfrac{2\Delta_{so}^2}{9}}
\end{cases}
\qquad \text{Eq.(1.8).}
$$

I.2.3 Conduction and valence bands effective masses

As shown in Eq.(1.4), the energy dispersions for small wave vectors are approximated by parabola and are characterized by effective masses m_{eff}. Accounting for the coupling of the conduction band with the valence bands, the *k.p* approximation yields an electron effective mass $m_e = 0.2\ m_0$ [Yu2005,Rinke2008], which is close to the what observed experimentally [Perlin1996]. For the valence bands, one has to account for the spin orbit interaction in addition to the *k.p* Hamiltonian [Yu2005]. In III-nitrides, the situation is even more complicated as:

(*i*) the spin-orbit coupling is weak, leading to a strong coupling between the C band and the higher energy A and B bands,

(*ii*) the wurtzite is modeled as a strained zinc-blende structure.

Provided the valence band parameters and the deformation potentials are known [Rinke2008], one can then diagonalize the full Hamiltonian to obtain the dispersion of the A, B and C valence bands close to the center of the Brillouin zone (Fig. 1.3). A pedestrian description of the method can be found in [Leroux2000], while more succinct ones are given in [Gallart2001,Winkelnkemper2008].

30

I.2.3 Effect of strain

The problem of GaN layers grown on lattice-mismatched substrates has been treated by the deformation potentials method by Gil and coworkers for polar [Gil1995,Alemu1998] and non-polar GaN [Gil1997b]. Assuming that the deformation tensor $\tilde{\varepsilon}$ is known, one has access to the dispersion of the bands close to the center of the Brillouin zone (*see* [Gallart2001,Winkelnkemper2008] for analytical expressions]. We note that biaxial strain in the basal (0001) plane does not introduce any additional anisotropy in the structure: it therefore only changes the energy edges and the effective masses of the conduction and valence bands. Similarly to what observed in other semiconductors, basal tensile strain reduces the energy band gap while compressive strain increases it (*see* Figure 2 in [Gil1997a]). The effect of biaxial strain on the dispersion of holes in polar GaN has been discussed in [Gallart2001]. In his thesis, the author shows that that for wave vectors smaller than 5.10^6 cm^{-1}, the dispersion of electrons and A holes is nearly isotropic and well approximated by parabola. Regarding the extension in *k*-space of exciton wave function (*see* below), he then concludes that even in strained layers, exciton A can be treated as isotropic, while it is always mandatory to account for the anisotropicity of B and C effective masses (Fig. 1.3).

I.2.4 Selections rules for band-to-band transitions

In semiconductors, the emission resulting from the recombination of an electron from the conduction to the valence bands are in the optical energy range (from 0.7 to 6.2 eV for III-nitrides). The amplitude variation of the electric field is negligible at the atomic scale and the light-matter interaction can therefore be treated in the dipolar approximation. The interaction $W = \dfrac{e}{m} A.p$ between a harmonic radiation field $A = \dfrac{A_0}{2} e^{i(\vec{k}_{ph}.\vec{r} - \omega t)}$ and an electron with momentum *p* is usually seen as a perturbation, and we can express the electron-hole recombination probability with time W_{cv} with Fermi's Golden rule [Folliot2006]:

$$W_{cv} = \left\langle u_h(r) e^{i\vec{k}_h \vec{r}_h} \left| W \right| u_e(r) e^{i\vec{k}_e \vec{r}_e} \right\rangle = \frac{eA}{2m} |p_{cv}| \delta(\vec{k}_e - \vec{k}_h)$$ Eq.(1.9),

where we have neglected the photon wave vector and where $|p_{cv}| = \langle u_h(r)|p|u_e(r)\rangle$ is the momentum matrix element between the conduction and the valence bands. The recombination rate Γ is then given by:

$$\Gamma = \frac{e^2 \pi A^2}{2m^2\hbar}|p_{cv}|^2 \delta(\vec{k}_e - \vec{k}_h)$$ Eq.(1.10).

We are now able to qualitatively understand how the symmetry of the crystal affects the emission properties. The electron and hole wave functions u_e and u_h are respectively *s*- and *p*-like [Yu2005]. Developing u_h on an orthonormal basis (*X,Y,Z*), and accounting for the fact that the operators p_X, p_Y and p_Z are similar to derivatives with respect to *X*, *Y* and *Z*, respectively, then [Leroux2000]:

$$\Gamma \propto \left|\langle S|\partial/\partial x|X\rangle\right|^2 = \left|\langle S|\partial/\partial y|Y\rangle\right|^2 = \left|\langle S|\partial/\partial z|Z\rangle\right|^2 \neq 0$$ Eq.(1.11)

and

$$\Gamma = \left|\langle S|\partial/\partial x|Y,Z\rangle\right|^2 = \left|\langle S|\partial/\partial y|X,Z\rangle\right|^2 = \left|\langle S|\partial/\partial z|X,Y\rangle\right|^2 = 0$$ Eq.(1.12).

In 1957, [Dresselhaus1957] was the first to consider the consequences the anisotropy of wurtzite crystals on their emission properties. To treat this problem, we first set the *Z*-axis of the (*X,Y,Z*) orthonormal basis parallel to the *c*-axis. Accounting for the symmetry of the wurtzite and for the spin-orbit interaction, [Birman1959] demonstrated that the symmetry at the center of Brillouin zone was Γ_7 for the conduction band, while it was Γ_9 for the A-valence band and Γ_7 for the B and C valence bands [note1]. In other words, the wave function for the A-valence band is $X \pm iY$ while it is $N_1(X \pm iY) + N_2 Z$ for the B and C bands, where $N_{1,2}$ are constants [Leroux2000]. From the character table of the irreducible representations of C_{6v} [Hopfield1960], we obtain that a transition from Γ_7 to Γ_9 is allowed only for light polarized perpendicular to the *c*-axis (*Z*) while a transition from Γ_7 to Γ_7 is allowed for all polarization (Fig. 1.4). The selection rules for band-to-band transitions (also true for excitons) have been verified experimentally by [Dingle1971].

To treat the case of GaN under biaxial strain in (0001), it is important to study the decomposition of Γ_7 wave functions in the (X,Y,Z) basis with respect to the crystal field Δ_{cr}. It has indeed been demonstrated by Gil *et al.* that drastic changes in the oscillator strength should be observed for the $\Gamma_7 \otimes \Gamma_7$ transitions [Gil1997a]. If we consider a *c*-plane GaN layer under strong biaxial compressive strain in the (0001) plane, the wave function of the C-valence band tends indeed to Z (N_1 tends to 0): absorption (*emission*) from (*to*) the C-valence band is therefore forbidden for light polarized perpendicular to [0001]. Inversely, for strong tensile strain, absorption from the B valence band is not observed for light polarization in the *c*-plane.
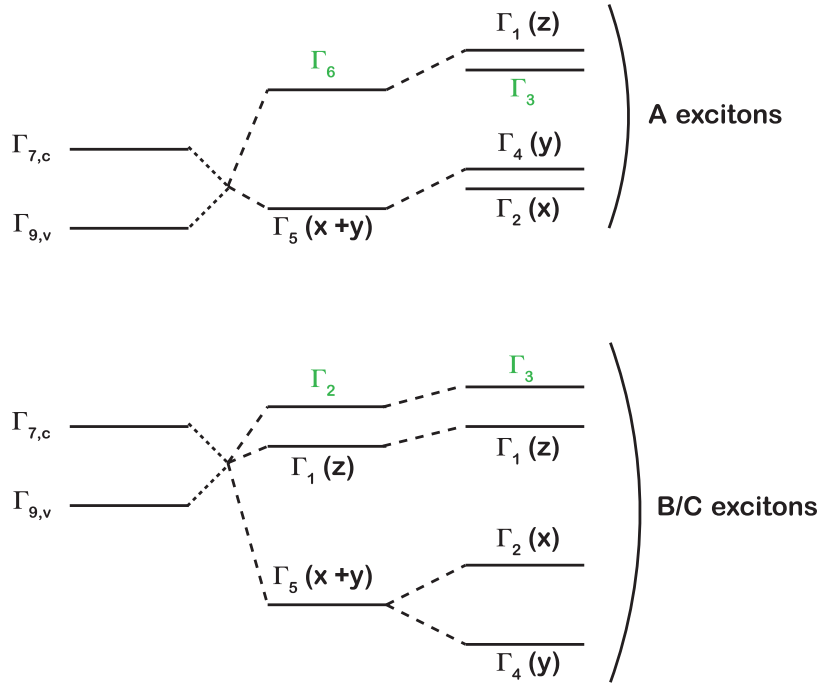
Figure 1.4: From the multiplication tables for the C_{6v} point group [Hopfield1960], one obtains the symmetry of A, B and C excitons. While exciton A is only coupled to light polarized perpendicularly to [0001], excitons B and C are optically active for all geometries. In the case of non-polar GaN grown on lattice-mismatched substrates, the crystal symmetry is reduced from hexagonal to orthorhombic, which gives rise to an additional splitting of the exciton states. The optically inactive states are labeled in green (see [Gil1997b]).

When growing GaN along a non-polar axis on lattice-mismatched substrates, the crystal symmetry is reduced from hexagonal to orthorhombic [Gil1997b]. Additional splittings of the valence band as well as further complications regarding the recombination

selection rules are then introduced (Fig. 1.4). Let us note, however, that the energy splittings of the A, B and C valence band edges are negligible compared to the inhomogeneous broadenings of the emission lines (Fig.1.5). The same goes for the selection rules: for *a*-plane GaN layers under "reasonable" strain, the excitonic luminescence at 10 K is essentially polarized perpendicular to [0001] (*see* [Gühne2007] and Chapter VI).
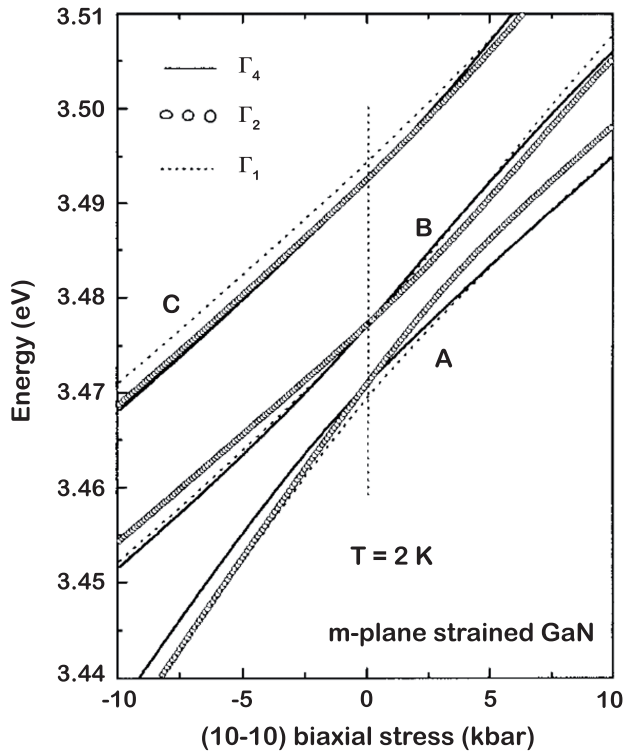
Figure 1.5: Energy of the optically active Γ₁, Γ₂, and Γ₄ excitons for GaN biaxially strained in the non-polar m-plane. Positive strain corresponds to biaxial compression (taken from [Gil1997b]).

I.3. EXCITONS IN BULK GaN

In the previous section, when discussing the electron-hole recombination, we systematically neglected the Coulomb interaction between these two particles. Consequently, after summing Eq.(1.9) over all possible transitions between the electron and the hole, one expects that the absorption is zero for photon of energy below E_g. This is not true experimentally, as sharp absorption lines are observed few meV below the bandgap [Sturge1962]. Similarly, the low-temperature emission spectra of semiconductors are dominated by transitions at energies lower than E_g.

In the following, we will first show that accounting for the Coulomb interaction between electron and hole strongly reshapes the absorption and emission edges of semiconductors as it gives rise to a bound state called the exciton. Then, we will detail the coupling of excitons with light and we will finally describe the energy relaxation of excitons in bulk semiconductors.

I.2.3 Exciton binding energy

As illustrated in Figure 1.3, the dispersions of electrons and A holes are nearly isotropic and can be approximated by parabola for small wave vectors:

$$E(k) = E_0 + \frac{\hbar^2 k_{e,h}^2}{2m_{e,h}}$$

Eq.(1.13),

where E_0, k_e (k_h) and m_e (m_h) are the electron (*hole*) conduction (*valence*) energy band edge, wave vector and effective mass, respectively. So far, however, we did not account for the Coulomb interaction between electrons and holes. Still, the motion of electrons and holes are correlated, giving rise to a bound state called exciton. In III-V and II-VI semiconductors, the strong dielectric constant ε results in a partial screening by the valence electrons of the Coulomb interaction between the electron in the conduction band and the hole in the valence band. As a consequence, excitons are weakly bound and the radius of the electron orbit around the hole is much larger than the inter-atomic distances [Wannier1937].

In continuous-wave experiments and under the assumption that the system is at thermal equilibrium, one safely expects excitons to dominate the emission spectrum. It is however questionable if it is also the case under pulsed experiments. To answer this question, [Toyozawa1959] has compared the rate for the radiative annihilation of an electron-hole pair with the one for the phonon-assisted binding of an electron-hole pair into excitons. He showed that the latter mechanism was the more efficient and that exciton recombination should therefore dominate the dynamics of charge carriers.

The Hamiltonian for a single exciton is given by

$$H_X = \frac{p_e^2}{2m_e} + \frac{p_h^2}{2m_h} - \frac{e^2}{4\pi\varepsilon\|\vec{r}_e - \vec{r}_h\|} + E_g \qquad \text{Eq.(1.14).}$$

The Coulomb term only affects the relative motion of the electron and the hole. The exciton Hamiltonian is therefore generally separated in two terms, H_{CM} and H_{rel}, that respectively describe the center-of-mass motion of the exciton and the relative electron and hole motion. With $M = m_e + m_h$ the exciton mass and $\vec{R}$ the position of its center-of-mass,

$$H_{CM} = \frac{\hbar^2}{2M}\nabla_R^2 + E_g \qquad \text{Eq.(1.15).}$$

Concerning electron and hole relative motion, we write

$$H_{rel} = \frac{\hbar^2}{2\mu}\nabla_r^2 - \frac{e^2}{4\pi\varepsilon r} \qquad \text{Eq.(1.16),}$$

where μ is the exciton reduced mass and $\vec{r} = \vec{r}_e - \vec{r}_h$ is the relative position of electron and hole. The exciton wave function Ψ is given by the product of the eigenstates of H_{CM} and H_{rel}, which corresponds to a plane wave multiplied by a hydrogen-like wave function. For the 1s ground-state exciton, it gives

$$\Psi(\vec{r}, \vec{R}) = \frac{1}{\sqrt{\Omega}} e^{i\vec{K}.\vec{r}} \left(\frac{1}{\pi a_B^3}\right)^{1/2} Exp\left(-\frac{r}{a_B}\right) \qquad \text{Eq.(1.17),}$$

where $\vec{K} = \vec{k}_e + \vec{k}_h$ is the exciton wave vector, Ω is the volume of the crystal and

$$a_B = \frac{4\pi\hbar^2\varepsilon}{\mu e^2} \qquad \text{Eq.(1.18)}$$

is the 1s exciton Bohr radius. The corresponding eigenenergy for an ns exciton is

$$E_n = E_g + \frac{\hbar^2 K^2}{2M} - E_B \qquad \text{Eq.(1.19),}$$

with E_B the exciton binding energy:

$$E_B = \frac{1}{n^2} \frac{\mu e^2}{32\hbar^2 \pi^2 \varepsilon^2}$$ Eq.(1.20).

III-nitrides exhibit a positive birefringence, with extraordinary axis parallel to [0001] (Table 1.2). However, using for GaN isotropic masses $m_e = 0.2\ m_0$, $m_h = 1.1\ m_0$ and dielectric constant $\varepsilon = 9.5$, we find $E_B = 25$ meV, which is close to the experimental reports [Kornitzer1999].

Material	GaN	AlN
$\varepsilon_\perp$	9.5	7.24
ε_z	10.4	8.69

Table 1.2: Ordinary ($\varepsilon_\perp$) and extraodinary (ε_z) dielectric constants for GaN [Barker1973] and AlN [Ikeda2007].

I.2.3 Intrinsic dynamics of exciton-polaritons

As shown by Eq.(1.17), excitons are delocalized in the crystal. As a consequence of the translational invariance, the wave vector of the exciton must be conserved, which means that an exciton with wave vector $\vec{K}$ can only emit a photon with wave vector $\vec{k}_{ph} = \vec{K}$. The exciton and the photon are thus strongly coupled and the eigenstates of this new system are called exciton-polaritons or, for simplicity, polaritons. In absence of damping and assuming that excitons have an infinite mass, a splitting appears between the two polariton branches and there is no allowed mode for energies comprised between E_g - E_B and E_g - E_B + Δ_{LT}. The longitudinal-transverse splitting Δ_{LT} arises from the electron-hole exchange interaction and is a direct measure of the coupling between exciton and light, as it can written as a function of exciton oscillator strength [Andreani1990]. In the quasi-particle model, the admixed polariton modes are referred as exciton-like and photon-like depending on the photon weight of their wave function [Hopfield1958].

As stationary states, polaritons in a perfect and infinite crystal have an infinite radiative lifetime. In a crystal with finite dimensions, the radiative decay of polaritons corresponds in fact to the relaxation and to the phonon-assisted conversion of exciton-like polaritons into photon-like ones [Toyozawa1959]. Under non-resonant excitation, exciton-like polaritons with high $\vec{K}$ form upon the binding of an electron-hole pair. These polaritons relax efficiently, through the emission of optical phonons, towards the flat region of the dispersion curve, also denoted as bottleneck (Fig. 1.6). Then, in order to escape the crystal, exciton-like polaritons must lose additional energy in order to reach regions of the dispersion curve where their photon weight is larger. This last step in the relaxation process of polaritons occurs through the emission of acoustic phonons and is not efficient for many reasons:

(*i*) the exciton-acoustic phonon scattering rate is much lower than the scattering rate of excitons with LO phonons [Viswanath1998],

(*ii*) the density of final states is reduced due to the small mass of photon-like polaritons,

(*iii*) the larger the wave vector of the emitted phonon, the lower the scattering rate.

Accounting for the boundary conditions imposed by the finite dimensions of the crystal [Pekar1958] and for the scattering of polaritons with acoustic phonons, [Rappel1988] have calculated the lifetime of polaritons to be of the order of 10 μs for a 1 μm thick GaAs crystal at 1 K. It should be noted that in ionic crystals such as ZnO or GaN, exciton-like polaritons in the bottleneck couple efficiently to optical phonons and give rise to transitions lying below the excitonic bandgap [Huang1950]. In GaN, these so-called LO-phonon replicas lie 91 meV below the zero-phonon line of the exciton ground state [Leroux1999a].
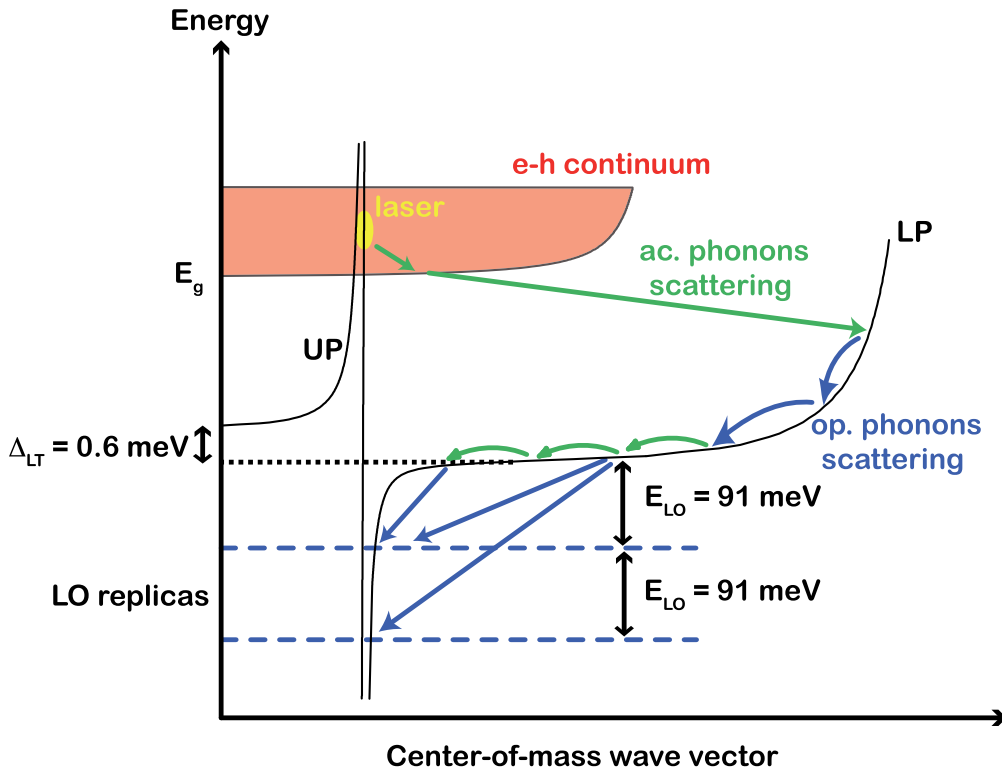
Figure 1.6: Schematic representation of the polariton dispersion assuming only one exciton branch. Electrons and holes bind into free excitons through the emission of acoustic phonons. High-K excitons relax through the emission of optical and acoustic phonons (blue and green arrows, respectively). The conversion of exciton-like polaritons give rise to emission at the bottleneck energy minus n-times the LO phonon energy, with n an integer.

In the specific case of GaN, the polariton picture described above is complicated by the fact that we have to deal with several exciton branches with distinct coupling strength with light [Paskov2004]. Such a refined treatment of the exciton-light coupling will be done in Chapter VII when studying the confinement of the center-of-mass motion of exciton-polaritons in a 200 nm thick GaN epilayer.

I.2.4 Charge carrier dynamics in "real" three-dimensional systems

In practice, however, the decay rate of exciton-polaritons is not limited by radiative phenomena described above. Excitons bind indeed to neutral donor and acceptor atoms to form neutral donor (D°X) and acceptor bound excitons (A°X), respectively. As demonstrated

experimentally by [Hwang1973], the effective decay time of free excitons in GaAs thick layers at 10 K is dominated by the capture on neutral impurities. He observed, in particular, an increase in free exciton PL lifetime when decreasing the concentration in donor and acceptor impurities. In the case of GaN, the initial dynamics of free excitons is dominated by their binding on Si and O donor atoms and Mg acceptor atoms (Fig. 1.7), and the resulting D°X and A°X complexes give rise, in strain free GaN, to emission lines at 3.471 and 3.465 eV, respectively [Kornitzer1999, *see also* Appendix II]. Once the impurity bound / free exciton system is at quasi thermal equilibrium, its decay is limited by the radiative lifetime of impurity bound excitons, as the latter species exhibit a much larger recombination rate [Rashba1962].

When increasing the temperature above typically 30 K in GaN [Leroux1999a], excitons get delocalized and the decrease of both emission intensity and lifetimes is observed. The latter observation thus testifies that excitons are also extremely sensitive to non-radiative point and extended defects such as vacancies or dislocations.

The interaction of excitons with particular kinds of defects will be investigated in this work. The case of excitons bound to impurities in dislocation-free nanostructures will be addressed in Chapter III, while we will consider in Chapter IV the diffusion and trapping of excitons by extended defects.
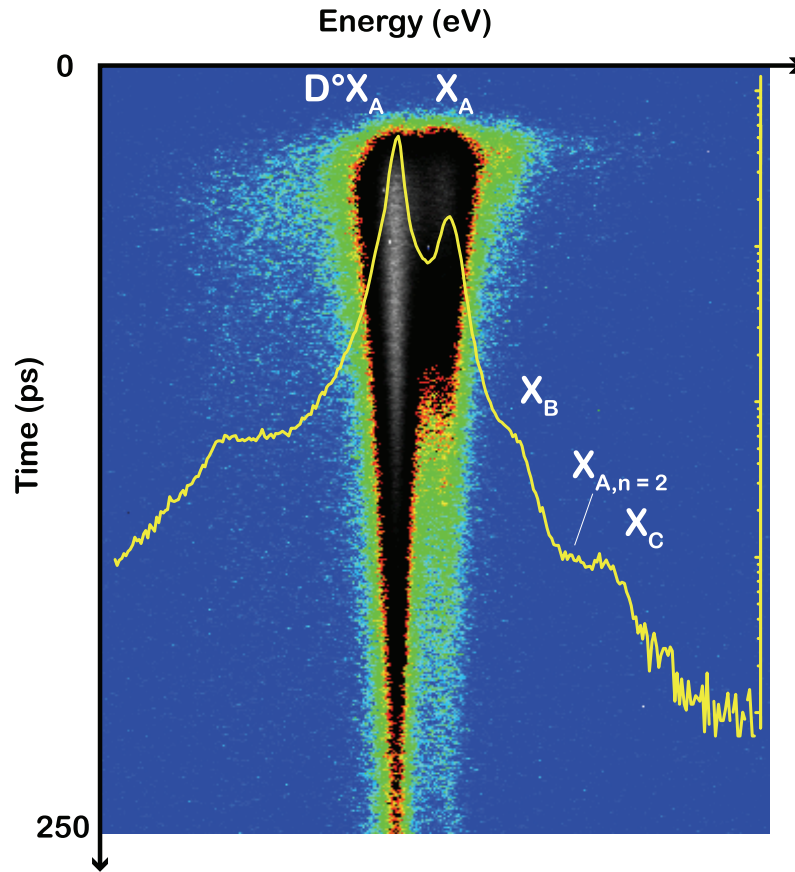
Figure 1.7: Time-resolved PL spectrum at 10 K of a c-plane GaN layer processed by ELO. Yellow solid line is the time-integrated PL spectrum in semi-log scale (the corresponding y-scale is shown in yellow). During the 10 first ps, the emission is dominated by free exciton A, B and C emissions. The fast initial decay of free excitons is due to thermalization and capture to the capture on donor. The rise of the D°X PL thus corresponds to the decay of free exciton lines. At long delays, D°X$_A$ and X$_A$ are in thermal equilibrium: their emissions show consequently the same effective decays.

I.3. POLARIZATION FREE (Al,Ga)N/GaN QUANTUM WELLS

Thanks to major improvements in the growth techniques during the seventies, the realization of complex semiconducting heterostructures was made possible. The interest in low-dimensional structures arises from the possibility of tuning the transport and emission properties of the structure [Capasso1987]. Another major implication of low-dimensional structures relies on their reduced density of states, allowing for a decrease of the lasing threshold.

Here, we discuss the properties of excitons confined in polarization-free (Al,Ga)N/GaN quantum wells. Contrary to III-arsenides, we will show that excitons dominate the emission properties of GaN QWs up to room temperature, as their binding energy is typically of 40-50 meV. Then, we describe how the lack of translational invariance along the growth axis modifies the coupling of exciton with light. We note, finally, that the case of GaN QWs with confinement axis parallel to [0001] will be treated in Section I.4.

I.3.1 Exciton binding energy in (Al,Ga)N/GaN quantum wells

Similarly to what we presented for bulk materials, excitons are also the elementary excitation of QWs [Dingle1974]. In a type I quantum well (QW), both electrons and holes are confined within the same layer by potential barriers $V_e(z_e)$ and $V_h(z_h)$, respectively (the case of type II QW will be treated in Chapter IV). In the case of the strong confinement regime, the QW width L is of the order or smaller than the bulk exciton Bohr radius a_B. We first consider an uncorrelated electron and hole pair confined along the z-axis and free to move along the QW plane. Its energy is given by:

$$\Delta_{EH} = E_g + e_1 + h_1 + \frac{\hbar^2 k_{e,\perp}^2}{2m_e} + \frac{\hbar^2 k_{h,\perp}^2}{2m_h} \qquad \text{Eq.(1.21)},$$

where e_1 (h_1), m_e (m_h) and $\vec{k}_{e,\perp}$ ($\vec{k}_{h,\perp}$) are the electron (*hole*) $n = 1$ confined energy, effective and wave vector, respectively. If we now account for the Coulomb interaction between electron and hole, then the Hamiltonian for the QW exciton is:

$$H_X = \frac{p_e^2}{2m_e} + \frac{p_h^2}{2m_h} - \frac{e^2}{4\pi\varepsilon \left\| \vec{r}_e - \vec{r}_h \right\|} + V_e(z_e) + V_h(z_h) + E_g \qquad \text{Eq.(1.22).}$$

The in-plane electron and hole positions are $\vec{\rho}_e$ and $\vec{\rho}_h$, while their in-plane wave vectors are $\vec{k}_{e,\perp}$ and $\vec{k}_{h,\perp}$, respectively. With $\vec{\rho}$ the electron-hole relative position in-plane position, and $\vec{R}_\perp$ and $\vec{K}_\perp$ the in-plane position and wave vectors of exciton center-of-mass, then [Bastard1990]:

$$H_X = -\frac{\hbar^2}{2}\frac{\partial}{\partial z_e}\left(\frac{1}{m_e}\frac{\partial}{\partial z_e}\right) - \frac{\hbar^2}{2}\frac{\partial}{\partial z_h}\left(\frac{1}{m_h}\frac{\partial}{\partial z_h}\right) + V_e(z_e) + V_h(z_h) + E_g$$
$$-\frac{\hbar^2}{2M}\nabla_{R_\perp}^2 - \frac{\hbar^2}{2\mu}\nabla_\rho^2 - \frac{e^2}{4\pi\varepsilon\sqrt{\rho^2 + (z_e - z_h)^2}}$$

Eq.(1.23).

Similarly to the procedure adopted for the bulk exciton, we separate the solution Ψ of $H_X\Psi = E_X\Psi$ into a plane wave propagating in the two-dimensional QW and a hydrogen-like wave function. For simplicity, we separate in the latter the electron and hole motions. This is justified by the fact that, in this thesis, the width of the studied QWs will in general be of the order or smaller than the bulk exciton Bohr radius [Bastard1982]. The 1s solution Ψ is thus of the form

$$\Psi(\vec{r}_e, \vec{r}_h) = \frac{1}{\sqrt{S}}e^{i\vec{K}_\perp \cdot \vec{R}_\perp}Nf_e(z_e)f_h(z_h)Exp\left(-\frac{\rho}{a_B}\right)$$

Eq.(1.24),

where S is the surface of the QW plane , N is a normalization coefficient and a_B is a pseudo in-plane Bohr radius. The electron and hole envelope functions f_e and f_h are obtained by variational calculations in the effective potential formalism, where the variational parameter is the in-plane extension of the exciton wave function a_B [Wu1988,Zimmermann1993]. In practice, we will not account for the dielectric constant mismatch between the well and the barrier. Although we use different effective masses for the well and the barriers, we will assume the in-plane and on-axis masses to be the same. In our opinion, when modeling excitons in nitride-based QW, these approximations are justified by the fact that:

(*i*) the hole effective masses depends strongly on the strain state of the QW, which is seldom known accurately

(*ii*) the conduction band offset $\Delta E_c/\Delta E_g$ is not determined precisely. In this thesis, we will use systematically $\Delta E_c/\Delta E_g = 0.7$ for (Al,Ga)N/GaN QWs.

Once the energy of the exciton, Δ_X, is minimized against a_B, one gets the 1s exciton binding energy:

$$E_B = \Delta_{EH} - \Delta_X \qquad\qquad \text{Eq.(1.25).}$$

The energy dispersion of an exciton free to move along the QW plane is then given by

$$E_X(K_\perp) = \Delta_{EH} - E_B + \frac{\hbar^2 K_\perp^2}{2M} \qquad\qquad \text{Eq.(1.26).}$$
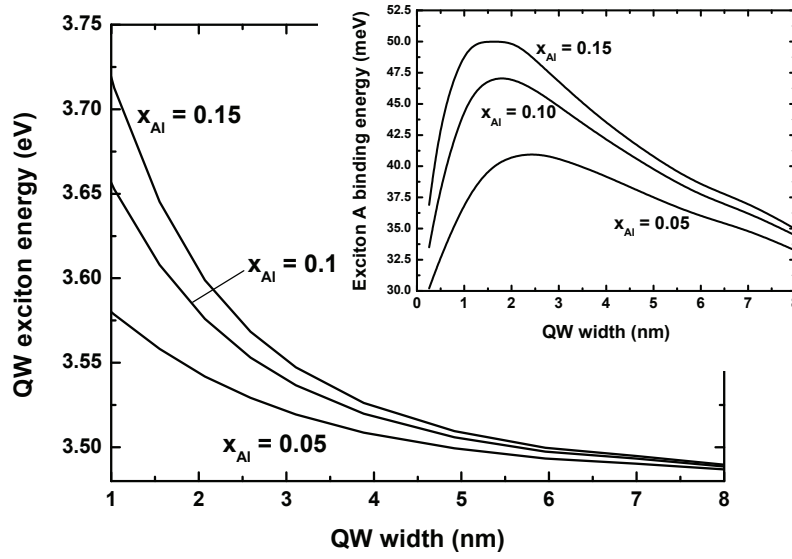
Figure 1.8: Energy of an exciton confined in a non-polar Al$_x$Ga$_{1-x}$N/GaN QW, with respect to the QW width, for x between 0.05 and 0.15. Insert: Exciton binding energy with respect to the QW width.

Assuming that only excitons with small in-plane wave vectors can recombine (*see* below and Appendix IV for justification), the exciton emission energy is equal to Δ_X. For an infinitely thin QW with infinitely high barriers, the exciton is truly bi-dimensional and its binding energy is equal to four times the bulk binding energy [Bastard1982]. For real QW structures, the exciton wave function leaks into the barriers. As a consequence, when decreasing the width L of the GaN layer embedded between two (Al,Ga)N barriers, the increase in exciton binding due to confinement saturates for $L \sim 2$ nm, and then decreases back towards the bulk (Al,Ga)N exciton binding energy (Fig. 1.8).

I.3.2 Exciton radiative lifetime

Contrary to the interaction between light and an exciton in a bulk semiconductor, the effect of a radiation field on an exciton confined in QW can be treated by the time-dependent perturbation theory. The radiative rate of an exciton can thus be calculated using Fermi's Golden rule. Moreover, as we are only interested here in one-photon emission processes, we restrict ourselves to the first order terms of the perturbation. As described thoroughly in [Andreani1995] and summarized in Appendix IV, the radiative recombination rate of excitons with in-plane wave vector $\vec{K}_\perp$ and polarized perpendicular to the confinement axis is

$$\Gamma_0 = \frac{e^2 f_{xy}}{2\varepsilon_0 n m_0 c S} \sum_{K_\perp} \left(\frac{1}{\sqrt{1-\left(K_\perp / k_0\right)^2}} + \sqrt{1-\left(K_\perp / k_0\right)^2} \right) \theta(k_0 - K_\perp) \qquad \text{Eq.(1.27).}$$

In Eq.(1.24), we have written that the exciton is delocalized along the whole plane of the QW. Contrary to the bulk case, the lack of translational invariance along the z-axis implies that only the in-plane components of the exciton wave vector must be conserved. As the electromagnetic field is three-dimensional, an exciton with in-plane wave vector $\vec{K}_\perp$ can couple with a continuum of photon states with wave vector $\vec{k}_0$. The z-component of the photon wave vector is given by $k_z = \sqrt{k_0^2 - K_\perp^2}$ and the radiative decay of an exciton is thus forbidden for $K_\perp > k_0 = \frac{1}{c}\sqrt{\frac{\varepsilon}{\varepsilon_0}}E_X(0)$, as illustrated by the Heaviside function θ in the right-hand side of Eq.(1.27). For the trial wave function chosen in Eq.(1.24), we find that the exciton oscillator strength per units area is:

$$\frac{f_{xy}}{S} = \frac{2p_{cv}^2}{ME_X}\left|\int f_e(z_e)f_h(z_h)dz\right|^2 \frac{2}{\pi a_B^2} \qquad \text{Eq.(1.28).}$$

Using the Kane parameters given in [Rinke2008], we find an oscillator strength of the order of 5.10^{13} cm^{-2} for an exciton confined in a thick (Al,Ga)N/GaN QW grown along a non-polar axis (thick enough for $\left|\int f_e(z_e)f_h(z_h)dz\right|^2 = 1$). At 0 K, only states lying within the light cone ($K_\perp < k_0$) are populated. The radiative decay of excitons is therefore efficient and occurs

within a few picoseconds [Andreani1991,Deveaud1991]. At higher temperatures, states with larger in-plane wave vectors are populated, which results in a linear increase of exciton radiative lifetime with temperatures. Note also that for real structures, the QW interfaces are rough, giving rise to localized exciton states, which usually dominate the low-temperature QW emission properties [Weisbuch1981]. In fact, the temperature-dependence of exciton radiative lifetime depends on the density in localized states, even when the delocalization of excitons towards the two-dimensional continuum of states is activated [Citrin1993]. For more detail, we refer the reader to Appendix IV and Chapter VIII.

I.4. INTERNAL POLARIZATIONS AND QUANTUM CONFINED STARK EFFECT

As previously demonstrated when presenting the band structure of GaN, the anisotropy of the wurtzite structure has strong consequences on the electronic properties of III-nitrides compared to the other III-V semiconductors. However, the most critical consequence of anisotropy emerges only when having a look to heterostructures. In Figure 1.1, we have shown that GaN exhibited an internal polarization aligned along [0001]. The polarization discontinuities at the interfaces of heterostructures, such as QW or quantum dots, grown perpendicular to the *c*-axis generate strong built-in electric fields, thus producing the quantum confined Stark effect.

In this section, we discuss the outcomes of the quantum confined Stark effect on the emission properties of (Al,Ga)N/GaN QWs grown along the polar *c*-axis. We especially stress the role of built-in electric fields on the recombination dynamics of excitons confined in such QWs, and we finally understand the importance of growing III-nitrides along non-polar axes.

I.4.1 Spontaneous polarization

Due to the non-centrosymmetry of wurtzite binary crystals, the barycenters of positive and negative charges are not superimposed, which leads to the apparition of a spontaneous polarization along the *c*-axis. The amplitude of this spontaneous polarization depends on the

structural properties of the crystal such as the lattice parameter c and the internal parameter u [Bernardini1997]. In particular, it can be shown than when going from GaN to InN and AlN, the crystal structure deviates from the ideal wurtzite structure and the amplitude of the spontaneous polarization increases (Table 1.4)

Materials	GaN	InN	AlN
u	0.3769	0.3787	0.3814
P_{sp} (C/m^2)	-0.034	-0.042	-0.090
C_{13}	106	92	108
C_{33}	398	224	373
e_{13}	-1.6	-3.5	-2.1
e_{33}	3.1	7.6	5.4

Table 1.3: Internal displacement parameter u, spontaneous polarization P_{sp}, elasticity and piezoelectricity coefficients C_{ij} and e_{ij} for GaN, InN and AlN in the wurtzite phase [Butté2007,Vurgaftman2003].

It is also useful to express the spontaneous polarization of the ternary alloys $Al_xGa_{1-x}N$ and $In_xGa_{1-x}N$ as a function of x. Contrary to the lattice parameters, the polarization has a strong non-linear dependence on x [Bernardini2001]. Non-linearities arise from three distinct mechanisms, namely volume deformation of the crystal unit cell, internal strain effects due to variation in the cation-anion separation and disorder caused by the random incorporation of the atoms. Spontaneous polarization can nevertheless be expressed to the second order of x [Butté2007]:

$$P_{sp}(Al_xGa_{1-x}N) = -0.090x - 0.034(1 - x) + 0.019x(1 - x) \qquad \text{Eq.(1.29)},$$

$$P_{sp}(In_xGa_{1-x}N) = -0.042x - 0.034(1 - x) + 0.038x(1 - x) \qquad \text{Eq.(1.30)}.$$

I.4.2 Piezoelectric polarization

In the presence of strain, the deformation of the unit cell along [0001] as well as the modification in internal displacement parameter u lead to a change in the amplitude of the polarization. The difference between the polarization of the strained crystal and that of the relaxed one is the piezoelectric polarization P_{pz}. In presence of biaxial strain, the piezoelectric polarization along [0001] is given by

$$P_{pz} = \left(2e_{31} + 2\frac{C_{13}}{C_{33}} e_{33} \right) \varepsilon_{xx} \qquad \text{Eq.(1.31),}$$

where $\tilde{C}$ and $\tilde{e}$ are the elasticity and piezoelectric tensors of the strained compound. Contrary to the spontaneous polarization, the piezoelectric polarization of ternary alloys is given by a linear interpolation of the polarization of the two binary compounds [Bernardini2001].

I.4.3 Built-in electric fields in polar III-nitride heterostructures

When growing a III-nitrides based heterostructure, one deposits successively materials with different internal polarization. Let us consider, for instance, a semi-infinite layer of AlN deposited on a semi-infinite layer of GaN with interface between the two media perpendicular to the polar c-axis. As a consequence of the continuity of the displacement vector $\vec{D}$ at the interface between two dielectric media, there is an accumulation of charges at the interface between GaN and AlN, and the areal density of charge σ is given by

$$\sigma = \vec{n} \left(\vec{P}_{GaN} - \vec{P}_{AlN} \right) \qquad \text{Eq.(1.32),}$$

with $\vec{n}$ the normal vector of the interface between GaN and AlN and taken along [0001]. This interface can be seen as an infinite plane charged with σ: it therefore creates in both the GaN and the AlN layers electric fields $\vec{F}$ with amplitude:

$$\vec{F}_{GaN} = -\frac{\sigma}{2\varepsilon_{GaN}}\vec{n} \text{ and } \vec{F}_{AlN} = \frac{\sigma}{2\varepsilon_{AlN}}\vec{n} \qquad \text{Eq.(1.33).}$$

If one now considers a GaN layer embedded between two semi-infinite AlN barriers (*i.e.* a single AlN/GaN QW), the two GaN/AlN interfaces are oppositely charged and one obtains from the superposition principle that

$$\vec{F}_{GaN} = -\frac{\sigma}{\varepsilon_{GaN}}\vec{n} = \frac{\vec{P}_{AlN} - \vec{P}_{GaN}}{\varepsilon_{GaN}} \qquad \text{Eq.(1.34).}$$

In the case of a periodic multi-QW structure, one has also to consider, when calculating the built-in electric fields in the different layers, that the structure is electrically neutral. This periodical boundary condition writes

$$F_{GaN}L_{GaN} + F_{AlN}L_{AlN} = 0 \qquad \text{Eq.(1.35),}$$

where L_{GaN} and L_{AlN} are the respective thicknesses of the GaN and AlN layers. In other words, one has to correct the built-in electric field for a single QW by a geometrical factor that accounts for the screening of the electric field induced by the successive charged interfaces [Leroux1999b]. For an AlN/GaN multi-QW, one finds

$$\vec{F}_{GaN,MQW} = \vec{F}_{GaN,SQW}\frac{\varepsilon_{GaN}L_{AlN}}{\varepsilon_{GaN}L_{AlN} + \varepsilon_{AlN}L_{GaN}} \qquad \text{Eq.(1.36)}$$

and

$$\vec{F}_{AlN} = -\vec{F}_{GaN,SQW}\frac{\varepsilon_{AlN}L_{AlN}}{\varepsilon_{GaN}L_{AlN} + \varepsilon_{AlN}L_{GaN}} \qquad \text{Eq.(1.37).}$$

We note that. in GaN QWs. built-in electric fields as high as 1 MV/cm can be observed [Grandjean1999] (Fig.1.9). Still, despite the fact that these fields are much higher than the classical exciton ionization fields, which we estimate to be of the order of 100-200 kV/cm, the quantum confinement prevents from any ionization of the exciton [Miller1984].
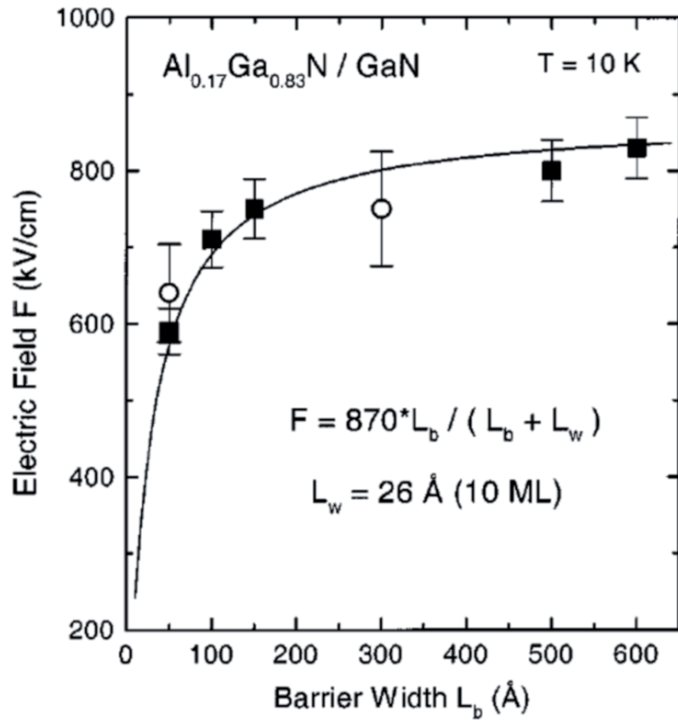
Figure 1.9: Barrier width dependence of the QW built-in electric field for a $Al_{0.17}Ga_{0.83}N/GaN$ multi-QW structure (taken from [Grandjean1999]).

I.4.4 Quantum confined Stark effect

The influence of built-in electric fields on the emission properties of an exciton confined in a polar QW can be easily modeled by envelope function calculations. Regarding the method described in Section I.3, one has only to "add" the electrostatic energy arising from the built-in electric fields $\vec{F}$ to the crystal potentials $V_e(z_e)$ and $V_h(z_h)$. The major consequences of built-in electric fields on the emission energy of $Al_xGa_{1-x}N/GaN$ single QWs are illustrated in Figure 1.10. First, we note that for QWs typically thinner than 2 nm, built-in electric fields have almost no influence on the emission properties of the exciton. For thicker wells, the QW emission energy is redshifted compared to the case of polarization free QWs. This redshift, known as Stark shift, is in first approximation given by $qF_{GaN}L_{GaN}$. It is thus possible to observe QWs emitting at energy below the bulk excitonic bandgap [Grandjean1999].

More important, built-in electric fields separate the electron and the hole wave functions of the exciton away from each other. As a consequence, the exciton oscillator strength is reduced (Eq.1.28) and the exciton radiative lifetime increases dramatically (Eq. 1.27). To our opinion, the most striking report was the observation of a 100 µs PL decay time

50

for a 3.5 nm thick GaN quantum dot embedded in AlN [Bretagnon2006]. Long radiative lifetimes alone are not a dramatic feature. However, regarding the fact that at 300 K, charge carriers in III-nitrides QW suffer from efficient non-radiative recombinations with non-radiative lifetime of typically 10 ps - 10 ns [*see for instance* Chichibu2005, Son2007, Yoshida2010, Langer2010], we expect the radiative efficiency of thick QWs to be considerably low.
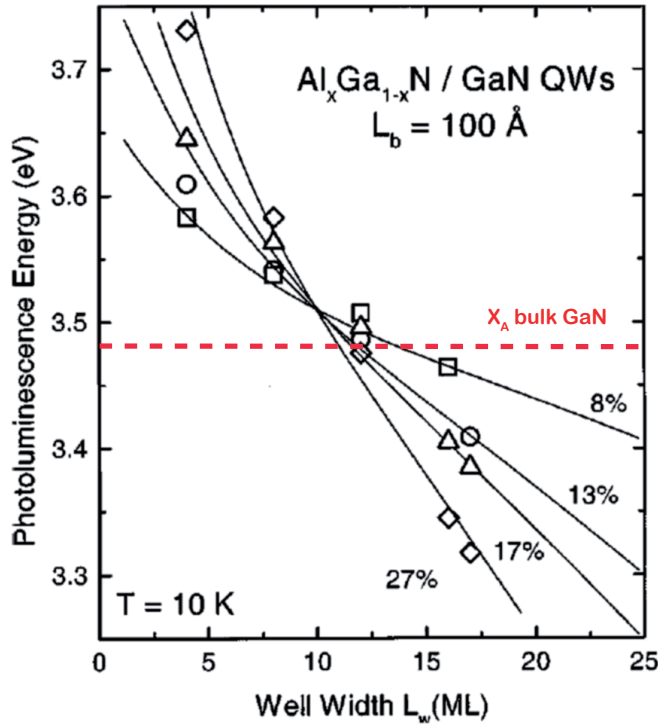
Figure 1.10: PL energies for c-plane Al$_x$Ga$_{1-x}$N/GaN QWs of different barrier Al-content x with respect to the well width. The full line corresponds to the calculated QW PL energy (taken from [Grandjean1999]). The red dashed line shows the excitonic bandgap of the GaN substrate.

I.4.5 Dynamical screening/de-screening of built-in electric fields

So far, we have considered that only one exciton was confined in the QW. This is generally not the case, when exciting optically or electrically a heterostructure. For most of our experiments, we indeed estimate to 5.10^{10} cm^{-2} the density of optically created electron-hole pairs (Chapter II). Under continuous-wave conditions, the injected free carriers screen partially or totally the polarization fields and it is mandatory to solve self-consistently the Schrödinger and Poisson equations to calculate the electron and hole band alignment along the heterostructure together with the exciton wave function [Fiorentini1999].

Further complications are introduced in the case of time-resolved PL experiments. First, the decaying population of charge carriers results in a de-screening of built-in electric fields and thus in a time-dependent redshift of the QW emission. In addition, the recovering of electric fields perpendicular to the QW plane leads to a spatial separation of electron and hole wave functions. As illustrated by Figure 1.11, that time-dependent overlap between electron and hole wave functions, leads to radiative lifetime that can increase by orders of magnitude within few hundreds of picoseconds [Reale2003,Lefebvre2004].
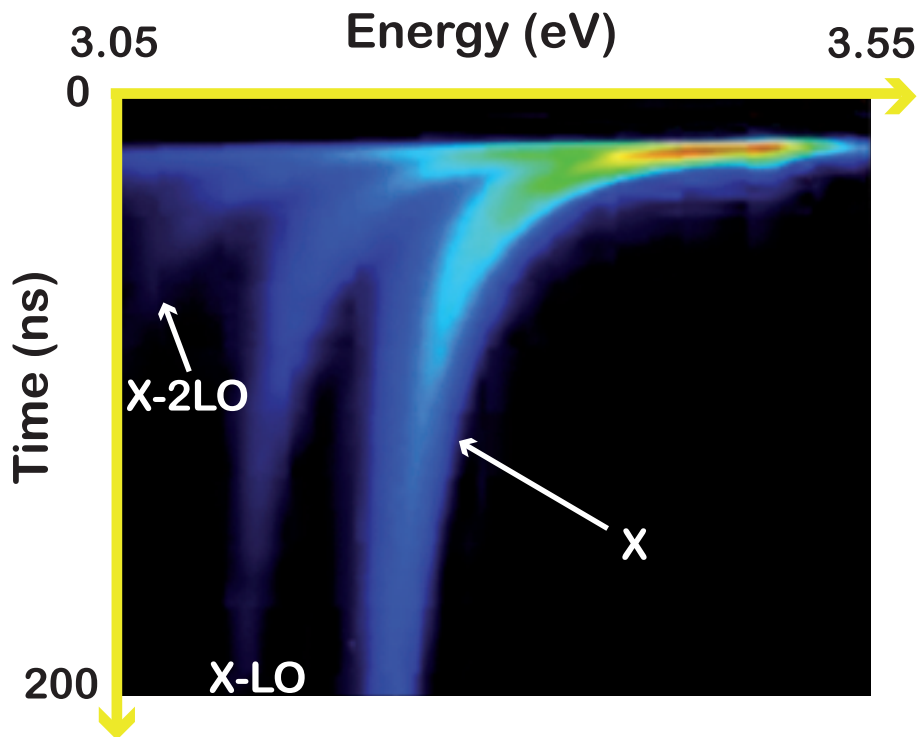
Figure 1.11: Time-resolved PL spectrum of a 7 nm thick $Al_{0.15}Ga_{0.85}N/GaN$ QW at T = 8 K, showing the dynamical descreening of built-in electric fields (taken from [Ref2,Lefebvre2004]). X, X-LO and X-2LO indicate the emission from QWexciton zero-phonon line, and first and second LO replica, respectively.

I.4. CONCLUSIONS

In this introductive Chapter, we have described the structural and electronic properties of III-nitrides. We now have key elements to understand the relaxation and recombination mechanisms of excitons in the various nitride-based systems studied in this manuscript.

This thesis is also part of the work carried out to achieve nitride-based structures with high structural quality. So far, one of the major Achilles' feet of III-nitrides is the dearth of lattice-matched substrates. As a consequence, a lot of research is conducted to reduce the density of extended defects and increase the radiative efficiency of nitride-based devices. We mention the growth of defect-free nanocolumns by MBE (Chapter III), the dislocation filtering through ELO-processing of GaN layers (Chapters IV and VI) and the homoepitaxy on GaN substrates grown by the high-pressure solution method (Chapters VII and VIII).

In addition, although from the structural point-of view, the growth of GaN heterostructures along the polar c-axis is the most mastered method [Feltin2007,Christopoulos2007,Stokker-Cheregi2008], the anisotropy of the wurtzite structure leads to built-in electric fields perpendicular to the growth axis. The consequences of these fields are twofold. First, the radiative efficiency of QW typically thicker than the exciton Bohr radius is extremely low: one is limited to the use of narrow QWs, which suffer from efficient Auger recombination. From a more fundamental point-of-view, the quantum confined Stark effect precludes studies on the intrinsic dynamics of excitons, as all effects are washed out by the de-screening of built-in electric fields. A huge interest has thus been paid, during this work, to heterostructures grown along non-polar axes (Chapter IV to VIII).

REFERENCES

[Ambacher1998] O. Ambacher, J. of. Phys. D: Appl. Phys. **31**, 2653 (1998).

[Ambacher2002] O. Ambacher, J. Phys.: Condens. Matter **14**, 3399 (2002).

[Andreani1990] L. C. Andreani, and F. Bassani, Phys. Rev. B **41**, 7536 (1990).

[Andreani1991] L. C. Andreani, F. Tassone, and F. Bassani, Solid State Comm. **77**, 641 (1991).

[Andreani1995] L. C. Andreani, Optical transitions, excitons, and polaritons in bulk and low-dimensional semiconductor structures in *Confined Electrons and Photons: New Physics and Devices*, p57, edited by E. Burstein and C. Weisbuch (Plenum, New York, 1995).

[Barker1973] A. S. Barker, Jr., and M. Ilegems, Phys. Rev. B **7**, 743 (1973).

[Bastard1982] G. Bastard, E. E. Mendez, L. L. Chang, and L. Esaki, Phys. Rev. B **26**, 1974 (1982).

[Bastard1990] G. Bastard, *Wave Mechanics Applied to Semiconductors Heterostructures*, Monographies de Physique, Les Editions de Physique (1990).

[Beaumont2001] B. Beaumont, P. Vennéguès, and P. Gibart, Phys. Stat. Sol. (b) **227**, 1 (2001).

[Bernardini1997] F. Bernardini, V. Fiorentini, and D. Vanderbilt, Phys. Rev. B **56**, R10024 (1997).

[Bernardini2001] F. Bernardini, and V. Fiorentini, Phys. Rev. B **64**, 085207 (2001).

[Birman1959] J. L. Birman, Phys. Rev. **114**, 1490 (1959).

[Butté2007] *Values taken in* R. Butté and N. Grandjean, "Effects of Polarization in Optoelectronic Quantum Structures", in *Polarization Effects in Semiconductors – from Ab InitioTheory to Device Application*, edited by C.E. Wood, Springer (2007).

[Capasso1987] F. Capasso, Science **235**, 172 (1987).

[Chichibu2005] S. F. Chichibu, T. Koida, M. D. Craven, B. A. Haskell, T. Onuma, T. Sota, J. S. Speck , S. P. DenBaars, and S. Nakamura, Phys. Stat. Sol. (c) **2**, 2700 (2005).

[Citrin1993] D. S. Citrin, Phys. Rev. B **47**, 3832 (1993).

[Craven2002] M. D. Craven, S. H. Lim, F. Wu, J. S. Speck, and S. P. DenBaars, Appl. Phys. Lett. **81**, 469 (2002).

[Christopoulos2007] S. Christopoulos, G. Baldassari Höger von Högersthal, A. J. D. Grundy, P. G. Lagoudakis, A.V. Kavokin, J. J. Baumberg, G. Christmann, R. Butté, J.-F. Carlin, and N. Grandjean, Phys. Rev. Lett. **98**, 126405 (2007).

[Deveaud1991] B. Deveaud, F. Clérot, N. Roy, K. Satzke, B. Sermage, and D. S. Katzer, Phys. Rev. Lett. **67**, 2355 (1991).

[Dingle1971] R. Dingle, D. D. Sell, S. E. Stokowski, and M. Ilegems, Phys. Rev. B **4**, 1211 (1971).

[Dingle1974] R. Dingle, W. Wiegmann, and C. H. Henry, Phys. Rev. Lett. **33**, 827 (1974).

[Dresselhaus1957] G. Dresselhaus, Phys. Rev. **105**, 135 (1957).

[Feltin2007] E. Feltin, D. Simeonov, J.-F. Carlin, R. Butté, and N. Grandjean, Appl. Phys. Lett. **90**, 021905 (2007).

[Feneberg2010] M. Feneberg, R. A. R. Leute, B. Neuschl, K. Thonke, and M. Bickermann, Phys. Reb. B **82**, 075208 (2010).

[Fiorentini1999] V. Fiorentini, F. Bernardini, F. Della Sala, A. Di Carlo, and P. Lugli, Phys. Rev. B **60**, 8849 (1999).

[Folliot2006] H. Folliot, *Cours d'Optique des Nanostructures*, Institut National des Sciences Appliquées de Rennes (2006).

[Gallart2001] M. Gallart, "*Dynamique de recombinaisons excitoniques dans les puits quantiques GaN/AlGaN*", PhD Thesis, Université de Montpellier II - Sciences et Techniques du Languedoc (2001).

[Gil1995] B. Gil, O. Briot, and R.-L. Aulombard, Phys. Rev. B **52**, R17028 (1995).

[Gil1997a] B. Gil, and O. Briot, Phys. Rev. B **55**, 2530 (1997).

[Gil1997b] B. Gil, and A. Alemu, Phys. Rev. B **56**, 12446 (1997).

[Gil1998] A. Alemu, B. Gil, M. Julier, and S. Nakamura, Phys. Rev. B **57**, 3761 (1998).

[Gradecak2004] S. Gradecak, P. Stadelmann, V. Wagner, and M. Ilegems, Appl. Phys. Lett. **85**, 4648 (2004).

[Grandjean1999] N. Grandjean, B. Damilano, S. Dalmasso, M. Leroux, M. Laügt, and J. Massies, J. Appl. Phys. **86**, 3714 (1999).

[Grzegory2001] I. Grzegory, J. Phys. Condens. Matter **13**, 6875 (2001).

[Gühne2007] T. Gühne, Z. Bougrioua, S. Laügt, M. Nemoz, P. Vennéguès, B. Vinter, and M. Leroux, Phys. Rev. B **77**, 075308 (2008).

[Haskell2003] B. A. Haskell, F. Wu, S. Matsuda, M. D. Craven, P. T. Fini, S. P. DenBaars, J. S. Speck, and S. Nakamura, Appl. Phys. Lett. **83**, 1554 (2003).

[Hopfield1960] J. J. Hopfield, J. Phys. Chem. Solids **15**, 97 (1960).

[Huang1950] K. Huang, and A.Rhys, Proc. Roy. Soc. (London) A **204**, 406 (1950).

[Hwang1973] C. J. Hwang, Phys. Rev. B **8**, 846 (1973).

[Ikeda2007] H. Ikeda, T. Okamura, K. Matsukawa, T. Sota, M. Sugawara, T. Hoshi, P. Cantu, R. Shama, J. F. Kaeding, S. Keller, U. K. Mishra, K. Koaka, K. Asai, S. Sumiya, T. Shibata,

M. Tanaka, J. S. Speck, S. P. DenBaars, S. Nakamura, T. Koyama, T. Onuma, and S. F. Chichibu, J. Appl. Phys. **102**, 123707 (2007).

[Imer2006] B. Imer, F. Wu, S. P. DenBaars, and J. S. Speck, Appl. Phys. Lett. **88**, 061908 (2006).

[Kumagai1998] M. Kumagai, S. L. Chuang, and H. Ando, Phys. Rev. B **57**, 15303 (1998).

[Langer2010] T. Langer, H. Jönen, D. Fuhrmann, U. Rossow, and A. Hangleiter, J. of Physics: Conference Series **210**, 012056 (2010).

[Lefebvre2004] P. Lefebvre, S. Kalliakos, T. Bretagnon, P. Valvin, T. Talierco, B. Gil, N. Grandjean, and J. Massies, Phys. Rev. B 69, 035307 (2004).

[Lei1991] T. Lei, M. Fanciulli, R. J. Molnar, T. D. Moustakas, R. J. Graham, and J. Scanlon, Appl. Phys. Lett. **59**, 944 (1991).

[Leroux1999a] M. Leroux, N. Grandjean, B. Beaumont, G. Nataf, F. Semond, J. Massies, and P. Gibart, J. Appl. Phys. **86**, 3721 (1999).

[Leroux1999b] M. Leroux, N. Grandjean, J. Massies, B. Gil, P. Lefebvre, and P. Bigenwald, Phys. Rev. B **60**, 1496 (1999).

[Leroux2000] M. Leroux, *Hamiltonien de Hopfield et effets de contrainte hétéroépitaxiale (0001) dans les wurtzites,* unpublished, Centre de Recherches sur l'Hétéro-épitaxie et ses Applications - CNRS (2000).

[Miller1984] D. A. B. Miller, D. S. Chemla, T. C. Damen, A. C. Gossard, W. Wiegmann, T. H. Wood, and C. A. Burrus, Phys. Rev. Lett. **53**, 2173 (1984).

[Ni2006] X. Ni, U. Ozgür, Y. Fu, N. Biyikli, J. Xie, A. A. Baski, H. Morkoç, and Z. Liliental-Weber, Appl. Phys. Lett. **89**, 262105 (2006).

[note1] *The names given to the irreducible representations of C_{6v} when studying the symmetry of III-nitrides are not the same than those given in chemistry.*

[Paskov2004] P. P. Paskov, T. Paskova, P. O. Holtz, and B. Monemar, Phys. Stat. Sol. (a) **201**, 678 (2004).

[Perlin1996] P. Perlin, E. Litwin-Staszewska, B. Suchanek, W. Knap, J. Camassel, T. Suski, R. Piotrzkowski, I. Grzegory, S. Porowski, E. Kaminska, and J. C. Chervin, Appl. Phys. Lett. **68**, 1114 (1996).

[Rappel1988] W. J. Rappel, L. F. Feiner, and M. F. H. Schuurmans, Phys. Rev. B **38**, 7874 (1988).

[Rashba1962] E.I. Rashba, and G. E. Gurgenishvili, Soviet Physics - Solid State **4**, 759 (1962).

[Reale2003] A. Reale, G. Massari, A. di Carlo, P. Lugli, A. Vinattieri, D. Alderighi, M. Colocci, F. Semond, N. Grandjean, and J. Massies, J. Appl. Phys. **93**, 400 (2003).

[Ref1] Image taken from http://www.optoiq.com/index.

[Ref2] *The color-coded streak image displayed in this Figure has been taken from* http://nqpo.ges.univ-montp2.fr/.

[Rinke2008] P. Rinke, M. Winkelnkemper, A. Qteish, D. Bimberg, J. Neugebauer, and M. Scheffler, Phys. Rev. B **77**, 075202 (2008).

[Ristic2006] J. Ristic, PhD Thesis, Universidad Politecnica de Madrid, Escuela Tecnica Superior de Ingenieros de Telecomunicacion (2006).

[Son2007] J. K. Son, S. N. Lee, H. S. Paek, T. Sakong, K. H. Ha, O. H. Nam, and Y. Park, Phys. Stat. Sol. (c) **4**, 2780 (2007).

[Stokker-Cheregi2008] F. Stokker-Cheregi, A. Vinattieri, E. Feltin, D. Simeonov, J. Levrat, J.-F. Carlin, R. Butté, N. Grandjean, and M. Gurioli, Appl. Phys. Lett. **93**, 152105 (2008).

[Sturge1962] M. D. Sturge, Phys. Rev. **127**, 768 (1962).

[Toyozawa1959] Y. Toyozawa, Suppl. Prog. Theor. Phys. **12**, 111 (1959).

[Varshni1962] Y. P. Varshni, Physica (Utrecht) **34**, 149 (1962).

[Viswanath1998] A. K. Viswanath, J. I. Lee, D. Kim, C. R. Lee, and J. Y. Leem, Phys. Rev. B **58**, 16333 (1998).

[Vurgaftman2003] I. Vurgaftman, and J. R. Meyer, J. Appl. Phys. **94**, 3675 (2003).

[Waltereit2000] P. Waltereit, O. Brandt, A. Trampert, H. T. Grahn, J. Menniger, M. Ramsteiner, M. Reiche, and K. H. Ploog, Nature **406**, 865 (2000).

[Wannier1937] G. H. Wannier, Phys. Rev. **52**, 191 (1957).

[Weisbuch1981] C. Weisbuch, R. Dingle, A. C. Gossard, and W. Wiegmann, Solid State Comm. **38**, 709 (1981).

[Winkelnkemper2008] M. Winkelnkemper, "*Electronic structure of nitride-based quantum dots*", PhD thesis, Institut für Festkörperphysik - Technische Universität Berlin (2008).

[Wu1988] J.-W. Wu, Solid State Comm. **67**, 911 (1988).

[Wu2002] J. Wu, W. Walukiewicz, K. M. yu, J. W. Ager III, E. E. Haller, H. Lu, W. J. Schaff, Y. Saito, and Y. Nanishi, Appl. Phys. Lett. **80**, 3967 (2002).

[Yoshida2010] H. Yoshida, M. Kuwabara, Y. Yamashita, K. Uchiyama, and H. Kan, Appl. Phys. Lett. **96**, 211122 (2010).

[Yu2005] P. Y. Yu, and M. Cardona, *Fundamentals of Semiconductors*, Third Edition, Springer (2005).

[Zhu2009] T. Zhu, PhD Thesis, n° 4563, EPFL (2009). *Manuscript available online* (http://library.epfl.ch/en/theses/?nr=4563)

[Zimmermann1993] R. Zimmermann, and D. Bimberg, Phys. Rev. B **47**, 15789 (1993).

Chapter II - Experimental set-ups

In this chapter, we present the experimental set-ups used to investigate the dynamics of charge carriers in GaN and nitride-based heterostructures. As we are not only interested in recombination mechanisms but also in the relaxation and the transport of free electron-hole pairs and excitons, we use spatially- and time-resolved luminescence techniques. We first describe our time-resolved (TR) photoluminescence (PL) apparatus, which allows for a temporal resolution in the picosecond range but that yields a poor spatial resolution of 50 μm. We then depict the cathodoluminescence (CL) technique in both continuous-wave (cw-) and TR modes. The purpose of this section is not to give the reader a thorough description of each experimental machine, but rather to provide him with the key characteristics of each set-up, including their advantages and limitations.

II.1. TIME-RESOLVED PHOTOLUMINESCENCE

Picosecond luminescence spectroscopy is a powerful tool to study charge carriers dynamics in semiconductors. As shown by [Deveaud1991], the characteristic lifetimes involved in the relaxation and the recombination dynamics of carriers in semiconductors are of the order of the picosecond. One therefore needs ultrafast excitation techniques combined with a detector with minimized temporal jitter to be able to track this dynamics. In our experiments, we excite the PL of our samples with picosecond excitation pulses obtained with a mode-locked Ti: Sapph laser and detect it with a synchroscan streak camera. The overall temporal resolution of the set-up is better than 10 ps while its spatial resolution is limited to 50 μm.

II.1.1 Excitation line

II.1.1.a. The Ti: Sapphire laser

Our Ti: Al_2O_3 laser is optically pumped by a frequency-doubled Nd: YVO_4 laser (λ = 532 nm). The emission band of the Ti: Al_2O_3 ranges from 670 to 1080 nm. This amplification medium is located in an optical cavity formed by a high reflectivity mirror and an output coupler (80% of reflectivity) separated by a distance L = 1.86 m. Any wavelength that satisfies stationary conditions in the cavity is called longitudinal mode. The frequency separation between each mode is the free spectral range of the cavity $\Delta v = c/2L$, where c is the speed of light, and where we have neglected the optical path of light inside the Ti: Al_2O_3 rod.

The longitudinal modes that fall in the emission band of the Ti: Sapph are uncoupled and we observe, at the output of the laser, modes with random phase and the laser is consequently quasi cw. In order to obtain ultrashort pulses, we need these modes to periodically interfere constructively, with a time period $T = 2L/c \approx 12.4$ ns corresponding to the time needed by light to make a round trip in the laser cavity. In a Ti: Sapph, mode-locking can be achieved passively thanks to the optical Kerr effect. The refractive index of the Ti: Sapph rod indeed depends on the intensity of the laser beam. It is therefore possible to design the optical cavity in order to favor the propagation of intense light pulses. The losses are then higher in cw than in pulsed mode, leading to mode locking. However, in order to gain in stability, the phase relation between longitudinal modes is in fact achieved by an acousto-optic modulator with modulation frequency equal to Δv. Of course, the higher the number of modes that interfere together, the shorter the width of the impulsion at the output of the laser. In our case, if we assume that all the modes comprised between 670 and 1080 nm interfere, we obtain that 2.10^6 modes should oscillate in phase. Practically, this number is first reduced as the mirror coatings are not optimized for the full 670-1080 nm range and as all the modes are not necessarily mode-locked. As a matter of fact, the most drastic reduction in the number of modes is produced by the Lyot filter present in the cavity that allows for the tuning of the laser wavelength. Such a filter is made of two or three birefringent plates and only those modes whose polarization remains linear after travelling through the plates can propagate

back and forth in the cavity without losses. Each pulse results finally from the constructive interference between only ~3000 longitudinal modes, allowing for the generation of 2 ps pulses (average energy of 12 nJ per pulse). One should also note that the group velocity dispersion due to the propagation of the beam into the non-linear Ti: Sapph rod is compensated by a Gires-Tournois interferometer [Tsunami].

II.1.1.b. Frequency tripler

In order to excite wide bandgap semiconductors, we use the third harmonic of the picosecond Ti: Sapph mode-locked laser. The second harmonic is obtained by focusing the laser on a uniaxial birefringent crystal that gives one photon of pulsation 2ω from two photons of pulsation ω. The fundamental and the second harmonic are then recombined in a second non-linear crystal to obtain the third harmonic of the laser. Optimal harmonic generation is obtained when the momentum conservation is respected. Experimentally, this angle tuning is obtained by rotating the non-linear crystals. One should also note that in the case of frequency tripling, it is mandatory to ensure the spatial and temporal overlaps of the fundamental and the second harmonic in the non-linear crystal.

Figure 2.1: Time-resolved PL set-up. We use the third harmonic of a pulsed Ti: Sapph. laser to excite the luminescence of wide bandgap semiconductors. The PL is collected by a lens, if necessary attenuated or polarization-analyzed, and then sent to a monochromator and a streak camera synchronized with the mode-locked laser.
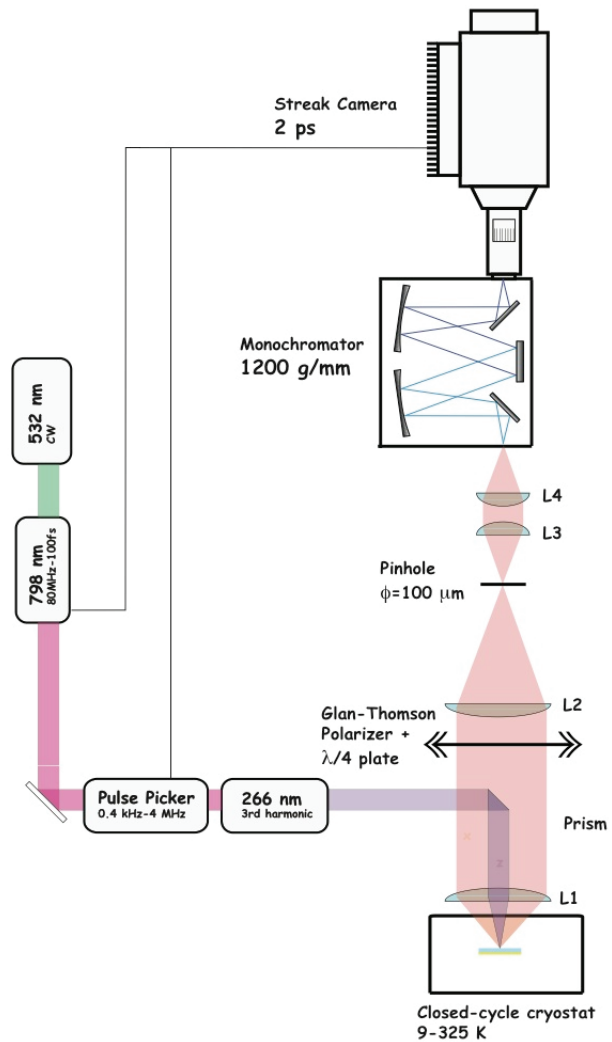
As already mentioned, lasing action is possible for wavelengths between 690 and 1040 nm. Consequently, we should have access to excitation wavelengths comprised 230 and 520 nm. However, the mirror coatings of the frequency doubler/tripler limit us to excitation wavelengths in the 270-330 and 400–480 nm ranges.

II.1.1.c. Extension of the excitation spot and typical photogenerated carrier densities

At the exit of the frequency tripler, the beam is far from being gaussian. As we use a picosecond laser, the non-linear crystals used for the harmonic generation have a non-negligible thickness. As a consequence, the crystals can in no way be considered as point sources for the second and the third harmonics and at the exit of the tripler, the beam exhibits

an elongated shape. We thus crudely filter spatially the beam (we estimate its diameter to $\phi = $ 1-2 mm) and then send it to the achromatic objective lens L1 (focal length F = 9.7 cm). Neglecting the divergence of the laser beam, astigmatism and spherical aberration, the diameter of the excitation spot is given by $\Phi = F\left(2.4\lambda\big/\phi\right)$. We obtain that the spatial extension of our excitation spot is 50 μm. Our excitation power is typically set between 10 and 200 μW. Assuming that free electron-hole pairs are uniformly generated within the excitation spot, we obtain that for λ = 280 nm the areal density of photogenerated charge carriers is comprised between 8.10^9 and $1.5.10^{11}$ cm^{-2} per pulse.

II.1.2. Detection line

II.2.1.a. Spatial filtering

Our PL set-up works in illumination-collection mode, *i.e.* the excitation laser and the PL are respectively focused and collected by the same lens L1. The PL is then focused by a second lens (L2) on a spatial filter (pinhole) with a diameter of either 50 or 100 μm. The use of such a pinhole allows for the analysis of a uniformly excited area of the sample, which is mandatory, when interpreting excitation dependent measurements or extracting from PL spectra the effective temperature of charge carriers [Zankel2002]. As shown in Figure 2.2, the excitation spot is imaged on the pinhole and only its central area is analyzed. The dimension of the analyzed spot is given by the diameter of the pinhole and by the ratio between the focal lengths of L1 and L2 (1/3 in our case).
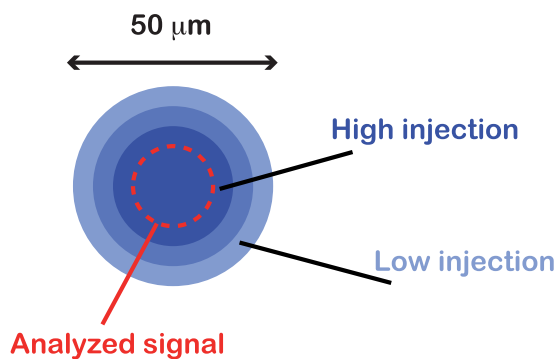

Figure 2.2: Imaging of the excitation spot on a spatial filter to analyze a uniformly photoexcited region of the sample.

II.1.2.b. Spectral dispersion

The PL is then sent to a 0.25 m monochromator for spectral dispersion. In this work, we have used 1 inch wide 600 and 1200 grooves / mm gratings with blazed wavelength at 350 and 300 nm, respectively. The intrinsic resolvance R of a grating is given by

$$R = \frac{\lambda}{\Delta\lambda} = knL$$

Eq.(2.1),

with λ, the wavelength, $\Delta\lambda$ the intrinsic spectral resolution, k the diffraction order, n the number of grooves per meter and L the width of the light spot on the grating. At the first order of diffraction and at 350 nm, we consequently obtain $\Delta\lambda = 2.3.10^{-2}$ and $1.2.10^{-2}$ nm for the 600 and 1200 grooves / mm gratings, respectively. As a matter of fact, such high spectral resolutions are not achieved experimentally. As discussed in [Blumer2006] who used the same experimental set-up, the dimension of the entrance slit of the monochromator is the main factor limiting the spectral resolution. The spectral resolution of our set-up is approximately 0.18 nm for the 1200 grooves / mm grating (Fig. 2.3), a resolution one order of magnitude lower than what we expect from the intrinsic resolution of the gratings.

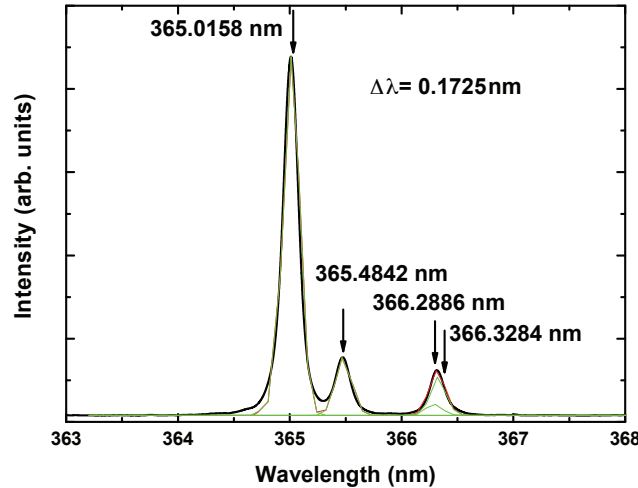*Figure 2.3: Spectrum of the emission of Hg obtained on our streak camera with a 1200 grooves / mm grating (black line) and with a 50 μm wide entrance slit. One expecst to observe four distinct lines in the vicinity of 365 nm, whose spectral positions have been determined by [Sansonetti1996]. The emission lines are fitted by Gaussian (green lines) to estimate the spectral resolution Δλ of our set-up.*

The energy resolution is given by the relation

$$\Delta E = E \frac{\Delta\lambda}{\lambda} \geq \frac{hc\Delta\lambda}{\lambda^2} \ ,$$
Eq.(2.2),

which gives, at 350 nm, 3.5 and 1.7 meV for the 600 and 1200 grooves / mm grating, respectively. We want to underline that a spectral resolution of 1.7 meV is high enough to study nitride-based QWs, where emission linewidth are dominated by inhomogeneous broadening (few meV at 10 K for state-of-the-art sample). Better resolution is however needed when studying nitride-based quantum dots where sub-meV emission linewidths have been reported [Simeonov2008].

II.1.2.c. Temporal dispersion

The time analysis of luminescence signal is obtained by a streak camera that converts the time information into a spatial one. At the exit of the monochromator, the spectrally resolved luminescence is sent to a photocathode. The photoelectrons are then deflected by a sinusoidal electric field, whose time frequency is given by the repetition rate of the mode-locked laser, and then swept on a phosphor plate. The signal is amplified by multiple photon/electron conversions and is finally sent to a CCD. At this stage, each pixel of the CCD provides the intensity of the signal for a given time and wavelength.

Our streak camera works in synchroscan mode, which means that the deflection field is driven by an internal sine function synchronized with the repetition rate of the laser (Fig. 2.4). The advantage of this method is that the streak camera is not sensitive to instabilities of the laser occurring over few pulses. However, we cannot eliminate small continuous drifts in the laser repetition rate that spoil the time resolution of the camera when long integrations are performed.
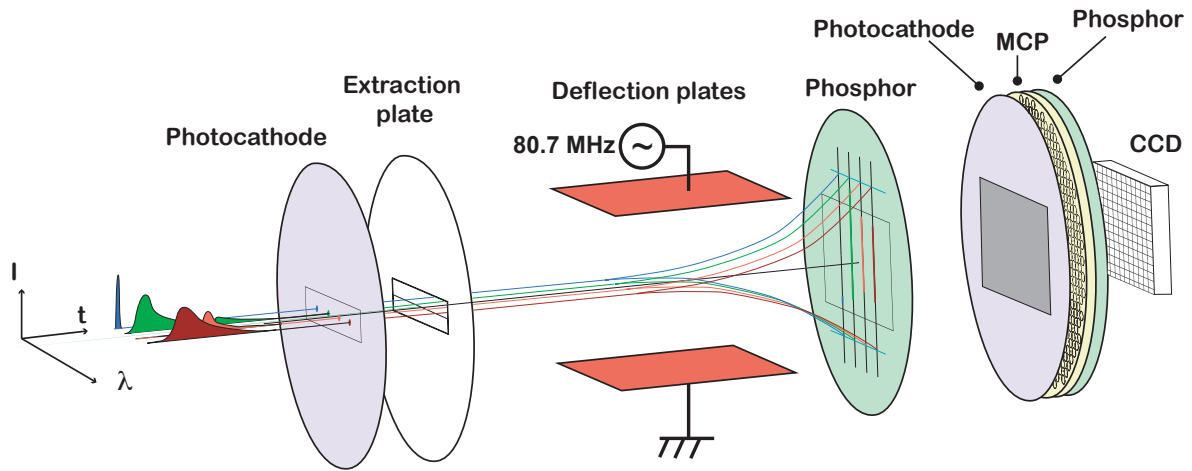
Figure 2.4: Temporal dispersion of a spectrally resolved luminescence signal by a streak camera in synchroscan mode (Figure courtesy of Dr. Jean-Daniel Ganière).

Although the intrinsic time-resolution of the streak camera is 2 ps, too high a spectral resolution would alter the time-resolution of our set-up. As shown in Eq.(2.3), temporal and energy resolutions are indeed correlated:

$$\Delta E \Delta t = \Delta\lambda\Delta t \frac{hc}{\lambda^2} = \frac{\hbar}{2} \qquad\qquad \text{Eq.(2.3).}$$

For the intrinsic spectral resolution determined in the previous section, we obtain $\Delta t = 0.95$ and 1.90 ps for the 600 and 1200 grooves / mm grating, respectively. We consequently do not expect our time resolution to be limited by the spectral resolution of the set-up.

II.2. CONTINUOUS-WAVE CATHODOLUMINESCENCE

II.2.1. Inelastic interactions between an electron beam and a semiconductor

When an energetic (several keV) electron beam is delivered on a solid, the incident electrons are scattered, elastically or not, by the atoms of the solid and are then re-emitted. The emitted electrons presenting an energy comparable with the primary electrons are called backscattered electrons. On the contrary, electrons emitted after several inelastic scatterings and of energy of typically few eV are called secondary electrons.

The particles excited by an inelastic electron / atom scattering can cover a wide range of energies. When the energy of the incoming electron is sufficiently high, it can promote an electron of the atom from a deep energy level to a higher energy one (for instance from K to L orbital). The excited electron will then relax by emitting an X-ray. When the energy loss of the incident electron is only of a few eV, it only excites an electron from the valence to the conduction band. In the case of semiconductors, the excited electron relaxes toward the bottom of the conduction band and then recombines. The light emission subsequent to the excitation by an electron beam is called cathodoluminescence (CL).

It is possible to estimate the density of electron-hole pairs generated in a semiconductor by an electron beam. It is usually admitted that, to create an electron hole pair of energy equal to the bandgap, an energy of the order of two times the bandgap is lost through different inelastic scattering mechanisms [Lappe1961]. Consequently, from the acceleration and the intensity of the incident electron beam, we know approximately the number of injected charge carriers. In order to access the density of charge carriers, we must determine the spatial extension of the volume in which electron-hole pairs are created, *i.e.* the generation volume. This can be done analytically [Bonard1996] or numerically by Monte-Carlo simulations [Casino].

II.2.2. Secondary electrons imaging mode

In a scanning electron microscope (SEM), an electron beam, with energy typically comprised between 1 and 20 keV, is focused on the surface of a sample. The re-emitted secondary electrons are collected by an Everhart-Thornley detector, which roughly consists of an anode polarized with a potential of a few hundreds volts. Depending on the position of the detector with respect to the orientation of the sample surface, the number of collected electrons varies. In a naïve view, we therefore have access to the topography of the surface of a sample by scanning it with the electron beam and collecting in parallel the emitted secondary electrons. For a more detailed description of the contrasts observed in secondary electron microscopy, we refer the reader to [Vicario1985]. The spatial resolution of this technique is given by the spatial extension of the volume emitting secondary electrons and is of the order of a few nm.

II.2.3. Cathodoluminescence imaging mode

In order to collect the cathodoluminescence signal, a parabolic mirror is introduced between the sample and the polar piece (objective lens) of the microscope (Fig. 2.5). The two main drawbacks yielded by the presence of the mirror are:

(*i*) reduction of the number of secondary electrons reaching the Everhart-Thornley detector, thus decreasing the signal-to-noise ratio of the secondary electron mapping,

(*ii*) increase in the working distance and therefore decreasing the spatial resolution of the set-up.

The CL signal is then sent to a monochromator followed by a photomultiplier tube or a CCD.

As is the case for SE mappings, CL mappings are obtained by scanning the electron beam on the surface of the sample while detecting in parallel the emitted CL. However, the spatial resolution of CL is more difficult to estimate, as one has to care not only for the extension of the generation volume, but also for the diffusion of charge carriers. Let us finally note that the penetration depth of the electron beam inside the material increases with the acceleration voltage. It is thus for instance possible to distinguish by depth-resolved CL the emission of near surface-states from that of the underlying material [Brillson1988].
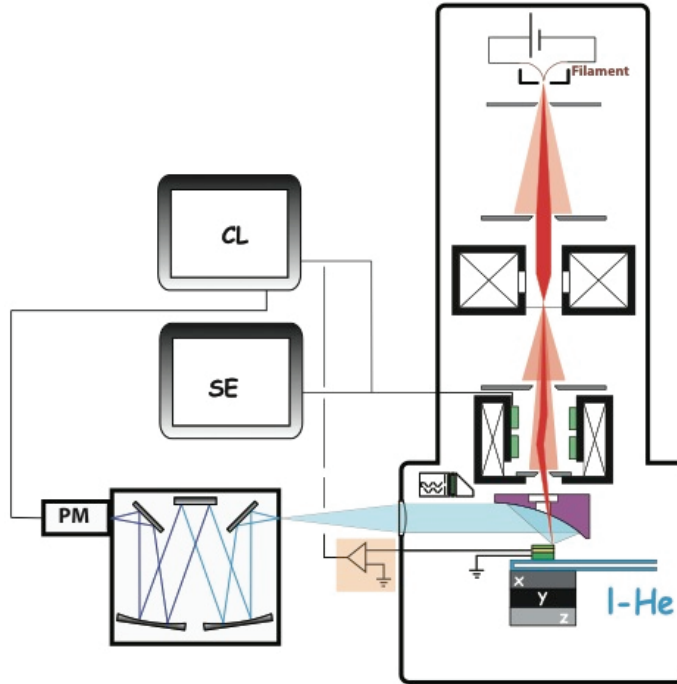
Figure 2.5: cw-CL set-up. Electrons are emitted from a heated tungsten filament and accelerated along the column of the microscope. The CL is collected by a parabolic mirror and sent to a monochromator followed by a photomultiplier tube.

II.3. TIME-RESOLVED CATHODOLUMINESCENCE

The purpose of the TR-CL is to combine the temporal resolution of TR-PL (a few ps) with the spatial resolution of a SEM (a few nm). The first demonstration of a TR-CL with a time resolution in the nanosecond scale has been reported by [Steckenborn1981]. Electron pulses were obtained by a beam blanking technique, where the electron beam was deflected by an electric field oscillating perpendicularly to the column of the microscope. These electron pulses are however several ns long. Regarding for instance the fact that excitons in bulk GaN are trapped by point or extended defects within 100 ps (see Chapters III-IV), such long pulses do not allow for the study of charge carrier transport in nitride-based semiconductors.

Alternatively to the beam blanking technique, one can take advantage of the photoelectric effect to generate electron pulses. As demonstrated by [Merano2005a], a pulsed electron beam can indeed be obtained by exciting a 50 nm thick gold photocathode by the third harmonic of mode-locked Ti: Sapph. laser (repetition rate and pulse width of 80.7 MHz and 100 fs, respectively) (Fig. 2.6). Although some metals such as Lithium present a much lower work function than gold, the latter does not oxidize fast and therefore allows for the

realization of cathodes with longer lifetime. The extracted electrons are then accelerated along the column of the microscope with an acceleration voltage set between 3 and 8 kV and then focused on the surface of the sample. For more details, we refer the reader to [Merano2005b].

Compared to usual CL setups, the main drawback of this time-resolved apparatus is the low current of the probe. While we measure a photocurrent of typically 1 nA right after the photocathode, we estimate that the probe current is only of 1-10 pA. Such reduction originates mainly from the shape of the photocathode and from the use of an alignment pinhole (diameter of 20, 50 or 100 μm) located in the column of the microscope. Such a low probe current, together with the presence of the parabolic mirror, limits the number of secondary electrons detected by the Everhart-Thornley detector and finally makes the acquisition of high-resolution SE image difficult. In addition, one should also note that the inelastic collisions of primary electrons are very fast compared to the pulse width (10 ps, *see* below). When performing a SE mapping, the useful signal is therefore only acquired during a few ps, while noise is accumulated during the 12 ns separating each pulse. As a consequence of that low signal-to-noise ratio in SE imaging mode, the alignment of the microscope column is arduous, limiting the spatial resolution of the TR-CL set-up in SE imaging mode to 50 nm.

As it is the case for our cw-CL set-up, the luminescence is collected by a parabolic mirror and sent to a monochromator. The spectrally resolved CL is then either sent to a photomultiplier tube, for monochromatic CL mapping, or to a streak camera synchronized with the Ti. Sapph., for time analysis. The temporal resolution of the set-up has been measured by excitation at 300 K of a highly defective GaN layer. From the rise-time of GaN CL, which is of the order or below 1 ps, the temporal width of the electron pulses was estimated to be roughly 10 ps [Merano2005a].

Finally, during this thesis, a homemade cryogenic stage has been mounted on the TR-CL set-up. This stage, consisting of a copper sample holder cooled down by liquid helium, allows us to routinely reach temperatures as low as 25 K. Note that below this 25 K limit, the stage suffers from too large thermal drifts to ensure the stable spatial positioning of the sample.
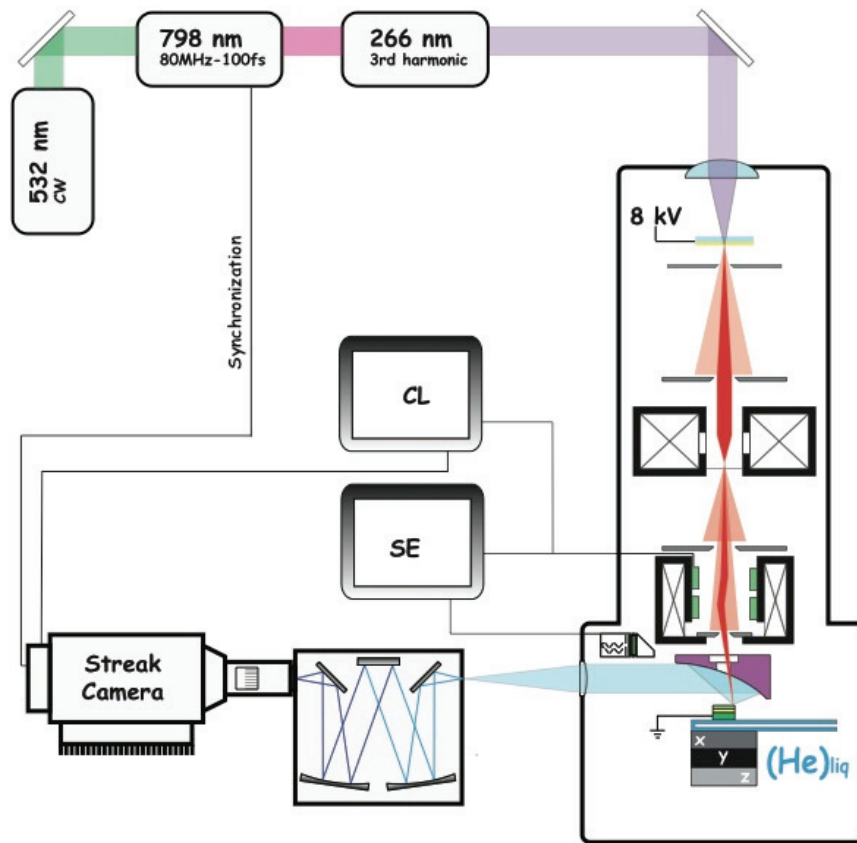
Figure 2.6: TR-CL set-up. The third harmonic of a pulsed Ti: Sapph laser is focused on a gold photocathode to create electron pulses. Electrons are then accelerated along the column of the microscope. The CL is collected by a parabolic mirror and dispersed in a monochromator followed by a streak camera for energy- and time-resolved analysis.

REFERENCES

[Blumer2006] C. Blumer, PhD Thesis, n° 3436, EPFL (2006). *Manuscript available online (*http://library.epfl.ch/en/theses/?nr=3436*).*

[Bonard1996] J.-M. Bonard, and J.-D. Ganière, J. Appl. Phys. **79**, 6987 (1996).

[Brillson1988] L. J. Brillson, and R. E. Viturro, Scanning Microscopy **2**, 789 (1988).

[Casino] *Simulations done with* CASINO, Version 2.42, *available online for free (*http://www.gel.usherbrooke.ca/casino/What.html*).*

[Devaud1991] B. Deveaud, F. Clérot, N. Roy, K. Satzke, B. Sermage, and D. S. Katzer, Physical Review Letters **67**, 2355 (1991).

[Lappe1961] F. Lappe, J. Phys. Chem. Solids **20**, 173 (1961).

[Merano2005a] M. Merano, S. Sonderegger, A. Crottini, S. Collin, P. Renucci, A. Malko, M. H. Baier, E. Kapon, B. Deveaud, and J.-D. Ganière, Nature **438**, 479 (2005).

[Merano2005b] M. Merano, PhD Thesis, n° 3206, EPFL (2005). *Manuscript available online (*http://library.epfl.ch/theses/?nr=3206*).*

[Sansonetti1996] C. J. Sansonetti, M. L. Salit, and J. Reader, Appl. Optics **35**, 74 (1996).

[Simeonov2008] D. Simeonov, A. Dussaigne, R. Butté, and N. Grandjean, Phys. Rev. B **77**, 075306 (2008).

[Steckenborn1981] A. Steckenborn, H. Münzel, and D. Bimberg, J. Luminescence, **24-25**, 351 (1981).

[Tsunami] *see instruction manual Tsunami-Spectra-Physics*

[Vicario1985] E. Vicario *in* "Pratique du microscope électronique à balayage", Edited by Association Nationale de la Recherche Technique, Paris (1985).

[Zankel2002] C. Zankel, "Propriétés optiques, sous forte injection, de structures à puits quantiques $Al_xGa_{1-x}As/GaAs$", Diploma work, LOEQ-EPFL (2002).

Part II

Recombination mechanisms
of impurity-bound excitons

Chapter III - GaN nanocolumns and surface donor bound excitons

III.1. GaN NANOCOLUMNS: STRUCTURALLY PERFECT CRYSTALS WITH LOW "OPTICAL QUALITY"

Sixteen years after the realization of the first nitride-based light emitting diode [Nakamura1994], the lack of cost-competitive substrates lattice-matched to GaN still remains one of the bottlenecks for a wide range of applications of nitride based devices. Indeed, while the realization of GaN crystals is still complicated and expensive, heteroepitaxial growth results in large densities of extended defects that deteriorate the performances and affect the lifetime of the devices (*see* Chapters IV to VII). One alternative proposed to overcome this problem is based on the fabrication of monocrystalline GaN nanocolumns (NCs).

NCs present several advantages compared to thick heteroepitaxial GaN layers. First, they are strain and defect free [Sanchez-Paramo2002], which is mandatory for the achievement of light emitters with narrow emission lines and high internal quantum efficiency. In addition, NCs present a large surface-to-volume ratio that allows for efficient light extraction. High external quantum efficiency should therefore be reached without any post-processing procedure such as the patterning of photonic crystals [David2005] or photoelectrochemical surface roughening [Shchekin2006]. Finally, it should also be noted that NCs can grow directly on Si(111) [Sanchez-Garcia1998] or Si(100) [Cerutti2006], which is promising towards the integration of GaN-based nano-lasers [Johnson2002] or nano-transistors [McAlpine2003] in usual optoelectronic circuits.

Whereas a lot of studies have been dedicated to understand the growth mechanism of GaN NCs [*see for instance* Ristić2008], there are only few reports on the peculiar emission properties of these nanostructures. Although GaN NCs are strain and defect free, and should *a*

priori present narrow emission lines, their near band-edge emission generally presents rather broad transitions and an intense emission centered at 3.449 eV, whose origin has not been ascertained yet. In the following, we first show that the large broadening of GaN NCs emission lines arises from the distortion of donor bound excitons (D°X) wave functions by surface. We then demonstrate that the emission centered at 3.449 eV observed in the thinnest NCs in no way originates from a surface defect specific to GaN NCs, and we instead attribute it to the recombination of D°X located close to the surface of the column. Finally, we present a model describing the peculiar dynamical behavior of GaN NCs near band-edge emission. The model also returns the thickness of the shell layer of the NCs where D°X properties are affected by surface.

III.2. GROWTH OF GAN NANOCOLUMNS

The GaN NCs that we study here have been provided by the group of Prof. Enrique Calleja, from the Universidad Politécnica de Mardrid. They have been grown on Si(100) and Si(111) substrates by plasma assisted molecular beam epitaxy (PAMBE) under non stoechiometric conditions (III/V ratio << 1). Variations in NCs diameter and density have been obtained by varying the III/V ratio: the smaller this ratio, the thinnest the NCs and the higher their density. The present NCs have diameters comprised between 30 and 70 nm and height of about one micron. They were proven by transmission electron microscopy and Raman spectrsocopy to be dislocation and strain-free structures [Calleja2000,Sanchez-Paramo2002,VanNostrand2006] (Fig. 3.1).
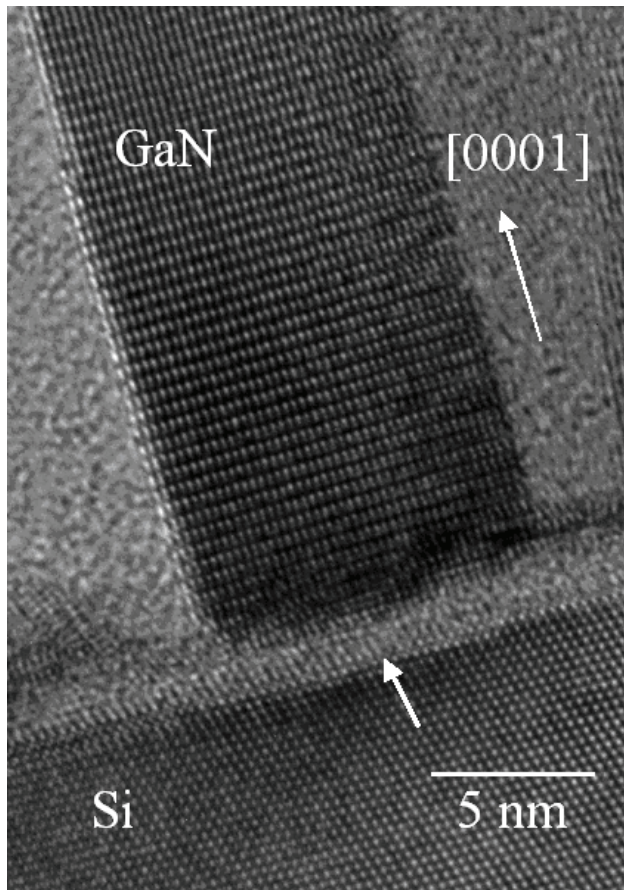
Figure 3.1: Cross-sectional TEM image of a GaN nanocolumns epitaxially aligned to the Si(111) substrate. GaN nanocolumns grown on Si are free of extended defects (courtesy of Dr. A. Trampert).

In general, NCs are separated one from each other and self-organized into dense arrays (Fig. 3.2). They grow vertically along the *c*-direction of the wurtzite, whatever the crystallographic orientation of the substrate used. We can already note that we observe no difference in the structural and optical properties between the NCs grown on Si(100) and Si(111). As shown in Figure 3.2, there is however a possible correlation between the morphology of the NCs and their emission spectra: the thinner the NCs, the higher the intensity ratio between the lines at 3.449 and 3.470 eV at 10 K. This issue will be discussed in detail further in this Chapter.
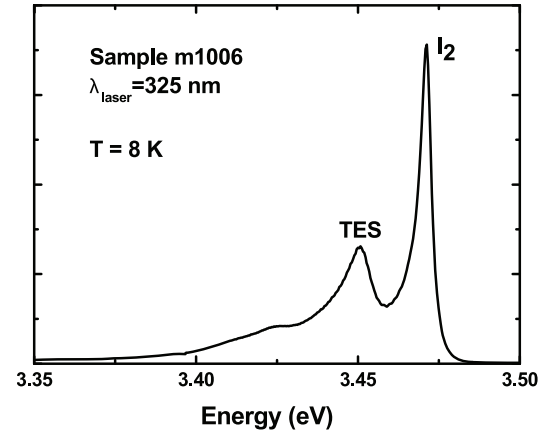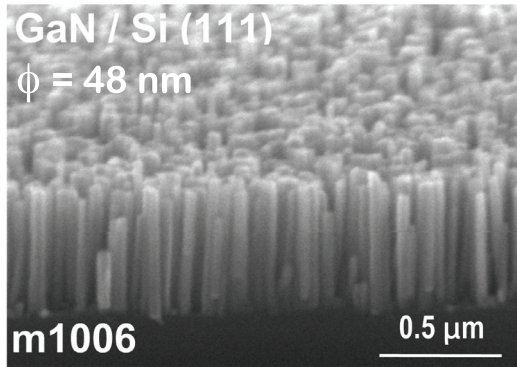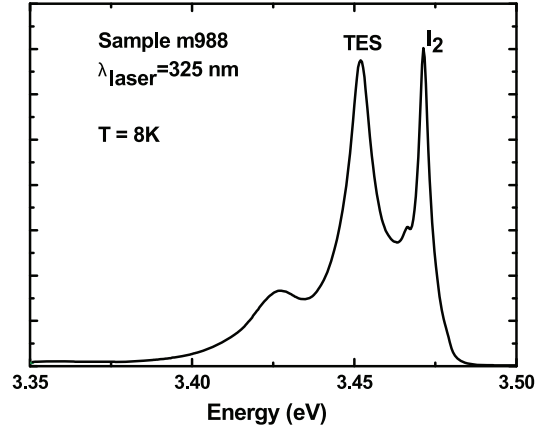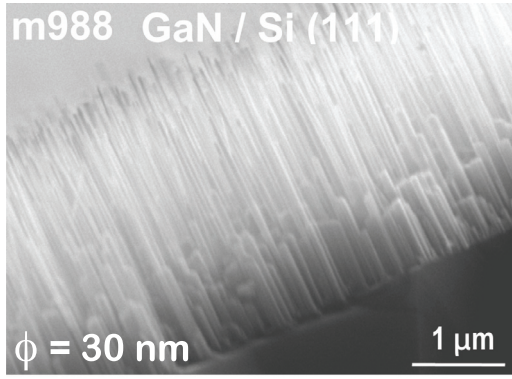
Figure 3.2: SEM images of GaN nanocolumns grown on Si(111) substrates (samples m988 and m1006), with respective continuous-wave PL spectra excited by cw laser radiation at 325 nm. The NC diameters (φ) are much smaller in sample m988, and the PL line at 3.449 eV is also much more intense than for sample m1006.

Samples	Name	m988	m1006	m1253	m1254
	Si substrate orientation	(111)	(111)	(111)	(100)
	Radius (nm)	15 ± 3	24 ± 4	25 ± 4	34 ± 5

Table 3.1: Characteristics of the GaN nanocolumns studied by time-resolved PL.

III.3. EMISSION PROPERTIES OF GaN NANOCOLUMNS

III.3.1. Time-integrated photoluminescence

Figure 3.3 displays the TI-PL spectra taken between 8 and 200 K for sample m1253 (Table 3.1). The spectrum at 8 K is typical of all the studied samples in terms of PL peak energies and broadenings. What really changes between the different samples is the intensity ratio between the two dominant lines at 3.470 and 3449 eV. In addition, weaker lines are observed at 3.477 and 3.485 eV. When T is increased, we observe a quenching of the PL at 3.470 eV to the benefit of the lines at higher energy, which we therefore attribute to free exciton A and B. Accordingly, the line at 3.470 eV is attributed to the so-called I_2 line, the recombination of exciton A bound to neutral donor (D°X), with the latter left in its ground state after the recombination:

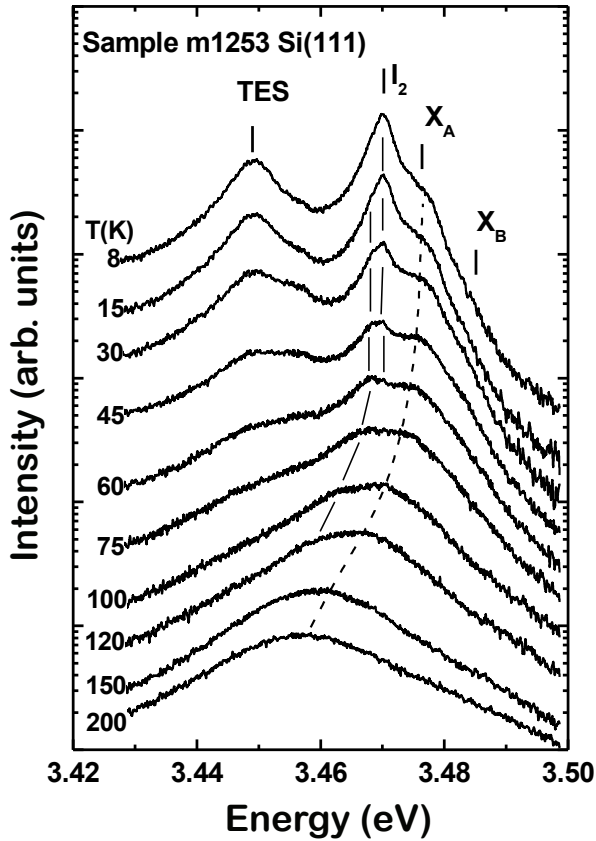$$D°X(0) \rightarrow D°_{n=1} + h\nu_{I_2}$$
Eq.(3.1).

Figure 3.3: Evolution with temperature of the time-integrated PL spectrum of sample m1253. When T is increased, the I_2 line quenches to the benefit of free exciton transitions lying at higher energy. Segments and dashed lines are guides to the eye, emphasizing, for instance, the double structure of the I_2 line.

In Eq.(3.1), $D°X(0)$ stands for the ground state of the donor-bound exciton and $D°_{n=1}$ denotes the final state of the transition, *i.e.* the ground state ($1s$) of the neutral donor. Although the emission energies reported here for free and bound excitons correspond to that of fully unstrained GaN [Kornitzer1999], we note that the large emission linewidths of 5 meV could seem contradictory with the absence of strain in nanocolumns.

Concerning the 3.449 eV line, the evolution of its intensity with temperature follows that of I_2, confirming its excitonic nature. Contrary to [Robins2007], we discard the possibility that the 3.449 eV line corresponds to the Y_1 transition assigned to inversion domains in N-face GaN [Reshchikov2003]. Although MBE growth may result in N-face GaN, recent convergent beam electron diffraction (CBED) studies have indeed established that GaN NCs grow with Ga-polarity [Cherns2008]. In addition, high-resolution transmission electron microscopy measurements have established that our nanocolumns contain no extended defect (Fig. 3.1), thus no inversion domain. Finally, the energy position of the line we observe here does not show any energy shift with the excitation density [Calleja2000], unlike what is reported for the Y_1 line [Reshchikov2003].

III.3.2 Donor bound exciton rotator states and two electron satellites

The position of the 3.449 eV line relatively to the I_2 emission coincides however with the two-electron satellites (TES) of the $D°X$ [Kornitzer1999,Freitas2003,Paskov2007]. The TES lines arise from some kind of Auger process internal to the neutral $D°X$. In this process, the remaining electron after the recombination of the $D°X$ is promoted to some excited state of the neutral donor rather than left in its ground state:

$$D°X(0,a,b,c,...) \rightarrow D°_{n=1,2,3...} + h\nu_{TES} \qquad \text{Eq.(3.2).}$$

The TES transitions lie therefore at lower energy than the I_2 line. In Eq.(3.2), 0, a, b, etc. stand for the ground and the rotational excited states of the $D°X$ complex [Neu2001,Paskov2007], while $n = 2, 3, ...$ represents the different possibilities for the principal quantum number of $D°$ final state. The different recombination channels are very sensitive to the symmetries of both the initial and final states, as recently demonstrated by

[Paskov2007] from a detailed spectroscopic study of high-quality GaN. In particular, when the D°X is in its excited states, then the favored TES line is the one leaving the donor atom with its electron in a *p*-state [Gil2007]. As a consequence, when the temperature is raised above 5 K, the thermal population of D°X excited states makes the transition to the 2*p* state of the D° more probable than the transition to the 2*s* state. This results in the dominance of the so-called D°X$_A$(*a*):2*p* transition lying 1.3 meV above the D°X$_A$(0):2*s* [Paskov2007].

As a rough approximation, the energy difference between the I$_2$ and TES transitions should be close to the energy difference between the first excited state D°$_{n=2}$ and the ground state D°$_{n=1}$ of the neutral donor, since the initial states of D°X are extremely close in energy. [Paskov2007]. Following the effective-mass approximation, the TES and I$_2$ lines are therefore separated by approximately 3/4 of the donor binding energy. In our case, the energy difference of 21.5 meV between the I$_2$ and the 3.449 eV line, multiplied by 4/3, yields an effective-mass donor binding energy of 28.7 meV. This strongly supports our assignment of the 3449 eV line to the TES of the D°X as this donor binding energy is very close to the one commonly reported for GaN [Note1]. In the present experiments, although the sample temperature was set to 8 K, the analysis of the high-energy side of the TR spectra reveals that the effective carrier temperature is rather of 35 K (Fig. 3.4). Following [Paskov2007], the TES band should therefore be dominated by the D°X$_A$(*a*):2*p* recombination, which is a further point toward our assignment of the 3.449 eV line to the TES of the D°X.

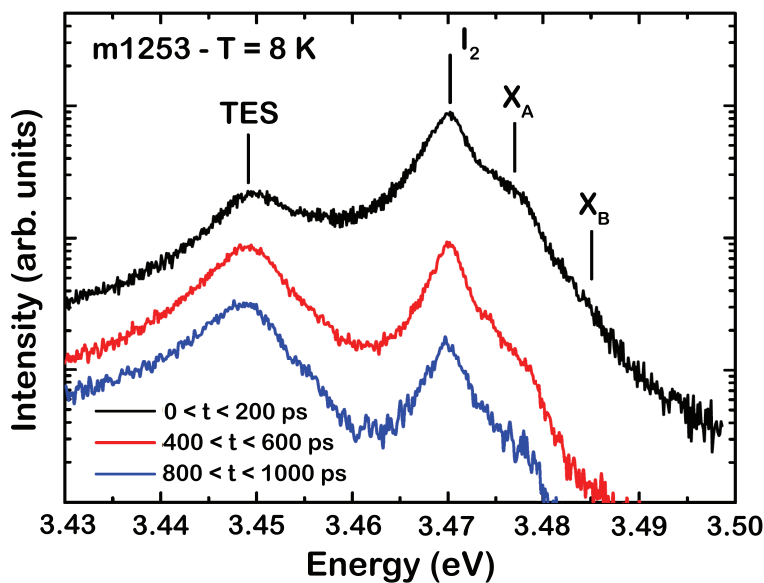*Figure 3.4: Evolution with time of PL spectra at T = 8 K for sample m1253. From the high-energy side of the spectrum, we estimate at short delays a carrier temperature of 35 K. This effective temperature then slowly decreases with time, until reaching the lattice temperature.*

III.4. DISTORSION OF DONOR ATOMS PROPERTIES BY SURFACE

In spite of these assignments, two points remain to be explained:

(*i*) the large emission broadening, unusual for unstrained GaN,

(*ii*) the high intensity of the TES line regarding that of the I_2. As a matter of fact, the intensity ratio between I_2 and the TES in GaN compact layers is quite commonly of the order of 100 [Skromme1999,Kornitzer1999] or 30 to 50 [Paskov2007], depending on the donor involved. In our NC samples, the time-integrated as well as continuous-wave PL intensities of these lines show, instead, a ratio comprised between 0.7 and 6. For the TR-PL experiments (*see* Table 3.1), these ratios at $t = 0$ range between 1 and 9, typically.

In the following, we will propose that these two features are both related to surface effects exacerbated by the nanocolumnar geometry of our structures.

III.4.1. Spatial extension of D° and D°X wave functions

We already noted above that 5 meV FWHM for both the I_2 and the TES lines was contrasting with the fact that our NCs were defect and strain free. Contrary to the case of thick layer samples, we believe that surface effects have to be taken into account here, since our structures present a large surface-to-volume ratio. Without calculation, we can infer that the donor ground state is affected by surface when the separation between the donor nucleus and the surface is smaller than a_D (a_D is the effective donor Bohr radius ~ 3 nm in GaN). To support this suggestion, we calculate the energy and wave function of the $n = 1$ level of a donor located close to a surface. The binding energy of a donor atom located in any given potential profile can indeed be easily estimated numerically (*see* Appendix I for more details on the procedure we used). Figure 3.5 shows the binding energy and the Bohr radius for a donor located close to an infinite potential barrier (such as surface). In agreement with the result by [Levine1965], if the donor is placed at the surface of a semiconductor, its effective

Rydberg energy is reduced by a factor of 4 and the wave function for the ground state is similar to a 2*p* state with a single probability lobe elongated perpendicular to the surface.
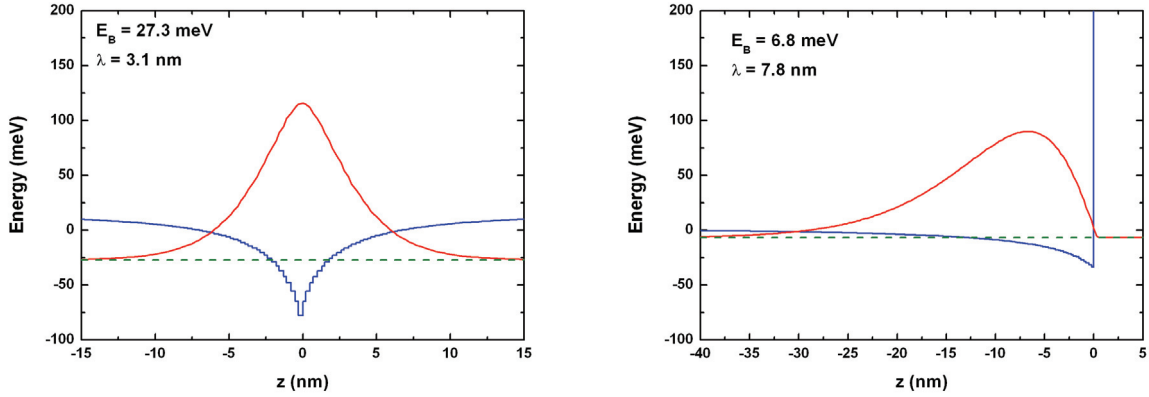
Figure 3.5: Potential profile (blue), energy (green) and wave function (red) of an electron bound to a donor nucleus located in bulk GaN (left panel) and close to a surface (right panel). The position of the donor nucleus is z = 0.

Our calculations also predict that donor atoms located $\sim 2a_D = 6$ nm away from a surface already present a slightly modified binding energy (Fig. 3.6). In addition, we can easily understand that $n = 2$ states, having a radial envelope function that decreases like $Exp(-r/2a_D)$, will be affected by the surface even when the nucleus is placed further than 6 nm from the surface. For more quantitative estimations, we refer the reader to the work by [Satpathy1983] who calculates the binding energy and the wave functions of $n = 2$ and $n = 3$ states of a D° located close to a surface.

Figure 3.6: Binding energy and wave function in-plane extension for an electron bound to a donor, with respect to the distance between the donor nucleus and the surface.

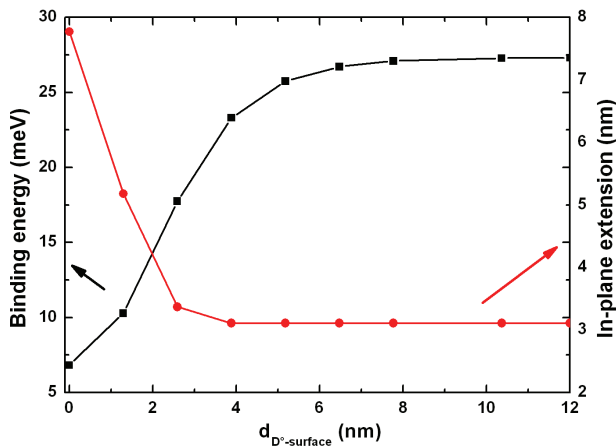The same reasoning stands for the D°X complex: the influence of the surface will be significant for a donor-to-surface distance smaller than the typical values for electron-nucleus and hole-nucleus distances. [Suffczynski1989] have calculated these distances as a function of the ratio between electron and hole effective masses. For GaN, the hole dispersion relation is anisotropic and m_e^* / m_h^* is comprised between 0.2 and 0.4 [Vurgaftman2003], which allows us to estimate, *for the D°X ground state*, the average distance of the hole (respectively of any of the 2 electrons) to the donor nucleus as $<r_h> = 6.3 \pm 0.7$ nm (respectively $<r_e> = 3.7 \pm 0.1$ nm). The inter-electron average distance is estimated at $<r_{12}> = 6.7 \pm 0.3$ nm. Similarly to what we did previously for the D°, the binding energy and the wave function of a D°X located close to a surface could be calculated with the variational method described in Appendix II. Note, however, that the trial wave function chosen for the hole in Appendix II is not suited for the study of D°X close to a surface but for D°X located in type-II quantum wells (*see* Chapter V).

III.4.2. Surface-induced broadening of the I_2 emission

From the considerations made above on the spatial extension of D° and D°X wave functions, we find that the energies and wave functions of both D°X and of the D° should be strongly modified when the donor nucleus lies closer than 5 nm from the surface. On the contrary, deeper in the core of the NCs, the energy of both D° and D°X should only be slightly altered by the surface. Since donor atoms are statistically distributed, the D°X binding and emission energies are necessarily distributed too. Thus, the random distribution of donor sites could be an *intrinsic* origin of the broadening of the I_2 emission band. In agreement, micro-PL experiments on single NCs performed recently at the Paul Drude Institute clearly support our assumption [Brandt2010]. While PL spectra taken on ensemble of strain-free NCs exhibit I_2 lines with a 3-4 meV linewidth, a single NC exhibits well-separated excitonic transitions with broadening below 300 μeV and with emission energies ranging between 3.47 and 3.48 eV (*see* Fig. 6(c) in [Brandt2010]). The authors thus conclude that the broadening of the D°X emission simply results from the "*dispersion of bound-exciton states as a function of their distance from the surface*".

III.4.3. Alteration of D° and D°X wave function by surface

As a matter of fact, we expect surface to have additional consequences on the emission properties of GaN NCs. The proximity of donor nuclei from the surface should deform enough the D°X and D° envelope functions to perturb profoundly the relative probabilities of the different allowed transitions. In other words, not only the emission energies but also the radiative lifetimes of D°X recombination channels should depend on the position of the donors in the column. On the one hand, a D°X in the core of a NC is equivalent to D°X in regular epilayers, *i.e.* the D°X recombines preferentially into the $D°_{n=1}$ state and seldom into the $D°_{n=2}$ state. On the other hand, when the donor nucleus lies closer to a surface, the envelope functions of the initial D°X states are necessarily deformed. Although only the calculation of D°X and D° wave-functions could predict correctly the evolution of I_2 and TES radiative lifetimes with respect to the distance between the surface and the donor nucleus, we infer that in some cases, the emission at 3.449 eV could be favored with respect to the one at 3.471 eV. As a strong support of our assumption, it is worth mentioning that unusually intense TES lines have also been observed in thin ZnO NCs [Mézy2006]. It should therefore be possible to extend our reasoning based on the deformation of D° and D°X wave functions to other material systems.

III.5. RECOMBINATION DYNAMICS OF SURFACE AND BULK DONOR-BOUND EXCITONS

III.5.1. Free exciton capture on donor nuclei

Time-resolved PL experiments have been carried out at 10 K to investigate the dynamical behavior of the I_2 and the TES lines in NCs grown on Si(111) and Si(100). As shown in Figure 3.7, we can analyze the respective decays of X_A, I_2 and TES. The initial decay of the free exciton PL is fast and correspond to the rise of the D°X related PL (I_2 and TES emission lines). After some transient phase, we observe that I_2 and X_A lines adopt the same recombination dynamics. Thermal equilibrium is therefore reached between these two exciton states.
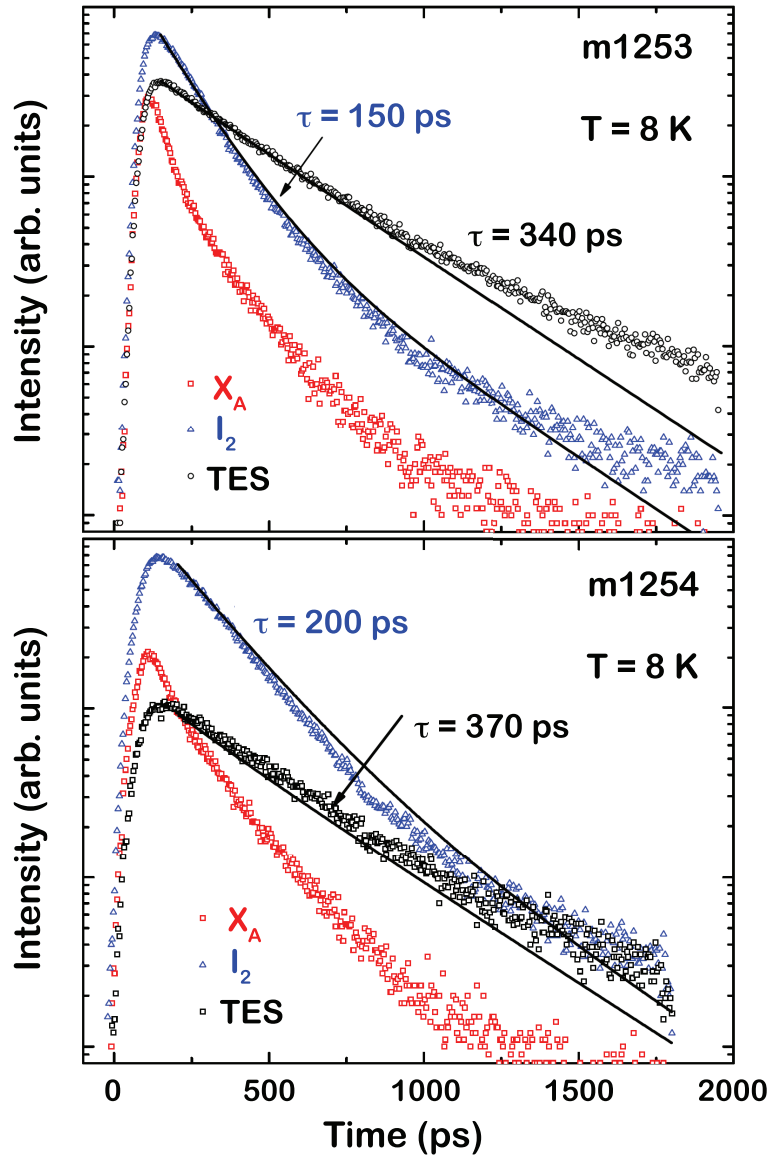
Figure 3.7: Time dependence of PL intensities of the X_A, I_2 and TES transitions at $T = 8K$ for samples m1253 and m1254. Decay time constants have been obtained by single-exponential fitting of the appropriate zones. Solid lines are the result of the core-shell model.

III.5.2. Necessity of a core-shell model

As we observe an efficient thermalization between free excitons and D°X, we can safely assume that there is also thermal equilibrium between D°X ground and rotator states. As a consequence, the I_2 and the TES lines should present the same PL decay. As it is not the case, we have developed a core-shell model to describe the recombination dynamics of D°X in NCs, accounting for the fact that:

(*i*) excitons bound to donor nuclei located in the core of the NC evolve independently of D°X in a shell region close to the surface.

(*ii*) the intrinsic characteristics of D°X → D° transitions (*i.e.* their emission energies and radiative lifetimes) depend on the donor position.

The main ingredient of that model, described thoroughly in Appendix III, is to separate a NC into three regions -a core, a shell and a surface layer- were the radiative properties of D°X differ drastically (Fig. 3.8). In the following, α will be the volume fraction of the core region with respect to the total volume of the NC, where D°X can form.

In the core region, D°X recombination dynamics are similar to that of bulk GaN and the $D°X(0) \rightarrow D°_{n=1} + h\nu_{I_2}$ process is the most efficient recombination channel. The radiative lifetime $\tau_{1(c)}$ of the I_2 line is therefore much shorter than that of the TES ($\tau_{2(c)}$) and we thus assume $\tau_{1(c)} / \tau_{2(c)} = 50$, in agreement with the report by [Paskov2007]. We then consider that the core of the NC is surrounded by a shell layer, where the relative recombination probabilities of the I_2 and the TES transitions are affected by the surface, while D°X and D° energies are almost not (Fig. 3.8). More precisely, an intense emission at 3.449 eV arises from this region of the NCs. The PL decay time of the 3.449 eV line is equal to the effective lifetime of D°X in the surface region, yielding $\tau_{PL}(TES) \approx \tau_{eff(s)} = \tau_{1(s)}\tau_{2(s)} / (\tau_{1(s)} + \tau_{2(s)})$. We finally consider that this shell layer is surrounded by an additional 3 nm thick surface layer that is free of D°X. We justify this dead layer by the fact that free excitons cannot come closer from the surface than their Bohr radius (3 nm).

We can then extract from our model the characteristic lifetimes $\tau_{1(c)}$, $\tau_{2(c)}$, $\tau_{1(s)}$, $\tau_{2(s)}$ as well as α. The result of our fitting procedure is shown in Figure 3.7 for samples m1253 and m1254 and the values of the fitting parameters are gathered in Table 3.2 for all samples.
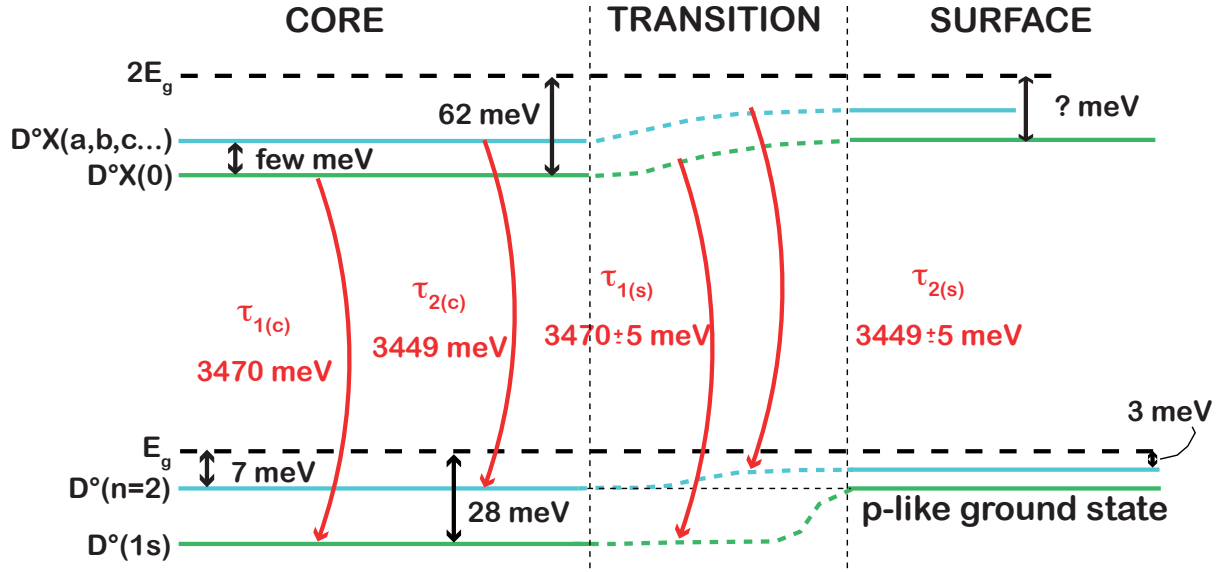
Figure 3.8: Our core-shell model. In the core of the NCs, D°X recombine predominantly by the I₂ process. When getting closer to the surface of the NC, D°X wave functions get distorted and the relative recombination probability of the TES transitions regarding I₂ is increased. Finally, at the surface, D°X energy and recombination processes are drastically altered. However, this surface layer also acts as a dead layer for free excitons and no D°X can form

III.5.3. Discussion

Given the simplicity of the model, the quality of the fitting is quite satisfactory (Fig. 3.7). This confirms that we can simultaneously describe the different decay dynamics as well as the intensity ratios of the TES and I₂ emission lines, by accounting for the existence of core and shell regions. It is however difficult to compare the evolution of these different radiative lifetimes with respect to the radius of the NCs because of the strong constraints imposed to the model:

(*i*) $\tau_{1(c)}$ has to be close to the overall decay time measured for I₂,

(*ii*) $\tau_{1(s)}$ and $\tau_{2(s)}$ are related to the experimental decay time of the TES by Eqs.(A3.5) and (A3.8),

(*iii*) the core and shell time constants are not independent [Eq.(A3.6)].

It could seem also interesting to compare our fitting decay times in the core region (Table 3.1) with those measured, *e.g.*, by [Paskov2007] for a high-quality GaN epilayer. The $\tau_{1(c)}$ and $\tau_{2(c)}$ deduced for our NCs are clearly shorter than those in bulk material, which we tentatively relate to the effective carrier temperature of 35 K that we estimate from the high-energy side of X_A emission (Fig. 3.4). By the way, it is difficult to know if we should compare our $\tau_{1(c)}$ (typically 0.2 ns) to the value of ~ 0.5 ns measured for I_2 in [Paskov2007], or if it is our $\tau_{2(c)}$ (typically 1 or a few ns, with large uncertainty) that should be compared to the 1.1 and 1.8 ns, measured respectively for SiX_A:$2s$ and OX_A:$2s$ transitions since, as mentioned in [Paskov2007], these different dynamics precisely correspond to different donor sites.

Samples	Name	m988	m1006	m1253	m1254
	radius (nm)	15 ± 3	24 ± 4	25 ± 4	34 ± 5
Experimental results	$\rho = \dfrac{I_{I_2}(0)}{I_{TES}(0)}$	1.1	2.2	1.9	8.6
	$\tau_{PL}(I_2)$ (ns)	0.12 ± 0.02	0.16 ± 0.02	0.15 ± 0.02	0.20 ± 0.02
	$\tau_{PL}(TES)$ (ns)	0.41 ± 0.02	0.32 ± 0.02	0.34 ± 0.03	0.37 ± 0.02
	α	0.17	0.4	0.35	0.57
Calculations / Fitting	$\tau_{2(s)}$ (ns)	0.5	0.4	0.4	1
	$\tau_{2(c)} = 50\,\tau_{1(c)}$ (ns)	5.0	7.0	7.0	9.5
	$\tau_{1(c)}$ (ns)	0.10	0.14	0.14	0.19
	$\tau_{1(s)}$ (ns)	2.8	1.5	1.6	0.6

Table 3.2: Results of the core-shell model for the studied nanocolumns. As expected, the volume fraction α increases with the radius of the nanocolumns.

The ratio α is nevertheless estimated with high precision. It indeed mainly involves the "dominant" times $\tau_{1(c)}$ and $\tau_{2(s)}$ together with the intensity ratio at zero delay between I_2 and TES emission, which are all measured with accuracy. We find that α generally increases with the average NC radius (Table 3.1). Despite the very large size dispersion of the NCs and the naivety of the model, this trend is quite clear. Given the measured NC radii, and

accounting for the 3 nm thick surface dead layer, we obtain from α that the shell layer where the relative probability of I_2 and TES are altered should present a thickness in the range of 8 ± 1 nm.

As a consequence, in addition to a 3 nm thick surface dead layer that should be free of D°X, we expect from our modeling procedure the presence of a 8 nm thick shell layer where the symmetry breaking induced by the vicinity between surface and D°X favors the emission at 3.449 eV to the detriment of to the usually dominant I_2 line at 3.470 eV.

III.6. CONCLUSIONS

In this Chapter, we have studied the consequences of the large surface-to-volume ratio of GaN NCs on their low-temperature emission properties. Although thin NCs with radius typically comprised between 15 and 35 nm are defect and strain free, these structures present broad near band-edge emission lines. Moreover, several groups have reported the observation of an intense emission line centered at 3.449 eV. As the thinner the NCs, the more intense the 3.449 eV line compared to the I_2, the emission at 3.449 eV is usually attributed to surface effects.

From comparisons between the spatial extension of D° and D°X wave functions with the radius of NCs, we have first shown that the broadening of the donor-related PL lines was related to the statistical distribution of donor atoms in the structure. Moreover, we have proposed that D°X located close to a surface should not only present a modified emission energy, but that there should be also drastic changes in the radiative lifetimes of the different possible D°X recombination channels.

Finally, from time-resolved PL experiments, combined with a core-shell model that accounts qualitatively for the donor position-dependent radiative recombination probabilities, we have estimated to 8 nm the thickness of the shell layer where the D°X recombination properties are affected by surface. Nevertheless, only the exact calculation of the energies and wave-functions of D°X and D° states, with respect to the distance between surface and the

donor nucleus, could definitely allow us to attribute the 3.449 eV line to D°X located close to the surface.

REFERENCES

[Brandt2010] O. Brandt, C. Pfüller, C. Chèze, L. Geelhaar, and H. Riechert, Phys. Rev. B 81, 045302 (2010).

[Calleja2000] E. Calleja, M. A. Sanchez-Garcia, F. J. Sanchez, F. Calle, F. B. Naranjo, E. Munoz, U. Jahn, and K. Ploog, Phys. Rev. B **63**, 16826 (2000).

[Cerutti2006] L. Cerutti, J. Ristic, S. Fernandez-Garrido, E. Calleja, A. Trampert, S. Lazic, and J. M. Calleja, Appl. Phys. Lett. **88**, 213114 (2006).

[Cherns2008] D. Cherns, L. Meshi, I. Griffiths, S. Khongphetsak, S. V. Novikov, N. Farley, R. P. Campion, and C. T. Foxon, Appl. Phys. Lett. **92**, 121902 (2008).

[David2005] A. David, C. Meier, R. Sharma, F. S. Diana, S. P. DenBaars, E. Hu, S. Nakamura, C. Weisbuch, and H. Benisty, Appl. Phys. Lett. **87**, 101107 (2005).

[Freitas2003] J. A. Freitas, W. J. Moore, B. V.Shanabrook, G. C. B. Braga, D. D. Koleske, S. K. Lee, S. S. Park, and J. Y. Han, Phys. Stat. Sol. (b) **240**, 330 (2003).

[Gil2007] B. Gil, P. Bigenwald, M. Leroux, P. P. Paskov, and B. Monemar, Phys. Rev. B **75**, 085204 (2007).

[Johnson2002] J. C. Johnson, H.-J. Choi, K. P. Knutsen, R. D. Schaller, P. Yang, and R. J. Saykally, Nature Mater. **1**, 106 (2002).

[Kornitzer1999] K. Kornitzer, T. Ebner, K. Thonke, R. Sauer, C. Kirchner, V. Schwegler, M. Kamp, M. Leszczynski, I. Grzegory, and S. Porowski, Phys. Rev. B **60**, 1471 (1999).

[MacAlpine2003] M. C. McAlpine, R. S. Friedman, S. Jin, K. Lin, W. U. Wang, and C. M. Lieber, Nano Lett. **3**, 1531 (2003).

[Levine1965] J. A. Levine, Phys. Rev. **140**, A586 (1965).

[Mézy2006] A. Mézy, S. Anceau, T. Bretagnon, P. Lefebvre, T. Talierco, G. C. Yi, and J. Yoo, Superlattices Microstruct. **39**, 358 (2006).

[Nakamura1994] S. Nakamura, T. Mukai, and M. Senoh, Appl. Phys. Lett. **64**, 1687 (1994).

[Neu2001] G. Neu, M. Teisseire, P. Lemasson, H. Lahreche, N. Grandjean, F. Semond, B. Beaumont, I. Grzegory, S. Porowski, and R. Triboulet, Physica B **302-303**, 39 (2001).

[Note1] *When accounting for the anisotropy of the material, the true binding energies for Si and O donors are rather of 30.4 and 33.2 meV, respectively.*

[Note2] *In a typical PL experiment on GaN compact layers, the penetration depth of the excitation laser is about 100-200 nm, thus reducing the surface-layer volume to 3-7% of the overall probed volume.*

[Paskov2007] P. P. Paskov, B. Monemar, A. Toropov, J. P. Bergman, and A. Usui, Phys. Stat. Sol. (c) **4**, 2601 (2001).

[Reshchikov2003] M. A. Reshchikov, D. Huang, F. Yun, P. Visconti, L. He, H. Morkoç, J. Jasinski, Z. Liliental-Weber, and R. J. Molnar, J. Appl. Phys. **94**, 5623 (2003).

[Ristić2008] J. Ristić, E. Calleja, S. Fernandez-Garrido, L. Cerutti, A. Trampert, U. Jahn, and K. H. Ploog, J. Cryst. Growth **310**, 4035 (2008).

[Robins2007] L. H. Robins, K. A. Bertness, J. M. Barker, N. A. Sanford, and J. B. Schlager, J. Appl. Phys. **101**, 113506 (2007).

[Sanchez-Garcia1998] M. A. Sanchez-Garcia, E. Calleja, E. monroy, F. J. Sanchez, F. Calle, E. Munoz, and R. Beresford, J. Cryst. Growth **183**, 23 (1998).

[Sanchez-Paramo2002] J. Sanchez-Paramo, J. M. Calleja, M. A. Sanchez-Garcia, E. Calleja, and U. Jahn, Physica E (Amsterdam) **13**, 1070 (2002).

[Satpathy1983] *Satpathy has in fact calculated the wave functions and the binding energies of n = 1 and n = 2 excitons close to a surface. However, as the hole is considered as "massive", the results of these calculations can be directly applied to the case of donor atoms.* S. Satpathy, Phys. Rev. B **28**, 4585 (1983).

[Shchekin2006] O. B. Shchekin, J. E. Epler, T. A. Trottier, T. Margalith, D. A. Steigerwald, M. O. Holcomb, P. S. Martin, and M. R. Krames, Appl. Phys. Lett. **89**, 071109 (2006).

[Skromme1999] B. J. Skromme, J. Jayapalan, R. P. Vaudo, and V. M. Phanse, Appl. Phys. Lett. **74**, 2358 (1999).

[Suffczynski1989] M. Suffczynski, and L. Wolniewicz, Phys. Rev. B **40**, 6250 (1989).

[VanNostrand2006] J. E. Van Nostrand, K. L. Averett, R. Cortez, J. Boeckl, C. E. Stutz, N. A. Sanford, A. V. Davydov, and J. D. Albrecht, J. Cryst. Growth **287**, 500 (2006).

[Vurgaftman2003] I. Vurgaftman, and J. R. Meyer, J. Appl. Phys. **94**, 3675 (2003).

Part III

# Exciton capture by radiative
and non-radiative extended defects

Chapter IV - Exciton diffusion and trapping processes in defective GaN layers

In the first Chapter of this thesis, we have shown that the polarization discontinuities at the interfaces of c-plane heterostructures were detrimental for the radiative efficiency of devices. Indeed, for polar QWs typically thicker than the bulk exciton Bohr radius, built-in electric fields drastically reduce the overlap between electron and hole wave functions. Consequently, the growth of thin QWs is mandatory to achieve devices with high radiative efficiency. Conversely, the growth of wide QWs is of key importance when designing high-power nitride-based optoelectronic devices: they indeed allow reducing the carrier density in the QW, hence lessening the efficiency of Auger-like mechanisms [Gardner2007].

However, in order to control the cost of fabrication, one usually grows non-polar GaN on non lattice-matched foreign substrates such as sapphire or $LiAlO_2$. The strain induced in the heteroepitaxial layers then relaxes through the generation of dislocations or basal stacking faults. In this Chapter, we present the luminescence properties of a-plane GaN layers grown on sapphire and processed by the epitaxial lateral overgrowth technique. These layers will be used later on as quasi-substrates on which will be grown the (Al,Ga)N/GaN QWs studied in Chapter VI. We first show that these layers present high density of basal plane stacking faults (BSFs), a radiative kind of planar extended defects. We focus particularly on the identification of BSFs by continuous-wave cathodoluminescence. Then, we pay peculiar attention to the relaxation and diffusion processes of excitons with respect to the local density in BSFs. We support our time-resolved experiments by a diffusion model to demonstrate that the diffusion of free excitons in the present layers is assisted, at low-temperature, by the presence of donor atoms.

IV.1. GROWTH AND ELO-PROCESSING OF *a*-PLANE GaN TEMPLATES

Several groups have already reported on the fabrication of *a*-plane GaN templates using the epitaxial lateral overgrowth (ELO) technique [Imer2006,Ni2006]. This processing technique results in layers with improved surface morphology and material quality in the so-called "wing" regions that grow along the +*c* (Ga-face) and –*c* (N-face) directions, respectively. The *a*-plane GaN layer studied here, grown by Dr. Tiankai Zhu and Denis Martin (LASPE-EPFL), has been obtained with a similar approach. First, a 1.7 μm thick planar *a*-plane GaN layer has been grown on *r*-plane sapphire by hydride vapor phase epitaxy (HVPE) [Zhu2007]. It was then patterned with SiO_2 stripes (200 nm thick and 40 μm wide) oriented along the [1-100] direction, separated by 5 μm-wide windows. These windows seeded the HVPE growth of a 22 μm thick uncoalesced *a*-plane GaN ELO epilayer with ELO-wing widths varying from 20 to 30 μm (Fig. 4.1).
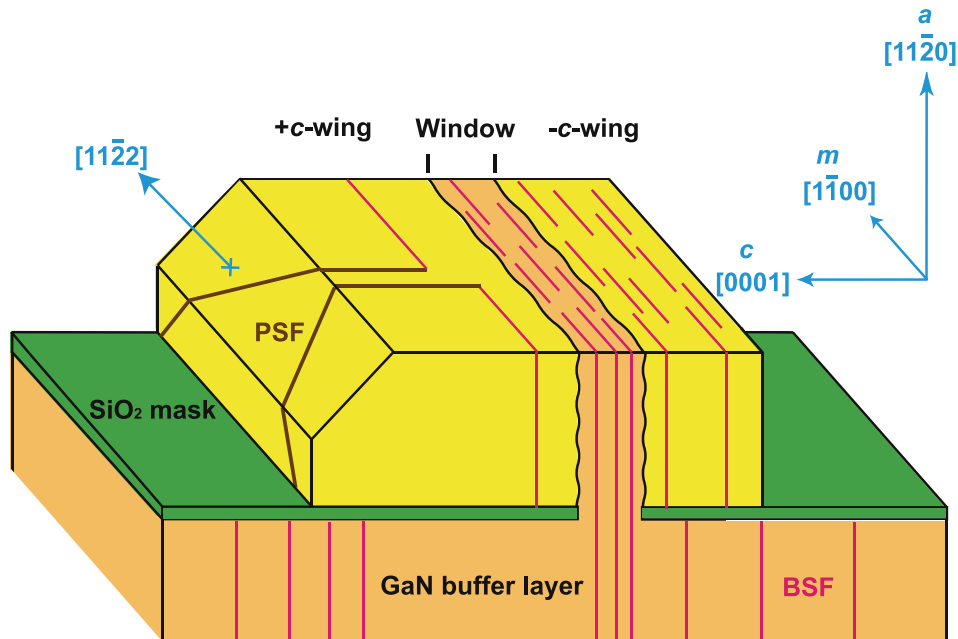
Figure 4.1: Schematic representation of our ELO a-plane GaN layer. The ELO mask consists of SiO₂ stripes aligned along the m-axis. The BSF-planes propagate from the substrate to the surface of the sample. BSF in the wings originate at the interface between SiO₂ and GaN. BSFs are closed either by partial dislocations or by prismatic stacking faults (PSFs).

Figure 4.2 is a TEM micrograph evidencing the efficient reduction of threading dislocation density in in the overgrown regions of the layer. While the dislocation density is estimated to larger than 10^{10}-10^{11} cm^{-2} in the openings, it can be reduced by more than one order of magnitude in the ELO-wings. High densities of basal plane stacking faults (BSFs) are also observed in both the wings and the openings. While in c-plane GaN, BSFs are seldom observed more than 15 nm away from the interface with substrate [Lorenz2000], they are found in high densities in non-polar GaN. Within the hexagonal phase, the atomic planes normally follow the stacking sequence …AaBbAaBbAaBb… along the [0001] direction, capital and lowercase letters corresponding to Ga and N atoms, respectively. However, fault can occur in the stacking sequence. The simplest violation of the stacking sequence is …AaBbAaBbCcBbCcBb… (Fig. 4.3). Such fault is called I_1 or type-I basal plane stacking fault and is observed in high density in our layer. Let us note, also, that I_2 and extrinsic faults have been observed in c-plane GaN [Ruterana2002] and recently in a-plane GaN grown at high temperature on c-plane sapphire [Tischer2011].
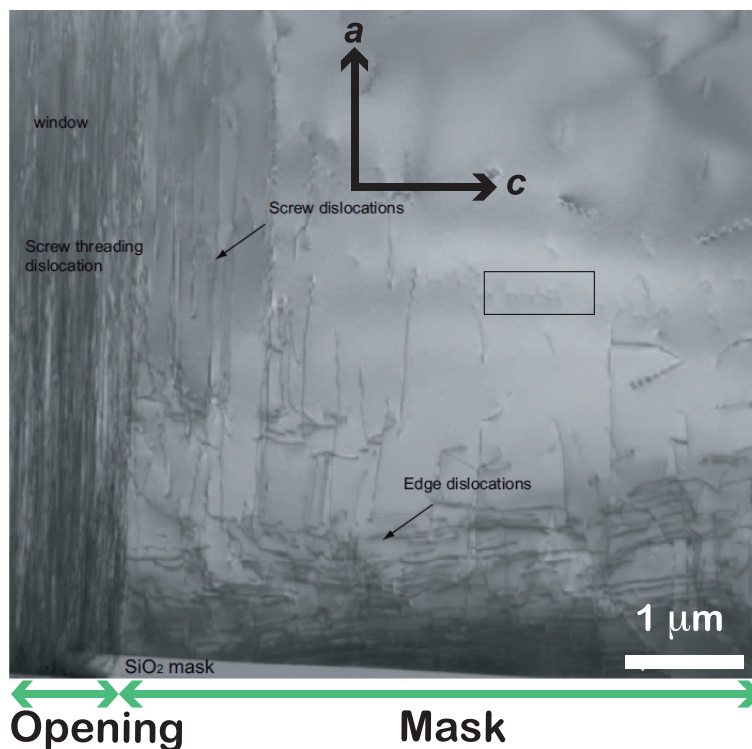
Figure 4.2: TEM micrograph of an a-plane ELO-GaN layer (courtesy of Dr. Y. Arroyo [Arroyo2009]). Patterning GaN with SiO₂ stripes and subsequent lateral overgrowth results in a drastic reduction of the dislocation density in the ELO-wings.

I_1-BSFs are formed by the dissociation of a perfect dislocation into two partial Franck-Schokley dislocations. BSFs thus do not extend infinitely in the c-plane and are "closed" either by partial dislocations or by prismatic stacking faults. The mechanism leading to the

dissociation of a perfect dislocation and to the formation of BSFs is not clear yet, and might be driven by impurities (*see* Chapter V). In any case, BSFs can appear at the interface between GaN and the sapphire substrate, but also during the lateral overgrowth. In the latter case, and under our growth conditions, BSF formation is favored when the growth occurs along the *-c*-axis. As a consequence, the ELO windows and *-c*-wings present much higher densities of BSFs ($\sim 10^6$ cm^{-1}) compared to what is observed in the *+c*-wings ($\sim 10^4$ cm^{-1}). In the following, we will show that one can qualitatively estimate the local density of BSF not only by TEM experiments, but also through continuous-wave CL experiments carried out in a SEM.
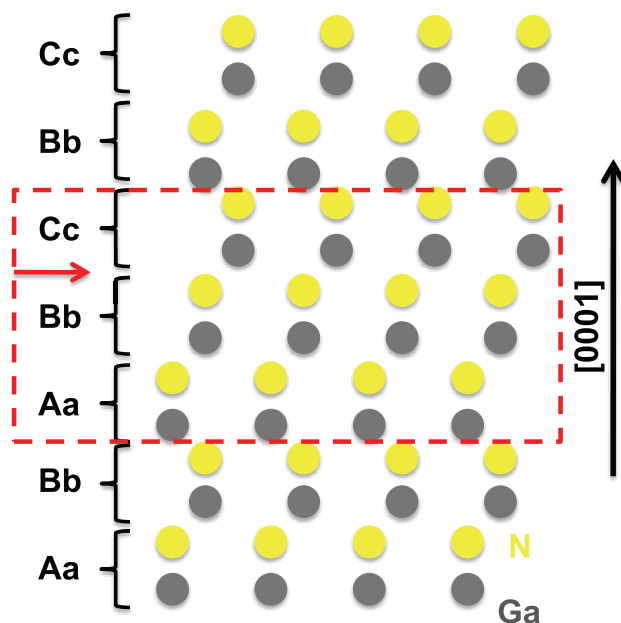
Figure 4.3: Ga and N stacking sequence in the vicinity of a type-I BSF. The red arrow points out the stacking fault, which can be seen as an inclusion of cubic-like GaN in the wurtzite matrix (dashed rectangle).

IV.2. CONTINUOUS-WAVE CATHODOLUMINESCENCE OF STACKING FAULTS

IV.2.1. CL Spectrum: identification of the BSFs

At 10 K, the CL spectrum of our layer shows two intense emission lines in the near band-edge region of GaN (Fig. 4.4(a)). We first observe one intense line at 3.471 eV related to donor-bound excitons (D°X). On the high-energy side of the D°X emission lies the

contribution from the recombination of A free exciton (FX) at 3.478 eV, as confirmed by reflectivity experiments (Fig. 4.4(b)). Although our sample is certainly strained, FX and D°X emissions lie at the same energy than in strain-free GaN [Kornitzer1999]. As discussed in [Paskov2005], such an absence of bandgap shift should in fact result from the combination of two different in-plane strain components. Similarly to what has been seen in *c*-plane HVPE GaN layers [Martin2006], our unintentionally *n*-doped sample also contains a residual doping by acceptors, which may give rise to a weaker emission at 3.465 eV related to acceptor bound excitons (A°X).

(a)   *(b)*
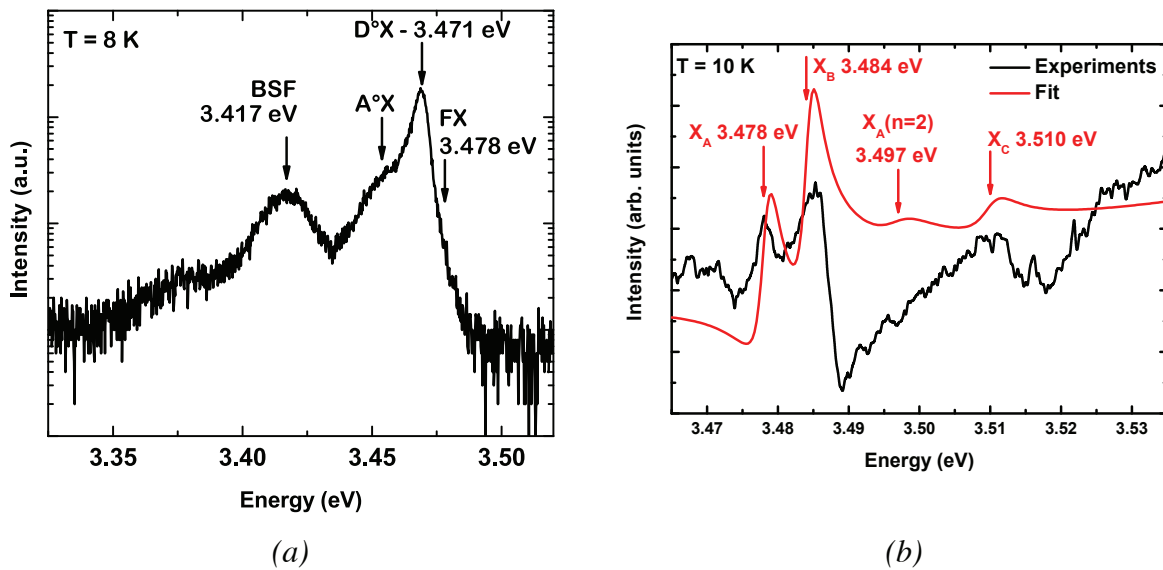
Figure 4.4: (a) CL spectrum of a-plane ELO-GaN taken at 8 K with an acceleration voltage of 20 kV and a current of 500 pA. The spectrum is dominated by the D°X and BSF emissions at 3.471 and 3.417 eV, respectively. (b) Reflectivity spectrum of a non-polar GaN layer at 10 K (courtesy of Jacques Levrat). From a crude fit of the spectrum, we deduce that exciton A resonance lies at 3.478 eV. Note that the excitonic reflectivity lineshapes are very different from what expected for bulk GaN, which results from the presence of an (Al,Ga)N layer deposited on top of the measured layer.

In agreement with other PL and CL reports on defective *a*-plane GaN layers, we observe an additional emission band centered at 3.417 eV. After a combined CL and TEM study of *a*-plane GaN layers[Liu2005] have attributed this broad line (linewidth ~ 30 meV) to the emission from I_1-type BSFs. In addition to this line, other emission bands usually related to BSFs are observed at 3.29 and 3.33 eV. It is not clear, however, if these additional

transitions arise from the prismatic stacking faults or the partial dislocations closing the BSFs, or from impurity decorations of these extended defects. A possible origin of the 3.29 and 3.33 eV lines will be proposed at the end of the fifth Chapter of this thesis.

IV.2.2. Basal plane stacking fault: a shallow type-II quantum well

As shown in Figure 4.3, a BSF leads to the apparition of an AaBbCc stacking sequence sandwiched between the ...AaBbAa... and the ...BbCcBc sequences. It has consequently been proposed by [Salviati1999] that BSFs could be seen as three monolayers thick insertions of cubic GaN inside the wurtzite phase. From *ab initio* calculations, [Stampfl1998] confirmed that the electronic properties of BSFs should be similar to that of a shallow, three monolayers thick type-II QW of cubic-like GaN. According to their calculations, the conduction and valence band offsets are ΔE_C = 270 meV and ΔE_V = -70 meV, respectively. Although the hole faces a potential barrier in the zinc-blende-like layer, it is kept in the surrounding of the QW because of the Coulomb attraction that binds it to the electron.

Such a type II exciton can be modeled efficiently by the so-called "effective potential" method [Bellabchara1994] which is a mathematical approximation based on the variational theorem, where everything turns as if the hole was confined in an *effective* (not real) potential induced by the presence of the electron in the BSF plane. We show in Figure 4.5 the estimated electron and hole wave functions for such type-II exciton. We find its emission energy equal to 3.432 eV, and quite interestingly, we find an overlap of 0.82 between electron and hole wave functions. Despite their type-II band alignment, BSFs are therefore efficient radiative emitters. [Rebane1997] also performed variational calculations to estimate the binding energy of BSF-excitons, and they found it equal to 45 meV. In our opinion, this binding energy seems quite high for a type II QW, as it is of the order of that of an exciton confined in a 2 nm thick (Al,Ga)N/GaN QW [*see* Chapter I]. With our method, we find a binding energy of 29 meV, showing that the binding energy of a BSF-exciton is only slightly reinforced compared to the bulk case. The discrepancy between the calculated BSF emission energy (3.432 eV) and that observed experimentally at 10 K (3.417 eV) could of course result from the uncertainty lying on the determination of the conduction and valence band offsets

proposed by [Stampfl1998], or be explained in terms of built-in electric fields perpendicular to the BSF-planes [Sun2002]. However, we emphasize that BSF excitons exhibit a spatial extension of 10 nm along the *c*-axis and should thus be extremely sensitive to potential fluctuations away from the BSFs. As a consequence, the difference between calculated and observed BSF exciton emission energies could be simply understood in terms of localization. The mechanisms leading to exciton localization along the BSF plane will be discussed in more details in Chapter V.
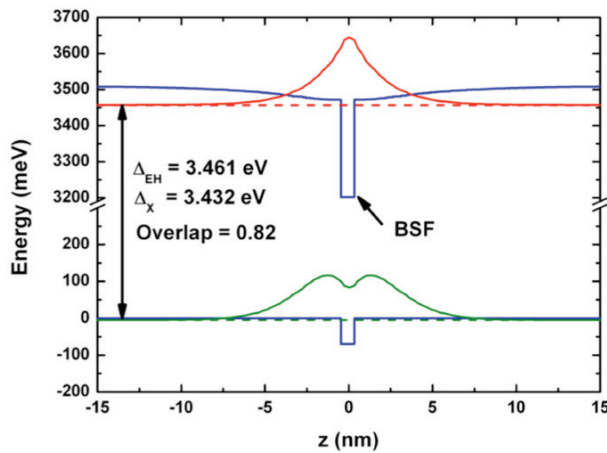

Figure 4.5: Band profiles (blue), electron and hole envelope functions (red and green curves, resp.) and energies (dotted line) for an exciton confined in a type-I BSF. We estimate the binding and the recombination energies of such BSF-exciton to 29 meV and 3.432 eV, respectively.

IV.2.3. Spatial distribution of BSFs

Figure 4.6 displays low-temperature top-view monochromatic CL map taken at 3.417 and 3.471 eV. We observe that the BSF emission at 3.417 eV can be excited not only in the ELO windows and -*c*-wings, but also in the +*c*-wings. Surprisingly, while the BSF-density is the highest in the -*c*-wings, the BSF CL in these regions is weak and presents a rather spotty distribution. Such behavior has already been studied by TEM and CL by [Wu2008], who related it to the particular shape of BSFs in the -*c*-wings. While BSF are several micrometers long in the windows and the +*c*-wings, they are much shorter in the -*c*-wings, resulting in the spotty CL contrast shown in Figure 4.6. Moreover, as a consequence of the high BSF-density combined with the short BSF spatial extension in the -*c*-wings, the local density in non-radiative partial dislocations and prismatic stacking faults closing the BSFs is high. In this region of the sample, exciton recombination is dominated by non-radiative mechanisms and the emission at 3.417 eV is therefore weak.
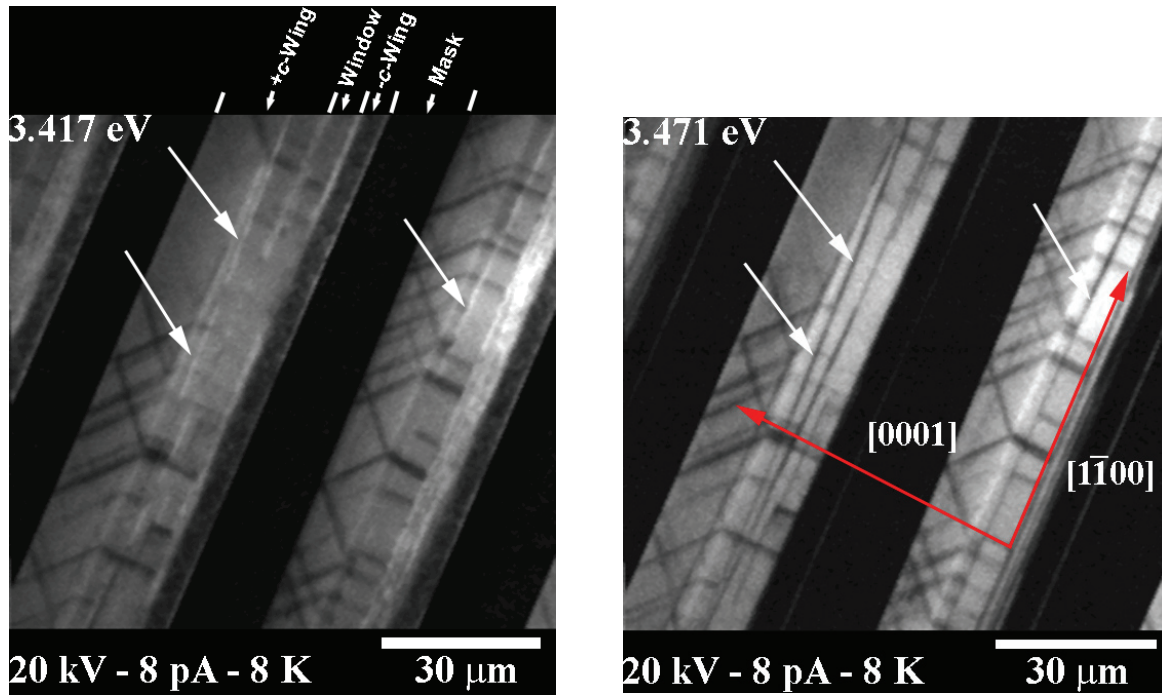
Figure 4.6: Cathodoluminescence maps of ELO a-plane GaN taken at the recombination energy of I₁ BSF-bound excitons (3.417 eV, left panel) and neutral donor-bound excitons (3.471 eV right panel). White arrows point out the emergence of dense systems of BSF planes and illustrate the anti-correlation between the emissions at 3.417 and 3.471 eV.

The most intense BSF CL comes from the window regions where it has the aspect of dashes oriented along the *m*-axis. However, the 3.417 eV emission can also be excited in the +*c*-wing: as also reported by [Netzel2008,Wu2008] the most salient contribution originates from narrow regions, elongated over several micrometers, perpendicular to the [0001] direction (Fig. 4.6). In these regions, the intense emission related to BSFs is clearly anti-correlated with the emission at 3.471 eV, related to D°X recombination (Fig. 4.7). Nevertheless, a weak signal at 3.417 eV is also detected over the entire +*c*-wing: the emission related to the BSFs is excited even when the electronic excitation beam is focused 10 μm away from the elongated regions of intense BSF-related emission. One may be tempted to attribute this emission to carriers that would diffuse from the excitation spot to the regions where intense BSF recombination is observed. However, the estimation of the excitation volume for our 20 kV electron beam with Monte-Carlo simulation [Casino], combined with the experimental determination of the diffusion length of excited carriers in GaN [Sonderegger2006] shows that carriers only diffuse ~1.5 μm away from the excitation spot.

Our sample therefore presents in the +*c*-wings a nearly homogeneous distribution of isolated BSFs. In addition to this distribution, we observe the emergence of bundles of BSFs that appear in the form of bright elongated regions, where the emission of D°X is inhibited. Similar bundles, of apparently shorter extension along the *m*-axis, are also visible in very high densities in the window region. In addition to I_1-BSFs, our CL maps also reveal the emergence of another type of planar defects that appear as dark lines even in polychromatic CL and that we will attribute later on to prismatic stacking faults.
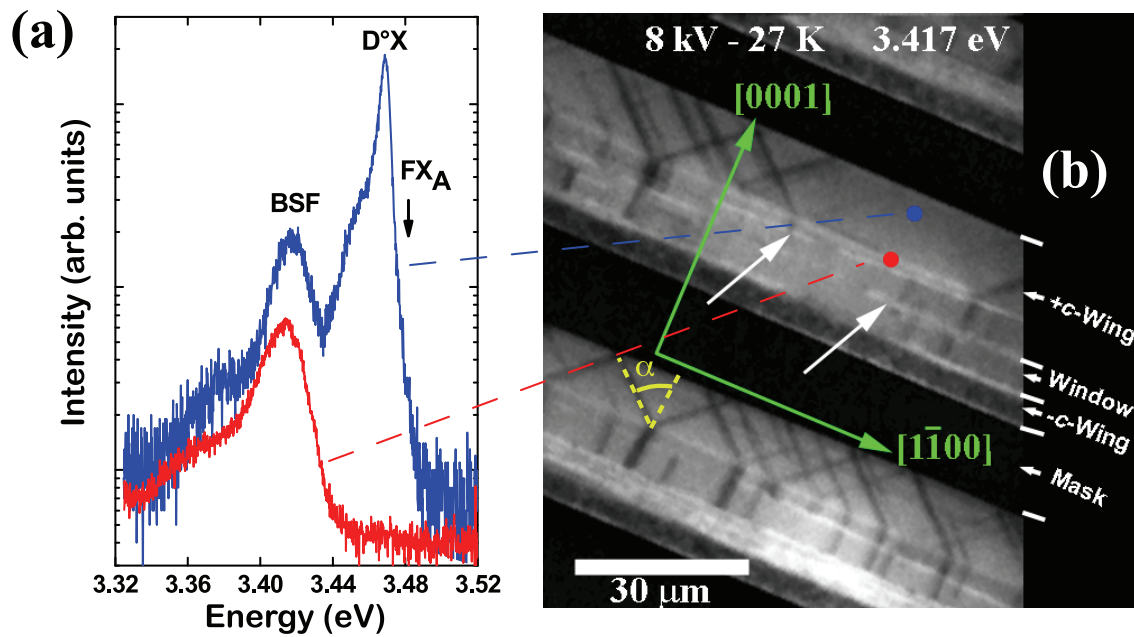
Figure 4.7: (a) Time-integrated CL spectra taken at 27 K with excitation away from and on bundles of BSFs (blue and red lines, resp.) (b) CL mapping taken at the emission energy of BSF. Blue and red dots correspond to excitation away from and on bundles of BSFs, respectively. Yellow dashed lines shows the angle α = 54 ° between the dark lines and [0001] on the (11-22) facets

IV.2.4. Prismatic stacking faults

Prismatic stacking faults (PSFs) are stacking faults perpendicular to the prismatic axes <11-20> and can be found at the extremities of BSFs. PSFs have been so far proposed as radiative defects giving rise to the 3.33 eV luminescence band of *a*-plane GaN [Liu2005]. On the contrary, as shown in Figure 4.7, we evidence that at 10 K, PSFs are non-radiative in the

3.1-3.5 eV range. As already mentioned, our ELO-layer is not coalesced. The +c-wings of our GaN layer therefore exhibit $(11\bar{2}0)$, $(11\bar{2}2)$ and (0001) facets (Fig. 4.8). As BSFs are (0001) planes, the normal of the PSFs closing BSFs is either parallel to $[2\bar{1}\bar{1}0]$ or to $[\bar{1}2\bar{1}0]$. As a consequence, the intersection between a PSF and the $(11\bar{2}0)$ facet is a straight line parallel to $[0001]$. In addition, the projection on the $(11\bar{2}0)$ plane of the intersection of a $(2\bar{1}\bar{1}0)$ PSF with the $(11\bar{2}2)$ facet makes a 54° angle with $[0001]$.

In Figures 4.6 and 4.7, we observe at the emission energies of BSF and D°X dark lines that:

(*i*) propagate along $[0001]$ on the $(11\bar{2}0)$ facets,

(*ii*) make an angle of approximately 54° with $[0001]$ on the $(11\bar{2}2)$ facets.

We also note that on our CL mappings, these dark lines are always linked with the emergence of bundles of BSFs. We therefore attribute these dark lines to the emergence of PSFs that close the BSFs. More precisely, using an argument similar to that used for distinguishing between the CL of isolated and bundles of BSFs, we relate these dark lines to the emergence of bundles of PSFs. It should be noted that such bundles of PSFs have already been observed experimentally by TEM investigations [Private2010]. Finally, when scanning the CL energy between 3.2 and 3.5 eV, bundles of PSFs always appear dark on our mappings. We thus rule out that the emission bands observed at 3.29 and 3.33 eV could be ascribed to the emission from PSFs.
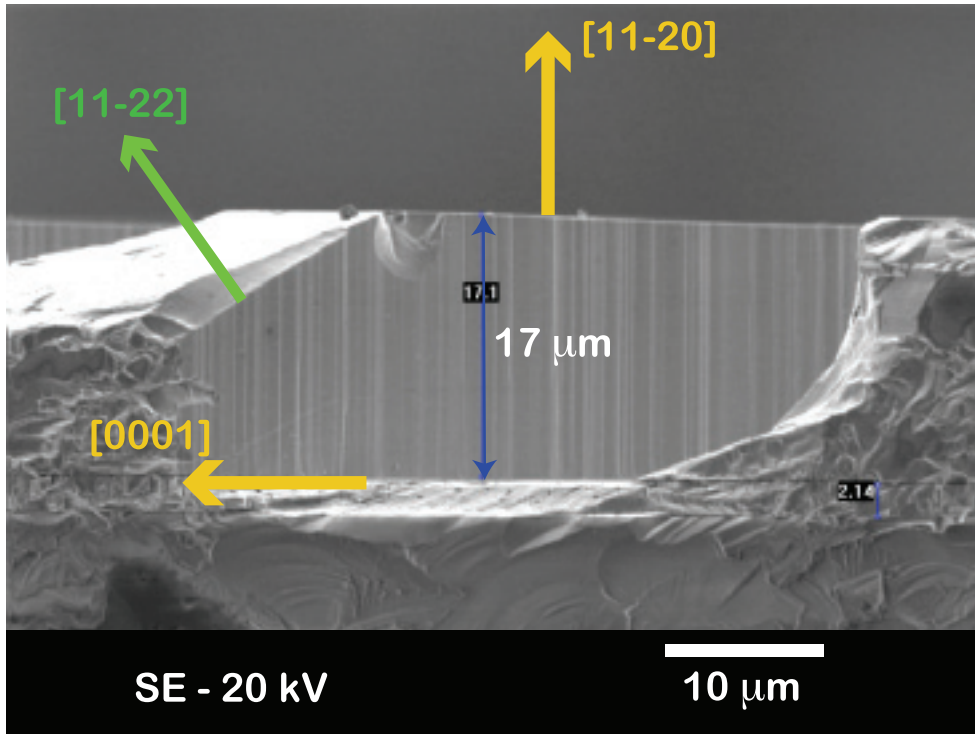
Figure 4.8: SEM cross-section of an a-plane ELO-GaN layer (courtesy of Dr. Tiankai Zhu). The +c-wings of the non-coalesced GaN layer exhibit (11-20), (11-22) and (0001) facets. The cross-section is not exactly perpendicular to the ELO-stripes axis.

So far, we got a quantitative description of the distribution of stacking faults in the ELO-wings and the windows of our *a*-plane GaN layer. While PSFs are non-radiative extended defects, we have shown that in the +*c*-wings, BSFs were efficient radiative emitters, where they form micrometer long type-II QWs perpendicular to [0001]. However, so far, we know neither the capture rate of excitons by these radiative defects, neither if BSFs gathered in high-density bundles present, or not, peculiar electronic properties compared to isolated BSFs. In the following, we will consequently probe by TR-CL the dynamics of excitons in both low- and high-density BSF regions of the layer.

IV.3. EXCITON CAPTURE DYNAMICS AS A FUNCTION OF THE LOCAL DENSITY IN STACKING FAULTS

IV.3.1. Exciton dynamics in low BSF-density regions

In the low BSF-density regions of the +*c*-wings, the CL spectrum (Fig. 4.7) and dynamics (Fig. 4.9) remain absolutely unaltered when we change from a few hundred nanometers to several micrometers, the distance between the excitation spot and the nearest bundle. In particular, the rise-time of the donor- and BSF-bound excitons CL does not depend on this distance, confirming that BSFs are homogeneously present in those regions.

The CL transients of free, D°X and BSF-bound excitons are shown in Figure 4.9. The FX line decays exponentially with a time constant of 85 ps, which corresponds to the rise-time of the D°X luminescence. The mechanism limiting the FX lifetime is therefore their capture by donors. Concerning the D°X line, it decays exponentially with a time constant of 135 ps. More surprising, the BSF CL, which decays exponentially with a time constant of 770 ps, exhibits a very slow rise: the maximum intensity is reached 300 ps after the excitation. *A priori*, one would expect the BSFs either to be directly populated by the excitation pulse or to capture free excitons by a scattering process. Similarly to the D°X CL, the BSF rise-time should then be of the order of a few tens of picoseconds, which is obviously not what we observe. The mechanism by which the BSFs trap excitons is therefore more complex.
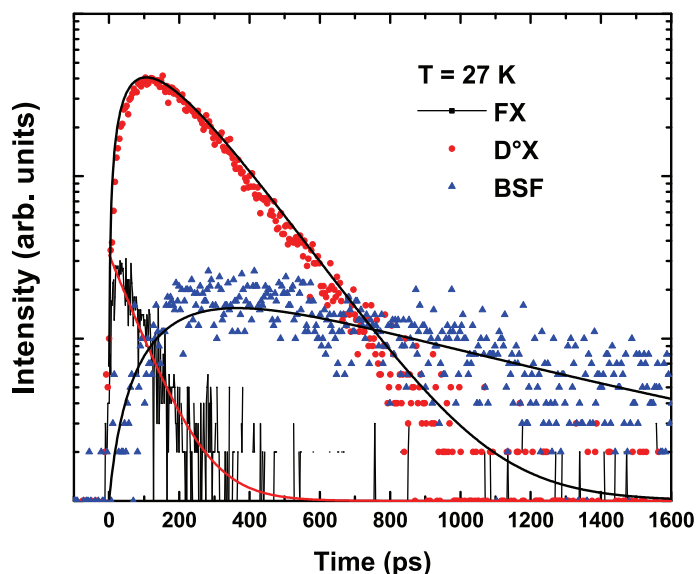

Figure 4.9: Luminescence decays of FX (black), D°X (red symbols) and BSF-excitons (blue triangles) when excitation is delivered on regions with isolated BSFs. Solid lines are the result of the fitting procedure described in the text.

IV.3.2. Carrier generation, relaxation and diffusion

We have therefore developed a one-dimensional diffusion model for excitons along the *c*-axis, *i.e.* perpendicular to the BSF planes. As sketched in Figure 4.10, we assume two BSFs separated by typically 2L = 1 μm, consistently with transmission electron microscopy that revealed, in the +*c*-wings of the ELO epilayer, typical BSF densities of 10^4 cm^{-1} [Gühne2007]. Using the model developed in [Bonard1996] and derived for GaN [Parish2006], we account for the pulsed electron-beam excitation at *t* = 0 by a Gaussian distribution of free excitons $n_{FX}(x,0) = h(x)$, with half-width of ~200 nm, along the *c*-axis, centered between the two BSFs:

$$h(x,z) = \frac{1}{2\sqrt{\pi}\sigma_x \sigma_z^3} Exp\left(-\frac{x^2}{\sigma_x^2}\right) z^2 Exp\left(-\frac{z}{\sigma_x}\right) \Rightarrow h(x) = \frac{1}{\sqrt{\pi}\sigma_x} Exp\left(-\frac{x^2}{\sigma_x^2}\right) \qquad \text{Eq.(4.1)}.$$

The parameters σ_x and σ_z characterize the lateral and the *z* extensions of the generation volume, respectively. In the case of GaN, with an acceleration voltage of 8 kV and an electron beam diameter of 50 nm (our experimental conditions), σ_x and σ_z are estimated to be 155 and 40 nm, respectively. These free excitons then diffuse (we used the ambipolar diffusion coefficient D_{FX} = 4 cm^2.s^{-1} determined in [Mickevicius2005]), and further recombine radiatively and non-radiatively (lifetimes τ_r and τ_{nr}). Free excitons can also be captured by neutral donors to form D°X. We denote by 1 / τ_c the capture rate of free excitons by donors. This rate depends on both the temperature and the doping of our layer.

$$\frac{\partial n_{FX}(x,t)}{\partial t} = D_{FX} \frac{\partial^2 n_{FX}(x,t)}{\partial x^2} - \frac{n_{FX}(x,t)}{\tau_r} - \frac{n_{FX}(x,t)}{\tau_{nr}} - \frac{n_{FX}(x,t)}{\tau_c}. \qquad \text{Eq.(4.2)}.$$

Concerning the capture of free excitons by BSFs, we consider that a free exciton reaching a BSF is instantaneously captured. We consequently model BSFs by absorbing barriers for excitons: $n_{FX}(|L|,t) = 0$. BSF-bound excitons can only recombine radiatively with decay time τ_{BSF}, whereas the radiative lifetime for donor-bound excitons is $\tau_{D°X}$. A crucial ingredient of the model is the time τ_{esc}, characteristic of the thermally assisted escape of excitons from neutral donors. As the thermal escape of excitons from D°X presents an

activation energy of 5-7 meV [Leroux1999], this delocalization mechanism is already activated at 30 K.

$$
\left\{
\begin{array}{l}
\dfrac{\partial n_{D°X}(x,t)}{\partial t} = -\dfrac{n_{D°X}(x,t)}{\tau_{D°X}} - \dfrac{n_{D°X}(x,t)}{\tau_{esc}} + \dfrac{n_{FX}(x,t)}{\tau_c} \\[4mm]
\dfrac{\partial n_{BSF}(t)}{\partial t} = \dfrac{\partial n_{FX \to BSF}(t)}{\partial t} - \dfrac{n_{BSF}(t)}{\tau_{BSF}}
\end{array}
\right.
\qquad \text{Eq.(4.3).}
$$

IV.3.3. Donor-assisted diffusion of excitons

Figure 4.10 illustrates the modeled time-dependence of FX and D°X density profiles. We used the same parameters as those that allowed us to fit simultaneously the relative intensities, rising and decaying dynamics of all three types of excitons (Fig. 4.9), for an inter-BSF distance of 1 μm. Given the fast capture of excitons onto donors, and despite some diffusion of those FX towards the BSFs, the D°X distribution after a few tens of picoseconds is quite similar to the initial distribution of FX. Therefore, if we do not include the thermally assisted reemission of excitons from the donors, we cannot fit the observed long rise-time for the BSF signal, because the BSFs would trap a very small amount of excitons, with a short time constant.

The best fit to our experimental results yields: $\tau_{esc} = 600$ ps, $\tau_c = 150$ ps, $\tau_{D°X} = 140$ ps and $\tau_{BSF} = 770$ ps. The latter two values, close to the measured CL decay times, characterize the dominant decay mechanisms of D°X and BSF excitons. They should therefore be determined with a good accuracy. The same comment goes to the capture time of FX onto donors (τ_c), which controls both the decay rate of FX and the rise rate of the D°X transition. We also find $\tau_{nr} = 600$ ps and $\tau_r = 6000$ ps, but these values are estimated with a lower accuracy: FX radiative and nonradiative recombinations are not the mechanisms that limit the FX lifetime, but rather control the instantaneous intensity.

Concerning the role played by donors in the diffusion process, we must stress the fact that the escape time τ_{esc} is neither independent on the inter-BSF distance, nor on the fixed diffusion coefficient D_{FX}. Nevertheless, whatever the values that we tried to set for D_{FX} or for

the inter-BSF distance, we absolutely need to include the thermally assisted escape of excitons from donors in order to fit the fast decay of FX and both the respectively fast and slow rise-times of D°X and BSFs CL. This demonstrates that, for T = 27 K, excitons cathodogenerated in the low BSF-density regions diffuse towards the BSFs *via* the donors, by some kind of hopping process.
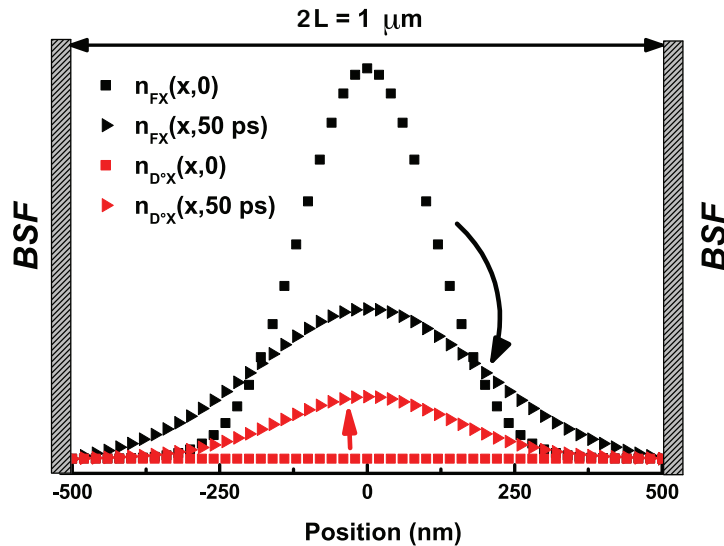
Figure 4.10: Calculated spatial distributions of FX and D°X (black and red symbols, respectively) at t = 0 and t = 50 ps (squares and triangles).

IV.3.4. Exciton dynamics in high BSF-density regions

Our model is not meant to describe the case of direct excitation of high-density bundles, where BSFs are typically separated from each other by 10 nm, *i.e.* only 3 times the donor (or exciton) Bohr radius and smaller by a factor of 1.4 than the characteristic diameter of the D°X complex [Suffczynski1989]. Consequently,

(i) the electron beam excites simultaneously several BSFs,

(ii) the lifetimes of free excitons should be dramatically short

 (*iii*) the D°X wave functions should be altered when located in bundles of BSFs.

This is confirmed by the experimental results shown in Figure 4.8: we only record the BSF-related line centered at 3.417 eV when excitation is delivered on a bundle of BSFs.

Although the rise-time is here much shorter than the one observed in the diluted regions (Fig. 4.11), the CL at 3.417 eV reaches its maximum after ~110 ps. The population of BSF-excitons is consequently not established instantaneously.
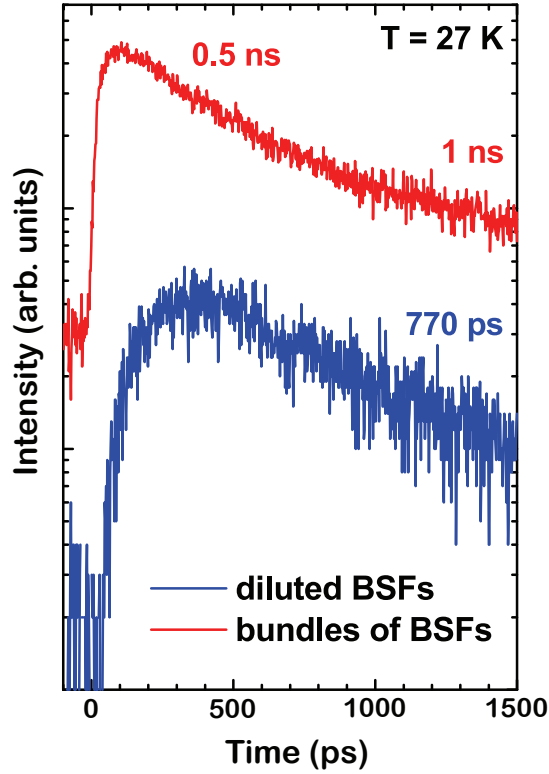
Figure 4.11: Time-dependence of the spectrally integrated BSF emission for excitation delivered on and away from bundles of BSFs (red and blue lines, respectively). CL transients have been shifted vertically for clarity. While the emission from isolated BSFs rises slowly and decays exponentially, the CL from bundles of BSFs rises within 110 ps and presents a non-exponential decay.

Figure 4.12 shows the time-dependence of bundles of BSFs CL. At short delays, the BSF luminescence is centered at 3.43 eV and its high-energy tail exhibits a high effective carrier temperature. At longer delays, the BSF CL redshifts to 3.417 eV and gets narrower. We relate this observation to slow relaxation mechanisms of BSF- excitons towards the potential fluctuations inside BSFs themselves. We also note [Badcock2010] have recently reported a similar temporal behavior for the BSF luminescence.

(a) *(b)*
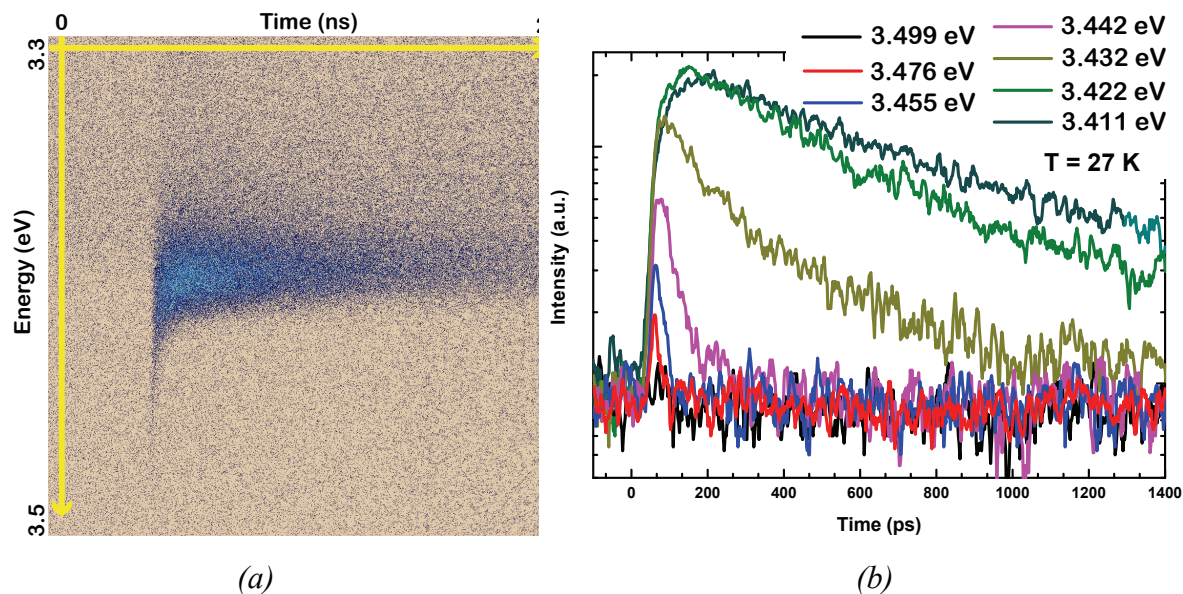
Figure 4.12: Time evolution of the BSF CL when excitation is delivered on a bundle of BSF. While the high-energy tail of the BSF CL exhibits an instantaneous rise, the CL at energy lower than 3.43 eV rises slower, as an evidencing of slow intra-BSF relaxation mechanisms.

IV.3.5. BSF-excitons oscillator strength with respect to the local density in BSFs

The decay of the 3.417 eV BSF-related CL are clearly different when excitons are created on (multi-exponential decay) and away from (exponential) the bundles (Fig. 4.11): we observe on the bundles components faster (0.5 ns) and slower (1 ns) than the decay measured on isolated BSFs. Although we do not exclude that the fast component of the bundle of BSF CL at 3.417 eV could arise from the dynamical transfer of excitons from shallow to deeper localized states, the slow component with characteristic lifetime of 1 ns evidences in the bundles a large variety of electron-hole wave functions overlaps that we relate to the distribution of inter-BSF distances.
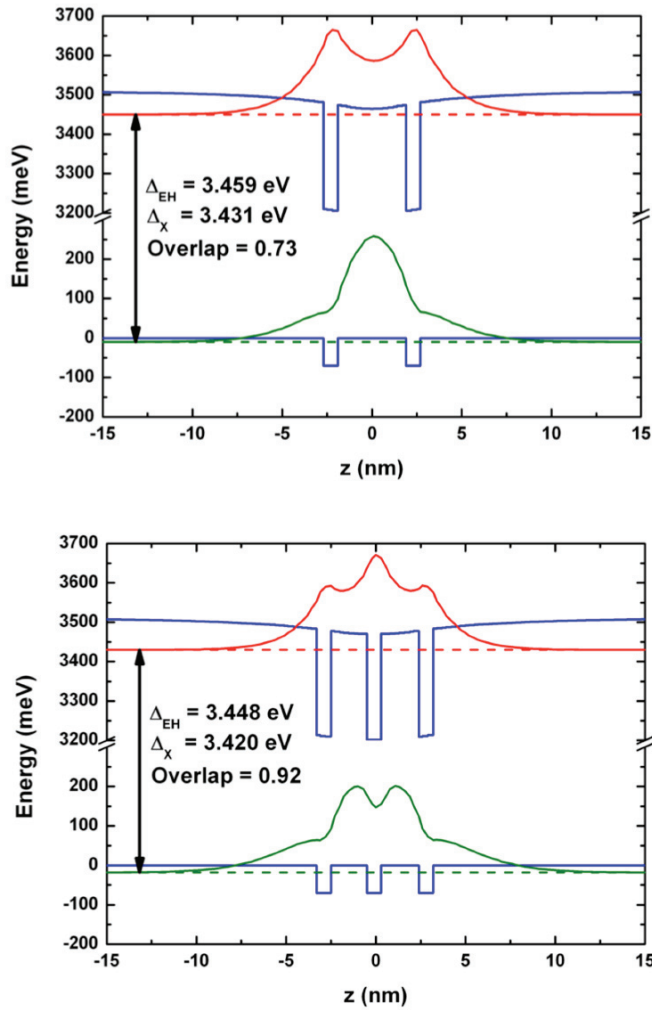
Figure 4.13: Band profiles (blue), electron and hole envelope functions (red and green curves, resp.) and energies (dotted line) for excitons confined in two coupled BSFs separated by 2 nm (a) and in three coupled BSFs separated by 3 nm (b).

Using effective potential calculations, we calculate the exciton binding energy and the electron / hole overlap for different BSF/BSF coupling schemes. Significant variations of oscillator strength can be found, but surprisingly, increased as well as decreased oscillator strengths can be obtained when coupling BSFs (Fig. 4.13). For an odd number of BSFs, the exciton wave function tends to be centered on the middle QW and, when increasing the barrier width, one tends rapidly towards the case of an isolated BSF: the change in energy and oscillator strength is small. For even numbers of BSFs, what happens is that the hole presence probability tends to be concentrated in the central layer and the exciton is then built upon this hole with symmetrical wings for the electron probability, corresponding to the BSFs. Increasing the barrier width, in this case, is equivalent to pulling these wings apart and away from the hole. Only this case can give rise to substantial variations of recombination probability. Due to the variety of coupling schemes existing in bundles of BSFs, the luminescence from these should be multi-expontential. On the contrary, the luminescence

from isolated BSF has to be mono-exponential, with a decay time corresponding to the calculated squared overlap integral of 0.82 (Figure 4.5).

Note, finally, that a type-I band line-up between cubic-like and wurtzite BSF could also provide an exciton emission energy at 3.43 eV, provided we use in our calculations a conduction band-offset of 0.4. Similar to the case of type-II QWs, bunching several of these type-I QWs lead to large variation in electron-hole overlap. Our time-resolved CL measurements on bundles of BSFs should therefore not be considered as an indirect proof of the type-II band alignment of BSFs in GaN. Nevertheless, a type-II band alignment between the zinc-blende and the wurtzite phases of a semiconductor seems a general feature, as predicted in [Murayama1994]. In addition, the type-II alignment between cubic and hexagonal GaAs has been verified experimentally by [Spirkoska2009].

IV.4. CONCLUSIONS

In conclusion of the fourth Chapter of this thesis, we have studied the recombination dynamics of excitons in *a*-plane GaN thick layers grown on sapphire and processed by epitaxial lateral overgrowth. We have shown that in addition to the trapping by neutral donors, excitons are extremely affected by the presence of basal plane stacking faults (BSFs). These extended defects, arising from the dissociation of mixed dislocations into two partial dislocations, can be seen as shallow three monolayers thick QWs of cubic GaN emitting at 3.42 eV.

The spatial distribution of BSFs in ELO-GaN is highly inhomogeneous and we have been able to distinguish by cathodoluminescence experiments between regions of the sample with isolated BSFs and regions with high BSF densities. Contrary to what usually assumed, we have also established that the prismatic stacking faults closing the BSFs acted as efficient non-radiative recombination centers.

We have then studied by time-resolved CL experiments exciton recombination dynamics with respect to the local density in BSFs. In regions where the BSF density is low, we have observed that the diffusion of excitons from the generation volume to the BSF planes

was assisted by the presence of neutral donor atoms. In other words, excitons diffuse to BSFs after successive capture and thermal detrapping from donor atoms, which results in a slow rise of the BSF luminescence. In bundles of BSFs, the CL rise time, albeit much faster than for regions with low BSF density, is not instantaneous. The latter behavior, which we attribute to exciton localization along the BSF plane, will be discussed thoroughly in the next chapter. Finally, while the luminescence decay observed for isolated BSF is exponential, it is not the case for BSFs. We related it to the large variety of BSF-BSF coupling schemes in bundles of BSFs that gives rise, with respect to the single BSF case, to increased as well as decreased BSF exciton radiative lifetime.

REFERENCES

[Arroyo2009] *This micrograph can also be found* Y. Arroyo Rojas Dasilva, PhD Thesis, n° 4193, EPFL (2009). *Manuscript available online* (http://library.epfl.ch/theses/?nr=4193).

[Badcock2010] T. J. Badcock, S. Hammersley, M. J. Kappers, C. J. Humphreys, and P. Dawson, Phys. Stat. Sol. (c) **7**, 1894 (2010).

[Bellabchara1994] A. Bellabchara, P. Lefebvre, P. Christol, and H. Mathieu, Phys. Rev. B **50**, 11840 (1994).

[Bonard1996] J.-M. Bonard, and J.-D. Ganière, J. Appl. Phys. **79**, 6987 (1996).

[Casino] *Simulations done with* CASINO, Version 2.42, *available online for free* (http://www.gel.usherbrooke.ca/casino/What.html).

[Gardner2007] N. F. Gardner, G. O. Müller, Y. C. Shen, G. Chen, S. Watanabe, W. Götz, and M. R. Krames, Appl. Phys. Lett. **91**, 243506 (2007).

[Gühne2007] T. Gühne, Z. Bougrioua, P. Vennéguès, M. Leroux, and M. Albrecht, J. Appl. Phys. **101**, 113101 (2007).

[Imer2006] B. Imer, F. Wu, S. P. DenBaars, and J. S. Speck, Appl. Phys. Lett. **88**, 061908 (2006).

[Kornitzer1999] K. Kornitzer, T. Ebner, K. Thonke, R. Sauer, C. Kirchner, V. Schwegler, M. Kamp, M. Leszczynski, I. Grzegory, and S. Porowski, Phys. Rev. B **60**, 1471 (1999).

[Leroux1999] M. Leroux, N. Grandjean, B. Beaumont, G. Nataf, F. Semond, J. Massies, and P. Gibart, J. Appl. Phys. 86, 3721 (1999).

[Liu2005] R. Liu, A. Bell, F. A. Ponce, C. Q. Chen, J. W. Yang, and M. A. Khan, Appl. Phys. Lett. **86**, 021908 (2005)

[Lorenz2000] K. Lorenz, M. Gonsalves, W. Kim, V. Narayanan, and S. Mahajan, Appl. Phys. Lett. **77**, 3391 (2000).

[Martin2006] D. Martin, J. Napierala, M. Ilegems, R. Butté, and N. Grandjean, Appl. Phys. Lett. **88**, 241914 (2006).

[Mickevicius2005] J. Mickevicius, M. S. Shur, R. S. Qhalid Fareed, J. P. Zhang, R. Gaska, and G. Tamulaitis, Appl. Phys. Lett. **87**, 241918 (2005).

[Murayama1994] M. Murayama, and T. Nakayama, Phys. Rev. B **49**, 4710 (1994).

[Netzel2008] C. Netzel, T. Wernicke, U. Zeimer, F. Brunner, M. Weyers, and M. Kneissl, J. Cryst. Growth **310**, 8 (2008).

[Ni2006] X. Ni, Ü. Özgür, Y. Fu, N. Biyikli, J. xie, A. A. Baski, H. Morkoç, and Z. Liliental-Weber, Appl. Phys. Lett. **89**, 262105 (2006).

[Parish2006] C. M. Parish, and P. E. Russel, Appl. Phys. Lett. **89**, 192108 (2006).

[Paskov2005] P. P. Paskov, R. Schifano, B. Monemar, T. Paskova, S. Figge, and D. Hommel, J. Appl. Phys. **98**, 093519 (2005).

[Private2010] *Private communication from* UCSB (2010).

[Rebane1997] Y. T. Rebane, Y. G. Shreter, and M. Albrecht, Phys. Stat. Sol. (a) **164**, 141 (1997).

[Ruterana2002] P. Ruterana *in* "Low-dimensional nitride semiconductors", Edited by Bernard Gil, Oxford (2002).

[Salviati1999] G. Salviati, M. Albrecht, C. Zanotti-Fregonara, N. Armani, M. Mayer, Y. Shreter, M. Guzzi, Y. V. Melnik, K. Vassilevski, V. A. Dmitiev, and H. P. Strunk, Phys. Stat. Sol. (a) **171**, 325 (1999).

[Sonderegger2006] S. Sonderegger, E. Feltin, M. Merano, A. Crottini, J.-F. Carlin, R. Sachot, B. Deveaud, and J.-D. Ganière, Appl. Phys. Lett. **89**, 232109 (2006).

[Spirkoska2009] D. Spirkoska, J. Arbiol, A. Gustafsson, S. Conesa-Boj, F. Glas, I. Zardo, M. Heigoldt, M. H. Gass, A. L. Bleloch, S. Estrade, M. Kaniber, J. Rossler, F. Peiro, J. R. Morante, G. Abstreiter, L. Samuelson, and A. Fontcuberta i Morral, Phys. Rev. B **80**, 245325 (2009).

[Stampfl1998] C. Stampfl, and C. G. Van de Walle, Phys. Rev. B **57**, R15052 (1998).

[Suffczynski1989] M. Suffczynski, and L. Wolniewicz, Phys. Rev. B **40**, 6250 (1989).

[Sun2002] Y. J. Sun, O. Brandt, U. Jahn, T. Y. Liu, A. Trampert, S. Cronenberg, S. Dhar, and K. H. Ploog, J. Appl. Phys. **92**, 5714 (2002).

[Tischer2011] I. Tischer, M. Feneberg, M. Schirra, H. Yacoub, R. Sauer, K. Thonke, T. Wunderer, F. Scholz, L. Dieterle, E. Müller, and D. Gerthsen, Phys. Rev. B **83**, 035314 (2011).

[Wu2008] Z. H. Wu, A. M. Fischer, F. A. Ponce, B. Bastek, J. Christen, T. Wernicke, M. Weyers, and M. Kneissl, Appl. Phys. Lett. **92**, 171904 (2008).

[Zhu2007] T. Zhu, D. Martin, R. Butté, J. Napierala, and N. Grandjean, J. Cryst. Growth **300**, 186 (2007).

Chapter V - Localization of excitons by extrinsic donors in type-II quantum wells

As presented in the previous Chapter, non-polar GaN layers grown on lattice-mismatched substrates present high densities of basal plane stacking faults (BSFs). In addition to the 3.471 eV line, ascribed to the recombination of donor bound excitons (D°X), we observed an intense emission band centered at 3.417 eV, which we related to the presence of BSFs. So far, despite some experimental indication of intra-BSF localization (Fig. 4.12), we only considered BSFs as ideal type-II QWs made of two binary materials: 3 monolayers of cubic GaN embedded in the hexagonal phase. However, because of the large spatial extension of their wave function out of the BSF plane (Fig. 4.5), BSF-excitons should be extremely sensitive to potential fluctuations located out of the BSF plane. In this Chapter, we address this problem by experimental and theoretical means. We first analyze the temperature and time dependencies of the BSF emission and demonstrate that BSF excitons are localized along the BSF plane. We then propose the statistical distribution of donor atoms as the origin of the localization mechanisms observed experimentally and we calculate the emission energy of such D°-BSF complexes. The results yielded by our calculations is finally compared with our experiments, as well as with reports by other groups.

V.1. EXPERIMENTAL EVIDENCE FOR INTRA-BSF EXCITON LOCALIZATION

V.1.1. Temperature dependency of the BSF emission

Figure 5.1 displays time-integrated photoluminescence (PL) spectra with respect to temperature for the *a*-plane ELO-GaN layer studied in the previous chapter. At 10 K, excitons are essentially localized on donors, giving rise to the emission at 3.471 eV. For temperature

higher than 25 K, the escape of D°X toward the three-dimensional continuum of exciton states is activated, and the near band-edge emission is then dominated by free exciton (FX) recombination [Leroux1999]. Figure 5.2 displays the temperature dependence of FX and BSF emission energies obtained by deconvolution of the spectra in Figure 5.1. Experimental points are compared with the result of Varshni's empirical formula $E(T) = E(0) - \alpha T^2 / (T + \beta)$ [Varshni1967]. For FX emission energies, we obtained the best fit for $E(0) = 3.478$ eV, $\alpha = 0.80$ meV / K and $\beta = 800$ K, values in the range of those reported for c- and a-plane GaN [Vurgaftman2003].
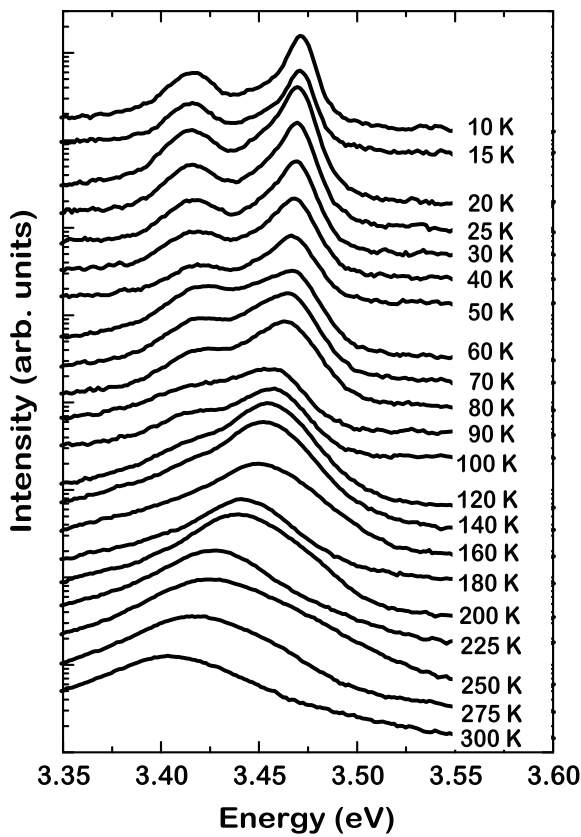
Figure 5.1: Time-integrated PL spectra of a-plane ELO GaN taken at different temperatures. The spectra have been shifted vertically for clarity.

At 10 K, the BSF emission is rather broad, as it exhibits a full width at half maximum of 30 meV. [Paskov2005] proposed that this large emission broadening might be caused by the fact that BSFs are gathered into high-density bundles. The variety of BSF-BSF coupling scheme would indeed result in variation in emission energy and therefore in the observation of a broad emission line in PL experiments. Although our calculations could reproduce this variety of emission energy in the bundles (Fig. 4.13), we have shown in the previous chapter that the emission from isolated BSF was as broad as the one from bundles of BSFs (Fig. 4.7).

As a consequence, the inhomogeneous spatial distribution of BSFs is not a convincing explanation for the broad emission line of BSF-excitons.

When temperature increases, and in agreement with previous observations made on *c*-plane [Fischer1998] and *a*-plane GaN [Paskov2005], the BSF energy position follows a S-shaped temperature dependence. It consists of a small redshift from 8 to 25 K followed by a blueshift that eventually merges with some Varshni curve for temperatures above 75 K. The blueshift part of the S-shaped temperature dependence is commonly observed in epitaxial type-I as well as type-II quantum wells, where it corresponds to the thermal escape of excitons bound to well-width fluctuations [Leroux1998]. However, it is unlikely that the quantum wells formed by stacking faults present such fluctuations because the distance between two faults in the stacking sequence is precisely determined by the type of the BSF. The width of I_1-stacking faults is therefore exactly equal to 1.5 c = 0.78 nm, where c is the unstrained lattice parameter of wurtzite GaN along the [0001] direction. The difference between the low-temperature extrapolated PL energy of ~3.433 eV and the measured minimum PL energy of 3.415 meV is the localization energy. We measure 18 meV for this localization energy, while [Paskov2005] reported ~ 20 meV.
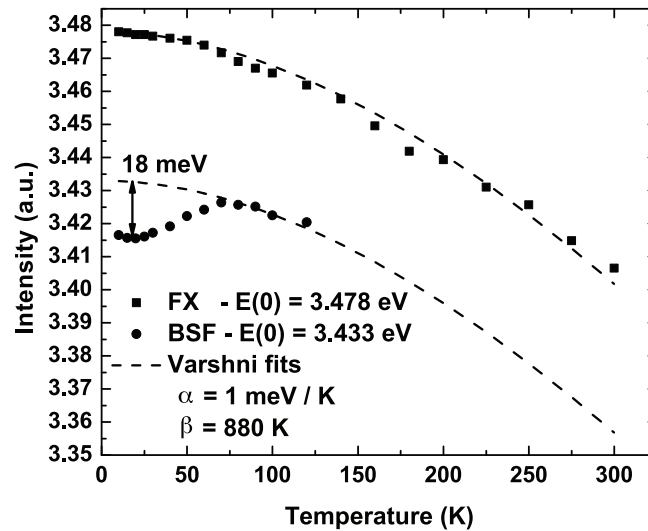

Figure 5.2: Energy position versus temperature of the free- and BSF-bound exciton lines (squares and circles, respectively). Dashed curves correspond to the result of Varshni's semi-empirical model.

[Paskov2005] have attributed the S-shaped temperature dependence of the BSF-related emission line to the delocalization of holes from the attractive -effective- potential created by the electron confined in the type-II quantum well. In other words, the blueshift would be due to a transition from a BSF-bound exciton to a free-to-bound recombination involving a bound electron and a free hole. According to this reasoning, the measured delocalization energy would be nothing but the binding energy of the type-II exciton. In our opinion, such interpretation is incorrect for two reasons:

(*i*) a binding energy of 18 meV seems, compared to the bulk value (25 meV), quite small for a type-II exciton in such shallow and narrow QWs. In agreement, our envelope function calculations yield an increase of the exciton binding energy compared to the bulk value (29 meV), since we have here a nearly bi-dimensional situation (*see* Fig. 4.5). In addition, we note that, for type-II QW, the presence of electric fields perpendicular to the confinement axis tends to minimize the electron-hole separation, thus increasing the exciton binding energy [Sun2002].

(*ii*) if such emission blueshift was related to the transition from an exciton bound to the BSF to a free-to-bound recombination, the spatial delocalization of the hole wave function should result in a huge decrease in BSF emission intensity. This is not what is seen in Figure 5.1 where the BSF emission is observed up to 140 K.

Given the fact that the wave functions of excitons bound to BSFs are quite extended in real space (Fig. 4.5), these excitons should in fact be extremely sensitive to potential fluctuations: there must consequently exist some localization effects for BSF-bound excitons. Intra-BSF exciton localization not only explains the blueshift part of BSF emission energy temperature dependence, but also the redshift from 8 to 25 K due to the ionization of excitons bound to the shallower potential fluctuation in favor of the deeper ones. This explanation is also consistent with the 4 meV blueshift and the vanishing of the low-energy tail of the BSF-related emission observed when increasing the excitation density [Paskov2005].

Concerning the possible origin of these localization effects, we first exclude the inhomogeneous spatial distribution of BSFs along the *c*-axis (*see* our previous discussion on the BSF emission broadening). We also rule out that strain fluctuation along the BSF plane could induce so strong localization effects. Indeed, the D°X emission energy shows almost no

shift in the +*c*-wings [Bastek2008]. The local strain variation along a BSF plane is therefore negligible and cannot explain the 18 meV localization energy observed for BSF excitons. We propose, however, that intra-BSF localization could arise from the random distribution of extrinsic donors located in the vicinity of the BSF. This hypothesis will be discussed thoroughly later on.

V.1.2. Time dependency of the BSF emission-energy

The temporal evolution of PL spectra brings additional evidence of localization effects inside BSFs (Fig. 5.3). During the first nanosecond of decay, while we observe a narrowing of the BSF-related emission from 26 to 18.5 meV, the high-energy tail becomes steeper. This results in a spectral redshift of the BSF emission from 3.425 eV at the beginning of the decay to 3.415 eV after one nanosecond. Decreasing the excitation density by two orders of magnitude does not result in any change in the time-dependence of the BSF-related line, indicating that the observed behavior does not stem from some descreening effects of internal electric fields [Lefebvre2004].
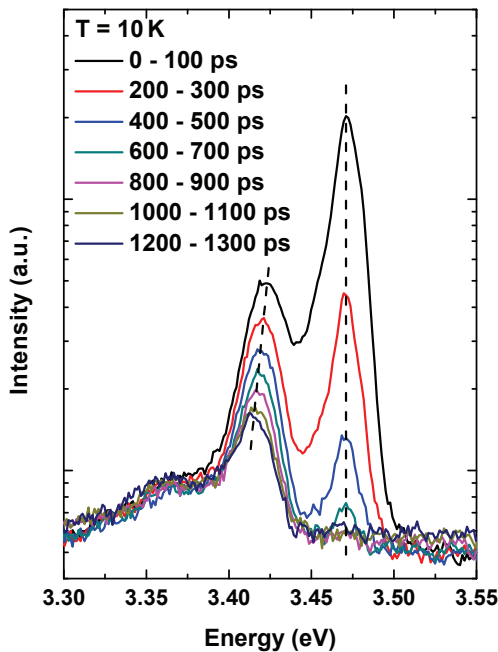

Figure 5.3: Time-evolution of the near band-edge PL of our ELO a-plane GaN, taken at 10 K. Dashed lines are guides-to-the-eye.

In contrast, this redshift is consistent with the existence of different degrees of localization that can originate from extrinsic localization centers such as donors distributed in

the vicinity of the BSFs. During the first hundred picoseconds after the excitation, BSF-excitons are distributed over a large energy range, resulting in a broad emission line centered at 3.425 eV. We remark that, when excitation is delivered directly on bundles of BSFs, the BSF emission at short delays is broad (Fig. 5.4), evidencing some band-filling effects [Kash1984]. These high-energy BSF-excitons then relax toward lower energy states and get localized along the BSF-plane, resulting in the very fast lifetime observed for the high-energy tail of the BSF emission (Fig. 4.12). In the case of isolated BSFs, the observed emission redshift and narrowing result from slight differences in radiative lifetime between shallow and deep potential fluctuations [Rashba1962] and from the transfer of excitons toward deeper states [Deveaud1987]. Note, however, that in the case of bundles of BSFs, the interpretation of the lifetimes is certainly trickier. In addition to the different localization depths, one has indeed to account for the variety of BSF-BSF coupling schemes, which yields to a variation in BSF exciton radiative lifetime (Fig. 4.13).
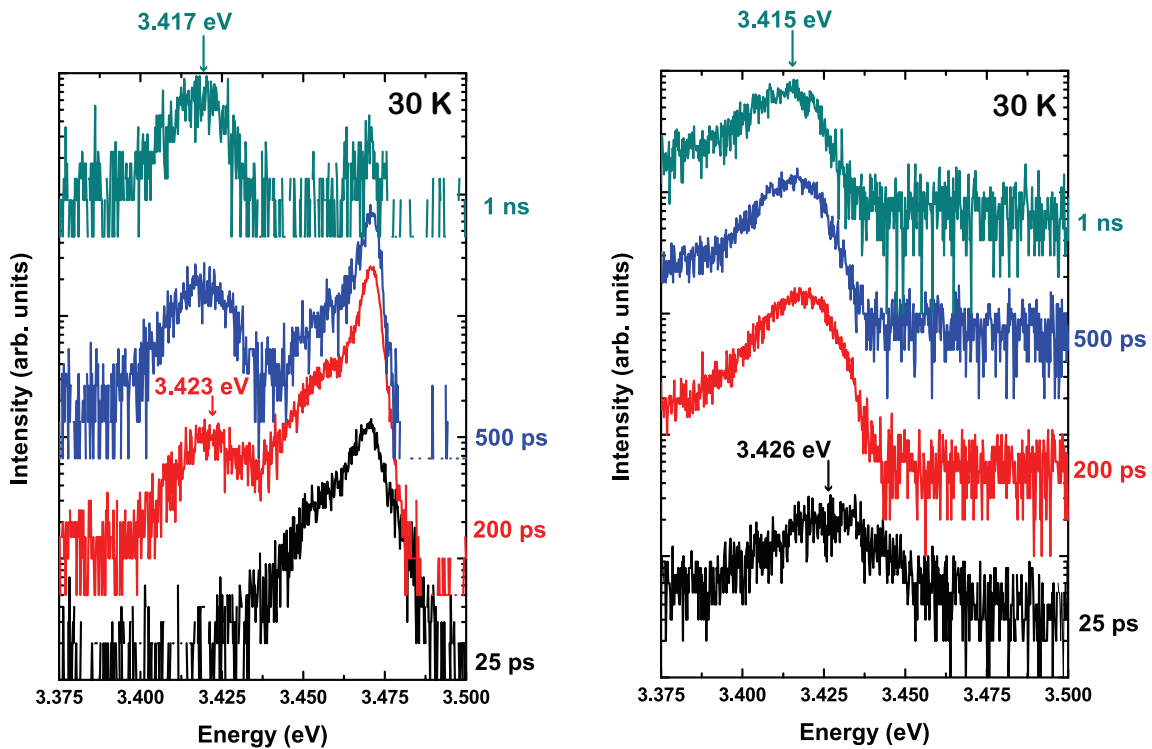

Figure 5.4: Time-evolution of the CL near band-edge at 30 K, when excitation is delivered on isolated (left panel) or on bundles of BSFs (right panel).

In any case, to support our interpretation, we remark that at 10 K, 1 ns after the excitation, the BSF emission lies at the same energy as the time-integrated BSF emission

measured at 25 K (Figure 5.2). We therefore confirm *a posteriori* that the redshift of the BSF-emssion between 10 and 25 K results from the thermally enhanced transfer of BSF excitons bound to shallow potential fluctuations toward deeper ones.

As a conclusion, the optical properties of BSF-bound excitons are tributary to potential fluctuations in the vicinity of the BSFs, necessarily leading to some in-plane localization of those excitons. The time and temperature dependencies of BSF exciton emission energy have indeed revealed some localization mechanism of excitons inside BSFs themselves, with localization energy of 18 meV. In agreement with our envelope function calculations (Fig. 4.5), the emission of BSF free excitons lies at 3.433 eV, whereas the emission from BSF localized states is centered at 3.417 eV, with a full width at half maximum of 30 meV. As neither strain nor the spatial distribution of BSFs, nor BSF width fluctuation can be proposed as convincing origin of these localization mechanisms, we propose donors as possible origin of the localization of excitons in BSFs, the statistical distribution of donor-BSF distances thus explaining the broad emission line.

In order to confirm our assumption and to estimate the influence of donors on the recombination energy of BSF-excitons, we have however to calculate the energies of both the initial and the final states of this transition. In the following, we will consequently compute the energy ground state of both D°-BSF and (D°-BSF)X complexes: the former complex is a one mobile particle problem while the latter is much more complicated, as it involves three mobile particles: two electrons and a hole.

V.2. CALCULATION OF THE D°-BSF GROUND STATE ENERGY

In the present section, we discuss the effect of a donor atom on the energy of an electron confined in a BSF in wurtzite GaN. Conversely, we have also considered this situation as the effect of a BSF on the donor binding energy. By using a variational envelope-function calculation in the "effective potential" formalism, we demonstrate that the presence of a donor, less than ~10 nm away from the BSF, essentially localizes the electron along the BSF plane. We calculate, in particular, the dependence of the in-plane extension and of the localization energy with the distance between the donor and the BSF. Note that, for clarity,

we restrict ourselves to the case of a donor atom in the vicinity of a single BSF. Donor atoms in bundles of BSF will obviously exhibit an increased binding energy compared to the single BSF case.

V.2.1. Effective potential for an electron bound to a D°-BSF

The conduction band profile along the [0001] direction (*z*-axis), perpendicular to the BSF plane, is sketched in Figure 5.5. The QW width is L_w = 1.5 c_0 = 0.78 nm, and the potential discontinuity, V_0, between the well (cubic-like GaN) and the barriers (wurtzite GaN) was taken equal to 270 meV, according to the existing literature [Stampfl1998]. To calculate the sub-band extremum and the envelope function shown in Figure 5.5, we have used an electron effective mass of m_e = 0.2 m_0 [Vurgaftman2001], for both the well and barrier materials. Counted from the edge of the quantum well, we find a binding energy of the electron to the BSF equal to 46 meV.

Figure 5.5: Band profiles, electron envelope functions (black and red curves, respectively) and energy (dotted red line) for an electron confined in a single BSF.

Now, in order to study the influence of a donor nucleus on the binding energy of an electron confined in a BSF, we apply the method described in Appendix I. Basically, we treat this problem in the effective potential formalism, where everything turns out as if the electron

was confined in a one dimensional potential that accounts for both the crystalline potential (the BSF) and the Coulomb attraction between the electron and the charged donor nucleus. We minimize the electron energy with respect to the in-plane extension of the electron wave function, allowing us to access to the binding energy of an electron on a D°-BSF (Fig. 5.6).
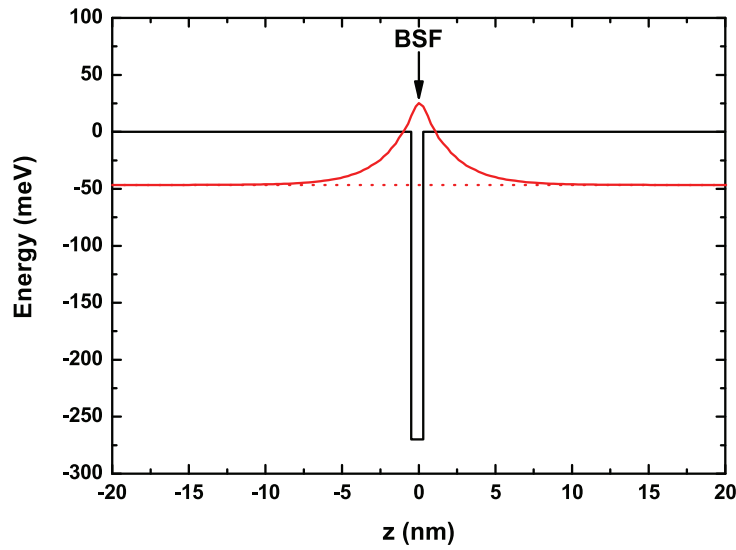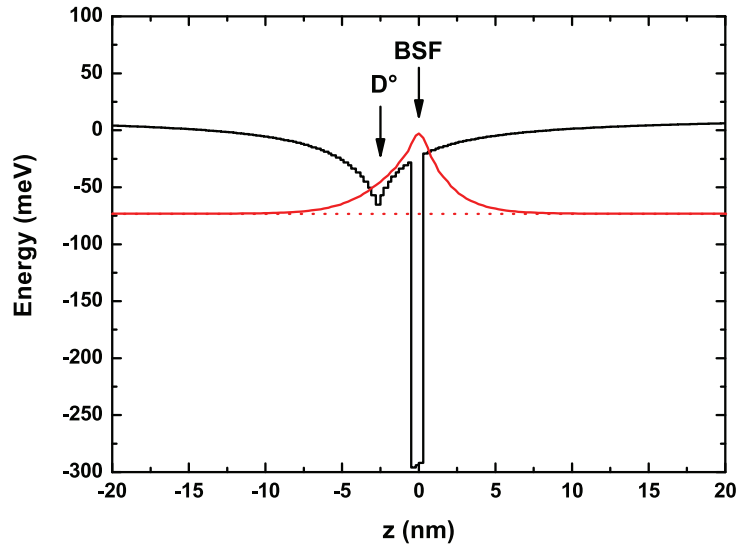

Figure 5.6: Band profiles, electron envelope functions (black and red curves, respectively) and energy (dotted red line) for an electron in the vicinity of a D° and a BSF separated by d = 2.5 nm.

V.2.2. Binding energy of the electron with respect to the D°-BSF distance

Figure 5.7 shows the spatial distribution in the *a*-plane of electron density of presence probability resulting from this calculation, for three different values of the distance *d* between the donor nucleus and the BSF plane. In all cases, the electron is strongly localized along the BSF plane. The larger the distance *d*, the weaker the localization, but it is important to remark that the effect of the donor nucleus remains significant even when *d* is as large as 10 nm. In terms of binding energy (*see* Fig. 5.8), when *d* tends to infinity, the minimum energy for the electron tends to 46 meV, *i.e.* electron localization energy on the bare BSF. When *d* is reduced to zero, the binding energy monotonously increases up to 99 meV. The difference of 99 – 46 = 53 meV is nothing but the binding energy of the donor increased by the confinement, *i.e.* ~1.8 times the binding energy of the donor in bulk GaN. The discrepancy of

this value from the binding energy of a two-dimensional donor [Bastard1981] comes naturally from the shallowness of the QW formed by the BSF, leading to a spreading of the electron wave function into the barriers. Conversely, this energy difference between the bare BSF (-46 meV) and the D°-BSF complex could as well serve as a definition of the in-plane localization energy for an electron along the BSF plane. This localization energy therefore reaches a maximum of 53 meV, for $d = 0$, and we note that it is still as large as 9 meV, for $d = 10$ nm. In practical cases, given the statistical distribution of donor-BSF distances, we expect a statistical distribution of localization energies and of characteristic localization radii.
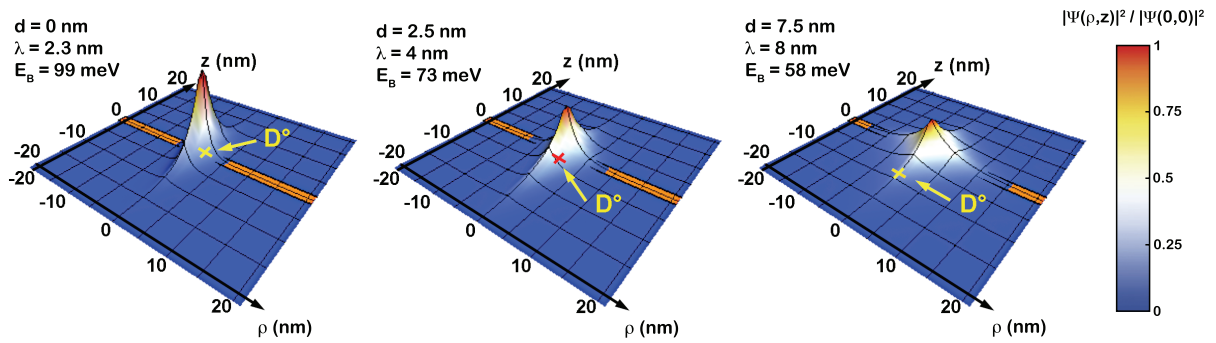
Figure 5.7: Spatial distribution of electron density of presence probability in the a-plane for d = 0, 2.5 and 7.5 nm. The cross and the orange rectangle represent the donor nucleus and the BSF plane, respectively.

The typical density of residual donors in non-intentionally doped GaN is of 10^{17} cm^{-3}, *i.e.* one donor every ~20 nm. In *a*-plane GaN, the density of BSFs can vary between 10^{6} cm^{-1} in the bundle regions to 10^{4} cm^{-1}, where BSFs are isolated [Gühne2007]. Even if we consider that the presence of BSFs has no influence on the spatial positioning of donors, we see clearly that the situation addressed here is extremely frequent:

(*i*) in bundles where the inter-BSF distance is of the order of 10 nm, there exists no such things as a "bare" donor or a "bare" BSF, and only D°-BSF complexes can occur. In agreement, we do not observe, even at short delays, any spectral signature of D°X emission when excitation is delivered on the bundles (Fig. 5.4).

(*ii*) in regions where the BSFs are isolated, the inter-BSF separation is ~1 μm. The volume fraction of material that is concerned by donor-BSF complexes is at least of 2%.
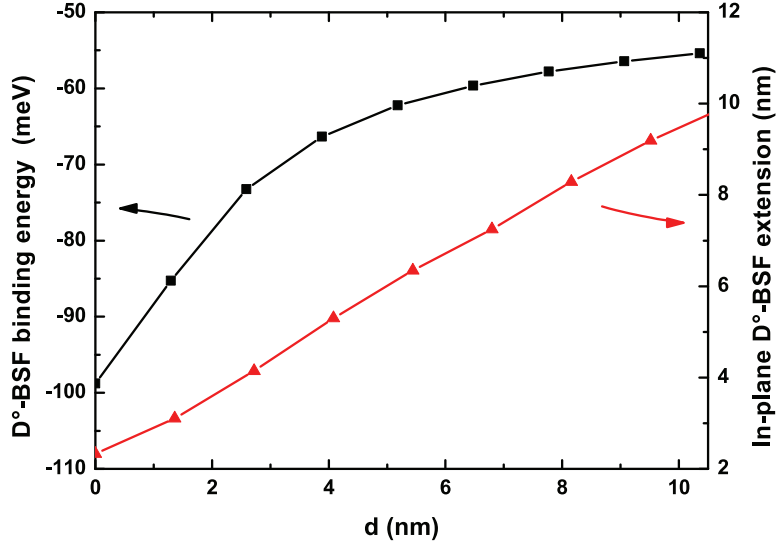
Figure 5.8: Binding energy and in-plane extension of the wave function for an electron bound to a D°-BSF, with respect to the D°-BSF separation d (squares and triangles, respectively).

In addition to the donor biding energies, we have now access to the energy of the unbound D°-BSF exciton state. In the previous Chapter, we estimated the energy of an exciton confined in a BSF to 3.432 eV. The energy of the unbound D°-BSF exciton state should therefore go from 6.84 eV, when the D° is in the BSF plane, to 6.88 eV when the D°-BSF separation is 10 nm (Fig. 5.9). Furthermore, we observed for the BSF-exciton an intra-BSF localization energy of 18 meV (Fig. 5.2). Assuming that the emission at 3.417 eV arises from BSF-excitons loosely bound to donors (*i.e.* donors located ~10 nm away from the BSF-plane), the energy of such a D°-BSF exciton complex should be of the order of 6.86 eV. For comparison, we estimate the energy of a D°X in bulk wurtzite GaN to 6.95 eV.
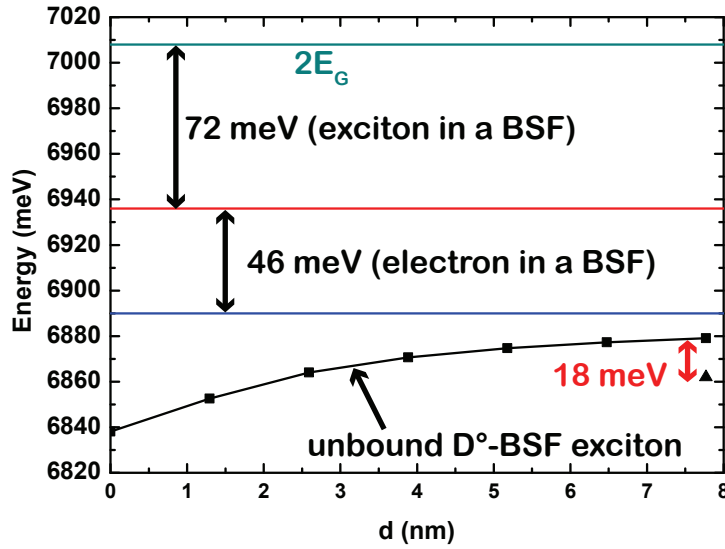
Figure 5.9: Calculated energy of an unbound D°-BSF exciton with respect to the distance d between the BSF plane and the donor nucleus. Triangle shows the energy of the localized BSF exciton expected from the experiments shown in Figures 5.2 and 5.3.

V.2.3. Consequences on the activation energies of donors and acceptors in non-polar GaN

Apart from the donor binding energies calculated above, we can draw some conclusions about the electrical properties of non-polar GaN. In the case of GaN layers with high BSF densities, the conductivity of GaN should indeed be affected by an enhanced donor binding energy. Even though full experimental evidence of such an effect is still lacking, we mention, for instance, that activation ratios between 0.1 and 0.5 have been measured at 300 K for Si donors in non-polar GaN layers [McLaurin2006], whereas this ratio is 1 in *c*-plane GaN. Such an incomplete ionization of donors may result from an increased donor binding energy in the presence of BSFs.

Our model also brings a qualitative evaluation about the interaction between an acceptor nucleus and a BSF in *p*-doped non-polar GaN. As BSFs exhibit a type-II band alignment, the acceptor binding energy should be reduced when the acceptor is located in a BSF. Confirming our expectation, recent Hall measurements have revealed that in *a*-plane

Mg-doped GaN, the activation energy of Mg acceptors with an Mg concentration of $4.0.10^{19}$ cm $^{-3}$ was found to be 118 meV, which is lower than that of *c*-plane GaN with the same Mg concentration [Tsuchiya2005,Iida2009]. Our model, however, is not meant to compute precisely the binding energy of acceptor atoms. Acceptors levels are indeed built from states belonging to the non-parabolic valence bands of the wurtzite lattice. The acceptor wave functions are therefore quite complex and the subsequent binding energies given by our model would be inaccurate.

V.3. CALCULATION OF THE (D°-BSF)X GROUND STATE ENERGY

Now that we have obtained the binding energy of an electron bound to a D°-BSF, we can focus on that of an exciton bound to a D°-BSF. Concerning the structure of these (D°-BSF)X complexes, we can safely infer that the two electrons will be essentially located in the BSF plane, with some repulsive Coulomb interaction between them. The hole, attracted by the two electrons, is repelled by both the BSF plane and the positively charged donor nucleus. The hole should then be located in the wurtzite material surrounding the BSF, at the opposite side from the donor nucleus (Fig. 5.10).
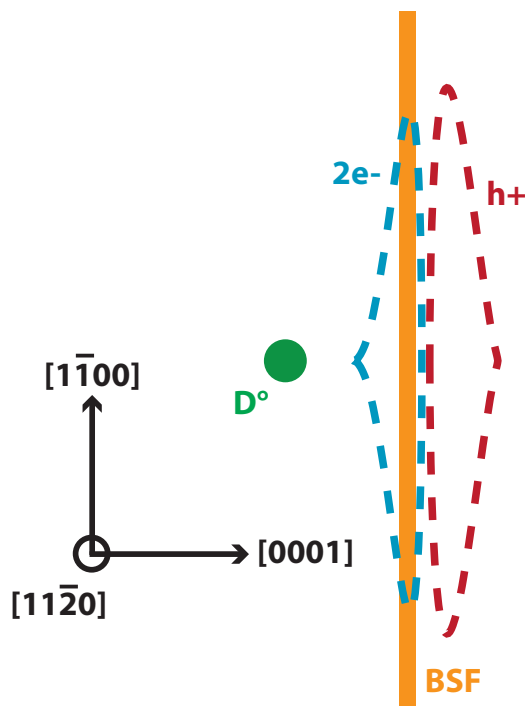

Figure 5.10: Sketch of the D°BSF-X complex. The orange line and the green dot stand for the BSF plane and the donor nucleus, respectively. The cyan and red dashed lines represent the expected electron and hole spatial locations, respectively.

V.3.1. (D°-BSF)X binding energy with respect to the D°-BSF separation

Using the method described in Appendix II, we first calculate the energy of an exciton confined in a BSF when the D° nucleus is located in the BSF plane. The emission energy that we deduce is 3.25 eV and the corresponding intra-BSF exciton localization energy is 183 meV. When the donor nucleus is located 2.5 nm away from the BSF, the localization energy is reduced down to 123 meV (Fig. 5.11). Note that for larger separation between the D° and the BSF plane, the resulting exciton complex gets a large spatial extension (as shown in Figure 5.11, a 25 nm x 25 nm calculation grid is already needed when the D° is placed 2.5 nm away from the BSF plane). Therefore, extremely long computation times are required

The (D°-BSF)X binding energies calculated here are, at first sight, quite surprising. While the calculated emission energies range from 3.25 to 3.31 eV, for D°-BSF separation below 2.5 nm, we would have rather expected them to cover energies from 3.410 to 3.435 eV, in agreement with the optical characterization carried out by PL and CL. More striking is the fact that in the context of the Variational Theorem, the *ansatz* we made for the exciton envelope function should lead to an overestimation of the complex energy. The binding energy should consequently be underestimated and our calculations should yield emission energies higher than what is observed experimentally. Overestimated binding energies could however be an artifact resulting from a too small calculation grid. We indeed force electron and hole wave functions to zero for $z = 0$ and 25 nm and for $\rho = 25$ nm. Although the computed electron and hole wave functions seem to tend smoothly to zero (Fig. 5.11), the spatial extension of electron and hole wave functions could be artificially limited by our border conditions, thus increasing the binding energy of the complex. As a consequence, the reader should be extremely cautious regarding the quantitative results yielded by our calculations and those discussed in the following.
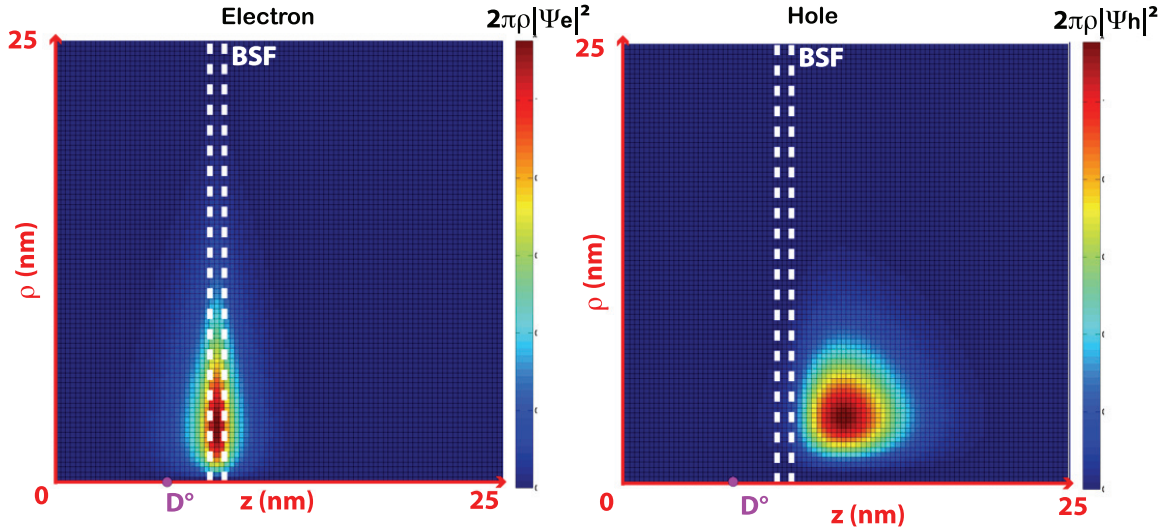
Figure 5.11: Electron and hole wave functions for a (D°-BSF)X complex. The distance between the donor nucleus and the BSF plane is 2.5 nm. The donor nucleus is represented by a magenta dot while the 3 monolayers thick type-II QW formed by the BSF is shown with the white dashed lines.

V.3.2. Sub-bandgap BSF-related emission

In spite of the uncertainty of the computed (D°-BSF)X emission energies, one should note that [Liu2005] have observed, through a combined TEM and CL study, additional BSF-related emission lines at 3.288, 3.322 and 3.340 eV. They have inferred that these three transitions originate from either the stair-rod dislocations located at the crossover between BSFs and PSFs, or from partial dislocations closing the BSFs. However, they could not be more conclusive on their origin because of both the spatial resolution of their CL imaging set-up and the broadening of the emission peaks. They also proposed that the emission between 3.28 and 3.34 eV could result from impurity decoration of the core of the stair-rod and partial dislocations.
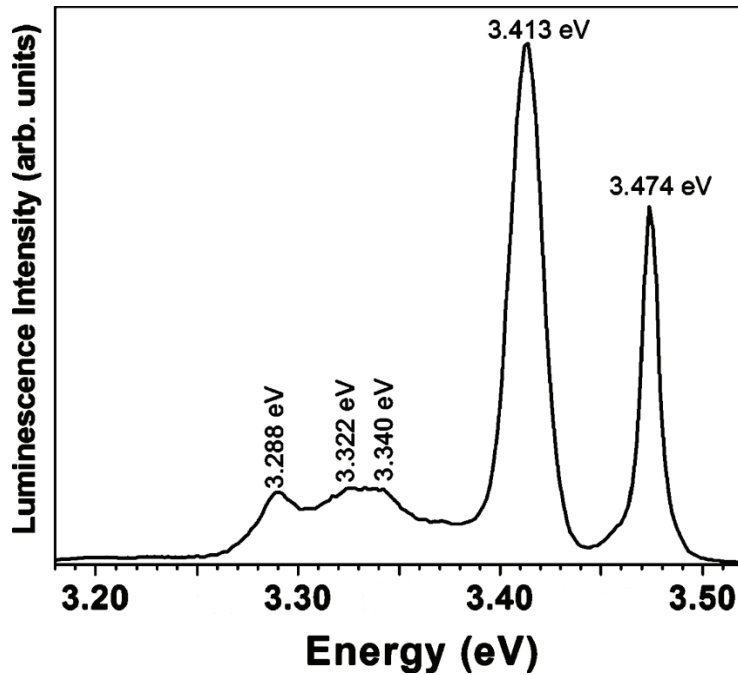
Figure 5.10: CL spectrum of a-plane GaN epilayer taken at 5 K (taken from [Liu2005]). These authors attribute the emission lines between 3.28 and 3.42 eV to BSFs.

Impurity decoration of extended defects such as dislocations and stacking faults is a usual mechanism in semiconductors. Density-functional calculations have shown that, in silicon, the formation of point defects and the incorporation of impurities were favored at the stacking faults compared to the fault-free material [Justo1999]. In the same theoretical framework, [Schmidt2001] have shown that, in GaAs, Si nuclei tend to segregate towards BSFs. Stacking faults also act as segregation centers of O and C impurities in zinc-blende GaN [Martinez-Guerrero2002]. These observations lead the authors to conclude that

(*i*) BSFs should present a high concentration of impurities,

(*ii*) BSFs should prevent the formation of D°X in the surrounding fault-free material.

Concerning wurtzite nitride-based materials, it seems that Si impurities drive the apparition of stacking faults [Molina1999]. Following a TEM and Electron Energy Loss Spectroscopy (EELS) study, [Arslan2005] showed that impurity segregation into the core of a mixed dislocation results in the separation of this dislocation into two partial dislocations and a stacking fault. This mechanism would then relieve the local strain induced by the impurity segregation. Nevertheless, the segregation of Si and O nuclei in stacking faults themselves has, to our knowledge, not been discussed yet.

134

V.3.3. BSF-related impurity segregation: deep and shallow D°-BSF excitons?

However, later PL and CL experiments indicated that the emissions lying between 3.28 and 3.34 eV were impurity *and* BSF-related. In their CL study, [Gühne2007] observed that, if these transitions had to be related to BSFs, they could nonetheless be recorded from regions where prismatic stacking faults and partial dislocations are absent, which is in contradiction with [Liu 2005]. Moreover, power-dependent PL measurements by [Paskov2005] confirmed that these emission lines, if induced by the partial dislocations closing the BSFs, had to be assigned to impurity incorporation in the dislocations rather than to dislocations alone.

As a summary of all the theoretical and experimental works presented above, the emission between 3.25 and 3.34 eV has to be ascribed to type-I BSFs. Although their initial assignment to partial dislocations and prismatic stacking faults is still debated, these transitions are clearly impurity-related. The segregation of impurities could occur in the dislocations closing the BSFs or simply in the BSFs themselves, as observed previously in zinc-blende semiconductors. Stacking faults would then present a high concentration of donors while the surrounding material would be free of dopant.

The emission energy that we calculate for D°-BSF exciton with donors centered on the BSF plane is in agreement with the assignment of the 3.25-3.34 eV emission lines to impurities segregated in BSF. The line at 3.417 eV would then be nothing but the recombination of excitons weakly localized along the BSF plane by donors located far away from the BSFs. Moreover, the absence of any BSF emission between 3.34 and 3.42 eV would simply result from the fact that the material in the close surrounding of the BSFs would be dopant-free. However, one should note that, at 10 K, we observe extremely long lifetimes (more than 6 ns) for the emission bands lying between 3.28 and 3.34 eV compared to the PL at 3.417 eV (770 ps). Since it is difficult to understand such increase in radiative lifetime only in terms of localization [Rashba1962], the mechanisms leading to the emission in the 3.3 eV energy range are therefore certainly more complex than the one considered in our model.

In any case, our initial question about the origin of the 18 meV energy localization for excitons confined in BSFs has not been answered by our calculations. Even if the question is still open, we nonetheless propose that donor nuclei located far away from the BSF plane

could weakly localize excitons, resulting in the average 18 meV localization energy observed experimentally. One however needs a better understanding of the role of BSFs on impurity incorporation in GaN to definitely answer this question. Let us note finally that careful analysis of the temperature dependence of the emission intensities in the 3.3 eV energy range and at 3.42 eV could also evidence the two degrees of intra-BSF exciton localization arising from BSF-driven impurity segregation.

V.4. CONCLUSIONS

To summarize this fifth Chapter, we have studied in detail intra-BSF localization mechanisms. We have first shown by temperature and time-dependent PL and CL that at low temperature, excitons are localized in isolated as well as in bundles of BSFs. Despite the fact that in bundles, there might be some coupling between successive BSFs, the intra-BSF localization energy depth is approximately independent of the local BSF-density, and we find it equal to 18 meV. This intra-BSF localization energy is similar to those reported by other groups. We then rule out that localization could arise from BSF width fluctuation or from strain variation along the BSF plane, and we rather propose that the distribution of donor atoms in the vicinity of the BSF plane efficiently localize BSF excitons.

To confirm our assumption, we have treated by envelope function calculations the problem of a BSF-bound exciton in presence of a donor nucleus. In order to estimate the emission energy of such complex, we have calculated the binding energy of an electron and of an exciton on a D°-BSF. From the computed energy of an electron bound to a charged donor nucleus located in the vicinity of a BSF, we have proposed that the peculiar electrical properties of *a*-plane GaN compared to polar GaN to arise from the interaction between dopant atom and BSFs. Concerning D°-BSF excitons, we have found that their emission energy should lie between 3.25 and 3.31 eV when the donor atom is closer than 2.5 nm from the BSF plane. This result should be regarded with caution, as it could only be an artifact of our finite element method. Moreover, the computed D°-BSF exciton energy is quite surprising compared to the one expected from experiments, since we get a localization energy of 180 meV instead of the expected 18 meV. Still, previous reports by other groups suggest that the emission bands between 3.28 and 3.34 eV are related to both BSFs and impurities. We have therefore proposed the latter lines to arise from (D°-BSF) excitons with donor atoms

in the BSF plane, while the 3.42 eV luminescence would originate from BSF-excitons weakly bound to donor atoms located several nm away from the BSFs.

REFERENCES

[Arslan2005] I. Arslan, A. Bleloch, E. A. Stach, and N. D. Browning, Phys. Rev. Lett. **94**, 025504 (2005).

[Bastard1981] G. Bastard, Phys. Rev. B **24**, 4714 (1981).

[Bastek2008] B. Bastek, F. Bertram, J. Christen, T. Wernicke, M. Weyers, and M. Kneissl, Appl. Phys. Lett. **92**, 212111 (2008).

[Deveaud1987] B. Deveaud, T. C: Damen, J. Shah, and C. W. Tu, Appl. Phys. Lett. **51**, 828 (1987).

[Fischer1998] S. Fischer, G. Steude, D. M. Hoffman, F. Kurth, F. Anders, M. Topf, B. K. Meyer, F. Bertram, M. Schmidt, J. Christen, L. Eckey, J. Holst, A. Hoffman, B. Mensching, and N. Rauschenbach, J. Cryst. Growth **189-190**, 556 (1998).

[Gühne2007] T. Gühne, Z. Bougrioua, P. Venneguès, M. Leroux, and M. Albrecht, J. Appl. Phys. **101**, 113101 (2007).

[Iida2009] D. Iida, M. Iwaya, S. Kamiyama, H. Amano, and I. Akasaki, Phys. Stat. Sol. (b) **246**, 1188 (2009).

[Justo1999] J. F. Justo, A. Antonelli, T. M. Schmidt, and A. Fazzio, Physica B **273-274**, 473 (1999)

[Kash1984] K. Kash, and J. Shah, Appl. Phys. Lett. **45**, 401 (1984).

[Lefebvre2004] P. Lefebvre, S. Kalliakos, T. Bretagnon, P. Valvin, T. Talierco, B. Gil, N. Grandjean, and J. Massies, Phys. Rev. B **69**, 035307 (2004).

[Leroux1998] M. Leroux, N. Grandjean, M. Laügt, J. Massies, B. Gil, P. Lefebvre, and P. Bigenwald, Phys. Rev. B 58, R13371 (1998).

[Leroux1999] M. Leroux, N. Grandjean, B. Beaumont, G. Nataf, F. Semond, J. Massies, and P. Gibart, J. Appl. Phys. **86**, 3721 (1999).

[Liu2005] R. Liu, A. Bell, F. A. Ponce, C. Q. Chen, J. W. Yang, and M. A. Khan, Appl. Phys. Lett. 86, 021908 (2005).

[Martinez-Guerrero2002] E. Martinez-Guerrero, E. Bellet-Amalric, L. Martinet, G. Feuillet, B. Daudin, H. Mariette, P. Holliger, C. Dubois, C. Bru-Chevalier, P. Aboughe Nze, T. Chassagne, G. Ferro, and Y. Monteil, J. Appl. Phys. **91**, 4983 (2002).

[McLaurin2006] M. McLaurin, T. E. Mates, F. Wu, and J. S. Speck, J. Appl. Phys. **100**, 063707 (2006).

[Molina1999] S. I. Molina, A. M. Sanchez, F. J. Pacheco, R. Garcia, M. A. Sanchez-Garcia, F. J. Sanchez, and E. Calleja, Appl. Phys. Lett. **74**, 3362 (1999).

[Paskov2005] P. P. Paskov, R. Schifano, B. Monemar, T. Paskova, S. Figge, and D. Hommel, J. Appl. Phys. **98**, 093519 (2005).

[Rashba1962] E. I. Rashba, and G. E. Gurgenishvili, Sov. Phys. Sol. State **4**, 759 (1962).

[Schmidt2001] T. M. Schmidt, J. F. Justo, and A. Fazzio, Appl. Phys. Lett. **78**, 907 (2001).

[Stampfl1998] C. Stampfl, and C. G. Van de Walle, Phys. Rev. B **57**, R15052 (1998).

[Sun2002] Y. J. Sun, O. Brandt, U. Jahn, T. Y. Liu, A. Trampert, S. Cronenberg, S. Dhar, and K. H. ploog, J. Appl. Phys. **92**, 5714 (2002).

[Tsuchiya2005] Y. Tsuchiya, Y. Okadome, A. Honshio, Y. Miyake, T. Kawashima, M. Iwaya, S. Kamiyama, H. Amano, and I. Akasaki, Jap. J. Appl. Phys. **44**, L1516 (2005).

[Varshni1967] Y. P. Varshni, Physica **34**, 149 (1967).

[Vurgaftman2001] I. Vurgaftman, J. R. Meyer, and L. R. Ram-Mohan J. Appl. Phys. **89**, 5815 (2001).

[Vurgaftman2003] I. Vurgaftman, and J. R. Meyer, J. Appl. Phys. **94**, 3675 (2003).

Chapter VI - Exciton capture by one-dimensional radiative defects in quantum wells

In this Chapter, we focus on the optical properties of *a*-plane (Al,Ga)N/GaN QWs grown on ELO HVPE GaN templates similar to those characterized in the fourth and fifth Chapters of this thesis. We first evidence by continuous-wave PL experiments the absence of electric fields in our heterostructures. We then demonstrate that similarly to the case of thick GaN epilayers, BSFs drastically affect the recombination dynamics of excitons in non-polar (Al,Ga)N/GaN QWs. We study in detail, by temperature-resolved PL experiments, the localization of excitons along the QW plane and in the BSFs. Finally, we check out a previous proposal by [Badcock2008] who stated that the intersection between the QW and the BSF planes should lead to the formation of quantum wires.

We emphasize that the present study on *a*-plane (Al,Ga)N/GaN QWs on ELO-GaN has been carried out in close collaboration with Dr. Amélie Dussaigne (LASPE-EPFL), who has not only been a dedicated sample grower, but has also performed a thorough micro-PL characterization.

VI.1. GROWTH OF *a*-PLANE (Al,Ga)N/GaN QUANTUM WELLS

ELO-GaN layers similar to the one studied in the two previous chapters have been used as substrates for the growth by molecular beam epitaxy of (Al,Ga)N/GaN QWs. A 500 nm thick GaN epilayer was first deposited, followed by 200 nm of $Al_xGa_{1-x}N$. Various *a*-plane QWs were prepared in order to study the combined influence of QW width (from 2 to 8 nm) and barrier Al-content (from 5 to 15 %) on the optical properties of the QWs. Finally, samples were capped with a 20 nm thick $Al_xGa_{1-x}N$ top barriers, of identical *x* than the bottom one.
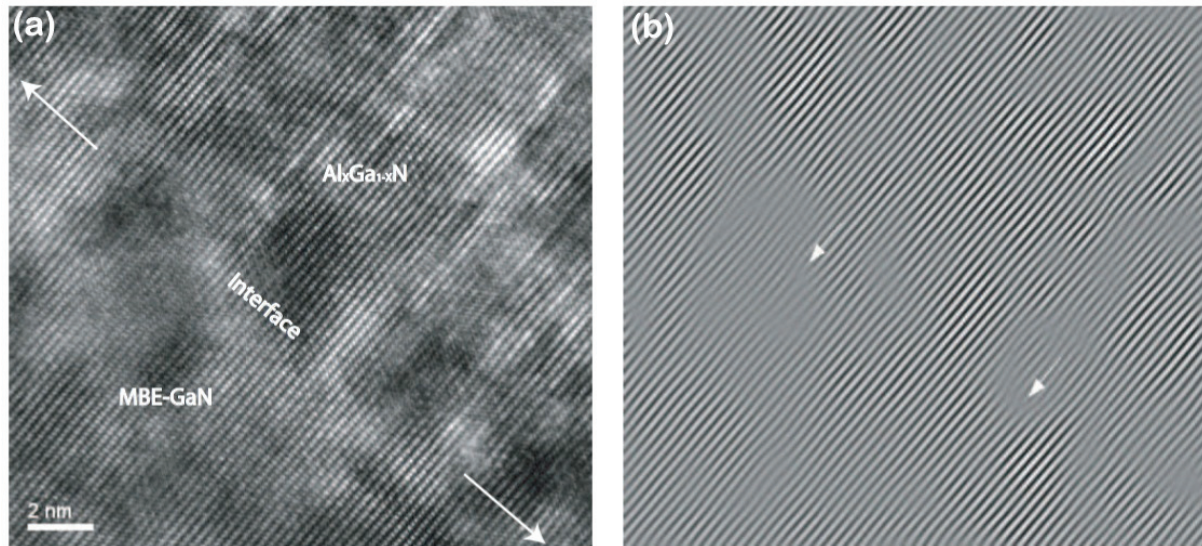
Figure 6.1: (a) High-resolution TEM attesting that the interface between GaN and $Al_{0.15}Ga_{0.85}N$ is sharp. (b) Filtered high-resolution TEM micrograph using the (0002) reflections. Misfit dislocations are shown by white arrows (raw and filtered TEM micrographs courtesy of Dr. Yadira Arroyo [Arroyo2009]).

We show in Figure 6.1 a TEM micrograph of the interface between the 500 nm thick GaN MBE epilayer and the first (Al,Ga)N barrier. The interface is sharp, and one can observe misfit dislocations induced by the lattice mismatch between GaN and (Al,Ga)N. Concerning BSFs, they propagate from the template to the surface of the sample, going through the QW and the (Al,Ga)N barriers (Fig. 6.2). Note also that BSFs can be generated at the different GaN/(Al,Ga)N interfaces [Speck2010]. Although the effect of the lattice mismatch between GaN and (Al,Ga)N on the generation of BSF has, to our knowledge, not been studied in detail, the BSF density in the present QW structures should, without any doubt, be higher than what reported for *a*-plane ELO-GaN layers.
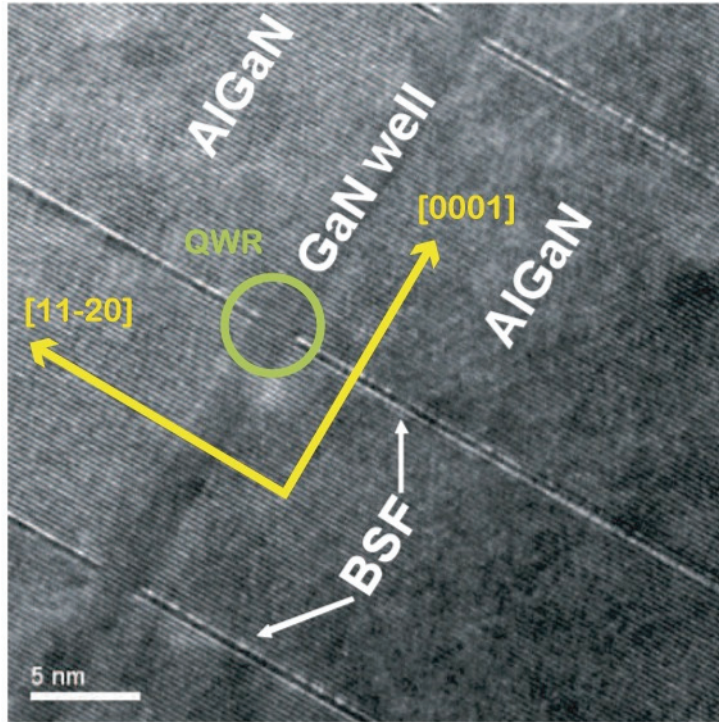
Figure 6.2: Cross-section TEM micrograph of a 2 nm thick $Al_{0.1}Ga_{0.9}N$/GaN QW showing the propagation of BSFs from the GaN template to the surface, going through the (Al,Ga)N barriers and the QW (courtesy of Yadira Arroyo). [Badcock2008] has proposed the intersection between the GaN QW and BSFs to form quantum wires (QWRs).

VI.2. EXPERIMENTAL EVIDENCES FOR THE ABSENCE OF BUILT-IN ELECTRIC FIELDS

VI.2.1. Quantum well emission energy with respect to Al-content and well-width

Figure 6.3 shows the low-temperature PL spectra of *a*-plane QWs with barrier Al-content of 15 %. All spectra exhibit a dominant emission peak that we assign to the recombination of the ground-state QW exciton. Contrary to what observed in polar (Al,Ga)N/GaN QWs [Leroux1999], the well-width dependence of QW emission energy follows the one expected for polarization free QWs [Greene1984]. At such low temperatures, the observed excitons are most certainly localized along the QW plane by well width fluctuations of one or two monolayers [Leroux1998,Natali2009], as well as by local variations of the Al-composition in the barriers [Gallart2000]. We observe at higher energy (3.72 - 3.8 eV) the recombination of excitons localized at potential fluctuations in the $Al_{0.15}Ga_{0.85}N$ barriers. One can also observe weaker bands centered at 3.42 and 3.70 eV, which we relate to excitons bound to I_1-BSFs in the GaN template and in the $Al_{0.15}Ga_{0.85}N$ barriers, respectively.
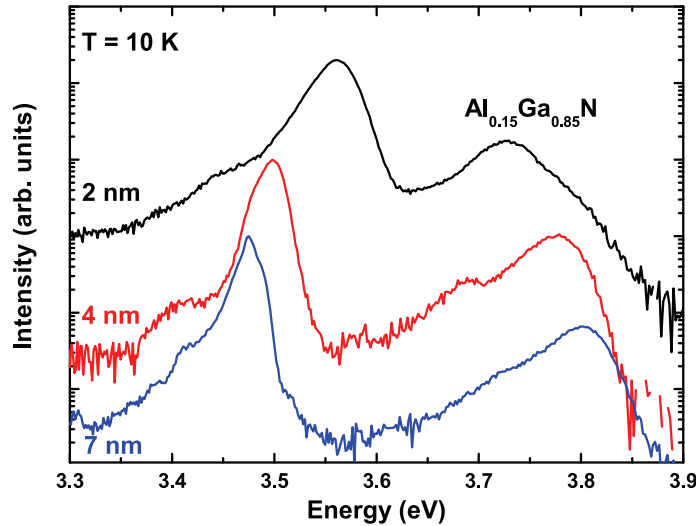
Figure 6.3: Low-temperature PL spectra on 2, 4 and 7 nm thick $Al_{0.15}Ga_{0.85}N$/GaN QWs (black, red and blue lines, resp.). The spectra have been shifted vertically for clarity. We observe the emission from the GaN QW and the (Al,Ga)N barriers. Weaker transitions from BSFs in the GaN template and in the barriers are also resolved.

Figure 6.4(a) displays low temperature PL spectra of $Al_{0.1}Ga_{0.9}N$/GaN *a*-plane QWs. QWs with lower barrier Al-content generally present PL spectra with sharper structures, thanks to reduced barrier alloy disorder in the barriers [Feltin2007]. In agreement, two transitions are now clearly resolved for all samples with Al contents set to 5 and 10 % (for the sake of clarity, we only plot the PL spectra of $Al_{0.1}Ga_{0.9}N$/GaN *a*-plane QWs). According to envelope function simulations, the high-energy transition originates from the emission of QW fundamental exciton localized along the QW plane. We note, however, that for 2 nm thick QWs, the experimental emission energies are lower than what is expected from calculations. We believe that such a discrepancy results from an enhanced localization effect at regions of lower Al concentration, thus of lower energy. Indeed, due to the higher penetration of their wave function into the barriers, excitons confined in 2 nm thick QWs are more sensitive to barrier alloy fluctuations than in wider wells. We suggest that these somewhat large Al-composition fluctuations are related to the expected Al adatom incorporation anisotropy when growing on non-polar planes [Lymperakis2009].
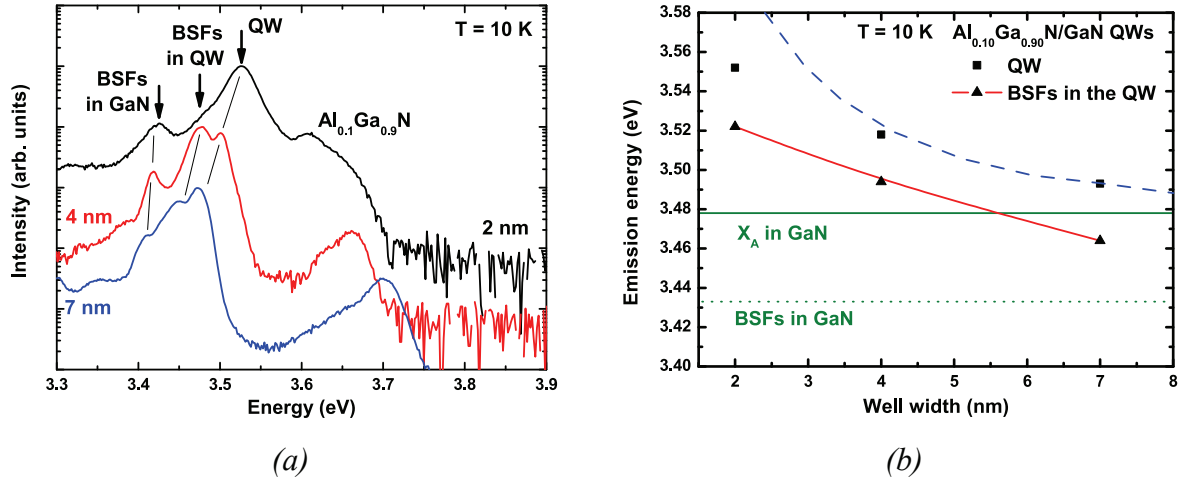
Figure 6.4: (a) Low-temperature PL spectra of 2, 4 and 7 nm thick Al$_{0.10}$Ga$_{0.90}$N/GaN QWs (black, red and blue lines, resp.). The spectra have been shifted vertically for clarity. The narrow emission lines of Al$_{0.10}$Ga$_{0.90}$N/GaN QWs make it possible to separate the emission of exciton confined in the QW from that of BSF-bound QW excitons. (b) QW (squares) and BSF-bound (triangles) QW exciton emission energy with respect to the QW width. Solid lines are guides to the eyes. Blue dashed lines are the result of our envelope function calculations (reproduced from Fig. 1.8).

VI.2.2. Quantum well emission broadening with respect to Al-content and well-width

The evolution of the full-width at half maximum (FWHM) of the QW emission at 10 K with respect to the QW width is depicted in Figure 6.5 for low and high Al-content QWs. Our QWs all exhibit a decreasing emission linewidth when the well width is increased from 2 to 7 nm. Such behavior is typical of polarization free QWs such as (Al,Ga)As/GaAs QWs [Bimberg1987] because in thick QWs:

(*i*) well width variations have a small effect on quantized energies,

(*ii*) the wave function penetration into the disordered alloy barriers is reduced.

145
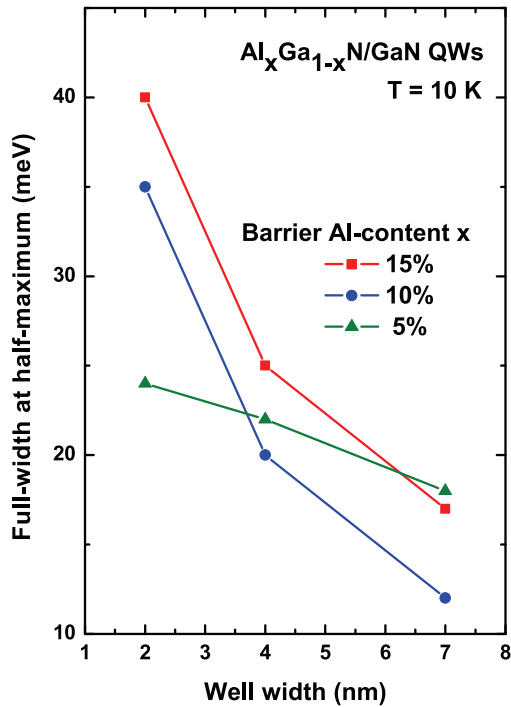
Figure 6.5: QW emission full-width at half-maximum with respect to the QW width. When the well-width is increased, the emission lines narrow thanks to reduction of the influence of interface roughness on the quantized energies.

On the contrary, in (Al,Ga)N/GaN QWs grown along the polar *c*-axis, 2.5 nm thick wells correspond to the best compromise -in terms of emission linewidth- between thin QWs characterized with strong quantum confinement effects and wider ones presenting a large quantum confined Stark effect. This phenomenon was ascribed to the combined effects of well-width and barrier Al-content fluctuations, on the one hand, and of internal electric field, on the other hand [Natali2005]. The latter indeed strengthens, for large well widths, the effect of interface roughness by enhancing the presence probability of carriers at the interfaces and by red shifting the emission energy at these potential fluctuations. The steady narrowing of the emission linewidth with respect to the well width observed for the present *a*-plane QWs is therefore another evidence for the absence of built-in electric field in these structures.

One should nevertheless note that, thanks to reduced alloy fluctuations in the barriers, QWs with barrier Al-content set to 5 % show only a 6 meV reduction in emission linewidth when the well-width is increased from 2 to 7 nm. As a matter of fact, local strain fluctuations [Bastek2008] as well as high local densities of extended defects play for the latter heterostuctures the most important part in the inhomogeneous broadening of the emission.

VI.3. QUANTUM WELL EXCITONS BOUND TO BASAL PLANE STACKING FAULTS

VI.3.2. Spatial distribution of BSFs in (Al,Ga)N/GaN quantum wells

We now turn our attention to the additional emission peak observed for QW samples with Al-content set to 5 or 10 % (Fig. 6.4). Similarly to the QW emission, this peak redshifts when the well width increases and the Al-content decreases. Due to its large energy separation with the QW emission, and because in thick QWs this emission lies below the excitonic bandgap of bulk GaN, we rule out that this transition could arise from exciton localization on well width fluctuations. Moreover, this emission band is absent from PL spectra measured on homoepitaxial *a*-plane (Al,Ga)N/GaN QWs grown under the same conditions (*see* Chapter VIII and [Teisseyre2005]). Instead, as already observed and commented by [Badcock2008], this transition is more likely to arise from I_1-BSFs that intersect the QW plane.

In order to support this assumption, we performed CL mappings of the near band-edge luminescence (Fig. 6.6). Although similar observations can be made for the whole set of samples, we decide, for clarity reasons, to only discuss here the results obtained on a 4 nm thick $Al_{0.1}Ga_{0.9}N$/GaN QW. At 10 K, the near band-edge emission from this sample is dominated by two lines centered at 3.501 and 3.476 eV (Fig. 6.4). In agreement with the discussion in Section VI.2.1., we ascribe the transition at 3.501 eV to the emission from QW excitons localized on well-width fluctuations and/or barrier alloy disorder. When imaging the 3.476 eV CL, we observe long bright stripes perpendicular to the *c*-axis, anti-correlated with the QW emission at 3.501 eV but in coincidence with the emission of BSF-bound excitons in bulk GaN at 3.417 eV.

Such a spatial correlations between the 3.501, the 3.417 and the 3.476 eV lines allows us to relate the latter transition to the recombination of QW excitons bound to BSFs. We therefore attribute the clearer stripes in Figure 6.6(b) to the intersection of the QW with BSFs gathered into high-density bundles. Inversely, regions emitting mainly at the QW emission energy are associated with material where the BSF density is much smaller. It should be noted, however, that the anti-correlation between CL mappings taken at the emission energies

of the QW and of BSFs is not as clear as for GaN epilayers. First, when performing CL experiments, we also excite the non-polar GaN template, which gives rise to an intense emission band at 3.471 eV (*see* Chapter IV). Thus, the QW-BSF emission superimposes spectrally with the emission from D°X in the GaN template, reducing the contrast of the mappings displayed in Figure 6.6(b). In addition, the QW and (Al,Ga)N emissions in the +*c*-wings are respectively blueshifted and redshifted, compared to the emission from the -*c*-wings and the windows. This strain fluctuation arises from weak strain relaxation in the +*c*-wings due to the local low density of extended defects. In these regions, while the GaN QW undergoes a slight compressive strain, the (Al,Ga)N barriers suffer from small in-plane dilatation. These variations in strain state make it even more difficult to clearly distinguish between regions with bundles of BSFs and regions with low BSF-density.
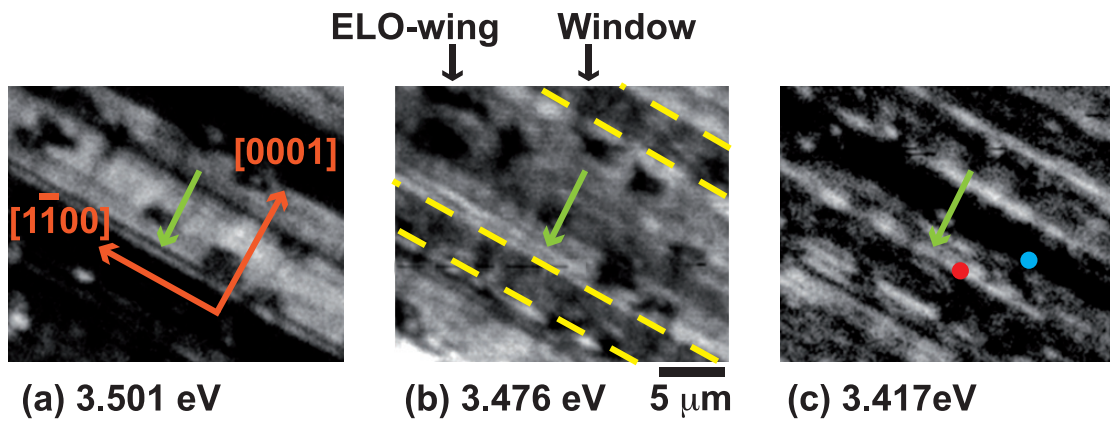
Figure 6.6: CL mappings taken at the emission energy of QW excitons (a), BSF-bound QW excitons (b) and BSF in the GaN template (c). Green arrows point at bundles of BSFs. Blue and red dots on (c) show the excitation spots where CL transients shown in Figure 6.10(a) and (b) have been acquired. Dark spots correspond to micrometer-sized V-pits terminated by threading dislocations (see Fig. 6.7).

We note, finally, that micrometer-sized dark spots can be observed on the CL mappings taken at the emission energies of the QW and of the BSF-bound QW excitons (Fig. 6.6). Interestingly, these dark spots appear bright on CL mappings taken at the (Al,Ga)N or at the GaN emission energy (Fig. 6.7). As confirmed by TEM, when growing GaN by MBE on the HVPE template, V-shaped pits are formed at the end of threading dislocations. These pits allow for a better light extraction for the (Al,Ga)N CL and for a direct excitation of the MBE-GaN buffer layer. These pits consequently appear bright on CL mappings taken at the (Al,Ga)N and at the GaN emission energies
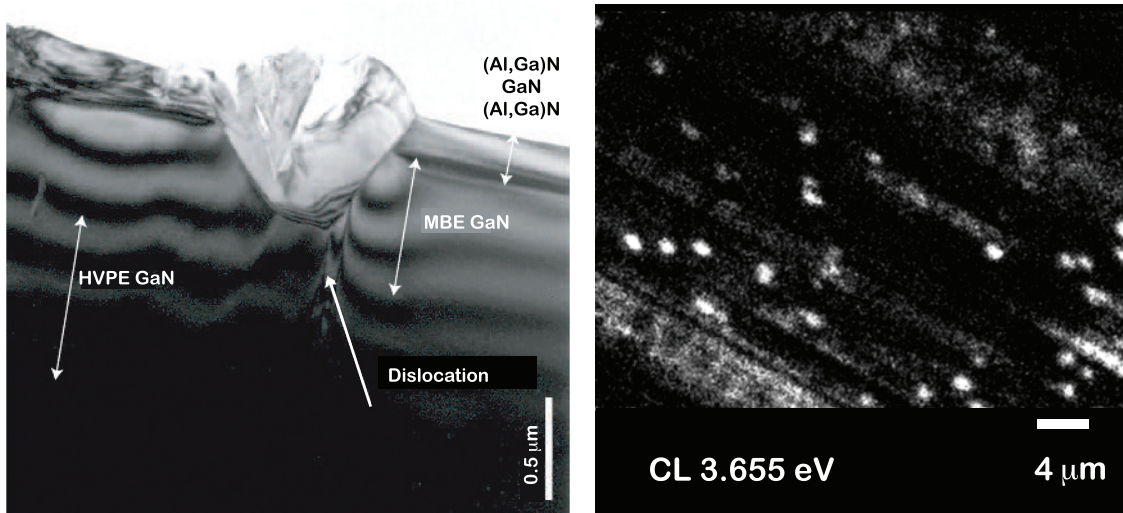
Figure 6.7: (a) Bright field TEM cross-section micrograph of a V-shaped pit in a-plane (Al,Ga)N/GaN QW (courtesy of Dr. Y. Arroyo [Arroyo2009]). (b) Low-temperature CL mapping taken at the emission energy of (Al,Ga)N. The pits allow for better excitation and extraction of the (Al,Ga)N luminescence.

VI.3.2. Band alignment for I_1-BSFs in (Al,Ga)N/GaN quantum wells

For all samples, the energy separation between the emissions from QW and BSF excitons (Fig. 6.4 and [Badcock2008]) is reduced compared to the 45 meV reported for bulk GaN: in a 7 nm (2 nm) wide QW, one observes an energy difference of 30 meV (10 meV) between these two transitions. Therefore, BSF-excitons are *a priori* more sensitive to the confinement caused by the (Al,Ga)N/GaN QW than excitons present in non-faulted regions of the QW. Due to the particular band alignment of I_1-BSFs in wurtzite GaN, electrons are weakly confined in the BSF plane while holes are repelled into the hexagonal phase. Consequently, the wave function of the resulting type-II exciton exhibits a large spatial extension. Our calculations yield an in-plane pseudo-Bohr radius of 3.9 nm for the BSF-exciton (*see* Fig. 4.5), *i.e.* an extension ~1.3 times larger than the exciton Bohr radius in bulk wurtzite GaN. The enhancement of the exciton binding energy in a QW essentially depends on the ratio between the well thickness and the Bohr radius of the non-confined exciton [Bastard1982]. As a consequence, for a given well-width, we expect the increase in binding energy for BSF-exciton to be larger than for an exciton in defect-free material, explaining in a first approximation the dependencies shown in Figure 6.4.

As a matter of fact, the case of a QW intersected by a BSF is complicated, as excitons experience confinement into two orthogonal directions. They are indeed confined along the growth axis by the type-I (Al,Ga)N/GaN QW and along [0001] by the type-II QW formed by the BSF. As a result, [Badcock2008] proposed that the intersection between a BSF and an *a*-plane QW results in a quantum wire (QWR) aligned along the *m*-axis, though clear optical evidence of the one-dimensional character of BSF-bound QW excitons is missing. The exact calculation of the binding energy and wave function of such spatially indirect QWR excitons is arduous. Nevertheless, we can safely presume that the electron wave function is weakly confined along the wire axis whereas the hole wave function is repelled into the wurtzite regions of the QW, as sketched in Figure 6.8. The large extension of the BSF-bound QW exciton wave function would consequently make them sensitive to localization centers located in and away from the BSFs, resulting in the inhomogeneous broadening of the emission, as displayed in Figure 6.4. Experimental indications for intra-BSF localization will be given in Section VI.5.
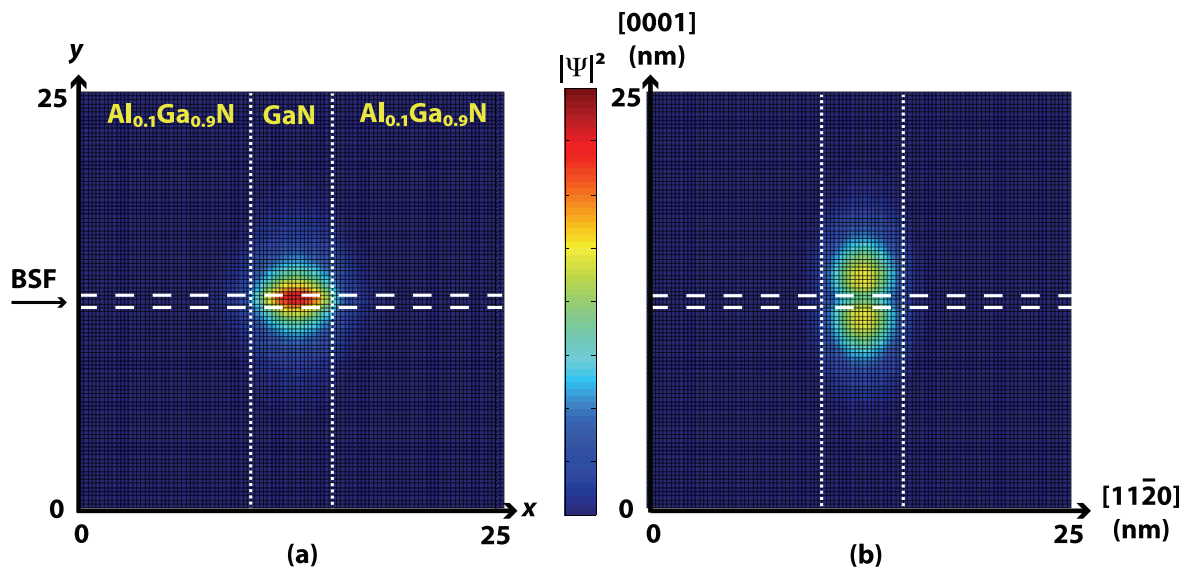

Figure 6.8: Presumed electron (a) and hole (b) densities of probability for an exciton confined in a 4 nm thick $Al_{0.1}Ga_{0.9}N$/GaN QW intersected by an I_1-BSF. Dotted and dashed lines represent the interfaces of the QW and the BSF, respectively.

VI.4. SPATIALLY-DEPENDENT DYNAMICS OF QUANTUM WELL EXCITONS

VI.4.1 Time-resolved photoluminescence of the quantum well emission

So far, we have observed that the intersection of a non-polar QW with BSFs gives rise to an intense emission lying at an energy lower than that of the QW. Similarly to what is observed in bulk ELO-GaN, the spatial distribution of BSFs in the QW plane is highly inhomogeneous: we have indeed been able to identify regions with bundles of BSFs as well as regions with low-density BSFs. It is still not clear, however, how the confinement and the disorder affect the dynamical trapping of excitons by BSFs. Consequently, we have performed a combined time-resolved PL and CL study on our a-plane QW samples. For clarity reasons, we only present and discuss results obtained on a 4 nm thick $Al_{0.1}Ga_{0.9}N/GaN$ QW sample (complementary results with other well widths are coherent with the picture developed here).

The time-evolution of QW and BSF-related PL at 10 K is shown in Figure 6.9. While the PL of BSF-bound QW excitons exhibits a monexponential decay, with characteristic lifetime of 430 ± 10 ps, the QW emission shows a non-exponential behavior with fast and slow components of 50 ± 5 and 350 ± 10 ps, respectively. The PL of polar nitride-based QWs is expected to exhibit a non-exponential decay in specific cases: in ternary QWs such as (In,Ga)N/GaN due to strong localization effects induced by alloy disorder in the well [Lefebvre2001], or even in binary QWs because of dynamic de-screening of built-in electric fields [Reale2003,Lefebvre2004]. Non-exponential decays are also generally observed when analyzing temporally the PL of non-polar (Al,Ga)N/GaN QW [Waltereit2000,Akopian2005]. Although not yet discussed, this behavior is quite surprising as one would presume these polarization free (Al,Ga)N/GaN QWs to exhibit a luminescence with a mono-exponential decay. However, one has to keep in mind that in usual PL experiments, the focus spot of the excitation laser beam has a diameter of several tens of micrometers. In our sample, where the periodicity of the ELO-mask is 15 μm, the laser beam excites simultaneously the windows and both the $+c$ and $-c$ ELO-wings, *i.e.* morphologically different regions of the sample where the linear density of BSFs along [0001] ranges between 10^4 and 10^6 cm^{-1} [Gühne2007].

Therefore the observed PL certainly averages the signatures of excitons recombining in regions presenting a variety of BSF densities.
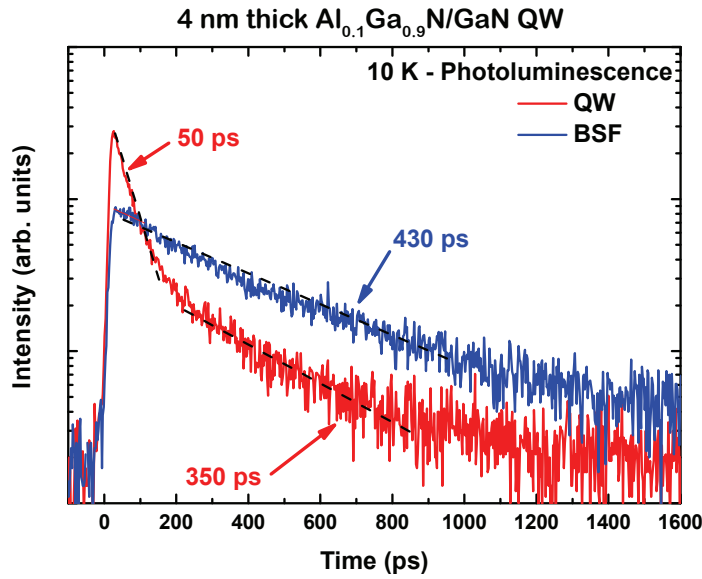
Figure 6.9: Time-resolved PL decays for QW excitons (red) and BSF-bound QW excitons (blue) at 10 K. The QW emission exhibits a non-exponential behavior with fast and slow components of 50 and 350 ps, respectively.

VI.4.1 Spatially dependent dynamics of quantum well excitons

To get a better insight into the role played by BSFs on QW exciton dynamics, we performed TR-CL experiments. The first remarkable result is that, at 30 K, the BSF-related QW CL shows a single-exponential decay with a characteristic decay time of 400 ± 20 ps, independently of the local BSF density (Fig. 6.10). The time constant agrees with TR-PL measurements at the same temperature. On the other hand, the QW emission decay is now systematically found exponential, but the characteristic decay time depends drastically on where the excitation is delivered. When exciting directly on dense bundles of BSFs, the CL from QW excitons is weak, with a decay time that falls below the time resolution of our TR-CL set-up [note1], indicating an efficient capture of these excitons by the BSFs (Fig. 6.10(b)). When moving the excitation spot away from the bundles, *i.e.* to regions with lower densities in BSFs, the QW emission is enhanced and its decay-time is about 360 ps (Fig. 6.10(a)). TR-CL results confirm experimentally that the lifetime of QW excitons in non-polar (Al,Ga)N/GaN QWs reflects the local density in BSFs. Where BSFs are gathered into bundles, the QW PL lifetime is limited by the capture of excitons onto BSFs. Elsewhere, when exctions are mostly localized at well-width fluctuations: the transfer towards BSFs is not efficient and the oberved 360 ps decay time of the QW PL is certainly close to the radiative lifetime of localized excitons. Accordingly, comparable decay time of 300-400 ps

has been reported for localized excitons in 2.5 nm thick *c*-plane $Al_{0.07}Ga_{0.93}N$/GaN QWs [Lefebvre1998].
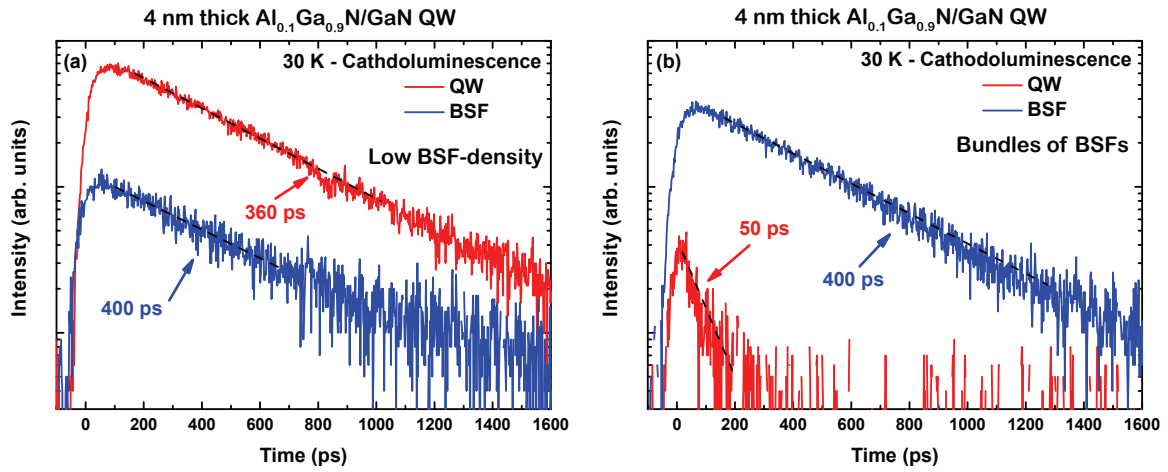
Figure 6.10: TR-CL of the QW (red) and the BSF-related (blue) emissions at 30 K. (a) When excitation is delivered away from bundles of BSFs, the QW emission decays monoexponentially with a decay time of 360 ps. (b) When excitation is delivered on the bundles, the QW emission decay time is below 50 ps. In both cases, the BSF-related QW emission decays monoexponentially with a decay time of 400 ps.

From these results, we clearly see that some precautions should be taken, when analyzing the time-resolved PL of non-polar (Al,Ga)N/GaN QWs:

(i) one should consider the slower component of the QW PL decay to account for the radiative recombination rate of excitons in the QW. At low temperature, these excitons are essentially localized at well-width fluctuations, and therefore one can be confident that the measured PL decay time is the radiative lifetime. The PL decay times presented by [Akopian2005] consequently underestimate QW exciton radiative lifetime.

(ii) the faster component of the decay only represents the PL emission from excitons located in regions with high density bundles of BSFs. There, QW excitons experience a fast capture by the BSFs.

(iii) the intensity ratio between the fast and slow decaying components of the QW PL gives a qualitative indication of the statistical distribution between low and high BSF-density regions, within the area probed by the laser beam.

Now, regions with low BSF-densities do not exhibit the slow but efficient exciton capture rate (three hundred picosecond long) observed previously in bulk *a*-plane GaN (Chapter IV). Compared to the case of bulk GaN, the diffusion of excitons in the plane of the QW is indeed hindered by the presence of localization centers, such as well-width fluctuations [Leroux1998] or alloy fluctuation in the barriers [Gallart2000]. Whatever their origin, these potential fluctuations result in a reduced in-plane diffusion length of excitons: BSFs are therefore mostly populated either directly by the excitation pulse, or by the trapping of excitons through scattering processes occurring prior to their binding on usual QW potential fluctuation.

Finally, we note that the decay of the BSF-related QW emission at 30 K is constantly equal to 400 ps, whatever the local density in BSFs. Such a behavior attests that the interaction between successive BSFs in bundles in reduced compared to what has been observed in thick *a*-plane GaN epilayers,. We tentatively attribute this observation to deeper intra-BSF exciton localization for BSF in QWs compared to the case of bulk GaN, as will be discussed in the following section.

VI.5. LOCALIZATION MECHANISMS FOR QUANTUM WELL EXCITONS BOUND TO STACKING FAULTS

VI.5.1. Temperature-dependencies of the quantum well and quantum wire emission energies

In the previous section, our low-temperature time-resolved CL experiments lead us to the conclusion that the localization of excitons in BSF was deeper in QW than in bulk samples. We therefore perform temperature-dependent PL measurements in order to quantify the localization energy of QW excitons on well-width fluctuations and on BSFs. Again, we only discuss here the results obtained on a 4 nm thick $Al_{0.05}Ga_{0.95}N/GaN$, where the intra-BSF exciton localization/delocalization mechanisms have been observed the most clearly.

The evolution with T of the QW emission energy (Fig. 6.11) exhibits the usual half S-shaped behavior reported for polar (Al,Ga)N/GaN QWs [Leroux1998]. At low T, QW

excitons are localized on shallow potential fluctuations induced by well-width fluctuations and/or alloy disorder. When T is increased, carrier delocalization into the whole QW leads to a slightly blue-shifted PL emission. At higher T, the excitonic emission energy follows the T-dependence of the bandgap, resulting in a red-shifted PL. Assuming that excitons are totally delocalized in the two-dimensional QW at 300 K, we performed a fit to the experimental results by using Varshni's semi-empirical formula. We used the fitting parameters given in [Vurgaftman2003], which, by extrapolation to T = 0 K, allows us to estimate QW exciton localization energy.

The emission energy of BSF-bound QW excitons also displays an S-shaped T-dependence (Fig. 6.11). As discussed thoroughly in the previous Chapter, we have attributed intra-BSF localization in *a*-plane GaN to the presence of donor nuclei in the vicinity of the BSF planes. After a Varshni fit of the high temperature-dependence of the BSF emission energy, we deduce an intra-BSF localization energy of 33 meV for the 4 nm thick *a*-plane $Al_{0.05}Ga_{0.95}N$/GaN QW. Intra-BSF localization is consequently stronger in (Al,Ga)N/GaN QWs than in bulk GaN, where localization energies comprised between 15 and 18 meV have been reported [Paskov2007]. Similar behavior has recently been reported for BSFs in non-polar (Al,Ga)N alloys by [Huang2011], who observed an increase of intra-BSF localization energy with barrier Al-content. We tentatively attribute the increased intra-BSF binding energy observed in QWs compared to bulk GaN to the combined localization of BSF-excitons induced by the QW-width variations and barrier alloy disorder, thus reproducing in a one dimensional system the localization scheme usually observed in (Al,Ga)N/GaN QWs. We do not exclude either that donors, with increased binding energies when located in QWs [Bastard1981], may also efficiently localize BSF-bound QW excitons.
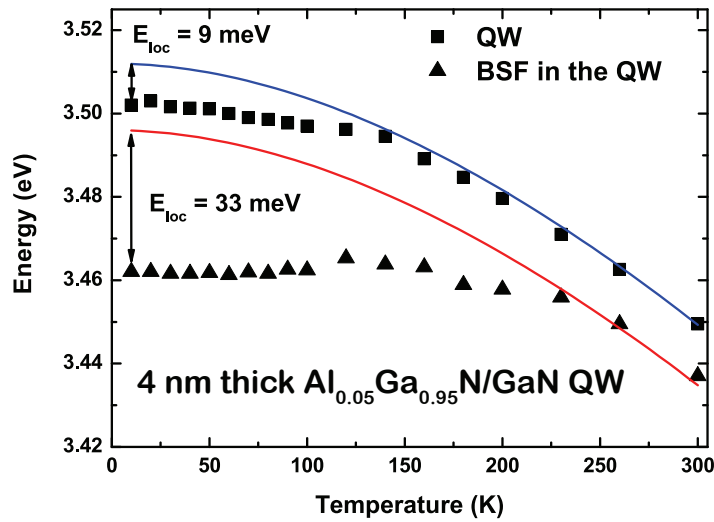
Figure 6.11: Temperature-dependence of the emission energies for a 4 nm thick $Al_{0.05}Ga_{0.95}N/GaN$ QW. Emission from QW excitons and from BSFs are shown by squares and triangles, respectively. Varshni fits of emission energies in the high-temperature range are shown by solid lines.

VI.5.2. Temperature-dependency of quantum wire emission lifetime

The evolution with T of BSF-bound QW exciton decay time gives additional evidence for intra-BSF localization (Fig. 6.12). For a 4 nm thick $Al_{0.1}Ga_{0.9}N/GaN$, this decay keeps almost constant between 10 and 60 K. The evolution with T of BSF-bound QW excitons decay rate therefore resembles that of a localized state: this rate remains constant for T < 60 K, which is characteristic of zero-dimensional excitons. We assume the decay of BSF-bound QW excitons at temperatures below 60 K to be essentially radiative and we attribute the longer decay time of BSF-QW excitons compared to that of localized QW excitons (400 and 360 ps, respectively)

(*i*) principally to the reduced overlap between electron and hole wave functions for BSF-bound excions due to the type-II band alignment of I_1 stacking faults.

(*ii*) as a secondary effect to the larger degree of localization of BSF-bound QW excitons and consequently to the larger expansion of their wave function in reciprocal space [Rashba1962],
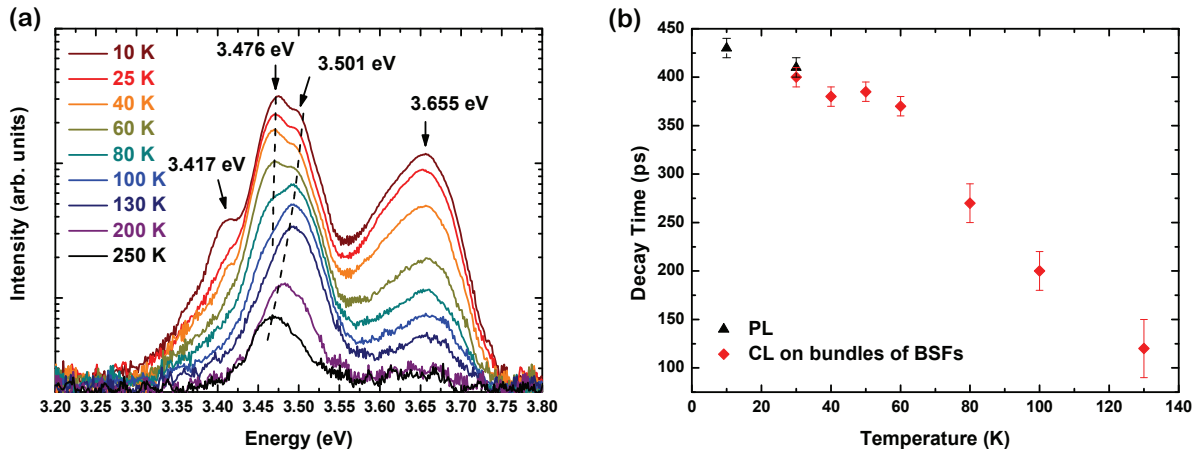
Figure 6.12: (a) Time-integrated PL spectra of the 4 nm thick a-plane $Al_{0.1}Ga_{0.9}N/GaN$ QW. For T > 60 K, the intensity of the 3.476 eV emission quenches to the benefit of the line at 3.501 eV. (b) PL (triangles) and CL (diamonds) decay time of the BSF-QW luminescence with T. Above 60 K, BSF luminescence lifetime decreases dramatically.

For temperatures above 60 K, these zero-dimensional excitons get delocalized into the whole BSF and then can start reaching non-radiative centers. This results in an increased effective decay rate of these excitons. For example, partial dislocations bounding the BSFs could be one cause of the quenching [Wu2008]. The situation is actually made complex by the fact that the increase of T allows simultaneously the thermally activated escape of excitons from the BSF toward the QW. This induces the overall quenching of the BSF luminescence to the benefit of QW emission (Fig. 6.12(a)), so that it is difficult to ascertain the role of non-radiative defects.

VI.6. EVIDENCE FOR THE ONE-DIMENSIONNAL CHARACTER OF STACKING FAULT-BOUND QUANTUM WELL EXCITONS

So far, we got a global understanding of the dynamics of BSF-bound QW excitons with respect to T. While at low-T, BSF-QW excitons are localized, an increase in T leads to the escape of these excitons towards the QW plane. The study of the intrinsic dynamics of BSF-bound QW excitons as a function of T is therefore hindered: one cannot conclude, for instance, on the 1D character of BSF-bound QW excitons through temperature- and time-resolved PL experiments [Citrin1992].

One expects, however, peculiar polarization properties for the emission from narrow GaN quantum wires (QWRs) with axis parallel to the *c*-axis [Maslov2005]. It has for instance been predicted that cylindrical GaN QWRs aligned along [0001] and with radius smaller than 3.5 nm should exhibit an emission linearly polarized along the *c*-axis, due to strong mixing of the different valence subbands. For the *a*-plane heterostructures presented in this study, the QWRs resulting from the intersection of the QW and the BSF planes should be aligned along the *m*-axis. It is of course difficult to know how to extend the calculations by [Maslov2005] for excitons confined in our thin and shallow type-II nitride-based QWRs aligned along [1-100]. However, in case of strong confinement into two orthogonal directions, we expect noticeable change in selection rules for ground state BSF-QW excitons compared to excitons confined in unfaulted material.

When performing polarization-resolved PL experiments, one has also to take into account the peculiar selection rules of excitons in GaN that result from the crystal symmetry (*see* Section I.2). In the orthogonal basis (*X,Y,Z*), with *Z* parallel to the *c*-axis of the wurtzite, exciton A is built on *X* and *Y* states [Dingle1971]. It therefore does not interact with photon with electric field parallel to the [0001] direction. Interestingly, these selection rules are verified even in presence of biaxial strain in the *c*-plane [Gil1997a], as such a stress does not modify the symmetry of the lattice. Although GaN grown along a non-polar axis on a foreign substrate exhibits a lower symmetry (orthorhombic C_{2v} against hexagonal C_{6v}), exciton selection rules are still not dramatically altered [Gil1997b]. In particular, for layers under slight compression or dilatation, the oscillator strength of A-like excitons along [0001] is small compared to that in the polar plane. This has been confirmed by [Gühne2008], who performed polarization-resolved PL and reflectivity experiments on ELO *a*-plane GaN epilayers. Concerning (Al,Ga)N/GaN QWs, selection rules similar to that of bulk GaN should hold for samples with QW thickness larger than 1.5 nm and barrier Al-content lower than 15 % [Leroux2004].

Figure 6.13 shows that, for a 4 nm thick $Al_{0.1}Ga_{0.9}N$/GaN QW sample, both QW and BSF emissions are principally polarized perpendicularly to the *c*-axis. Assuming that the anisotropy of the QW emission originates solely from the crystal symmetry, BSF-bound QW excitons should exhibit a similar or lower polarization anisotropy, compared to the emission from the bare QW. It is indeed usually admitted that the deeper the localization, the larger the loosening of selection rules. Still, we observe experimentally the opposite behavior. While the

polarization degree, defined as $\Gamma = \dfrac{I_{\perp c} - I_{//c}}{I_{\perp c} + I_{//c}}$, is equal to 0.76 for BSF-bound QW excitons, it is only 0.51 for the QW emission. The emission from BSF-bound QW excitons thus exhibits a polarization anisotropy stronger than the QW emission, while the opposite behavior is expected for deeply localized exciton states.

As a conclusion, although it is difficult to consider the intersection between an I_1-BSF and an (Al,Ga)N/GaN QW as a true one-dimensional system, regarding the large spatial extension of BSF-bound QW excitons along the c-axis (Fig. 6.8), the emission from such a QWR is mainly polarized along the wire axis. We infer that the lateral confinement by the BSF induces sufficient valence band mixing to modify the polarization rule of these excitons compared to the one confined in the hexagonal phase of the QW (Fig. 6.13). Nevertheless, full calculation of the valence band structure similar to that described in [Vouilloz1998] is required to support this assumption.
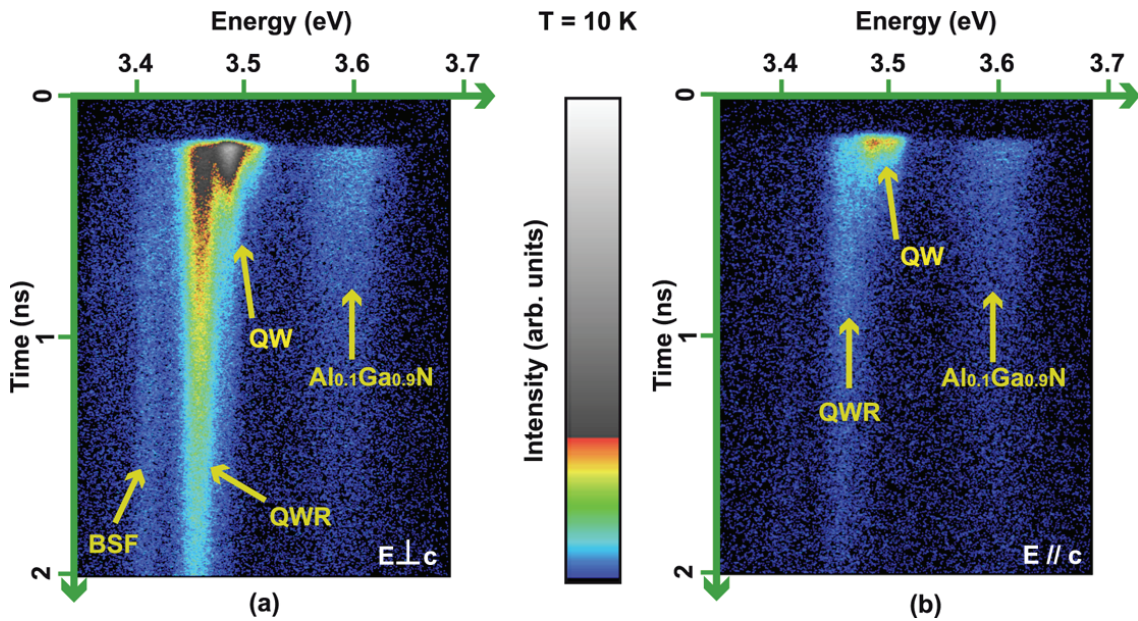
Figure 6.13: Low-temperature time-resolved PL of a 4 nm-thick a-plane $Al_{0.1}Ga_{0.9}N$/GaN QW analyzed with a polarizer (a) perpendicular and (b) parallel to the c-axis. The horizontal and vertical axes correspond to energy and time, respectively. Polarization ratios Γ of 0.76 and 0.51 are found for QWR and QW emissions, resp. Note that the BSF luminescence at 3.42 eV exhibits a long rise time corresponding to the decay of the QWR PL. The GaN template is thus excited by the QW/QWR PL rather than by direct excitation by the laser.

VI.6. CONCLUSIONS

To conclude, we have studied in this Chapter the emission properties of *a*-plane ELO (Al,Ga)N/GaN QWs with various widths and barrier Al-contents. The evolution of both QW emission energy and linewidth with respect to the QW width have lead us to the conclusion that our *a*-plane heterostructures were as expected free of any built-in electric fields. We have then shown that, in addition to the emission from excitons localized on interface roughnesses, our QWs exhibit an intense emission line that we attribute to BSFs intersecting the QW plane. Our QW samples present indeed high densities of BSFs, whose spatial distribution reproduces that of the GaN template. In addition, and similarly to what observed for ELO-GaN epilayers, the dynamics of QW excitons is limited by their trapping by BSFs.

We have then focused on the recombination dynamics of BSF-bound QW excitons. From considerations on the peculiar band-alignment of BSFs in GaN, we expect the intersection between BSF and QW planes to lead to the formation of a quantum wire aligned along the *m*-axis: the electron wave function would be pinned along the wire axis while the hole wave function would be repelled in the hexagonal phase of the GaN QW. Such BSF-bound QW excitons are extremely sensitive to potential fluctuations in the vicinity of the BSF, as confirmed experimentally by the 33 meV localization energy measured for BSF-excitons in a 4 nm thick $Al_{0.05}Ga_{0.95}N$/GaN QW. We underline also that the emission from BSF-bound QW excitons is mainly polarized along the *m*-axis, indicating strong valence band mixing that results from confinement along two orthogonal directions.

From a more technological point of view, we note that our study is not extremely promising regarding the use of such structures as efficient UV emitters at 300 K. For the whole set of samples, QW exciton dynamics is indeed dominated by the capture on BSFs. We underline that, at high-temperature, BSF-excitons get delocalized along the wire axis and are therefore sensitive to the non-radiative dislocations and/or prismatic stacking faults closing the BSFs. Major improvements regarding the reduction of BSF density through ELO-processing are therefore needed. We mention, for instance, the work of [Polyakov2011], which study the influence of the III/V ratio on the generation of stacking faults. Alternatively, one could also strengthen exciton localization along the QW plane to get rid of non-radiative recombination on extended defects. That could be done, for instance, through the growth of ternary or even quaternary non-polar QWs. Finally, we mention that it is also possible to grow

directly (Al,Ga)N/GaN QWs on the *a*-facet of a bulk GaN crystal. The emission properties of such QWs with low defect density will be presented in Chapter VIII.

REFERENCES

[Akopian2005] N. Akopian, G. Bahir, D. Gershoni, M. D. Craven, J. S. Speck, and S. P. DenBaars, Appl. Phys. Lett. **96**, 202104 (2005).

[Arroyo2009] *This micrograph can also be found* Y. Arroyo Rojas Dasilva, PhD Thesis, n° 4193, EPFL (2009). *Manuscript available online* (http://library.epfl.ch/theses/?nr=4193).

[Badcock2008] T. Badcock, P. Dawson, M. J. Kappers, C. McAleese, J. L. Hollander, C. F. Johnston, D. V. Sridhara Rao, A. M. Sanchez, and C. J. Humphreys, Appl. Phys. Lett. 93, 101901 (2008).

[Bastard1981] G. Bastard, Phys. Rev. B **24**, 4714 (1981).

[Bastard1982] G. Bastard, E. E. Mendez, L. L. Chang, and L. Esaki, Phys. Rev. B **26**, 1974 (1982).

[Bastek2008] B. Bastek, F. Bertram, J. Christen, T. Wernicke, M. Weyers, and M. Kneissl, Appl. Phys. Lett. **92**, 212111 (2008).

[Bimberg1987] D. Bimberg, J. Christen, T. Fukanaga, H. Nakashima, D. E. Mars, and J. N. Miller, J. Vac. Sci. Tech. B **5**, 1191 (1987).

[Citrin1992] D. S. Citrin, Phys. Rev. Lett. **69**, 3393 (1992).

[Dingle1971] R. Dingle, D. D. Sell, S. E. Stokowski, and M. Ilegems, Phys. Rev. B **4**, 1211 (1971).

[Feltin2007] E. Feltin, D. Simeonov, J.-F. Carlin, R. Butté, and N. Grandjean, Appl. Phys. Lett. **90**, 021905 (2007).

[Gallart2000] M. Gallart, A. Morel, T. Talierco, P. Lefebvre, B. Gil, J. Allègre, H. Mathieu, N. Grandjean, M. Leroux, J. Massies, Phys. Stat. Sol. (a) **180**, 127 (2000).

[Gil1997a] B. Gil, and O. Briot, Phys. Rev. B **55**, 2530 (1997).

[Gil1997b] B. Gil, and A. Alemu, Phys. Rev. B **56**, 12446 (1997).

[Greene1984] R. L. Greene, K. K. Bajaj, and D. Phelps, Phys. Rev. B **29**, 1807 (1984).

[Gühne2007] T. Gühne, Z. Bougrioua, P. Veenéguès, M. Leroux, and M. Albrecht, J. Appl. Phys. **101**, 113101 (2007).

[Gühne2008] T. Gühne, Z. Bougrioua, S. Laügt, M. Nemoz, P. Veenéguès, B. Vinter, and M. Leroux, Phys. Rev. B **77**, 075308 (2008).

[Huang2011] H.-M. Huang, Y.-C. Wu, and T.-C. Lu, Journal of the Electrochemical Society **158**, H491 (2011).

[Maslov2005] A. V. Maslov, and C. Z. Ning, Phys. Rev. B **72**, 125319 (2005).

[Lefebvre1998] P. Lefebvre, J. Allègre, B. Gil, A. Kavokine, H. Mathieu, W. Kim, A. Salvador, A. Botchkarev, and H. Morkoç, Phys. Rev. B **57**, R9447 (1998).

[Lefebvre2001] P. Lefebvre, A. Morel, M. Gallart, T. Talierco, J. Allègre, B. Gil, H. Mathieu, B. Damilano, N. Grandjean, and J. Massies, Appl. Phys. Lett. **78**, 1252 (2001)

[Lefebvre2004] P. Lefebvre, S. Kalliakos, T. Bretagnon, P. Valvin, T. Talierco, B. Gil, N. Grandjean, and J. Massies, Phys. Rev. B **69**, 035307 (2004).

[Leroux1998] M. Leroux, N. Grandjean, M. Laügt, J. Massies, B. Gil, P. Lefebvre, and P. Bigenwald, Phys. Rev. B **58**, R13371 (1998).

[Leroux1999] M. Leroux, N. Grandjean, J. Massies, B. Gil, P. Lefebvre, and P. Bigenwald, Phys. Rev. B **60**, 1496 (1999).

[Leroux2004] *see Figure 10 in* M. Leroux, F. Semond, F. Natali, D. Byrne, F. Cadoret, B. Damilano, A. Dussaigne, N. Grandjean, A. Le Louarn, S. Vézian, and J. Massies, Superlattices & Microstruct. **36**, 659 (2004).

[Lymperakis2009] L. Lymperakis, and J. Neugebauer, Phys. Rev. B **79**, R241308 (2009).

[Natali2005] F. Natali, D. Byrne, M. Leroux, B. Damilano, F. Semond, A. Le Louarn, S. Vézian, and J. Massies, Phys. Rev. B **71**, 075311 (2005).

[Natali2009] F. Natali, Y. Cordier, J. Massies, S. Vézian, B. Damilano, and M. Leroux, Phys. Rev. B **79**, 035328 (2009).

[note1] *When we performed the present TR-CL experiments, the estimated time-resolution of the set-up was of the order of 50 ps instead of the usual 10 ps.*

[Paskov2007] P. P. Paskov, R. Schifano, B. Monemar, T. Paskova, S. Figge, and D. Hommel, J. Appl. Phys. **98**, 093519 (2005).

[Polyakov2011] A. Y. Polyakov, N. B. Smirnov, A. V. Govorkov, H. Amano, S. J. Pearton, I.-H. Lee, Q. Sun, J. Han, and S. Y. Karpov, Appl. Phys. Lett. **98**, 072104 (2011).

[Rashba1962] E.I. Rashba, and G. E. Gurgenishvili, Soviet Physics - Solid State **4**, 759 (1962).

[Reale2003] A. Reale, G. Massari, A. Di Carlo, P. Lugli, A. Vinattieri, D. Alderighi, M. Colocci, F. Semond, N. Grandjean, and J. Massies, J. Appl. Phys. **93**, 400 (2003).

[Speck2010] J. Speck, "*Progress in nonpolar and semipolar GaN-based materials and devices*", Invited Presentation at the 6th International Workshop on Nitride Semiconductors, Tampa (2010).

[Teisseyre2005] H. Teisseyre, C. Skierbiszewski, B. Lucznik, G. Kamler,A. Feduniewicz, M. Siekacz, P .Perlin, I. Grzegory, and S. Porowski, Appl. Phys. Lett. **86**, 162112 (2005).

[Vouilloz1998] F. Vouilloz, D. Y. Oberli, M.-A. Dupertuis, A. Gustafsson, F. Reinhardt, and E. Kapon, Phys. Rev. B 57, 12378 (1998).

[Vurgaftman2003] I. Vurgaftman, and J. R. Meyer, J. Appl. Phys. **94**, 3675 (2003).

[Waltereit2000] P. Waltereit, O. Brandt, A. Trampert, H. T. Grahn, J. Menniger, M. Ramsteiner, M. Reiche, and K. H. Ploog, Nature **406**, 865 (2000).

[Wu2008] Z. H. Wu, A. M. Fischer, F. A. Ponce, B. Bastek, J. Christen, T. Wernicke, M. Weyers, and M. Kneissl, Appl. Phys. Lett. **92**, 171904 (2008).

Part IV

Intrinsic dynamics of excitons in the weak and strong confinement regimes

Chapter VII - Relaxation of center-of-mass quantized exciton-polaritons in GaN epilayers

The present Chapter and the next one are both devoted to the study of *a*-plane nitride-based heterostructures grown directly on GaN single crystals. Although the growth of GaN crystals by the high-pressure solution method is complicated, as it requires very high pressure and temperature conditions [Grzegory2001], it brings about spectacular results. As an illustration, we mention the work of in [Kornitzer1999], who presented PL and reflectivity experiments on a *c*-plane homoepitaxial GaN layer with highly resolved near-band edge emission lines (*see* Figure 1 in [Kornitzer1999]). We also point that the achievement of high-quality *c*-plane homoepitaxial GaN layers enabled a precise determination of crystal-field and spin-orbit splittings for wurtzite GaN, of the longitudinal transverse splittings for A, B and C excitons [Stepniewski1997] and, finally, the sole observation of the quantization of exciton center-of-mass motion in thick polar GaN epilayers [Morel2001]. Concerning (Al,Ga)N/GaN QWs, the reduction of dislocation density for structures directly grown on GaN crystal allowed for a drastic increase in radiative efficiency at 300 K compared to QWs on sapphire [Grandjean2001]. However, there is, to our knowledge, only few time-resolved PL studies on excitons confined in such high quality polar (Al,Ga)N/GaN QWs [Gallart2001,Talierco2001]. In addition, it seems to us that, in these studies, the authors focused exclusively on the transfer at low-temperature of charge carriers from the (Al,Ga)N barrier to the QW, which is surprising regarding the expected quality of these samples. Coming to non-polar GaN, the successful growth of (Al,Ga)N/GaN QWs on the *a*-facet of a GaN crystal has been reported in [Teisseyre2005], paper in which the elimination of built-in electric fields in such heterostructures was demonstrated. Then, comparative electroreflectance and pressure-dependent PL studies between polar and non-polar QWs were carried out [Teisseyre2009,Kudrawiec2011]. However, the dynamics of excitons confined in polarization-free and low-defect quantum well has not been investigated so far.

In this Chapter, we first demonstrate that, contrary to the non-polar nitride-based layers grown on ELO-GaN studied in Chapter IV to VI, a-plane GaN epilayers grown by MBE on bulk GaN crystals are free of basal plane stacking fault and present a low dislocation density of only approximately 2.10^5 cm^{-2}. Then, we determine by cathodoluminescence an exciton diffusion length of approximately 100 nm at 300 K, leading us to the conclusion that in a PL experiment, excitons are almost not affected by dislocations. The consequences of the negligible role played by dislocations on the radiative efficiency of QW excitons will be discussed in the next Chapter.

We then focus on the low-temperature emission properties of a 200 nm thick a-plane GaN epilayer grown by molecular beam epitaxy on the a-facet of a bulk GaN crystal. We show that, thanks to the low-density of threading dislocations in our layer, excitons present a coherence length of more than 400 nm at 10 K. This is evidenced experimentally through the observation of center-of-mass quantized exciton-polariton emission modes. We support our assignment by a model that accounts for the dispersion of exciton-polaritons as well as for the photon character of the different allowed modes. Finally, we discuss the relaxation mechanisms of such exciton-polaritons with respect to the excitation density.

VII.1. GROWTH OF a-PLANE (Al,Ga)N/GaN QUANTUM WELLS ON GaN CRYSTALS

VII.1.1. Growth of GaN single crystal

In this first section, we detail the approach adopted for the realization of high quality a-plane (Al,Ga)N/GaN QWs. The GaN single crystals used here as substrates for the growth of (Al,Ga)N/GaN QWs have been provided by Dr. Henryk Teisseyre from the Institute of High-Pressure Physics (Unipress) in Poland. They have been elaborated by a combination of high-pressure solution method and hydride vapor phase epitaxy (HVPE) [Lucznik2010]. Thin hexagonal platelet crystals, with dislocation density of 10^2 cm^{-2}, have first been grown by the high-pressure solution method from liquid gallium at a nitrogen gas pressure of the order of 1.0 GPa. These platelets have then been used as seeds for HVPE growth to obtain crystals of about a few millimeters in thickness, and with dislocation density of the order of 5.10^5 cm^{-2}.

The single crystals have then been cut by a wire saw along (11-20) planes and have been finally polished mechanically.

As shown by B. Heying *et al.*, the dislocation density in a crystal can be estimated by analyzing the full width at half maximum (FWHM) of anisotropic planes X-ray rocking curves [Heying1996]. Here, for an illuminated area of 0.8 mm x 1 mm, the reciprocal map shape for the (110) reflection is fully regular, evidencing a perfect crystal quality. As a further evidence of the high material quality of the present substrates, the full width at half maximum for the (110) rocking curve is 0.008° for our GaN crystal (Figure 7.1) while it is 0.2° for *a*-plane GaN layers grown by HVPE on *r*-plane sapphire [Zhu2007].
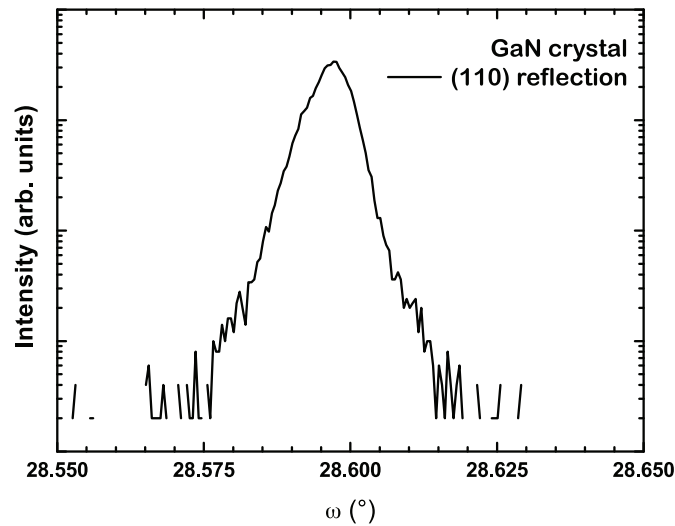
Figure 7.1: (110) reflection rocking curve of a-plane GaN single crystal. The FWHM of 27 arcsec (~0.008°) is close to the value expected theoretically for the (110) reflection of a perfect GaN crystal measured with a Ge(220) Bartels type asymmetric monochromator with slits set to 0.05 mm (courtesy of Dr. Henryk Teisseyre, Institute of Physics, Poland).

VII.1.2. Molecular beam epitaxy of the non-polar quantum wells

a-plane (Al,Ga)N/GaN QW samples have then been grown by molecular beam epitaxy by Dr. Amélie Dussaigne (LASPE-EPFL) on top of the (11-20) facet of the GaN crystals. Nitrogen source is provided by pyrolytic decomposition of ammonia at the sample surface. A 200 nm thick GaN epilayer has first been deposited, followed by 160 nm of $Al_xGa_{1-x}N$. Various *a*-plane QWs were grown, with QW width from 2 to 8 nm and barrier Al-content

from 6 to 12 %. Finally, samples were capped with a 30 nm thick $Al_xGa_{1-x}N$ top barriers, of identical x than the bottom one. Note that the samples have been grown by NH_3-MBE rather than by plasma-assisted (PA) MBE, as the latter technique is likely to induce bilayer QW-width fluctuation [Natali2009]. The subsequent stronger exciton localization for PAMBE-grown QWs would have been detrimental to our study of QW free excitons dynamics (Chapter VIII).

In Section VII.3 of this Chapter, we focus principally on the emission properties of the 200 nm thick GaN layer grown by MBE and sandwiched between the GaN crystal and the $Al_{0.06}Ga_{0.94}N$/GaN QW. For that reason, it is worth noting that while the GaN substrate is slightly n-doped (free electron concentration n of about 5.10^{17} cm^{-3}), the layer grown by MBE is unintentionally n-doped ($n = 5.10^{16}$ cm^{-3}). Therefore, the n-$n+$ interface between the homoepitaxial layer and the substrate prevents holes and thus excitons from leaving the GaN homoepitaxial layer. Note that the doping difference between the substrate and the epilayer also leads to a slight change in refractive index between the two layers [Morel2001].

VII.2. NEGLIGIBLE IMPACT OF DISLOCATIONS ON CHARGE CARRIERS DYNAMICS

VII.2.1. Estimation of the threading dislocation density

As shown by X-ray diffraction measurements, our GaN crystals are of very high structural quality. We therefore expect our QWs to present a dislocation density similar to that of the GaN substrates, as only few misfit dislocations should be formed at the interface between GaN and the low Al-content $Al_{0.06}Ga_{0.94}N$ barriers. As a consequence, transmission electron microscopy (TEM) is not an adequate technique to assess the dislocation density of our layers, as the spatial area that can be investigated with a TEM is limited to only a few square micrometers. In other words, we expect that even TEM micrographs taken with the largest scale would not provide us with a large enough statistic to conclude on the dislocation density in our samples.

On the contrary, and as demonstrated [Sugahara1998], CL is an ideal tool to determine

the dislocation density in GaN. From a combined TEM and CL study of a GaN layer grown on sapphire, these authors indeed report that there is a one to one correspondence between the dark spots seen in CL and dislocations observed by TEM. We therefore performed a room temperature CL mapping of the 4 nm thick $Al_{0.06}Ga_{0.94}N$/GaN QW taken at the QW emission energy. The acceleration voltage is set to 3 kV and we estimate the extension of the generation volume along the growth axis to 100 nm [Bonard1996,Parish2006]. From the CL map, we deduce a dislocation density of 2.10^5 cm^{-2}. Such a dislocation density is four orders of magnitude smaller compared to what reported for non-polar GaN grown on sapphire [Gühne2007,Moram2010]. Contrary to what is observed for structures grown on foreign substrates, the absence in the CL mapping of striped contrasts parallel to the *c*- or to the *m*-axes also evidences that our sample is free of basal plane and prismatic stacking faults (*see* Chapters IV and VI).
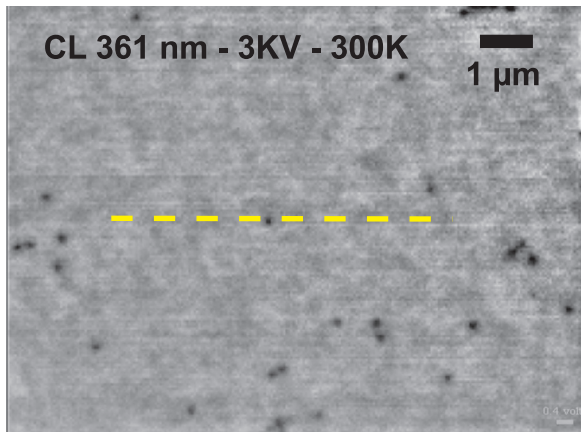
Figure 7.2: Room-temperature CL mapping taken at the QW emission energy. Electron-hole pairs are generated exclusively in the $Al_{0.06}Ga_{0.94}N$/GaN QW. We deduce from the CL mapping a dislocation density of 2.10^5 cm^{-2}. The yellow dashed line indicates the line scan used for the analysis in Figure 7.3.

VII.2.2. Exciton diffusion length and its consequences on the QW emission properties at 300 K

Threading dislocations are generally seen as radial straight-line defects that, in our case, propagate along the [11-20] axis. Within the radius of the defect, carriers are supposed to recombine non-radiatively and instantaneously [Sonderegger2007]. Away from the radial defect, carriers recombine either radiatively or non-radiatively with an effective lifetime τ_{eff}. The distribution of carriers in the vicinity of a dislocation can then be obtained by solving the diffusion equation for excited carriers. One then gets that the CL intensity I at a distance r from a dislocation is given by

$$I(r) = I_0 \left(1 - Exp \left[-\frac{r}{L_{diff}} \right] \right) \qquad \text{Eq.(7.1),}$$

where L_{diff} is the diffusion length of excited carriers. From the analysis of the CL intensity in the vicinity of a dislocation (Fig. 7.3), we obtain an exciton (or charge minority carrier) diffusion length L_{diff} = 100 nm at 300 K [note1]. For the PL experiments performed in the following, we estimate an excitation spot of 50 μm diameter (*see* Chapter II). Therefore, the low dislocation density of 2.10^5 cm^{-2} combined with the diffusion length of 100 nm lead us to the conclusion that, in the PL experiments shown in the following, dislocations will only affect a small fraction of photogenerated excitons.
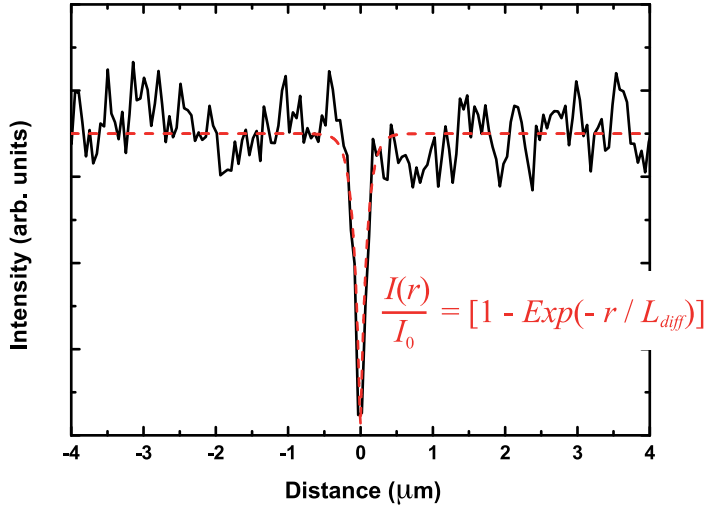
Figure 7.3: CL intensity profile in the vicinity of a dislocation. Fitting this profile with Eq.(7.1), we deduce an exciton (or minority carrier) diffusion length L_{diff} of 100 nm at 300 K.

VII.3. EXCITON CENTER-OF-MASS QUANTIZATION

In this section, we discuss the emission properties of the 200 nm thick GaN epilayer sandwiched between the GaN substrate and the first (Al,Ga)N barrier of a 4 nm thick Al$_{0.06}$Ga$_{0.94}$N/GaN QW sample. We particularly focus on narrow emission lines observed between 3.474 and 3.486 eV that we attribute to the emission of center-of-mass quantized (CMQ) exciton-polariton modes confined in the 200 nm GaN epilayer.

VII.3.1. Low-temperature emission

We show in Figure 7.4(a) the time-integrated PL spectrum of the 4 nm thick $Al_{0.06}Ga_{0.94}N$/GaN QW sample at 10 K. The spectrum is dominated by an intense band at 3.494 eV that we attribute to the emission from excitons localized in the 4 nm thick GaN QW. We attribute the broad and weaker emission at 3.58 eV to the emission from the $Al_{0.06}Ga_{0.94}N$ barriers. The emission properties of the QW structure will be discussed thoroughly in Chapter VIII. We observe an additional line at 3.471 eV that corresponds in energy to the emission from donor bound excitons in the GaN template. Finally, the emission from four narrow (FWHM = 2 meV) lines at 3.474, 3.478, 3.483 and 3.486 eV is recorded (Fig. 7.4(b)).
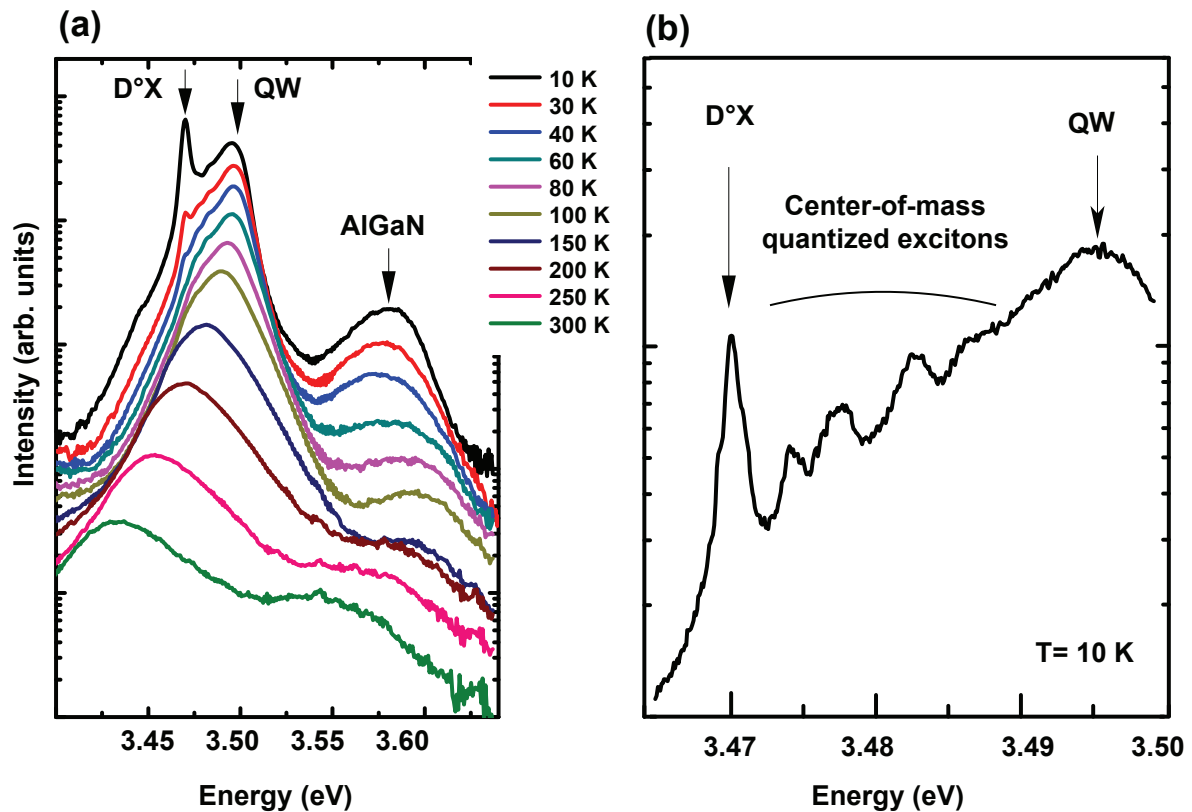

Figure 7.4: (a) Time-integrated PL spectra taken between 10 and 300 K (spectra have been shifted vertically for clarity). The absence of emission at 3.42 eV shows that our sample is free of basal plane stacking faults. (b) Continuous-wave PL spectrum taken at 4 K, showing the signature of center-of-mass quantized excitons-polaritons in the 200 nm thick GaN layer.

VII.3.2. Intrinsic origin of the 3.474-3.486 eV lines

Given their energy separation from the QW emission, we safely discard that the lines between 3.474 and 3.486 eV could originate from monolayer fluctuations of the QW width. We indeed estimate, by envelope function calculations, the localization energy for an exciton on single well width fluctuation to 3 meV. Moreover, increasing the excitation density does not lead to any saturation of these lines, as would be the case for localized states. We note also that when moving the excitation spot on the surface of the sample, neither energy shift nor change in the relative intensities of these transitions, are observed.

We exclude as well D°X excited states as possible origin of the emission at 3.474 eV for several reasons. The intensity ratio [Paskov2007] as well as the energy separation between D°X ground and excited states [Neu2001] indeed only depend on the internal structure of the D°X and do not match at all with the lines observed here (Fig. 7.4). We also do not detect at 3.45 eV the sharp transitions from D°X two electrons replica that always accompany the observation of D°X rotator states (Fig. 7.4) [*see* Chapter III]. Moreover, while an increase in temperature leads as expected to a fast quenching of the D°X luminescence [Leroux1999], it is not the case for the lines between 3.474 and 3.478 eV. Similarly to what is observed in Figure 3.3, if these lines were related to bound excitons, we would have on the contrary observed a faster luminescence quenching for the high energy lines as these bound excitons would have been ionized more easily. These four emission lines have therefore an intrinsic origin.

Finally, despite the fact that the emissions at 3.478 and 3.483 eV correspond to the recombination energies of A and B free excitons ground states in strain free GaN, the emission from A and B exciton excited states as well as that from the C exciton ground state lie at too high energy to be related with the 3.486 eV transition [Kornitzer1999].

VII.3.3. Exciton center-of-mass quantization

The observation of emission lines with comparable intensities over so broad an energy range (12 meV) rather reminds of the emission from center-of-mass confined exciton-polariton modes. Exciton center-of-mass quantization has first been observed in thick CdS

and CdSe layers in the early 1970s [Kiselev1963]. Almost twenty years later, it has then been observed in CdTe [Tuffigo1988] and GaAs [Tredicucci1993], and finally in a thick homoepitaxial polar GaN layer in 2001 [Morel2001]. In parallel the propagation of center-of-mass quantized excitons-polaritons was theoretically investigated during the 1990s [D'Andrea1990].

Generally, when a carrier is confined by a potential well, its momentum along the confinement direction can only assume discrete values. For QWs with a width of the order or smaller than the bulk exciton Bohr radius a_B, electron and hole momenta are individually quantized, which leads to the strong confinement regime. The latter regime has been described in Chapter I. Nevertheless, in thicker layers, an exciton can also be considered confined *as a whole*. This for instance the case for excitons in the 200 nm thick GaN epilayer comprised between the bottom (Al,Ga)N barrier and the n^{++} GaN substrate. As pointed out in [Morel2001], the interface between the n^{++} substrate and the undoped MBE-GaN induces a potential barrier, which prevents holes and therefore excitons from escaping the GaN epilayer. As the thickness of the GaN epilayer L is much larger than $a_B = 3$ nm, the relative motion of electrons and holes remains unaffected by the potential well in the major part of the layer. The momentum of the exciton center-of-mass along the growth direction, however, is quantized and can only assume the values that fulfill, in a first approximation, $k_n = n\pi/L_{eff}$, where k_n is the wave number of exciton center-of-mass for the nth allowed mode and $L_{eff} = L - 2d$. The equivalent thickness L_{eff} accounts for the region of material where the exciton wave function is non-zero, while the thickness d of the dead-layers is of the order of a_B. Nevertheless, as for excited states the penetration of exciton wave function into the barriers increases, a more refined approach is needed to correctly predict the selected k_n [D'Andrea1990]:

$$\begin{cases} k_n \tan\left(k_n L / 2\right) + \tanh\left(L / 2a_B\right) / a_B = 0 & ; \quad n = 1,3,5,... \\ \\ \tan\left(k_n L / 2\right) / k_n - a_B \tanh\left(L / 2a_B\right) = 0 & ; \quad n = 2,4,6,... \end{cases} \qquad \text{Eq.(7.2).}$$

Additional selection rules can also appear due to the parity of exciton wave function along the confinement direction. For our given photon wave vector $k_{ph} = 2\pi\sqrt{\varepsilon_b} / \lambda$ and layer thickness L, we obtain $k_{ph}L \approx 7\pi / 2$: resonances with odd as well as even eigennumbers n

should be observed [Tuffigo1988]. The wave numbers determined with Eq. (7.2) correspond to allowed confined mode energies, according to the exciton-polariton dispersion curves of the material. In wurtzite GaN, one needs to consider the dielectric background constant ε_b and exciton A, B and C resonances to compute the dielectric function. A, B, and C transverse excitons of energies E_T and masses M are modeled as damped harmonic oscillators with oscillator strength f_{osc} and damping constant Γ. In the framework of this semi-classical approach, the polariton dispersion curve $E(k)$ is obtained by equating the dielectric function to the photon dispersion [Hopfield1963]:

$$\frac{\hbar^2 c^2 k^2}{E} = \varepsilon_b + \sum_{i=1}^{3} \frac{f_{osc} E_{T,i}^2}{E_{T,i}^2 - E^2 + \hbar^2 E_{T,i} k^2 / M_i - i\hbar\Gamma_i E} \qquad \text{Eq.(7.3).}$$

(a)
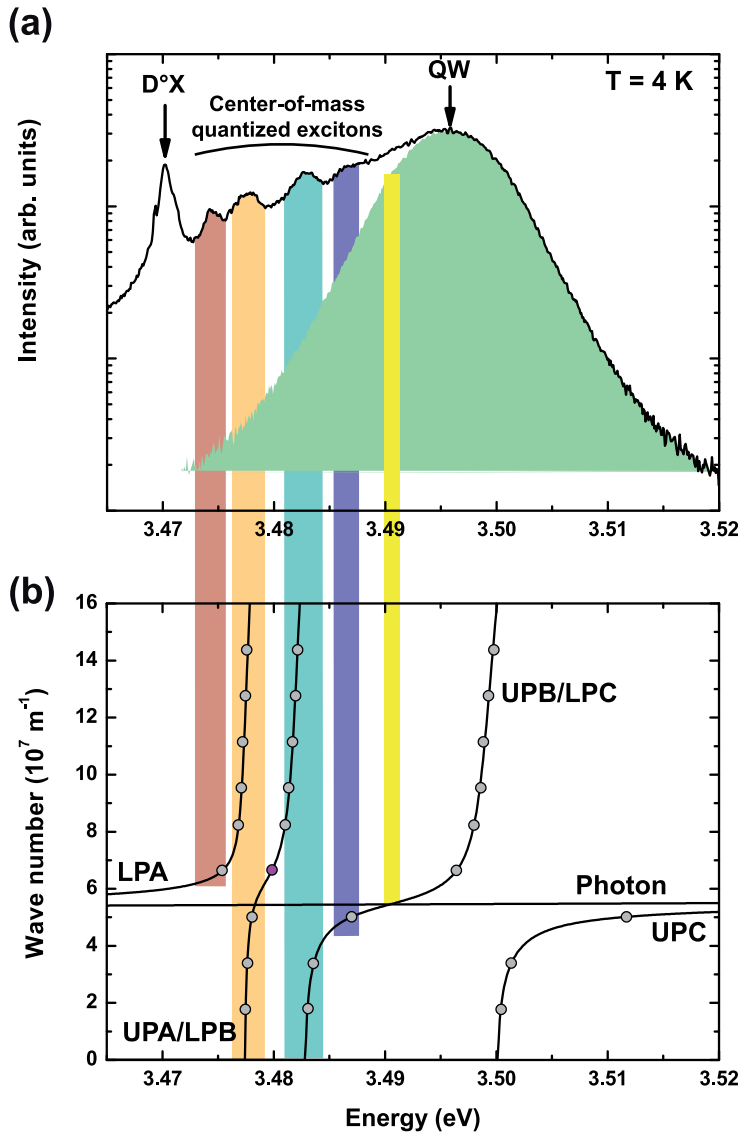
Figure 7.5: (a) Time-integrated PL spectrum at 10 K. The emission lines at 3.474, 3.478, 3.483 and 3.486 eV are attributed to center-of-mass quantized exciton-polaritons in the 200 nm thick GaN epilayer. (b) Light and polaritons dispersion curves (solid lines) and allowed emission modes (circles) in the 200 nm-thick GaN epilayer. Lower and upper polariton branches are respectively denoted by LP and UP. The QW PL at 3.492 eV (yellow line) is resonant with the UPB/LPC polariton branch of the GaN epilayer.

176

The parameters f_{osc}, Γ and ε_b are those given in [Paskov2004], while we took for E_T the values reported for homoepitaxial GaN in [Kornitzer1999]. Figure 7.5(b) shows that the emission lines at 3.478 and 3.483 eV result from the superposition of allowed modes on the weakly dispersive parts of A and B branches. On the contrary, the transitions at 3.474 and 3.486 eV are related to single confined photon-like modes located on strongly dispersive parts of the dispersion curves. Although there is so far a good agreement between the computed results and the experimental spectra, an emission mode expected at 3.480 eV is not observed (Fig. 7.5). We have consequently applied the quasi-particle model [Hopfield1958] to access for all k to the expansion coefficients of each polariton on a basis built with excitons A-B-C and photon eigenstates. Figure 7.6 shows, for the four polariton branches, the photon fraction $|C_k|^2$ with respect to k. We have not included the exciton linewidth in our model since their impact is negligible for broadening smaller than 25 meV [Butté2006,Christmann2008]. We find first that the mode at 3.486 eV is the one with the strongest photon character, explaining why the PL intensity of this single polariton mode is comparable to the total contribution of the numerous exciton-like modes lying at 3.478 and 3.483 eV. Finally, the single mode at 3.480 eV exhibits a photon fraction one order of magnitude smaller than the modes at 3.486 and 3.478 eV. This mode therefore appears dark on Figure 7.5 because of

(*i*) its poor exciton-light coupling,

(*ii*) its weak oscillator strength, compared to the 3.474 eV mode, due to its large exciton B character,

(*iii*) its large total exciton weight, resulting in a scattering rate towards lower energy states which is more efficient than for the modes at 3.474 and 3.486 eV.
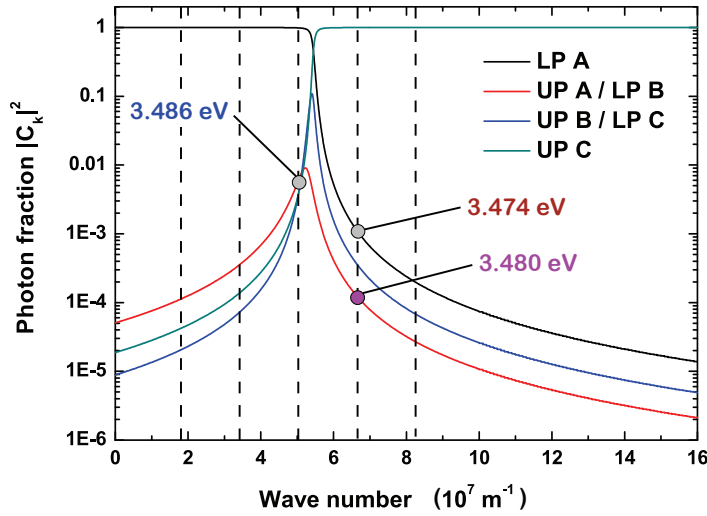
Figure 7.6: Calculated photon fraction with respect to the wave vector for LPA, UPA/LPB, UPB/LPC and UPC polariton branches (black, red, blue, and cyan solid lines, respectively). Dashed vertical lines show the quantized wave vectors in the 200 nm thick GaN epilayer. The emission from the polariton mode at 3.480 eV (magenta dot) is not observed because of its weak photon character.

VII.3.4. Relaxation of center-of-mass quantized exciton-polaritons

Now comes the question of how these modes are excited. We immediately discard the direct excitation by the laser beam: the total thickness of the (Al,Ga)N/GaN QW grown on top of the GaN epilayer is almost 200 nm, *i.e.* twice the estimated penetration length of our laser in the material. However, one can note from Figure 7.5 that the low-energy tail of the QW PL is resonant with the upper B / lower C polariton branch. The low-energy tail of the QW PL can therefore excite quite efficiently these polaritons. They subsequently undergo scattering and relaxation amongst the different allowed states and are finally trapped by neutral donors to form D°X complexes emitting at 3.471 eV. However, if the whole population of center-of-mass quantized excitons would follow a Boltzmann distribution, one would expect the emission from the polariton modes at 3.483 and 3.486 eV to be totally quenched at 10 K. As we observe the PL from non-thermal polariton states over a 12 meV range, this has to mean that the relaxation of center-of-quantized polaritons is not efficient. In the low-excitation regime, exciton relaxation from high to low *k*-states occurs mainly through the emission of acoustic phonons. The inefficiency of the latter mechanism results in a relaxation bottleneck for excitons and is explained in terms of

(*i*) low-density of exciton states available at low *k*,

(*ii*) reduction of exciton / acoustic phonon scattering rate for high phonon wave vectors.

It should be noted that, compared to an infinite crystal, the absence of dispersion along the confinement axis for excitons in our 200 nm thick GaN layer should further hinder acoustic-phonon-assisted relaxation. On the contrary, the quantization of exciton-polariton wave vector along the growth axis opens new radiative paths at the energies calculated within Eqs. 7.3 and 7.4. The combination of the two mechanisms allows finally the observation of several polariton modes.

When increasing the excitation density, exciton relaxation is facilitated due to exciton elastic scattering with other excitons, electrons or holes [Honold1989]. In the present case, the upper B / lower C polariton branch is resonantly excited by the QW PL and we only have to deal with exciton - exciton scattering. Under high excitation densities, the exciton distribution in *k*-space is broadened and scattered excitons gain enough energy to relax through the emission of an LO phonon [Umlauff1998]. As the latter mechanism is much more efficient than the emission of acoustic phonons ($\tau_{ac} \sim 100\tau_{LO}$ [Tsen1997,Viswanath1998]), the whole population of center-of-mass quantized excitons relaxes more efficiently, promoting the emission from the fundamental confined state at 3.474 eV to the detriment of the higher-energy modes at 3.478, 3.483 and 3.486 eV (Fig. 7.7). Finally, let us note that for higher excitation densities, lasing occurs on the low-energy side of the GaN emission band.
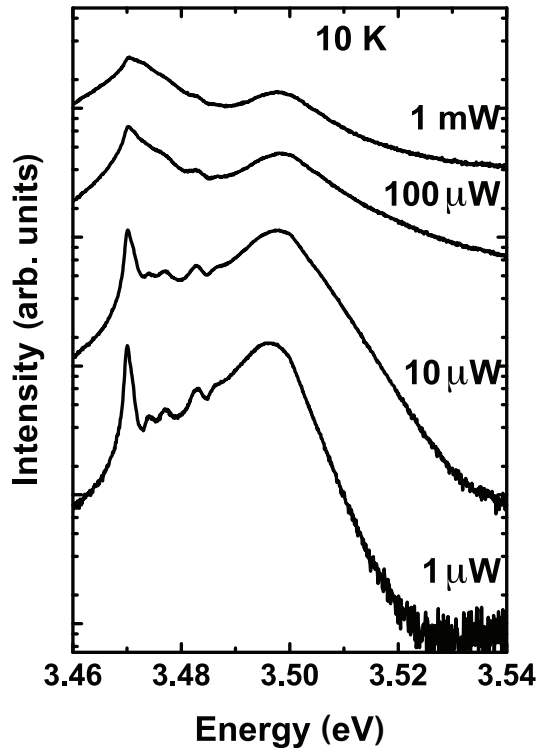
Figure 7.7: Quasi continuous wave PL at 10 K carried out with a pulsed Nd: YAG laser. Increasing the excitation density does not lead to any saturation of the emission lines at 3.474, 3.478, 3.483 and 3.486 eV. On the contrary, increasing the excitation density from 1 μW to 1 mW increases the density of upper B / lower C polaritons excited by the QW PL. Under high excitation conditions, the emission from the fundamental confined state at 3.474 eV is promoted compared to the higher-energy modes at 3.478, 3.483 and 3.486 eV.

VII.3.5. Influence of disorder on the formation of polariton stationary waves

The observation of exciton-polariton center-of-mass quantization clearly implies the formation of standing waves along the confinement axis (here the [11-20] growth axis). As it is the case for a photon in a microcavity, such standing waves exist only if exciton-polaritons can propagate back and forth along the confinement axis without being scattered. In our case, this means that exciton-polaritons propagate at least 400 nm along the *a*-axis while keeping the same phase relation. Consequently, the coherence length of excitons - *i.e.* the distance covered by an exciton between two dephasing events- largely exceeds 400 nm along the *a*-axis.

The lateral disorder also plays a role on the formation of exciton standing waves. As a matter of fact, one has first to make the difference between the disorder occurring at the exciton-scale (typically a few nanometers) and that at the photon scale (typically the light wavelength). The exciton-scale disorder is mostly generated by width fluctuations of the GaN layer in which the exciton are center-of-mass confined. In the case of a 200 nm thick layer, such fluctuations result of course in variations of the quantized wave numbers as well as in a broadening of the center-of-mass quantized exciton-polariton emission modes. However, in

our sample, the variation in quantized wave numbers is small enough not to affect the formation of standing waves along the *a*-axis. Dislocations are much more critical as they efficiently scatter exciton-polaritons. However, the lateral in-plane extension of polariton is given by the photon wavelength and the minimal in-plane separation between two dislocations has to be larger than a few hundreds of nanometers in order standing waves to form. As the dislocation density in our sample is 2.10^5 cm^{-2}, we *a posteriori* verify that the scale of the in-plane disorder is large enough to make possible the observation of center-of-mass quantized exciton-polaritons.

VII.4. CONCLUSIONS

In conclusion, we have studied in this Chapter the emission properties of a thick *a*-plane GaN epilayer grown on a bulk GaN crystal. We have first demonstrated by cathodoluminescence that our sample is free of stacking faults and we have estimated a threading dislocation density of 2.10^5 cm^{-2}. Such a low dislocation density, combined with the fact that exciton diffusion length is of the order of 100 nm, lead us to the conclusion that in a photoluminescence experiment performed on these non-polar samples, photogenerated charge carriers should not suffer from efficient non-radiative recombination on dislocations.

We have also shown that such a low dislocation density reduces considerably the number of scattering events undergone by excitons, making it possible to observe exciton-polariton center-of-mass quantization in non-polar GaN. Supported by a model that accounts for the quantization of exciton motion in the layer and for the respective photon weight of the allowed modes, we have been able to describe qualitatively the emission spectrum at 10 K. Finally, based on excitation-dependent photoluminescence experiments, we have described qualitatively the acoustic and optical phonon assisted relaxation of center-of-mass quantized exciton-polaritons.

To follow up, we should of course study the emission properties of (Al,Ga)N/GaN QWs grown on these low-defect GaN substrates. In particular, will the reduction of dislocation density drastically change the T-dependence of the dynamics of QW excitons? Regarding the studies by [Gallart2001,Talierco2001] on polar (Al,Ga)N/GaN QWs grown on

similar substrates, it seems indeed that there is no striking difference between polar QWs grown on bulk or low-dislocation density ELO-GaN. This study will be carried out in the next Chapter.

REFERENCES

[Bonard1996] J.-M. Bonard, and J.-D. Ganière, J. Appl. Phys. **79**, 6987 (1996).

[Butté2006] R. Butté, G. Christmann, E. Feltin, J.-F. Carlin, M. Mosca, M. Ilegems, and N. Grandjean, Phys. Rev. B **73**, 033315 (2009).

[Christmann2008] G. Christmann, PhD Thesis, n° 4285, EPFL (2009). *Manuscript available online* (http://library.epfl.ch/theses/?nr=4285).

[D'Andrea1990] A. D'Andrea, and R. Del Sole, Phys. Rev. B **41**, 1413 (1990).

[Gallart2001] M. Gallart, A. Morel, T. Talierco, P. Lefebvre, B. Gil, J. Allègre, H. Mathieu, N. Grandjean, J. Massies, I. Grzegory, and S. Porowski, Mat. Sci. Eng. B **82**, 140 (2001).

[Grandjean2001] N. Grandjean, J. Massies, I. Grzegory, and S. Porowski, Solid State Comm. **16**, 358 (2001).

[Grzegory2001] I. Grzegory, J. Phys.: Condens. Matter **13**, 6875 (2001).

[Gühne2007] T. Gühne, Z. Bougrioua, P. Vennéguès, and M. Leroux, J. Appl. Phys. **101**,113101 (2007).

[Heying1996] B. Heying, X. H. Wu, Y. Li, D. Kapolnek, B. P. Keller, S. P. DenBaars, and J. S. Speck, Appl. Phys. Lett. **68**, 643 (1996).

[Honold1989] A. Honold, L. Schultheis, J. Kuhl, and C. W. Tu, Phys. Rev. B **40**, 6442 (1989).

[Hopfield1958] J. J. Hopfield, Phys. Rev. **112**, 1555 (1958).

[Hopfield1963] J. J. Hopfield, and D. G. Thomas, Phys. Rev. **132**, 563 (1963).

[Kiselev1973] V. A. Kiselev, B. S. Razbirin, I. N. Uraltsev, Pis'ma Zh. Eksp. Teor. Fiz. **18**, 504 (1973) [JETP Lett. **18**, 296 (1973)].

[Kornitzer1999] K. Kornitzer, T. Ebner, K. Thonke, R. Sauer, C. Kirchner, V. Schwegler, M. Kamp, M. Leszczynski, I. Grzegory, and S. Porowski, Phys. Rev. B **60**, 1471 (1999).

[Kudrawiec2011] R. Kudrawiec, M. Gladysiewicz, A. Dussaigne, H. Teisseyre, M. Bockowski, I. Grzegory, T. Suski, J. Misiewicz, and N. Grandjean, J. Appl. Phys. **109**, 026103 (2011).

[Leroux1999] M. Leroux, N. Grandjean, B. Beaumont, G. Nataf, F. Semond, and J. Massies, J. Appl. Phys. **86**, 3721 (1999).

[Lucznik2010] B. Lucznik, B. Pastuszka, G. Kamler, I. Grzegory, and S. Porowski in Growth of Bulk GaN Crystals by HVPE on Single Crystalline GaN Seeds. Technology of Gallium

Nitride Crystal Growth Chap. 3, edited by D. Ehrentraut, E. Meissner, and M. Bockowski (Springer-Verlag, Heidelberg, 2010, ISBN 978-3-642-04828-9), pp. 61-78.

[Moram2010] M. A. Moram, C. F. Johnston, M. J. Kappers, and C. J. Humphreys, J. Phys. D: Appl. Phys. **43**, 055303 (2010).

[Morel2001] A. Morel, T. Talierco, P. Lefebvre, M. Gallartz, B. Gil, N. Grandjean, J. Massies, I. Grzegory, S. Porowski, Mater. Sci. Eng. B **82**, 173 (2001).

[Natali2009] F. Natali, Y. Cordier, J. Massies, S. Vezian, B. Damilano, and M .Leroux, Phys. Rev. B **79**, 035328 (2009).

[Neu2001] G. Neu, M. Teisseire, P. Lemasson, H. Lahreche, N. Grandjean, F. Semond, B. Beaumont, I. Grzegory, S. Porowski, R. Triboulet Physica B **302-303**, 39 (2001).

[note1] *As a matter of fact, regarding the lateral extension of the generation volume, 100 nm is an upper bound for L_{diff}.*

[Parish2006] C. M. Parish, and P. E. Russel, Appl. Phys. Lett. **89**, 192108 (2006).

[Paskov2004] P. P. Paskov, T. Paskova, P. O. Holtz, and B. Monemar, Phys. Stat. Sol. (a) **201**, 678 (2004).

[Paskov2007] P. P. Paskov, B. Monemar, A. Toropov, J. P. Bergman, and A. Usui, Phys. Stat. Sol. (c) **4**, 2601 (2007).

[Sonderegger2007] *for a thorough discussion of the electronic properties of dislocations and of the diffusion of carriers in the vicinity of such defects, we refer the reader to* S. Sonderegger, PhD Thesis, n° 3060, EPFL (2007). *Manuscript available online* (http://library.epfl.ch/theses/?nr=3960).

[Stepniewski1997] R. Stepniewski, K. P. Korona, A. Wysmolek, J. M. Baranowski, K. Pakula, M. Potemski, G. Martinez, I. Grzegory, and S. Porowski, Phys. Rev. B **56**, 15151 (1997).

[Sugahara1998] T. Sugahara, H. Sato, M. Hao, Y. Naoi, S. Kurai, S. Tottori, K. Yamashita, K. Nishino, L. T. Romano, and S. Sakai, Jpn. J. Appl. Phys. **37**, L398 (1998).

[Talierco2001] T. Talierco,M. Gallart, P. Lefebvre, A. Morel, B. Gil, J. Allègre, N. Grandjean, J. Massies, I. Grzegory, and S. Porowski, Solid State Comm. **117**, 445 (2001).

[Teisseyre2005] H. Teisseyre, C. Skierbiszewski, B. Lucznik, G. Kamler,A. Feduniewicz, M. Siekacz, P .Perlin, I. Grzegory, and S. Porowski, Appl. Phys. Lett. **86**, 162112 (2005).

[Teisseyre2009] H. Teisseyre, A. Kaminska, G. Franssen, A. Dussaigne, N. Grandjean, I. Grzegory, B. Lucznik, and T. Suski, J. Appl. Phys. **105**, 063104 (2009).

[Tredicucci1993] A. Tredicucci, Y. Chen, F. Bassani, J. Massies, C. Deparis, and G. Neu, Phys. Rev. B **47**, 10348 (1993).

[Tsen1997] K. T. Tsen, D. K. Ferry, A. Botchkarev, B. Sverdlov, A. salvador, and H. Morkoç, Appl. Phys. Lett. **71**, 1852 (1997).

[Tuffigo1988] H. Tuffigo, R. T. Cox, N. Magnea, Y. Merle d'Aubigné, and A. Million, Phys. Rev. B **37**, 4310 (1988).

[Umlauff1998] M. Umlauff, J. Hoffmann, H. Kalt, W. Langbein, J. M. Hvam, M. Scholl, J. Söllner, M. Heuken, B. Jobst, and D. Hommel, Phys. Rev. B **57**, 1390 (1998).

[Viswanath1998] A. K. Viswanath, J. I. Lee, S. Yu, D. Kim, Y. Choi, and C.-H. Hong, J. Appl. Phys. **84**, 3848 (1998).

[Zhu2007] T. Zhu, D. Martin, R. Butté, J. Napierala, and N. Grandjean, J. Cryst. Growth **300**, 186 (2007).

Chapter VIII - Radiative recombination governed lifetimes in (Al,Ga)N/GaN quantum wells

In this Chapter, we investigate the recombination dynamics of excitons confined in *a*-plane (Al,Ga)N/GaN grown by molecular beam epitaxy on bulk GaN crystals. As demonstrated in the previous Chapter, the epitaxial growth on the (11-20) facet of GaN crystals allows for the realization of nitride-based heterostructures with a threading dislocation density of the order of 2.10^5 cm^{-2}.

We first study the emission properties of our QWs at 10 K. In particular, we discuss the characteristics of the localized states of the present QWs compared to those of (Al,Ga)N/GaN QWs grown on ELO-GaN. Then, we observe, for the first time in the III-nitrides, purely radiative free exciton recombinations for temperatures typically below 150-200 K. The non-significance of non-radiative recombinations is evidenced through the observation of increased PL effective lifetime with temperature. For higher temperatures, we observe, for all $Al_{0.06}Ga_{0.94}N$/GaN QW samples, a reduction in QW emission lifetime combined with an increase in (Al,Ga)N PL decay time. From the analysis of barrier and QW respective emission intensities, we show that the main mechanism limiting the radiative efficiency in our set of samples is related to the thermal escape of excitons from the QW to the (Al,Ga)N barriers. We propose thus that non-radiative recombination in the disordered (Al,Ga)N barriers is the mechanism limiting the QW PL decay time at 300 K.

VIII.1. EXCITON LOCALIZATION ALONG THE QUANTUM WELL PLANE

We study here the emission properties of a 2 nm thick $Al_{0.12}Ga_{0.88}N$/GaN QW (sample N1) and of 2, 4 and 7 nm thick $Al_{0.06}Ga_{0.94}N$/GaN QWs (samples N2, N3 and N4, resp.) (Table

8.1). The growth procedure for the samples studied here has been detailed in Section VII.1.2. We also note that sample N3 was the one on which we carried out the study on exciton-polariton center-of-mass quantization presented in the previous Chapter.

Samples			QW emission properties at 10 K				Calculations
Name	x_{Al} (%)	L_{QW} (nm)	E_{10K} (eV)	δ (meV)	E_{loc} (meV)	τ_{loc} (ps)	E_{loc} (meV)
N1	12	2	3.585	15	7±2	160	14
N2	6	2	3.540	13	11±1	150	8
N3	6	4	3.494	10	4±1	110	3
N4	6	7	3.483	8	2±1	100	1

Table 8.1: QW width L_{QW} and (Al,Ga)N barriers Al-content x_{Al} of the investigated samples. The emission properties of the different samples at 10 K are also given: E_{10K}, δ, E_{loc} and τ_{loc} stand respectively for the QW emission energy, the QW emission full width at half maximum, the exciton localization energy and localized QW exciton PL lifetime. In the last column, we provide the QW localization energies E_{loc} calculated accounting for a one-monolayer fluctuation of the QW width.

VIII.1.1. Low-temperature time-integrated photoluminescence

Figure 8.1 shows time-integrated PL spectra for the 2 and 4 nm thick $Al_{0.06}Ga_{0.94}N$/GaN QWs (samples N2 and N3). At 10 K, the emission from the 2 nm thick QW is centered at 3.54 eV and presents a full width at half maximum (FWHM) δ = 13 meV. While we ascribe the emission at 3.6 eV to the $Al_{0.06}Ga_{0.94}N$ barriers, the one at 3.471 eV arises from excitons bound to donors in the GaN substrate (D°X). Note the absence of any emission at 3.42 eV, evidencing that our sample is free of stacking faults. The low-temperature QW emission energies and broadenings are reported in Table 8.1 for the whole set of samples. As expected for polarization-free QWs, δ is the lowest for thick QWs with low Al-content QWs [Bimberg1987,Natali2005]: for the 7 nm thick QW, the emission linewidth at 10 K is 8 meV, which is only 2 meV larger than what is reported for state-of-the-art *c*-plane $Al_{0.05}Ga_{0.95}N$/GaN QWs grown by metal-organic vapor phase epitaxy [Feltin2007].
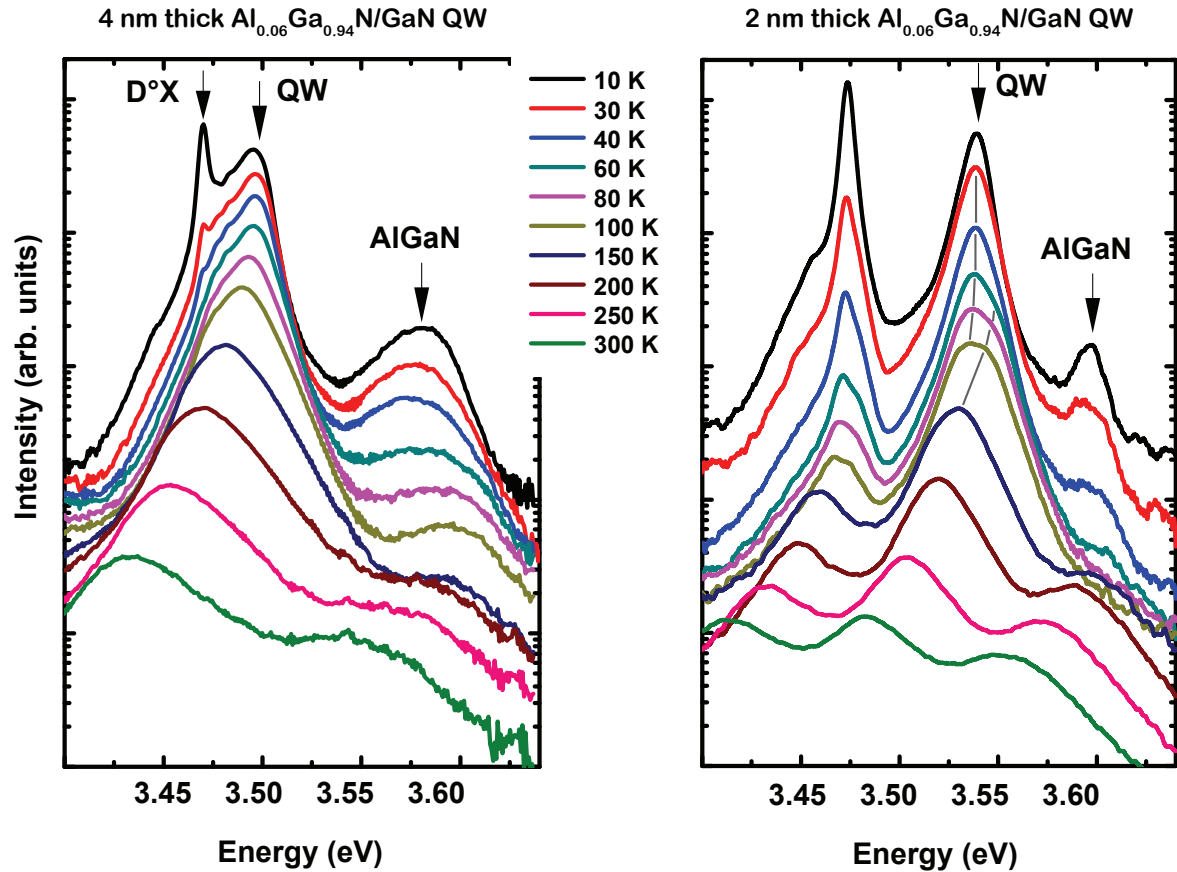
*Figure 8.1: Time-integrated PL spectra between 10 and 300 K for samples N3 (a) and N2 (b).
At 10 K, the PL spectra are dominated by the QW and the (Al,Ga)N emissions. The D°X
emission line arises from donor bound excitons in the 200 nm thick GaN epilayer and is
optically excited by the QW and the (Al,Ga)N emissions. Grey lines in (b) show the
delocalization of excitons, resulting in a blueshift of the QW emission.*

VIII.1.2. Exciton localization along the QW plane and in the barriers

At low temperature, the QW emission is dominated by the recombination of excitons
localized along the QW plane [Weisbuch1981,Leroux1998]. When T increases, exciton
delocalization into the whole two-dimensional quasi-continuum of states is activated,
resulting in a blueshift of the QW emission (Fig. 8.2). From the difference between QW
emission energy at 10 K and the extrapolation at 0 K of the high-T dependence of QW
emission energy, we have access to QW exciton localization energy E_{loc}. For a constant
barrier Al-content of 6 % (samples N2, N3 and N4), when decreasing the well width from 7 to
2 nm, E_{loc} increases from 2 to 11 meV. This tendency agrees with the calculated localization

energy for exciton on single monolayer well-width fluctuation (Table 8.1).

Figure 8.2: QW PL peak energy with respect to T for samples N1 to N4 (squares, triangles, diamonds and stars symbols, resp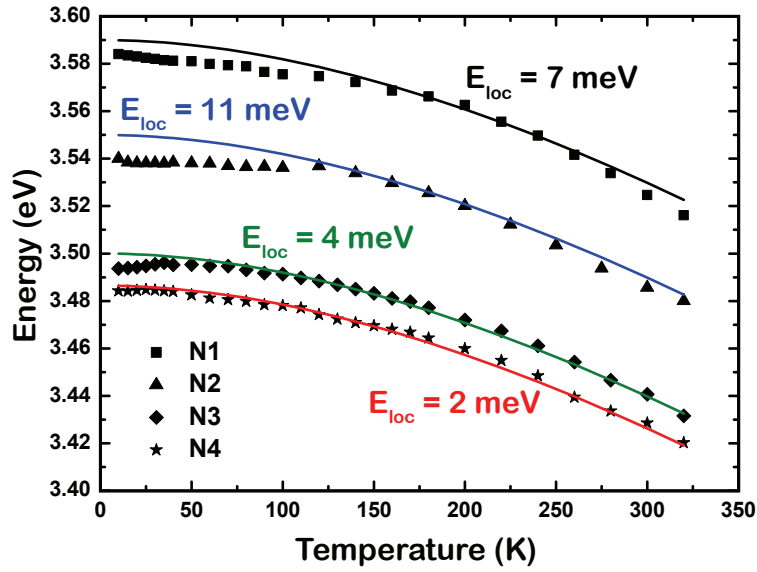.). Solid lines are the results of Varshni fits to the high-T dependence of the QW emission energy for samples N2 to N4, yielding the localization energy E_{loc} of excitons for each QW sample.

Concerning the emission energy of $Al_{0.06}Ga_{0.94}N$ barriers, its T-dependence exhibits a full S-shaped behavior (Fig. 8.1): a clear indication of exciton localization inside the disordered alloy. Between 10 and 30 K, the (Al,Ga)N emission redshifts, which we attribute to the ionization of excitons bound to the shallower potential fluctuation in favor of the deeper ones. Concerning the blueshift part of the S-shape, it is related to the delocalization of excitons towards the three-dimensional continuum of states of the barriers. From the extrapolation towards 0 K of the temperature dependence of (Al,Ga)N free exciton energy, we extract an exciton localization energy of 18 meV in the barriers. Here, exciton localization arises from potential fluctuations that we relate to local variations of Al-composition in the barriers. Similarly to what we observed in *a*-plane (Al,Ga)N/GaN QWs grown on ELO-GaN (*see* Section VI.2.2), we attribute these fluctuations in barrier Al-composition to anisotropic incorporation of Al atoms when growing along non-polar planes. More precisely, we estimate that the barrier Al-content varies between 5.6 and 6.4 %, when it is nominally set to 6 %. From these variations in (Al,Ga)N energy band gap, we deduce by envelope function

calculations that barrier disorder should induce a ±3 and ±1 meV variation of exciton emission energy for 2 and 4 nm thick $Al_{0.06}Ga_{0.94}N/GaN$ QWs, respectively. This agrees qualitatively with the larger linewidth observed at 10 K for sample N2 compared to sample N3.

VIII.1.3. Localized exciton radiative lifetime

Regarding the dynamical behavior of the QW PL, the decay times at 10 K range between 100 and 150 ps for samples N2, N3 and N4 (Table 8.1). At first sight, the low-temperature PL decays observed here seem quite fast compared to what reported in [Waltereit2000,Akopian2005,Garrett2005,Badcock2010,Dussaigne2011], which may suggest, misleadingly, that the PL of the present QWs is governed by non-radiative processes (Fig. 8.3). Still, as discussed above, excitons at 10 K are localized along the QW plane and are therefore not likely to suffer from any non-radiative recombination. In addition, we observe that, for constant barrier Al-content, the thinner the QW the longer the PL lifetime (Fig. 8.3). As a matter of fact, this is not surprising as the deeper the localization, the larger the extent of QW localized exciton wave function in reciprocal space [Rashba1962,Citrin1993] and the longer the radiative lifetime, as observed experimentally in [Bellessa1998].

The evolution of QW decay times at 10 K with respect to the QW width is therefore a further indication for the structural quality of our samples compared to QWs grown on ELO-GaN. For a given QW width, the radiative decay time of excitons localized in QWs grown on bulk GaN is indeed by a factor of 4 shorter than that of localized excitons in QWs grown on ELO-GaN. Consequently, the area of QW interface states for the samples studied here is approximately four times larger than for QWs grown on ELO-GaN. It is worth noting that the same procedure has been used to grow the samples studied in this Chapter and in [Dussaigne2011,ChapterVI]: the use of bulk GaN crystals thus allows for a better control of the QW interface roughness.

Coming to what occurs for sample N1, with the same QW width as for sample N2 but with higher barrier Al-content (12 % for sample N1 against 6% for sample N2), we expect deeper exciton localization. This deeper localization is evidenced by a longer QW PL lifetime at 10 K, for the reasons already evoked (Table 8.1). Now, we extract from the T-dependence

of sample N1 QW PL energy a localization energy of only 7 meV (Fig. 8.2). The latter energy seems at first contradictory with the expected deeper localization of excitons in this sample. It should be noted, however, that when extracting a localization energy from the extrapolation at 0 K of a Varshni fit of the QW PL peak energy at high temperatures, one assumes that excitons are totally delocalized at 300 K. This assumption is not necessary valid, as observed experimentally by [Leroux1998] for 5 monolayer-thick $Al_{0.1}Ga_{0.9}N$/GaN multi QWs. Similarly, for the present 2 nm thick $Al_{0.12}Ga_{0.88}N$/GaN QW, the 7 meV localization energy deduced from Figure 8.2 is certainly underestimated. This is confirmed by our calculations that yield, for sample N1, a localization energy of 14 meV for QW excitons (Table 8.1).
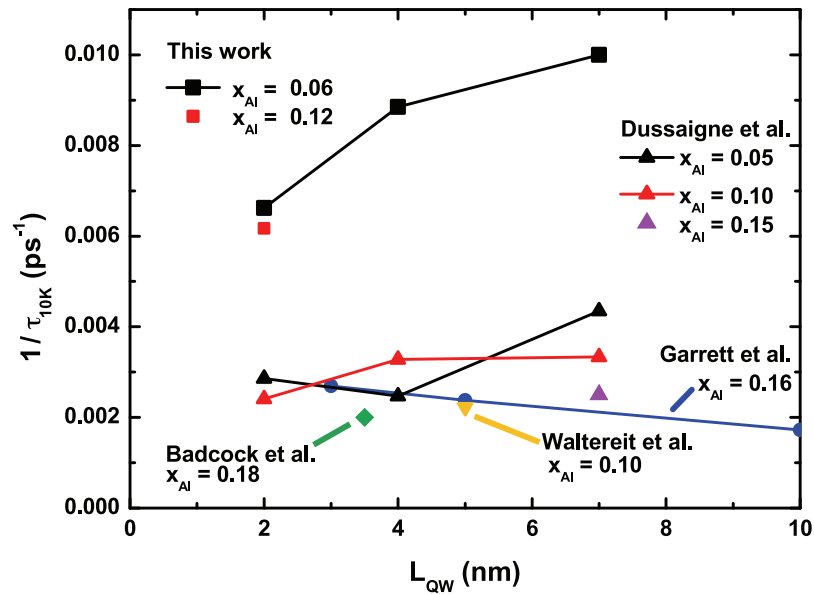
Figure 8.3: QW PL decay time at 10 K for non-polar (Al,Ga)N/GaN QWs grown on GaN crystals (squares - this work) and grown on lattice-mismatched substrates (triangles and diamonds). Solid lines are guides to the eyes. Data is taken from [Waltereit2000,Garrett2005, Badcock2010,Dussaigne2011]. Note that we did not include the results from [Akopian2005], as the reported lifetimes are more likely to account for the transfer of QW excitons to BSFs rather than for the radiative lifetime of localized QW excitons (see Section VI.4.1).

VIII.2. EXCITON DELOCALIZATION IN REAL AND RECIPROCAL SPACES

VIII.2.1. Purely radiative recombination of quantum well excitons

For $Al_{0.06}Ga_{0.94}N$/GaN QWs, the effective PL decay time τ_{eff}, averaged spectrally over the contributions of both localized and free excitons, increases with T. As shown in Figure 8.4 for sample N3, τ_{eff} goes from 110 ps at 10 K up to 350 ps at 150 K and then steadily decreases for higher T (Fig. 8.5). In parallel, the initial PL intensity $I(t=0)$ continuously decreases between 10 and 320 K. Let us consider a distribution of excitons n_X that recombine radiatively or non-radiatively with decay times τ_r and τ_{nr}, respectively. The emission intensity with time $I(t)$ is proportional to the radiative part of the derivative with time of n_X. Then,

$$I(t) \propto \frac{1}{\tau_r} Exp\left(-\frac{t}{\tau_{eff}}\right)$$
$$\text{Eq.(8.1),}$$

where $\tau_{eff} = \left(\tau_r^{-1} + \tau_{nr}^{-1}\right)^{-1}$ is the effective decay time of excitons. Above 10 K, the thermal escape of QW bound excitons towards the whole two-dimensional continuum of states is activated (Fig. 8.2). The increase of τ_{eff} combined with the decrease of $I(t=0)$ therefore indicates that the average radiative decay time of free and localized excitons increases with T. Although the direct observation of longer radiative lifetime through the increase in effective lifetime is now common in III-arsenides or II-VI QWs (*see for instance* [Gurioli1992]), it has, to our knowledge, only been reported once in polar (Al,Ga)N/GaN multiple QWs for T between 10 and 60 K [Smith1996].

In most of polar and non-polar nitride-based QWs, even when processed by epitaxial lateral overgrowth, non-radiative processes are dominant and mask the intrinsic increase of QW exciton radiative lifetime with T (*see* Chapter VI). Deconvolution of the experimental decay between radiative and non-radiative contributions as well as guesses on the QW low-T radiative efficiency have then to be done to estimate exciton radiative lifetime, a procedure resulting in radiative lifetimes determined with a low-accuracy (*see for instance Fig. 4 in* [Lefebvre1998]). Here, the entire suppression of electric fields and the reduction of

dislocation density allow on the contrary for the direct measurement of the QW radiative lifetime increase with T. Note, finally, that the T-dependence of the radiative efficiency of our low Al-content barrier (Al,Ga)N/GaN QW cannot be compared directly with that of (In,Ga)N-based QWs. In (In,Ga)N/GaN QWs, excitons are indeed strongly localized along the QW plane and are therefore preserved, even at 300 K, from reaching non-radiative recombination centers [Oliver2010]. This is absolutely not the case here as we observe for samples N2, N3 and N4 the delocalization of QW excitons for temperatures typically above 30-40 K (Figure 8.2).
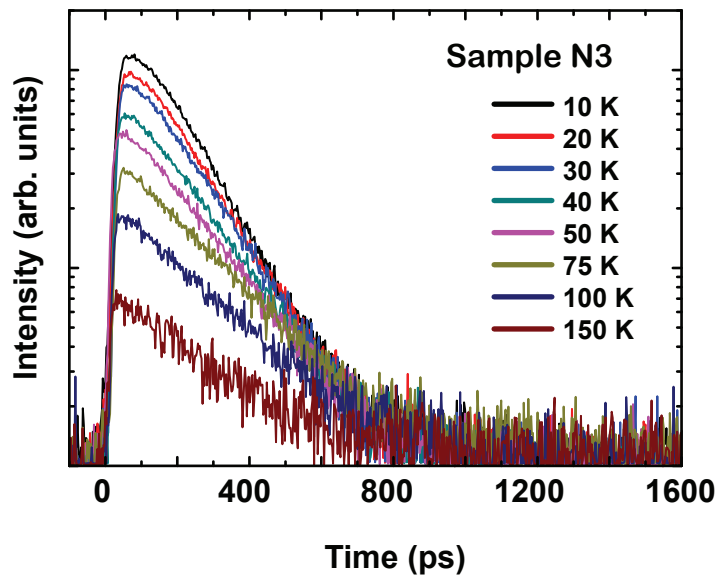
Figure 8.4: PL transients between 10 and 150 K for a 4 nm thick Al$_{0.06}$Ga$_{0.94}$N/GaN QW. The QW emission intensity at zero delay is inversely proportional to the radiative lifetime τ$_r$. The reduction in PL intensity at zero delay combined with the increase in effective lifetime with temperature evidence the expected increase of radiative lifetime with T and the minor role played by non-radiative recombinations in that temperature range.

VIII.2.2. Temperature-dependence of quantum well exciton radiative lifetime

Accounting for both the delocalization of bound excitons [Citrin1993] and the thermal distribution of free excitons in *k*-space [Andreani1991], it is possible to express the T-dependence of the average decay time τ_{eff} for QW excitons. As a matter of fact, even in the high-temperature regime, the QW PL decay time is conditioned by N_D, the density of

localized states along the QW plane [Citrin1993]. As described in detail in Appendix IV, we consider a distribution of excitons that are either free or localized along the QW plane. As relaxation processes are much faster than recombination, we assume free and localized exciton distributions to be at thermal equilibrium. While localized excitons recombine radiatively with a lifetime τ_{loc} independent of T, free excitons recombine radiatively or non-radiatively with lifetimes τ_r and τ_{nr}, respectively. At 0 K, τ_r is of the order of a few ps and is inversely proportional to the exciton oscillator strength f_{osc} [Deveaud1991]. Despite f_{osc} for an exciton confined in a QW is a function of both the QW width and the barrier Al-content [Andreani1990], we assume it constant for the set of samples studied here. Similarly to what done in [Lefebvre1998], we obtain from exciton A longitudinal transverse splitting $\Delta_{LT} = 0.6$ meV [Hoffman1997] that f_{osc} and τ_r(T = 0 K) are equal to 2.10^{13} cm^{-2} and 2.4 ps, respectively. When T is increased, the thermal population of exciton states lying out of the light cone leads to a linear increase of τ_r with T, with a slope proportional to the exciton mass [Andreani1991]. We consider that free exciton non-radiative recombinations are thermally activated and we therefore set $\tau_{nr} = \tau_1 Exp(-E_a / kT)$, where E_a is an activation energy.

The experimental evolution of τ_{eff} *versus* T is accounted for by adjusting three parameters: E_a, τ_1 and N_D. While E_a and τ_1 only play a significant role in the high-T regime, the main fitting parameter for the low-T dependence of τ_{eff} is N_D. Applying this fitting procedure for samples N2, N3 and N4, we obtain $N_D = 3.0 \pm 1.5 \ 10^{12}$ cm^{-2} for Al$_{0.06}$Ga$_{0.94}$N/GaN QWs (Table 8.2). Such a high density might be surprising compared to the best (Al,Ga)As/GaAs QWs, where exciton localization occurs on flat islands resulting from step-like monolayer variations of the well width, with typical densities between 10^{10} and 10^{11} cm^{-2} [Deveaud1987]. The estimation of localization centers density is however more complex in (Al,Ga)N/GaN QWs. First, the growth is step-flow and the growth rates are different for the in-plane *c*- and *m*-axes [Lymperakis2009]. We note also that the interatomic distances in GaN are smaller than those in GaAs. The areal atomic density in III-nitrides is therefore approximately by a factor of two higher than in III-arsenides. From this steric consideration, we conclude that the areal density of localization centers in GaN QWs must be higher than that in GaAs QWs.
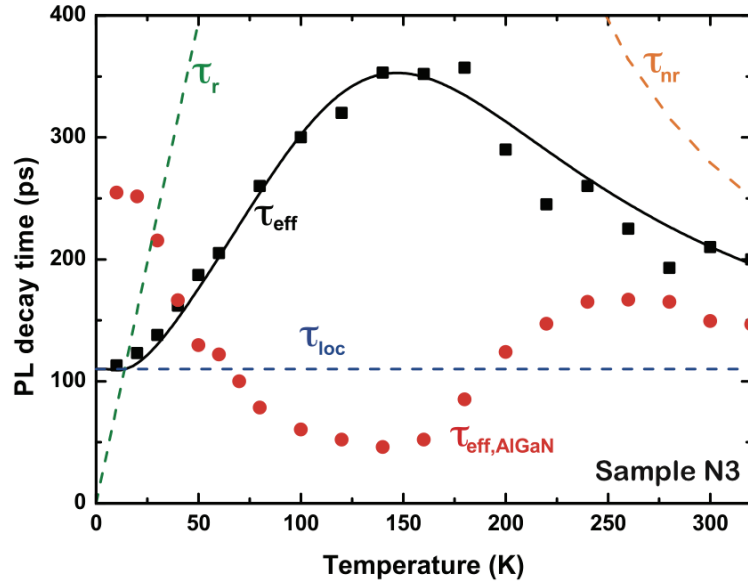
Figure 8.5: Experimental (black squares) and calculated (solid line) effective lifetime T-dependence for QW excitons in sample N3. Experimental $Al_{0.06}Ga_{0.94}N$ barriers PL decay time ($\tau_{eff,AlGaN}$) is shown with red circles. Blue, green and orange dashed lines show the T-dependence of localized exciton radiative lifetime (τ_{loc}) and free exciton radiative (τ_r) and non-radiative lifetimes (τ_{nr}), respectively. Fitting QW exciton decay time evolution in the low temperature range yields a QW localized states density of 3.10^{12} cm^{-2}. Above 150 K, the QW PL effective lifetime decreases due to the thermal escape of QW excitons towards the (Al,Ga)N barriers. In parallel, $\tau_{eff,AlGaN}$ increases, until QW and barriers exciton populations are fully thermalized and exhibit the same PL lifetimes.

Sample	f_{osc}/S (10^{13} cm^{-2})	N_D (10^{12} cm^{-2})	E_{loc} (meV)	E_a (meV)	τ_1 (ps)
N1	2.0	10 ± 2	14	55 ± 15	45 ± 25
N2	2.0	2.2 ± 0.5	8	17 ± 7	47 ± 15
N3	2.0	3.0 ± 0.5	3	43 ± 7	50 ± 13
N4	2.0	4.0 ± 0.5	1	50 ± 5	66 ± 15

Table 8.2: Localization state density N_D and non-radiative recombination rate activation energy E_a deduced from the fitting procedure of the T-dependence of QW effective lifetime. Despite exciton oscillator strength should vary from one QW to another, we have set it to 2.10^{13} cm^{-2} to reduce the number of free fitting parameters. The localization energy for exciton bound to single monolayer well width fluctuation has been estimated by envelope function calculations.

It should also be noted that due the large effective mass of holes in GaN, QW excitons should be quite sensitive to the statistical distribution of Al atoms in the barriers [Gallart2009]. This is qualitatively confirmed here, as we estimate N_D to $1.0 \pm 0.2 \; 10^{13}$ cm^{-2} for sample N1, with barrier Al-content set to 12 %.

Whereas in the low-T regime, the recombination of QW excitons is purely radiative, we have clearly to account for thermally activated non-radiative recombination processes to fit the high-T evolution of τ_{eff} (Fig. 8.5). As already discussed in Section VII.2.2, only excitons generated less than 100 nm away from a dislocation can diffuse to it and recombine non-radiatively, at 300 K. We therefore rule out that exciton capture on dislocation could be the main non-radiative process responsible for the decrease of τ_{eff} in the high-T range. Although we observe so far that the stronger the confinement, the larger E_a (Table 8.2), a more detailed study of exciton recombination mechanisms in the high-T range is needed to understand the origin of these non-radiative recombinations.

VIII.3. THERMAL ESCAPE OF CHARGE CARRIERS OUT OF THE QUANTUM WELLS

VIII.3.1. Possible origin of non-radiative recombinations in high quality (Al,Ga)As/GaAs quantum wells

We now need indeed to understand, as non-radiative processes come into play at higher T, what is the dominant process that limits/promotes non-radiative recombinations. We can study that in detail, for the first time in nitrides, because in previous work, fast and efficient carrier capture by extended defects washed out all possible effects and limited the lifetimes, including at the lowest T [Badcock2008, *see* also ChapterVI]. As shown in Figures 8.5 and 8.6 for $Al_{0.06}Ga_{0.94}N$/GaN structures, QW PL lifetimes do not steadily increase up to 300 K: they rather start decreasing above some critical T and then tend towards a value of 100-150 ps at room-temperature.
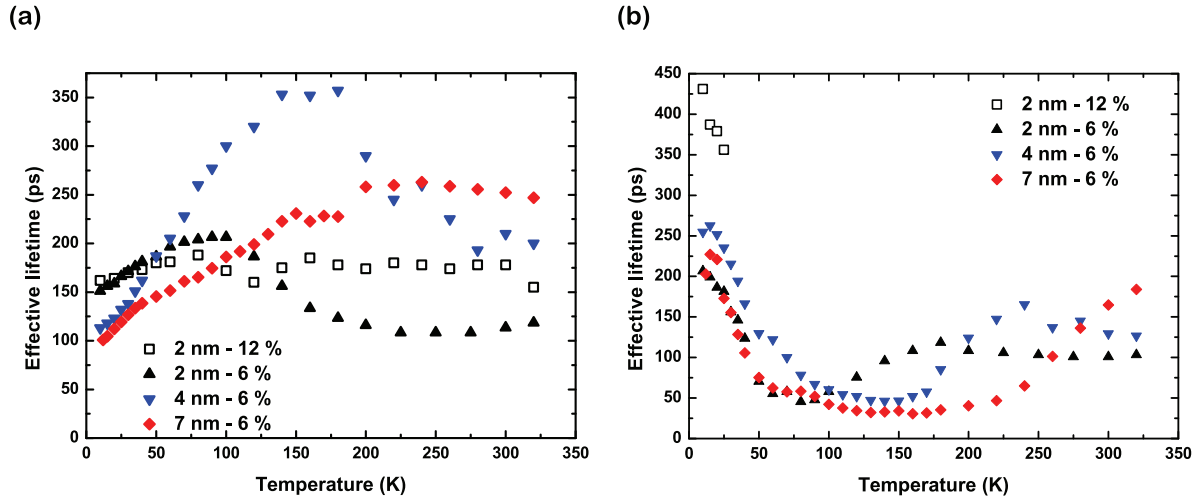
(a)

(b)

Figure 8.6: QW (a) and (Al,Ga)N barriers (b) effective PL lifetimes as a function of T for samples N1 (squares) N2 (triangles), N3 (reversed triangles) and N4 (diamonds).

Time- and temperature-resolved PL studies performed on high-quality III-arsenide QWs also revealed drops of both intensity and lifetime when increasing temperature. Such decreases were first ascribed to the thermal escape of charge carriers out of the QW into barriers states, but with disagreements on the associated activation energies reported by different groups. These energies indeed ranged from the electron-hole confinement energy [Bacher1993], to half the total confinement energy [Michler1992], or to the binding energy of the less-confined species [Gurioli1992,Vening1993]. [Gurioli1992] inferred that the discrepancies between the different reports simply came from the different methods used to extract activation energies. From the analysis of the temperature dependence of QW PL effective lifetime, they deduced that the main non-radiative mechanism for QW charge carriers was related to the unipolar escape of carriers out of the QW. However, in their model, [Gurioli1992] modeled (Al,Ga)As barriers as non-radiative "sinks" for carriers. This model is not appropriate here considering the room-temperature PL spectra shown in Figure 8.1, where intense PL from the (Al,Ga)N barriers is observed. Based on excitation dependent measurements, [Weber1995] then proposed the competition between non-radiative recombinations at QW interface states [Krahl1990,Hillmer1990] and the bipolar escape of carriers towards the barriers followed by subsequent surface recombination to be at the origin of the deviation between the different reports.

Here, such reduction in QW exciton lifetime cannot be ascribed to the capture of charge carriers by non-radiative states located in the QW or at its interfaces. First, and accordingly with the discussion in Section VII.2.2, only a small fraction of photogenerated excitons are affected by the presence of dislocations. Second, if mechanisms requiring the in-plane diffusion of QW excitons toward non-radiative point defects in the plane QW were involved in the drop of QW PL lifetime at high-T, one would expect this process to be activated more easily for samples with shallower exciton localization. We observe experimentally the opposite behavior (Fig. 8.6): in sample N2, where E_{loc} = 11 meV, QW PL lifetime starts decreasing at T = 100 K, while this reduction starts at 150 and 240 K for samples N3 and N4, respectively.

VIII.3.2. Thermalization between quantum wells and (Al,Ga)N barriers excitons

Monitoring the (Al,Ga)N barriers PL lifetime in the whole 10-320 K temperature range brings further understanding on the dynamics of excitons at high T (Fig. 8.6). First, (Al,Ga)N PL lifetime quenches between 10 and 50 K. When T is increased, excitons in the disordered alloy get spatially delocalized. Their decay is then dominated by their capture into the QW, which is assisted by LO phonon or impurity scattering [Deveaud1993]. However, we observe the increase of (Al,Ga)N PL lifetime in the highest-T range (Fig. 8.6). At 300 K, the emissions from the barriers and the QW present the same PL decay for all $Al_{0.06}Ga_{0.94}N$/GaN heterostructures, as an evidence of full thermalization of exciton populations in the well and the barriers. We would like to bear in mind that, contrary to (Al,Ga)As/GaAs QWs [Bacher1993], no cladding layers are needed here for the observation at 300 K of both intense PL and non-instantaneous decay time for those (Al,Ga)N barriers. In agreement with PL experiments on GaN surface QWs [Muth2005] and on GaN nancolumns of diameter of few tens of nanometers (*see* Chapter III), surface recombinations are not efficient in low Al-content (Al,Ga)N, indicating that states induced by dangling bonds are energetically far from mid-gap in that material system [Nolte1990]. It is nonetheless clear that charge carriers in the QW and in the barriers are thermalized and that the recombination lifetime of carriers in the (Al,Ga)N barriers -whatever its radiative or non-radiative origin- is, at 300 K, the limiting decay time for the whole charge carriers population in the heterostructure.

Analyzing the high-energy side of PL peaks for QWs and barriers, we can determine the effective carrier temperature, as a function of the lattice temperature (Fig. 8.7). We can therefore determine the temperature T_{th} above which exciton populations in QW and barriers are fully thermalized. As expected for the thermal emission of carriers from a QW, the deeper the confinement, the higher T_{th} (Table 8.3). As relaxation processes are much faster than recombination mechanisms, QW and barrier PL show the same recombination dynamics for T > T_{th} (Figure 8.7).
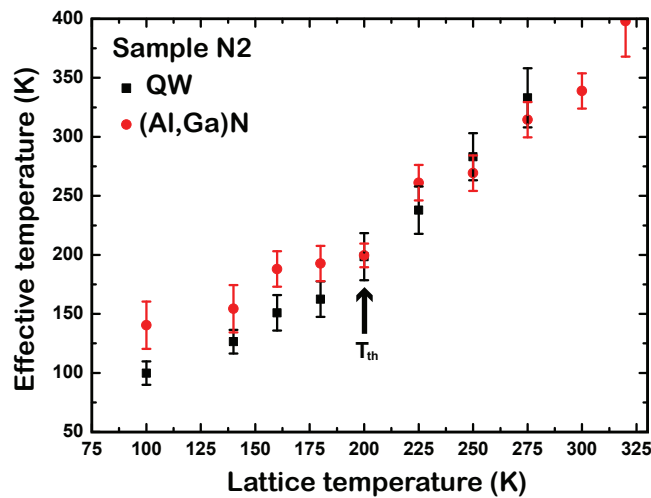
Figure 8.7: Effective QW (black) and barrier (red) carrier temperature with respect to the lattice temperature for sample N2, obtained from the analysis of the high-energy side of QW and (Al,Ga)N PL spectra. Above 200 K, QW and (Al,Ga)N carriers effective temperatures are identical, evidencing full thermalization of both exciton populations. The arrow points the temperature T_{th} above which (Al,Ga)N barriers and QW carrier populations are fully thermalized.

VIII.3.2. Theoretical modeling of the thermal equilibrium between the GaN quantum well and the (Al,Ga)N barriers

Still, we do not have, so far, any quantitative information -in terms of activation energy- about the thermal escape of charge carriers out of the QW. For that reason, we study in the following the evolution with T of QW and (Al,Ga)N relative emission intensities. Under thermodynamic equilibrium, the intensity ratio between QW and barrier emissions is given by:

$$\frac{I_{AlGaN}}{I_{QW}} \propto \frac{\tau_{r,QW}}{\tau_{r,AlGaN}} \frac{N_{X,AlGaN}}{N_{X,QW}} \qquad\qquad \text{Eq.(8.2).}$$

$N_{X,AlGaN}$ and $N_{X,QW}$ are respectively barrier and QW exciton densities, which decay radiatively within the characteristic times $\tau_{r,AlGaN}$ and $\tau_{r,QW}$. If we assume a constant ratio between QW and (Al,Ga)N radiative lifetimes in the 200-320 K temperature range, then:

$$Ln\left(\frac{I_{AlGaN}}{I_{QW}}\right) = A + Ln\left(\frac{N_{X,AlGaN}}{N_{X,QW}}\right) \qquad\qquad \text{Eq.(8.3),}$$

where A is a constant. The intensity ratio between the emissions from the QW and the (Al,Ga)N barriers is plotted as a function of the inverse of T in Figure 8.8 for samples N2, N3 and N4. Note that we were not able to plot this ratio for sample N1 because of too weak emission from the $Al_{0.12}Ga_{0.88}N$ barriers for T > 50 K. For samples N2 to N4, the T-dependence of $Ln\left(I_{X,AlGaN}/I_{X,QW}\right)$ is nearly monoexponential for T_{th} < T < 320 K. The slopes of the semi-logarithmic plots displayed in Figure 8.8 correspond to the activation energies for the escape of charge carriers from the QW to the (Al,Ga)N barriers. As expected, we observe that, the deeper the confinement, the larger the carrier thermal escape activation energy.

In order to support our experimental observations, we have computed the respective densities of excitons, electrons and holes in both the QW and the (Al,Ga)N barriers, with respect to T, in order to have access to the T-dependence of $Ln\left(I_{X,AlGaN}/I_{X,QW}\right)$. The main ingredients of our model is to account for

(*i*) the dissociation of excitons into free carriers in both the QW and the (Al,Ga)N barriers,

(*ii*) the thermal escape of free electrons and holes from the two-dimensional QW to the three-dimensional barriers.
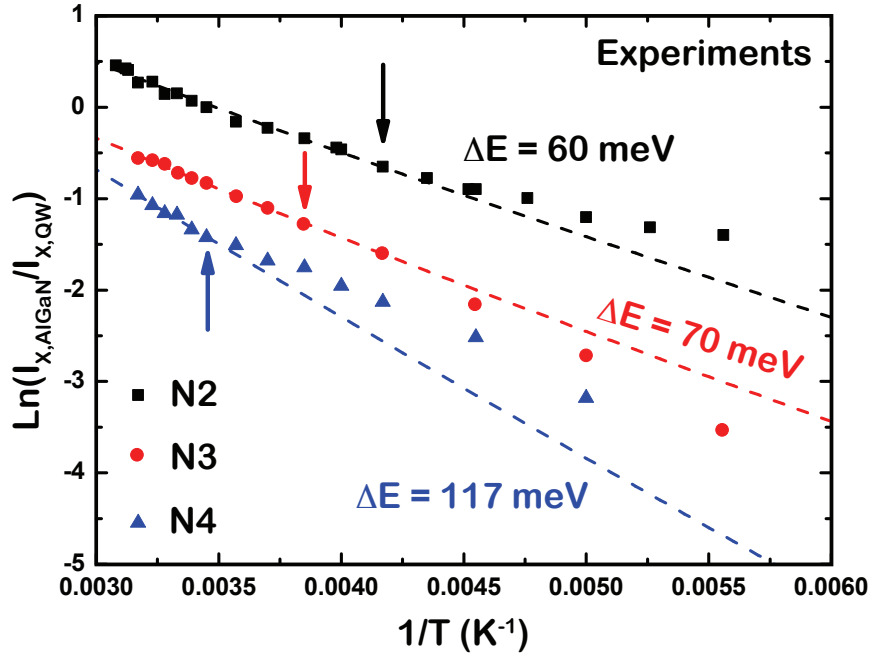
Figure 8.8: Experimental time-integrated intensity ratio between barrier and QW emissions plotted against (1/T) for samples N2, N3 and N4 (black, blue and red symbols). Dashed lines are the result of the fitting procedure described in the text [Eq. (8.10)]. We obtain that the thermal escape of QW excitons towards the barriers presents activation energies of 60, 70 and 117 meV for samples N2, N3 and N4, respectively. Arrows shows the temperature T_{th} above which full thermalization is achieved between QW and (Al,Ga)N barriers.

With N_e and N_h electron and hole densities, the mass action law between free carriers and excitons is [Chemla1983,Colocci1990]:

$$\frac{N_{e,QW} N_{h,QW}}{N_{X,QW}} = \frac{\mu kT}{2\pi\hbar^2} Exp\left[-\frac{E_{b,QW}}{kT}\right] \qquad \text{Eq.(8.4)}$$

in the two-dimensional QW and it is

$$\frac{N_{e,AlGaN} N_{h,AlGaN}}{N_{X,AlGaN}} = L\left(\frac{\mu kT}{2\pi\hbar^2}\right)^{3/2} Exp\left[-\frac{E_{b,AlGaN}}{kT}\right] \qquad \text{Eq.(8.5)}$$

in the three-dimensional barriers. $E_{b,QW}$ and $E_{b,AlGaN}$ are exciton binding energies in the QW and in the (Al,Ga)N, respectively, while μ is the exciton reduced mass. We have calculated $E_{b,QW}$ by envelope function calculations for the whole set of samples (Table 8.3). Notice that in our calculations, we have separated the in-plane and on-axis motions of the exciton. We therefore slightly underestimate its binding energy for samples N3 and N4, QWs wider than 1.4 times the bulk GaN ground-state exciton A Bohr radius [Bastard1982]. We also assume electron and hole effective masses to be the same in the QW and in the low Al-content ternary alloy. We however take $E_{b,AlGaN}$ equal to 27 and 29 meV in $Al_{0.06}Ga_{0.94}N$ and $Al_{0.12}Ga_{0.88}N$ [Feneberg2010]. Finally, $L = 190$ nm is the total thickness of the (Al,Ga)N barriers. Under the assumption that electron and hole populations follow a Boltzmann distribution and accounting only for the first QW confined state, the ratio of the QW electron density $N_{e,QW}$ (*respectively hole density $N_{h,QW}$*) to that in the barrier $N_{e,AlGaN}$ ($N_{h,AlGaN}$) is given in Eq.(8.6) [*Eq.(8.7)*]:

$$\frac{N_{e,AlGaN}}{N_{e,QW}} = \frac{N^*_{e,AlGaN}}{N^*_{e,QW}} Exp\left[-\frac{\Delta E_e}{kT}\right] \qquad \text{Eq.(8.6)},$$

$$\frac{N_{h,AlGaN}}{N_{h,QW}} = \frac{N^*_{h,AlGaN}}{N^*_{h,QW}} Exp\left[-\frac{\Delta E_h}{kT}\right] \qquad \text{Eq.(8.7)}.$$

ΔE_e (*resp. ΔE_h*) is the energy difference between barrier conduction (*resp.* valence) band and the electron (*resp.* hole) ground-state of the QW. As it was the case for QW exciton binding energies, ΔE_e and ΔE_h can be obtained by finite difference calculations (Table 8.3). $N^*_{e,AlGaN}$ and $N^*_{h,AlGaN}$ are the three-dimensional effective electron and hole densities of states for the barriers while $N^*_{e,QW}$ and $N^*_{h,QW}$ are the QW two-dimensional effective electron and hole densities of states. Considering that the electric charge is conserved and that the material is electrically neutral, one gets:

$$N_{e,AlGaN} + N_{e,QW} + N_{X,AlGaN} + N_{X,QW} = N_{tot} \qquad \text{Eq.(8.8)},$$

and

$$N_{h,AlGaN} + N_{h,QW} + N_{X,AlGaN} + N_{X,QW} = N_{tot} \qquad \text{Eq.(8.9)}.$$

Samples	Calculations						Experimental results / Fitting		
Name	E_{loc} (meV)	ΔE_e (meV)	ΔE_h (meV)	$E_{B,QW}$ (meV)	$E_{B,AlGaN}$ (meV)	ΔE_{th} (meV)	T_{th} (K)	ΔE_{exp} (meV)	$\tau_{r,QW}$ / $\tau_{r,AlGaN}$
N1	14	122	78	48	29	219	-	-	-
N2	8	43	33	42	27	91	200	60	3.0
N3	3	74	42	40	27	129	260	70	3.5
N4	1	97	47	35	27	152	290	117	2.3

Table 8.3: QW localization energy E_{loc} calculated accounting for a one-monolayer fluctuation of the QW width. Calculated QW and barrier exciton binding energies ($E_{B,QW}$ and $E_{B,AlGaN}$, resp.), energy differences ΔE_e (resp. ΔE_h) between barrier conduction (resp. valence) band and ground-state energy of the QW. ΔE_{th} is the equivalent activation energy for the escape of excitons from the QW to the barriers. The temperatures T_{th} above which barrier and QW excitons are thermalized are obtained from the procedure shown in Figure 8.7. The experimental activation energies ΔE_{exp} and the ratio $\tau_{r,QW} / \tau_{r,AlGaN}$ between QW and (Al,Ga)N radiative lifetimes result from the fits displayed in Figure 8.8. Note that for sample N1, we could not obtain experimentally T_{th}, ΔE_{exp} and $\tau_{r,QW} / \tau_{r,AlGaN}$ because of too weak emission from the (Al,Ga)N barrier in the high-T range.

The system of Eqs. (8.4) to (8.9) is solved to obtain the T-dependence of each charge carrier density for the whole set of samples. It is worth emphasizing that we do not account explicitly for the escape of excitons from the GaN QW towards the (Al,Ga)N barriers. In other words, at thermal equilibrium, the dissociation of QW excitons into free electron hole pairs has to be activated before there could be excitons in the (Al,Ga)N barriers. The result of our calculations, displayed in Figure 8.9, reproduce what we observe for the respective QW and (Al,Ga)N emission intensities for samples N1 to N4 (Fig. 8.8). In agreement with the PL spectra in Figure 8.1, we find for sample N2, where confinement is the shallowest, that at 320

K the exciton density in the $Al_{0.06}Ga_{0.94}N$ barriers is of the same order of magnitude than that in the QW. On the contrary, for sample N1, we compute an exciton density in the barriers two orders of magnitude smaller than QW exciton density, justifying qualitatively why even at 320 K, we do not detect any PL from the $Al_{0.12}Ga_{0.88}N$ barriers. More quantitatively, it is also possible to express analytically the ratio of (Al,Ga)N exciton density to that of the QW:

$$Ln\left(\frac{N_{X,AlGaN}}{N_{X,QW}}\right) = \frac{1}{2}Ln\left(\frac{m_e m_h}{\mu}\frac{kTL^2}{32\pi\hbar^2}\right) - \frac{\Delta E_e + \Delta E_h + E_{b,QW} - E_{b,AlGaN}}{kT} \qquad \text{Eq.(8.10).}$$
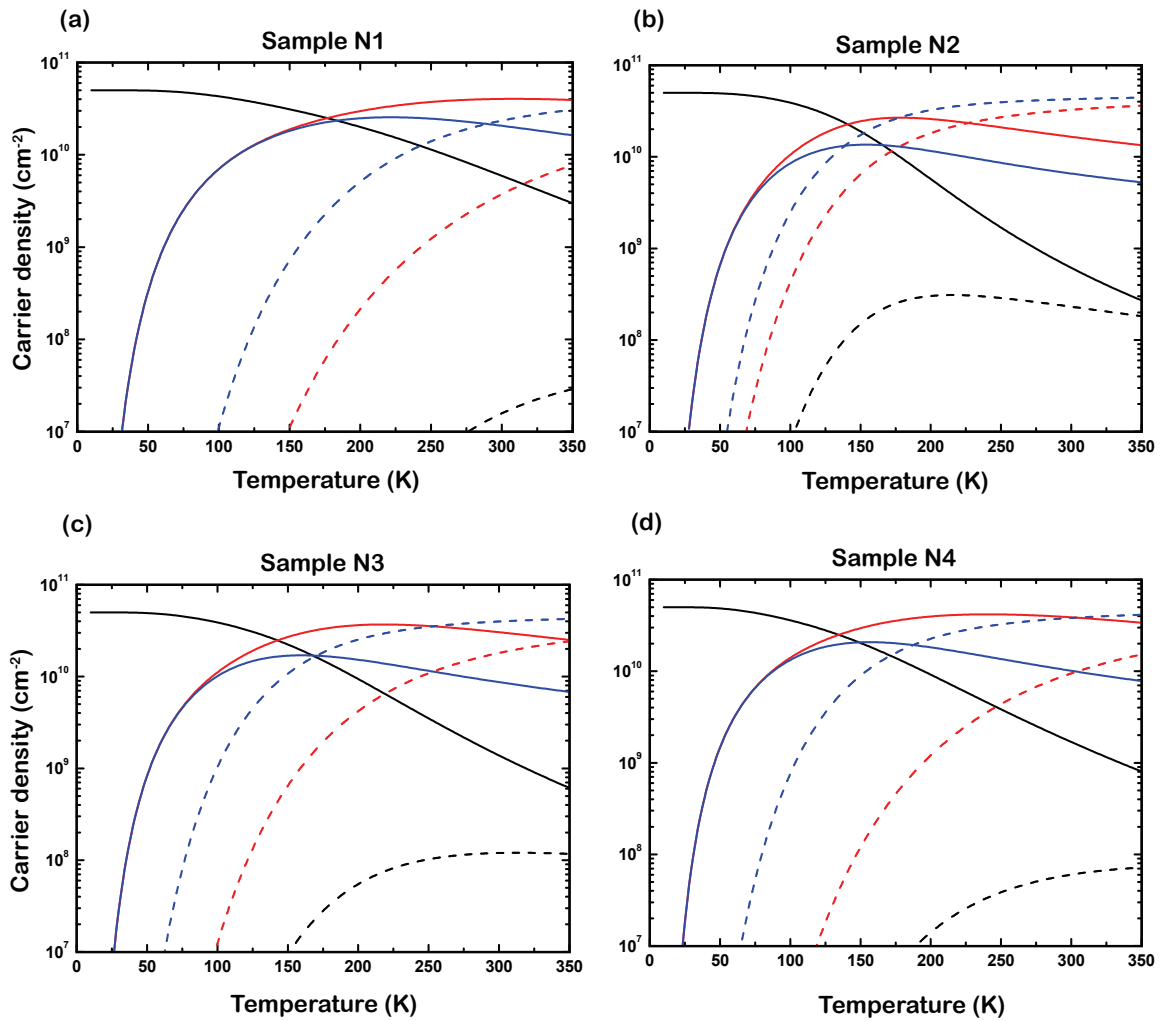

Figure 8.9: Calculated exciton, electron and hole densities (black, red and blue, resp.) in the QW (solid lines) and in the (Al,Ga)N barriers (dashed lines) using the parameters gathered in Table 8.3, for a photogenerated pair density of 5.10^{10} cm^{-2}. Panels (a), (b), (c) and (d) correspond respectively to samples N1, N2, N3 and N4.

The first term in the right-hand side of Eq.(8.10) is just a geometrical term, which actually plays a minor role in the evolution of $Ln\left(N_{X,AlGaN}/N_{X,QW}\right)$ for the temperature range studied here (typically comprised between 200 and 320 K). The numerator of the second term in the right-hand side of Eq.(8.10) is equivalent to an activation energy for the escape of excitons from the QW toward the (Al,Ga)N barriers. However, this activation energy ΔE_{th} depends not only on the total confinement $\Delta E_e + \Delta E_h$ but also on the difference between QW and (Al,Ga)N barriers exciton binding energies. As (Al,Ga)N barrier and QW populations are in thermal equilibrium, the ratio between (Al,Ga)N and QW exciton densities does not depend on the total carrier density in the structure. Injecting Eq.(8.10) into Eq.(8.3), we get the intensity ratio between (Al,Ga)N and QW time-integrated PL:

$$Ln\left(\frac{I_{X,AlGaN}}{I_{X,QW}}\right) = A + \frac{1}{2}Ln\left(\frac{m_e m_h}{\mu}\frac{kTL^2}{32\pi\hbar^2}\right) - \frac{\Delta E_e + \Delta E_h + E_{b,QW} - E_{b,AlGaN}}{kT} \qquad \text{Eq.(8.11).}$$

VIII.3.2. Activation energy for the thermal escape of carriers out of quantum wells

We show in Figure 8.8, the best fits to the intensity ratio between QW and (Al,Ga)N barriers emissions as a function of the inverse of T. When the width of $Al_{0.06}Ga_{0.94}N$/GaN QW is increased from to 2 to 7 nm, ΔE_{exp} increases from 60 to 117 meV. For comparison, we plot in Figure 8.10 the evolution of $Ln\left(N_{X,AlGaN}/N_{X,QW}\right)$ with the inverse of T for samples N1 to N4, using the ΔE_{th} determined by enveloped function calculations and displayed in Table 8.3. Despite the simplicity of our model, the computed T-dependences of the ratio between (Al,Ga)N and QW exciton densities reproduce the trends observed experimentally for $Ln\left(I_{X,AlGaN}/I_{X,QW}\right)$. This ratio increases nearly monoexponentially for T < 320 K, confirming that the geometrical terms in Eqs. (8.10) and (8.11) have a negligible influence on the evolution of $Ln\left(N_{X,AlGaN}/N_{X,QW}\right)$ with T. By extension, accounting in our model for exciton A excited states as well as for B and C-like exciton branches should not significantly modify the result of our calculations, since it would change the absolute value but not the T-dependence of the geometrical term in Eq.(8.11). On the contrary, uncertainties on the actual QW width and on the barrier Al-content, as well as on the conduction-band offset ratios, are

more likely to introduce discrepancies between experimental and calculated activation energies. In any case, we reproduce that the deeper the confinement, the larger the carrier thermal escape activation energy ΔE_{exp}, and we definitely confirm that the reduction in QW PL lifetime occurs once the thermal escape of electrons and holes out of the QW is activated.
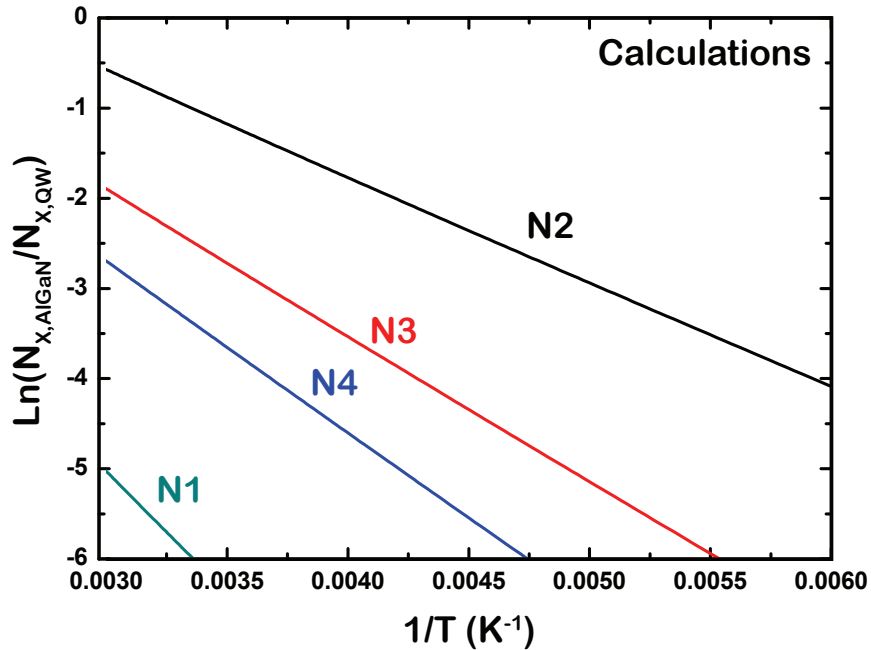
Figure 8.10: Calculated ratio between (Al,Ga)N and QW exciton populations versus the inverse of temperature using Eq.(8.9) and the parameters gathered in Table 8.3. Cyan, black, red and blue lines correspond to samples N1, N2, N3 and N4, respectively.

VIII.4. CONCLUSIONS

From our detailed study, two points should be emphasized. First, we have shown that thanks to the use of GaN substrates grown by the combination of high-pressure solution method and HVPE, we could fabricate (Al,Ga)N/GaN QWs where recombinations are dominated by radiative phenomena up to 250 K. Contrary to what occurs in (In,Ga)N/GaN QWs [Oliver2010], our observation was made in QWs with low localization energy. *It is consequently now possible to achieve non-polar room-temperature UV emitters combining a good radiative efficiency with a rather narrow emission line*. Second, we have demonstrated

that the mechanism limiting the efficiency of the QW was due to the thermal escape of free charge carriers towards barriers and their subsequent non-radiative recombination. Thanks to the elimination of built-in electric fields in a-plane heterostructures, *we thus propose to tackle the thermal escape of carriers by the growth of thick QWs rather than increasing the barrier Al-content*, which is important from the defect/strain generation point of view.

Now, a thorough study of the mechanisms limiting charge carriers lifetime in (Al,Ga)N barriers has still to be performed in order to further improve the efficiency of the UV-light emitters based on non-polar (Al,Ga)N/GaN QWs with low Al-content barrier. First, we intend to measure the temperature-dependence of exciton radiative lifetime in $Al_{0.06}Ga_{0.94}N$ thick layers. In Eq.(8.3), we have assumed that the ratio $\tau_{r,QW}$ / $\tau_{r,AlGaN}$ was constant. It is certainly not the case, and it may affect the fitting of our experimental results with Eq.(8.11). Then, more sophisticated QW samples should be studied. We propose, for instance, to grow QW samples with AlN cap layer or with passivated surface. An increase in radiative efficiency after such a process would indeed lead us to the conclusion that surface recombinations are more efficient than assumed in (Al,Ga)N. Alternatively, non-radiative recombinations could also arise from the capture of exciton by point defects [Reynolds1998], and high radiative efficiency at room-temperature could be recovered after annealing the sample [Kaufmann2011].

REFERENCES

[Andreani1990] *see Figure 7 in* L. C. Andreani, and A. Pasquarello, Phys. Rev. B **42**, 8928 (1990).

[Andreani1991] L. C. Andreani, F. Tassone, and F. Bassani, Solid State Comm. **77**, 641 (1991).

[Andreani1994] L. C. Andreani, in *Confined Electrons and Photons: New Physics and Devices*, ed. by E. Burstein and C. Weisbuch (Plenum, New York, 1994).

[Akopian2005] N. Akopian, G. Bahir, D. Gershoni, M. D. Craven, J. S. Speck, and S. P. DenBaars, Appl. Phys. Lett. **86**, 202104 (2005).

[Bacher1993] G. Bacher, C. Hartmann, H. Schweizer, T. Held, G. Mahler, and H. Nickel, Phys. Rev. B **47**, 9545 (1993).

[Badcock2008] T. J. Badcock, P. Dawson, M. J. Kappers, C. McAleese, J. L. Hollander, C. F. Johnston, D. V. Sridhara Rao, A. M. Sanchez, and C. J. Humphreys, Appl. Phys. Lett. **93**, 101901 (2008).

[Badcock2010] T. J. Badcock, S. Hammersley, M. J. Kappers, C. J. Humphreys, and P. Dawson, Phys. Stat. Sol. (c) **7**, 1894 (2010).

[Bastard1982] G. Bastard, E. E. Mendez, L. L. Chang, and L. Esaki, Phys. Rev. B **26**, 1974 (1982).

[Bellessa1998] J. Bellessa, V. Voliotis, R. Grousson, X. L. Wang, M. Ogura, and H. Matsuhata, Phys. Rev. **58**, 9933 (1998).

[Bimberg1987] D. Bimberg, J. Christen, T. Fukunaga, H. Nakashima, D. E. Mars, and J. N. Miller, J. Vac. Sci. Technol. B **5**, 1191 (1987).

[Chemla1983] D. S. Chemla, Helv. Phys. Acta **56**, 607 (1983).

[Citrin1993] D. S. Citrin, Phys. Rev. B **47**, 3832 (1993).

[Colocci1990] M. Colocci, M. Gurioli, and A. Vinattieri, J. Appl. Phys. **68**, 2809 (1990).

[Deveaud1987] B. Deveaud, T. C. Damen, J. Shah, and C. W. Tu, Appl. Phys. Lett. **51**, 828 (1987).

[Deveaud1991] B. Deveaud, F. Clérot, N. Roy, K. Satzke, B. Sermage, D. S. Katzer, Phys. Rev. Lett. **67**, 2355 (1991).

[Deveaud1993] B. Deveaud, A. Chomette, D. Morris, and A. Regreny, Solid State Comm. **83**, 367 (1993).

[Dussaigne2011] A. Dussaigne, P. Corfdir, J. Levrat, T. Zhu, D. MArtin, P. Lefebvre, J.-D. Ganière, R. Butté, B. Deveaud-Plédran, N. Grandjean, Y. Arroyo, and P. Stadelmann, Semicond. Sci. Technol. **26**, 025102 (2011).

[Feltin2007] E. Feltin, D. Simeonov, J.-F. Carlin, R. Butté, and N. Grandjean, Appl. Phys. Lett. **90**, 021905 (2007).

[Feneberg2010] *We consider that exciton binding energy in $Al_xGa_{1-x}N$ varies linearly with x. Exciton binding energy in AlN is 55 meV, as reported in* M. Feneberg, R. A. R. Leute, B. Neuschl, K. Thonke, and M. Bickermann, Phys. Rev. B **82**, 075208 (2010).

[Gallart2000] M. Gallart, A. Morel, T. Talierco, P. Lefebvre, B. Gil, J. Allègre, H. Mathieu, N. Grandjean, M. Leroux, and J. Massies, Phys. Stat. Sol. (a) **180**, 127 (2000).

[Garrett2005] G. A. Garrett, H. Shen, M. Wraback, B. Ilmer, B. Haskell, J. S. Speck, S. Keller, S. Nakamura, and S. P. DenBaars, Phys. Stat. Sol. (a) **202**, 846 (2005).

[Gurioli1992] M. Gurioli, J. Martinez-Pastor, M. Colocci, C. Deparis, B. Chastaingt, and J. Massies, Phys. Rev. B **46**, 6922 (1992).

[Hillmer1990] H. Hillmer, A. Forchel, R. Sauer, and C. W. Tu, Phys. Rev. B **42**, 3220 (1990).

[Hoffmann1997] A. Hoffmann, Mater. Sci. Eng. B **43**, 185 (1997).

[Kaufmann2011] N. A. K. Kaufmann, A. Dussaigne, D. Martin, P. Valvin, T. Guillet, B. Gil, and N. Grandjean, private communication (2011).

[Krahl1990] M. Krahl, D. Bimberg, R. K. Bauer, D. E. Mars, and J. N. Miller, J. Appl. Phys. **67**, 434 (1990).

[Lefebvre1998] P. Lefebvre, J. Allègre, B. Gil, A. Kavokine, H. Mathieu, W. Kim, A. Salvador, A. Botchkarev, and H. Morkoç, Phys. Rev. B **57**, R9447 (1998).

[Michler1992] P. Michler, A. Hangleiter, M. Moser, M. Geiger, and F. Scholz, Phys. Rev. B **46**, 7280 (1992).

[Muth2005] J. F. Muth, X. Zhang, A. Cai, D. Fothergill, J. C. Roberts, P. Rajagopal, J. W. Cook, Jr., El L. Piner, and K. J. Linthicum, Appl. Phys. Lett. **87**, 192117 (2005).

[Natali2005] F. Natali, D. Byrne, M. Leroux, B. Damilano, F. Semond, A. Le Louarn, S. Vézian, and J. Massies, Phys. Rev. B **71**, 075311 (2005).

[Nolte1990] D. D. Nolte, Solid State Electronics **33**, 295 (1990).

[Oliver2010] *For a review, see* R.A. Oliver, S. E. Bennett, T. Zhu, D. J. Beesley, M. J. Kappers, D. W. Saxey, A. Cerezo, and C. J. Humphreys, J. Phys. D: Appl. Phys. **43**, 354003 (2010).

[Rashba1962] E.I. Rashba, and G. E. Gurgenishvili, Soviet Physics - Solid State **4**, 759 (1962).

[Reynolds1998] D. C. Reynolds, D. C. Look, B. Jogal, J. E. Van Nostrand, R. Jones, and J. Jenny, Solid State Comm. **106**, 701 (1998).

[Smith1996] M. Smith, J. Y. Lin, H. X. Jiang, A. Salvador, A. Botchkarev, W. Kim, and H. Morkoç, Appl. Phys. Lett. **69**, 2453 (1996).

[Vening1993] M. Vening, D. J. Dunstan, and K. P. Homewood, Phys. Rev. B **48**, 2412 (1993).

[Weber1995] S. Weber, W. Limmer, K. Thonke, R. Sauer, K. Panzlaff, G. Bacher, H. P. Meier, and P. Roentgen, Phys. Rev. B **52**, 14739 (1995).

Part V

Conclusions and perspectives

Conclusion and perspectives

In this thesis we have studied, by time-integrated and time-resolved photo- and cathodoluminescence techniques, the dynamics of excitons in low-dimensional GaN-based structures. Thanks to the combination of these characterization tools, we have been able to track, at the nanometer and picosecond scales, the diffusion and recombination mechanisms of charges carriers in semiconductor nanostructures. We emphasize that carrying out picosecond time-resolved cathodoluminescence experiments at temperatures as low as 25 K was itself a challenge. We are confident that the experimental demonstrations reported in this work are promising regarding further development of this tool for a wider use in both the scientific and industrial worlds.

The variety of the investigated nitride-based systems allowed us to provide a clear picture of the interaction of excitons with light but also with structural imperfections. We have been able to study the capture dynamics of excitons on donor impurities, and we have analyzed the effect of surface on the emission from donor bound excitons complexes. In more defective layers, we have paid a particular attention to the interaction between point and extended defects, which gives rise to multiple localization levels for excitons. In particular, we have examined how the nature and the local density of these defects affect the diffusion and recombination dynamics of excitons. Finally, we have been able to investigate the intrinsic recombination processes of excitons confined in the weak and strong confinement regimes.

We present in the following of this section the main outcomes of our work, together with some prospects for further investigation.

Recombination mechanisms of impurity-bound excitons

The first part of this work is devoted to the emission properties of GaN nanocolumns. Although these nano-objects are free of strain and of any extended defects, the low-temperature emission from donor bound excitons (D°X) is broad. In addition, an intense emission line centered at 3.45 eV and absent from the PL spectra of thick GaN layers is systematically observed in thin nanocolums. Regarding that the donor binding energy, and thus the emission energy of D°X, depends on the distance between the donor nucleus and the surface, we have shown that the statistical distribution of donor atoms in the nanocolumns must result in broad emission lines. Concerning the 3.45 eV line, and contrary to previous reports, we rule out that it could arise from a surface defect specific to nanocolumns. As this transition corresponds in energy to the recombination of a D°X that leaves the donor into its 2p state, we have proposed the 3.45 eV transition to arise from D°X with donor nucleus located close to the surface of the nanocolumn.

We have then developed a core-shell model to qualitatively describe the recombination dynamics of excitons in nanocolumns. The main ingredient of our model is to divide a nanocolumn into a core region, where the dynamics of D°X are similar to those in thick GaN layer, and into a shell layer, where the wave function of D°X are distorted by surface. From our model, we have deduced that the thickness of the shell layer where the wave function of D°X is affected by surface should be of the order of 8 nm. This thickness agrees well with the calculated spatial extension of D°X wave function in GaN, supporting *a posteriori* the result of our model.

Our conclusions on the emission properties of GaN nanocolumns has lead to:

- A systematical study of the correlations between the nanocolumns structural and optical properties [Lefebvre2011].

- A micro-photoluminescence study of single GaN nanocolumns, which concludes that the broadening of D°X emission arises indeed from the statistical distribution of donor atoms in the columns [Brandt2010].

- An animated discussion on the origin of the 3.45 eV line [Pfüller2010].

- A debate that will, in our opinion, be definitely closed only once the emission energy of surface D°X will be calculated. For that purpose, we propose to the readers of this thesis to apply the methods described in Appendixes I and II with a more sophisticated D°X trial wave function.

Exciton capture by radiative and non-radiative extended defects

We have then focused on the relaxation of excitons in *a*-plane GaN thick layers and (Al,Ga)N/GaN quantum wells (QWs) grown on sapphire. We have shown that these structures exhibit high densities of basal plane stacking faults (BSFs), radiative planar defects, which can be seen as three monolayers thick type II QWs of cubic GaN embedded in the wurtzite phase. We have first studied the diffusion of excitons with respect to the local density of BSFs. Where this density is low, we have evidenced that the diffusion of excitons from the fault-free material to the BSF planes occurs through successive capture / detrapping processes involving donor atoms. On the contrary, where BSFs are organized into high-density bundles, there exists nothing as a D°X and we have shown that the interaction between successive stacking faults leads to substantial variation in BSF-excitons radiative lifetime.

We have then demonstrated that whatever the local density in BSFs, BSF-excitons were localized along the BSF planes. Supported by envelope function calculations, we have proposed the distribution of donor atoms in the vicinity of the BSF to efficiently localize excitons. As a result of this interaction between BSFs and dopant impurities, we have been able to explain the peculiar conduction properties of non-polar GaN layers compared to layers grown along the polar *c*-axis.

Coming to *a*-plane (Al,Ga)N/GaN QWs grown on GaN processed with epitaxial lateral overgrowth, we have shown that the spatial distribution of BSFs in the QW and in the (Al,Ga)N barriers reproduces the one in the underlying GaN template. In addition, we have given the key to correctly interpret the luminescence decay of excitons confined in such QWs. We have then turned our attention to exciton localization mechanisms in such structures and

we have observed clear evidences for intra-BSF localization for QW excitons. Finally, supported by indirect experimental indications, we have proposed that the intersection of BSFs with a QW could be seen as a quantum wire.

As further implications of the present work, we mention the following topics:

- While at low-temperature, BSF-excitons in GaN thick layers or (Al,Ga)N/GaN QWs are localized, the delocalization of excitons along the whole BSF plane at higher temperature leads to efficient non-radiative recombinations on the partial dislocations closing the BSFs. It is therefore mandatory, when aiming at increasing the room-temperature radiative efficiency of non-polar GaN layers grown on sapphire, to understand the mechanisms leading to the formation of BSFs. This work is currently carried out by many groups [*e.g.* Polyakov2011]

- Our combined experimental and theoretical study on the emission of (D°-BSF)X complexes have clearly indicated that the mechanisms leading to the emission bands at 3.3 and 3.42 eV were complicated, as they involve stacking faults, dislocations and dopant impurities [*see for instance* Tischer2011]. Further studies on the nucleation of stacking faults and on the possible segregation of donor atoms by the BSF planes have thus to be performed before one could pretend to fully describe the low-temperature emission spectrum of heteroepitaxial non-polar GaN.

- Our results on the respectively increased and reduced donor and acceptor binding energies in non-polar GaN is part of the current research on the peculiar electric properties of these kind of layers [Baik2010,Konar2010]. As one of the bottlenecks regarding the *p*-doping of GaN is the large binding energy of Mg atoms, we believe that the experimental demonstration of the "benefic" role of BSFs on the activation of acceptor atoms could be great of interest.

Intrinsic dynamics of excitons in the weak and strong confinement regimes

We have finally studied nitride-based heterostructures grown on the *a*-facets of GaN crystals. We have estimated the threading dislocation density in the heterostructures to be of the order of 2.10^5 cm^{-2}. In addition, as the diffusion length of excitons is about 100 nm at 300 K, we have deduced that in a photoluminescence experiments, photogenerated carriers are not affected by dislocations.

After these general considerations on the structural quality of our epilayers, we have turned our attention to a 200 nm thick GaN layer. At 10 K, and in addition to the D°X recombination, the near band-edge photoluminescence spectrum of the GaN layer exhibits sharp transitions with similar intensities over a 12 meV energy range. These lines are the optical signatures of the quantization of exciton-polariton center-of-mass motion along the growth axis. As the weak confinement regime can be seen as the establishment of exciton-polariton standing waves along the confinement axis, our observation testifies that the coherence length of exciton-polaritons in our structure exceeds 400 nm.

We have then studied the temperature-dependence of the recombination dynamics of excitons strongly confined in (Al,Ga)N/GaN QWs. Regarding the recombination rate of excitons localized along the QW plane, we have shown that the use of bulk GaN substrates results in heterostructures with better control of the interface roughness. We have then observed the delocalization of excitons in both real and reciprocal spaces through the increase of their effective decay time for temperatures up to 200 K. The latter result is of high importance, as it evidences that the recombination of excitons is purely radiative up to temperatures close to room-temperature. For higher temperatures, we have analyzed the emission intensities of both the GaN QWs and the (Al,Ga)N barriers, and we have proposed the drop in QW radiative efficiency to be linked with the thermal escape of confined charge carriers towards the barriers.

The outcomes of the latter part of our work are manifold:

- In our work, the emission from center-of-mass quantized exciton-polaritons has been excited by an indirect way. We are confident that a resonant photoluminescence study

of the relaxation of exciton-polaritons in the weak confinement regime would bring about more spectacular results.

- The observation of exciton-polariton center-of-mass quantization in non-polar GaN epilayers attests to the maturity of the material for fundamental studies on light-matter interaction. As a consequence, our work will certainly motivate the growth of more complicated structures, such as microcavities, on the *a-* or *m-* facets of GaN crystals.

- So far, the temperature-dependence of (Al,Ga)N radiative lifetime is unknown, resulting in uncertainties when analyzing the relative QW and barrier emission intensities. A careful study of the dynamics of excitons in low Al-content (Al,Ga)N grown on non-polar GaN crystal should thus be carried out.

- The origin of the non-radiative processes in the (Al,Ga)N barriers is still not answered. For that reason, we propose for instance a comparative study of the room temperature emission properties of the present QW samples with that of surface-passivated samples (to suppress surface recombination), or annealed samples (to suppress non-radiative point defects such as vacancies).

- More generally, we expect that the present report of GaN quantum well samples with high radiative efficiency at room-temperature will stimulate further developments towards the realization of cost-effective GaN single crystals.

References

[Baik2010] K. H. Baik, Y. G. Seo, S. K. Hong, S. Lee, J. Kim, J. S. Son, and S. M. Hwang, IEEE Photonics Technology Letters 22, 595 (2010).

[Brandt2010] O. Brandt, C. Pfüller, C. Chèze, L. Geelhaar, and H. Riechert, Phys. Rev. B **81**, 045302 (2010).

[Konar2010] A. Konar, T. Fang, N. Sun, and D. Jena, Phys. Rev. B **82**, 193301 (2010).

[Lefebvre2011] P. Lefebvre, S. Fernandez-Garrido, J. Grandal, J. Ristic, M.-A. Sanchez-Garcia, and E. Calleja, Appl. Phys. Lett. **98**, 083104 (2011).

[Pfüller2010] C. Pfüller, O. Brandt, F. Grosse, T. Flissikowski, C. Chèze, V. Consonni, L. Geelhaar, H. T. Grahn, and H. Riechert, Phys. Rev. B **82**, 045320 (2010).

[Polyakov2011] A. Y. Polyakov, N. B. Smirnov, A. V. Govorkov, H. Amano, S. J. Pearton, I.-H. Lee, Q. Sun, J. Han, and S. Y. Karpov, Appl. Phys. Lett. **98**, 072104 (2011).

[Tischer2011] I. Tischer, M. Feneberg, M. Schirra, H. Yacoub, R. Sauer, K. Thonke, T. Wunderer, and F. Scholz, Phys. Rev. B **83**, 035314 (2011).

Part VI

Miscellaneous

Appendix I - Calculation of donor binding energy

The purpose of this Appendix is to calculate, within the effective mass approximation, the energy of an electron bound to a shallow charged donor nucleus located in a potential *V*. Usually, such calculations are used to predict the activation energy of donor atoms in semiconductors and thus the material conduction properties with respect to temperature. Here, the purpose is different: we indeed intend to calculate the emission of donor bound excitons located in any given potential profile. The computation of donor binding energy is therefore mandatory, as the final state of the recombination of donor bound excitons is constituted by a neutral donor atom.

We will first of all calculate the energy of electron bound to a donor located in bulk material. The crystalline potential $V(x,y,z)$ being constant, we will use for the electron a spherical trial wave function. We will then apply the effective potential formalism to calculate the binding energy of an electron bound to a charged donor nucleus located in a crystalline potential $V(x,y,z) = V(z)$, which seems appropriate for the study of donor bound excitons in quantum wells or close to a surface.

AI.1. DONOR BINDING ENERGY IN BULK MATERIAL

In this first situation, the donor atom is located in an isotropic medium with dielectric constant ε and the crystalline potential is constant. We therefore work in spherical coordinates and the Hamiltonian *H* for an electron of effective mass m_e is given by:

$$H = -\frac{\hbar^2}{2m_e}\left(\frac{\partial^2}{\partial\rho^2} + \frac{2}{\rho}\frac{\partial^2}{\partial\rho^2}\right) - \frac{e^2}{4\pi\varepsilon\rho}.$$

The donor nucleus is placed at the origin of the referential and ρ is the distance between the electron and the donor nucleus. We use for the electron envelope function a three-dimensional $1s$ square normalized hydrogenic wavefunction:

$$\Psi_\lambda(\rho) = \frac{1}{\sqrt{\pi\lambda^3}} e^{-\rho/\lambda} \qquad \text{Eq.(A1.1),}$$

The Bohr radius of the electron, λ, is used as variational parameter. The electron energy E_λ is given by:

$$\langle \Psi | H | \Psi \rangle_\lambda = E_\lambda \langle \Psi | \Psi \rangle_\lambda \Leftrightarrow \frac{\hbar^2}{2m_e\lambda^2} - \frac{e^2}{4\pi\varepsilon\lambda} = E_\lambda \qquad \text{Eq.(A1.2).}$$

While the second term in the left-hand side of Eq(A1.2) accounts for the Coulomb interaction between the electron and the charged donor nucleus, the first one represents the kinetic energy of the orbiting electron. The donor binding energy $E_B = -E_\lambda$ is then obtained by minimizing $\langle \Psi | H | \Psi \rangle_\lambda = E_\lambda$ against λ. We obtain an analytical expression for the donor Bohr radius:

$$\lambda = \frac{4\pi\varepsilon\hbar^2}{m_e e^2} \qquad \text{Eq.(A1.3)}$$

and for the donor binding energy:

$$E_B = \frac{m_e e^4}{32\pi^2\varepsilon^2\hbar^2} = \frac{m_e}{\varepsilon_r^2} R_Y \qquad \text{Eq.(A1.4).}$$

$R_Y = 13.6$ eV and ε_r are the hydrogen atom Rydberg and the relative dielectric constant of the medium, respectively. In the case of GaN, we use $m_e = 0.2\ m_0$ and $\varepsilon_r = 9.5$ [Vurgaftman2001] and we obtain a donor binding energy of 30.1 meV.

AI.2. DONOR BINDING ENERGY IN ANY GIVEN POTENTIAL

In this section, we calculate the energy of an electron bound to a donor located in any given one-dimensional profile. We therefore restrict ourselves to the case where the potential $V(x,y,z) = V(z)$. Consequently, it is convenient to work in cylindrical coordinates (ρ, θ, z). The Hamiltonian H for the electron can therefore be written as:

$$H = -\frac{\hbar^2}{2m_e}\left(\frac{\partial^2}{\partial z^2} + \frac{1}{\rho^2}\frac{\partial^2}{\partial \theta^2} + \frac{1}{\rho}\frac{\partial}{\partial \rho} + \frac{\partial^2}{\partial \rho^2}\right) + V(z) - \frac{e^2}{4\pi\varepsilon\sqrt{(z-d)^2 + \rho^2}} \qquad \text{Eq.(A1.5).}$$

The potential profile $V(z)$ is determined by the geometry of the system. The donor is located in $(\rho = 0, z = d)$ and $r = \sqrt{(z-d)^2 + \rho^2}$ is the electron-nucleus distance.

We apply now the "effective potential" method, first developed by [Wu1988] for the study of low-dimensional excitons. The versatility of this approach, based on the possibility to calculate quantized states of one-dimensional quantum wells of arbitrary shape, was successfully applied to heterostructures with specific band alignments [Ivchenko1992, Zimmerman1993, Bellabchara1994], and readily extended to the treatment of donor states in GaN QWs [Morel2001]. According to this approach and in the context of the Variational Theorem, we use the following *ansatz* for the electron envelope-function:

$$\Psi_\lambda(\rho,z) = f(z)\varphi_\lambda(\rho) = f(z)\sqrt{\frac{2}{\pi}}\frac{e^{-\rho/\lambda}}{\lambda} \qquad \text{Eq.(A1.6),}$$

where the *z*-dependence of the electron motion, described by the square-normalized function $f(z)$, is separated from the in-plane dependence $\varphi_\lambda(\rho)$. The latter term is a square-normalized two-dimensional 1s hydrogenic envelope function, with an in-plane extension parameter (pseudo-Bohr radius) λ, which we use as variational parameter. The aim of the method is to minimize the expectation energy $\langle\Psi|H|\Psi\rangle_\lambda = E_\lambda$ against λ, yielding an approximation of the electron ground-state energy. For that purpose, we first average the envelope-function equation $H|\Psi\rangle = E_\lambda|\Psi\rangle$ over all possible in-plane positions:

$$\langle \varphi_\lambda | H | \Psi \rangle_\lambda = E_\lambda \langle \varphi_\lambda | \Psi \rangle_\lambda \Leftrightarrow \int_0^\infty \varphi_\lambda *(\rho)\, H\, \varphi_\lambda(\rho) f(z)\, 2\pi\rho\, d\rho = E_\lambda\, f(z) \qquad \text{Eq.(A1.7).}$$

Equation A1.7 can be rewritten as

$$-\frac{\hbar^2}{2m_e}\frac{d^2 f(z)}{dz^2} + \tilde{V}_\lambda(z) f(z) = E_\lambda f(z) \qquad \text{Eq.(A1.8),}$$

where $\tilde{V}_\lambda(z)$ is given by:

$$\tilde{V}(z) = \frac{2\hbar^2}{m_e}\left(\int_0^\infty \frac{1}{\lambda^3} e^{-\frac{2\rho}{\lambda}}\, d\rho - \int_0^\infty \frac{1}{\lambda^4} e^{-\frac{2\rho}{\lambda}}\rho\, d\rho \right) + V(z) - \int_0^\infty \frac{e^2}{\pi\lambda^2\varepsilon\sqrt{(z-d)^2+\rho^2}} e^{-\frac{2\rho}{\lambda}}\rho\, d\rho$$

$$= V(z) + \frac{\hbar^2}{2m_e\lambda^2} - \frac{e^2}{2\pi\varepsilon\lambda}\int_0^\infty \frac{x e^{-x}}{\sqrt{x^2+\left(\frac{2(z-d)}{\lambda}\right)^2}}\, dx$$

$$\text{Eq.(A1.9).}$$

The advantage of this method is that we are left with a one-dimensional effective-mass equation that $f(z)$ has to obey and where the usual potential term has now been replaced by the so-called "effective potential" $\tilde{V}_\lambda(z)$. The shape of $\tilde{V}_\lambda(z)$ is not *a priori* decided. It simply results, in a strictly mathematical way, from the *ansatz* we made on the shape of the envelope function. The two last terms in the right-hand side of Eq.(A1.9) correspond respectively to the kinetic energy of the electron and to the electrostatic interaction between the electron and the charged donor nucleus, averaged on all in-plane positions of the electron. For a given value of λ, one can determine the effective potential $\tilde{V}_\lambda(z)$ and then solve Eq.(A1.8) by a finite-element technique. We impose $f(z) = 0$ at the boundaries of the system, cut the *z*-axis into thin slabs of constant potential that mimic the overall potential profile, and finally apply the Numerov method. (For more information on the method, we refer the reader, *e.g.* to [Soba2009]). The resulting energy implicitly depends on the in-plane extension parameter λ. According to the Variational Theorem, λ has to be optimized in order to minimize the electron energy E_λ and as a consequence to maximize the overall binding energy of the donor.

If we apply this method to calculate the energy of an electron bound to a charged donor nucleus in GaN, we obtain $E_B = 28$ meV. It corresponds to an error of 7% with respect to the analytic result obtained with Eq.(A1.4).

REFERENCES

[Bellabchara1994] A. Bellabchara, P. Lefebvre, P. Christol, and H. Mathieu, Phys. Rev. B **50**, 11840 (1994).

[Ivchenko1992] E. L. Ivchenko, A. V. Kavokin, V. P. Kochereshko, G. R. Pozina, I. N. Uraltsev, D. R. Yakovlev, R. N. Bicknell-Tassius, A. Waag, and G. Landwehr, Phys. Rev. B **46**, 7713 (1992).

[Morel2001] A. Morel, P. Lefebvre, T. Talierco, M. Gallart, B. Gil, and H. Mathieu, Mat. Sci. Eng. B **82**, 221 (2001).

[Soba2009] A. Soba, Comm. Comp. Phys. **5**, 914 (2009).

[Vurgaftman2001] I. Vurgaftman, J. R. Meyer, and L. R. Ram-Mohan, J. Appl. Phys. **89**, 5815 (2001).

[Wu1988] J.-W. Wu, Solid. State. Comm. **67**, 911 (1988).

[Zimmerman1993] R. Zimmerman, and D. Bimberg, Phys. Rev. B **47**, 15789 (1993).

Appendix II - Calculation of donor bound exciton binding energy

In an infinite semiconductor crystal, thanks to the translational invariance, an exciton can be coupled to only one photon state. These coupled modes are called exciton-polaritons and are stationary states: exciton-polaritons therefore exhibit an infinite radiative lifetime [Hopfield1958]. However, a real crystal is of finite dimension. The radiative decay of polaritons can therefore be seen as the escape of photon-like polaritons out of the crystal. As a consequence, the lifetime of polaritons is given by the volume of the crystal and by the efficiency of acoustic phonon-mediated conversion from exciton-like to photon-like polaritons [Rappel1988]. Moreover, free excitons interact with impurities. In particular, excitons can bind to neutral donor atoms to form donor bound excitons (D°X). Such complex, made of three mobile particles (two electrons and a hole) and a fixed one (the charged donor nucleus) [Suffczynski1989], usually dominates the low-temperature emission properties of bulk semiconductors [HalBogardus1968]. For instance in GaN, excitons bind to oxygen or silicon atoms and their recombination gives rise to the so-called I_2 emission lines lying in unstrained GaN at 3.4701 and 3.4709 eV, respectively [Kornitzer1999, Freitas2003]. These recombination energies correspond to the energy difference between D°X and donor atom ground states. While the donor binding energy can be obtained by the method described in Appendix I, the energy of the former state has been calculated by [Suffczynski1989] for bulk material. However, as it is the case for donor atom, we expect the D°X energy (and therefore the energy position of the I_2 line) to show some large variation when the donor nucleus is located in heterostructures or close to a surface.

The purpose of this Appendix is to calculate the energy of a D°X located in a potential V in order to deduce the emission energy of such complex. We restrict ourselves to the case where the potential $V(x,y,z) = V(z)$. It is thus convenient to work in cylindrical coordinates (ρ, θ, z). This problem involved three mobile particles (2 electrons and a hole, with respective

effective masses m_e and m_h) and a charged donor nucleus. The donor nucleus is located at $(\rho = 0, z = 0)$, the electrons at $(\rho_{e1}, \theta_{e1}, z_{e1})$ and $(\rho_{e2}, \theta_{e2}, z_{e2})$, while (ρ_h, θ_h, z_h) corresponds to the hole position. The potentials felt by the electrons and the hole are $V_e(z_e)$ and $V_h(z_h)$, respectively. The Hamiltonian H of the system is:

$$H = H_{e1} + H_{e2} + H_h + H_{e1h} + H_{e2h} + H_{e1e2}$$
Eq.(A2.1),

where H_{e1} et H_{e2} are the electronic Hamiltonians, H_h is the hole Hamiltonian, H_{eih} account for the attraction between the hole and the ith electron and H_{ee} stands for the Coulomb repulsion between the two electrons:

$$H_{e1} = -\frac{\hbar^2}{2m_e}\nabla_{e1}^2 - \frac{e^2}{4\pi\varepsilon\sqrt{z_{e1}^2 + \rho_{e1}^2}} + V_e(z_{e1})$$
Eq.(A2.2),

$$H_{e2} = -\frac{\hbar^2}{2m_e}\nabla_{e2}^2 - \frac{e^2}{4\pi\varepsilon\sqrt{z_{e2}^2 + \rho_{e2}^2}} + V_e(z_{e2})$$
Eq.(A2.3),

$$H_h = -\frac{\hbar^2}{2m_h}\nabla_h^2 + \frac{e^2}{4\pi\varepsilon\sqrt{z_h^2 + \rho_h^2}} + V_h(z_h)$$
Eq.(A2.4),

$$H_{e1h} = -\frac{e^2}{4\pi\varepsilon\sqrt{(z_{e1} - z_h)^2 + \rho_{e1}^2 + \rho_h^2 - 2\rho_{e1}\rho_h\cos(\theta_{e1} - \theta_h)}}$$
Eq.(A2.5),

$$H_{e2h} = \frac{e^2}{4\pi\varepsilon\sqrt{(z_{e2} - z_h)^2 + \rho_{e2}^2 + \rho_h^2 - 2\rho_{e2}\rho_h\cos(\theta_{e2} - \theta_h)}}$$
Eq.(A2.6),

$$H_{e1e2} = \frac{e^2}{4\pi\varepsilon\sqrt{(z_{e1} - z_{e2})^2 + \rho_{e1}^2 + \rho_{e2}^2 - 2\rho_{e1}\rho_{e2}\cos(\theta_{e1} - \theta_{e2})}}$$
Eq.(A2.7).

The D°X wave function Ψ_{ex} describing the motion of the three mobile particles is solution of the equation $H\Psi_{ex} = E\Psi_{ex}$, where E is the ground state energy of the complex. In order to approximate E, we define the varational D°X wave function Ψ_{ex} as

$$\Psi_{ex}(\rho_{e1}, \rho_{e2}, \rho_h, \theta_{e1}, \theta_{e1}, \theta_h, z_{e1}, z_{e2}, z_h) = \Psi_{e1}(\rho_{e1}, \theta_{e1}, z_{e1})\Psi_{e2}(\rho_{e2}, \theta_{e2}, z_{e2})\Psi_h(\rho_h, \theta_h, z_h)$$
Eq.(A2.8),

where the motions of the three mobile particles are separated. We adopt for each particle the 2D approximation in order to reduce the computation time. The respective in-plane and on-axis motions of the hole and of the electrons are consequently separated. In a way similar to that presented in Appendix I, the electron variational wave functions are

$$\Psi_{ei,\lambda_{ei}}(\rho_{ei},z_{ei}) = f_{ei}(z_{ei})\varphi_{ei,\lambda_e}(\rho_{ei}) = f(z_{ei})\sqrt{\frac{2}{\pi}}\frac{e^{-\rho_{ei}/\lambda_{ei}}}{\lambda_{ei}} \ ; i = 1, 2 \qquad \text{Eq.(A2.9)},$$

where λ_{ei}, which we use as variational parameter, is the in-plane extension for the ith electron. As the hole wave function must be strictly zero on the donor ($z = 0$, $r = 0$), we use the following wave function:

$$\Psi_{h,\lambda_h}(\rho_h,z_h) = f_h(z_h)\varphi_{h,\lambda_h}(\rho_h) = f_h(z_h)\sqrt{\frac{4}{3\pi}}\rho_h\frac{e^{-\rho_h/\lambda_h}}{\lambda_h^2} \qquad \text{Eq.(A2.10)},$$

where the z-dependence, described by the square-normalized function $f_h(z_h)$, is separated from the in-plane dependence $\varphi_{h,\lambda_h}(\rho_h)$. This latter term is a square-normalized two-dimensional $2s$ hydrogenic envelope function, with a characteristic in-plane extension parameter (pseudo-Bohr radius) λ_h, which we also use as variational parameter. We underline that the ansatz made on $\varphi_{h,\lambda_h}(\rho_h)$ forces $\Psi_{h,\lambda_h}(0,z_h) = 0$, which is wrong in most cases. However, regarding the case of a D°X with donor nucleus located in a thin type-II QW (*e.g.* a donor nucleus in a I_1-type basal stacking fault plane), such hypothesis seems justified.

As it was the case for an electron bound to a charged donor nucleus, the aim is now to minimize E, the total energy of the complex, against the parameters λ_{e1}, λ_{e2} and λ_h. We will therefore express successively the envelope function equation $H\Psi_{ex} = E\Psi_{ex}$ in terms of one-dimensional effective-mass equations for the electrons and the hole. Assuming for instance that we know the shape of electrons envelope functions $f_{ei}(z_{ei})$, their corresponding ground state energies E_{ei} and their in-plane extension λ_{ei}, one injects Eq.(A2.8) into $H\Psi_{ex} = E\Psi_{ex}$. It is then possible to integrate the envelope function equation on all the possible electron positions and on the hole in-plane positions, which gives:

$$-\frac{\hbar^2}{2m_h}\frac{\partial^2 f_h(z_h)}{\partial z_h^2}+\tilde{V}_h(z_h)f_h(z_h)=Ef_h(z_h)$$

Eq.(A2.11).

The attractive potential $\tilde{V}_h(z_h)$ is the effective potential for a hole confined in the potential V_h in presence of two electrons and a charged donor nucleus. It is defined by

$$\tilde{V}_h(z_h)=V_h(z_h)$$
$$+E_{e1}+E_{e2}$$
$$+\frac{\hbar^2}{6m_h\lambda_h^2}+\frac{e^2}{12\pi\varepsilon\lambda_h}\int_0^\infty\frac{x^3e^{-x}}{\sqrt{x^2+\left(\frac{2z_h}{\lambda_h}\right)^2}}dx$$
$$-\frac{2e^2}{3\pi\varepsilon\lambda_h^4}\int_0^\infty\int_0^\infty\int_0^{2\pi}\int_{-\infty}^\infty\frac{\left|\Psi_{e1}(\rho_{e1},z_{e1})\right|^2\rho_{e1}\rho_h^3e^{-\frac{2\rho_h}{\lambda_h}}}{\sqrt{(z_{e1}-z_h)^2+\rho_{e1}^2+\rho_h^2-2\rho_{e1}\rho_h\cos(\theta)}}d\rho_{e1}\,d\rho_h\,d\theta\,dz_{e1}$$
$$-\frac{2e^2}{3\pi\varepsilon\lambda_h^4}\int_0^\infty\int_0^\infty\int_0^{2\pi}\int_{-\infty}^\infty\frac{\left|\Psi_{e2}(\rho_{e2},z_{e2})\right|^2\rho_{e2}\rho_h^3e^{-\frac{2\rho_h}{\lambda_h}}}{\sqrt{(z_{e2}-z_h)^2+\rho_{e2}^2+\rho_h^2-2\rho_{e2}\rho_h\cos(\theta)}}d\rho_{e2}\,d\rho_h\,d\theta\,dz_{e2}$$
$$+\frac{e^2}{2\varepsilon}\int_0^\infty\int_0^\infty\int_0^{2\pi}\int_{-\infty}^\infty\int_{-\infty}^\infty\frac{\left|\Psi_{e1}(\rho_{e1},z_{e1})\right|^2\left|\Psi_{e2}(\rho_{e2},z_{e2})\right|^2}{\sqrt{(z_{e1}-z_{e2})^2+\rho_{e1}^2+\rho_{e2}^2-2\rho_{e1}\rho_{e2}\cos(\theta)}}\rho_{e1}\rho_{e2}d\rho_{e1}d\rho_{e2}d\theta dz_{e1}dz_{e2}$$

Eq.(A2.12).

The fourth and fifth terms in the right-hand side of Equation A2.12 are similar to the two last terms of Eq.(A1.9) and correspond to the kinetic energy of the hole and to the repulsive interaction between the hole and the charged donor nucleus, respectively. The sixth and seventh terms both account for the attractive interactions between the electrons and the hole, while the last term stands for the repulsive interaction between the two electrons. Once the total energy E obtained when solving Eq.(A2.11) has been minimized against λ_h, the above procedure has to be applied successively to the two electrons, and must be repeated until the variation of E between two successive steps becomes negligible. At the end of the procedure, one has of course to find identical envelope functions for the two electrons.

REFERENCES

[Freitas2003] J. A. Freitas, Jr., W. J. Moore, B. V. ShanaBrook, G. C. B. Braga, D. D. Koleske, S. K. Lee, S. S. Park, and J. Y. Han, Phys. Stat. Sol. B **240**, 330 (2003).

[HalBogardus1968] E. Hal Bogardus, and H. Barry Bebb, Phys. Rev. **176**, 993 (1968).

[Hopfield1958] J. J. Hopfield, Phys. Rev. **112**, 1555 (1958).

[Kornitzer1999] K. Kornitzer, T. Ebner, K. Thonke, R. Sauer, C. Kirchner, V. Schwegler, M. Kamp, M. Leszczynski, I. Grzegory, and S. Porowski, Phys. Rev. B **60**, 1471 (1999).

[Rappel1988] W. J. Rappel, L. F. Feiner, and M. F. H. Schuurmans, Phys. Rev. B 38, R7874 (1988).

[Suffczynski1989] M. Suffczynski, and L. Wolniewicz, Phys. Rev. B **40**, 6250 (1989).

Appendix III - Position dependent recombination dynamics of donor bound excitons in nanocolumns

The near band-edge emission of GaN nanocolums (NC) is dominated at low-temperature by the recombination of excitons bound to neutral donor nuclei (*see* Chapter III). The aim of this third Appendix is to propose a model to qualitatively understand the temporal behavior of the 3.471 and 3.449 eV PL, which we attribute to the recombination of donor bound excitons (D°X) located in the core and close to the surface of the NC, respectively.

A3.1. DONOR BOUND EXCITONS GROUND AND EXCITED STATES

As shown by [Paskov2007] and discussed in the third Chapter of this thesis, several emission lines observed at 10 K are related to D°X. The most intense one is the I_2 line, that arises from the recombination of a D°X in its ground state, labeled as D°X(0), and that leaves the donor atom in its fundamental state:

$$D°X(0) \rightarrow D°_{n=1} + h\nu_{I_2} \qquad\qquad \text{Eq.(A3.1).}$$

The energy of the I_2 line is given by the energy difference between the D°X and the D° ground state energies, energies that can be obtain by variational methods (*see* Appendixes I and II). However, D°X excited states (*a*, *b*, *c*,...) can be thermally populated and the donor atom can also be left in an excited state:

$$D°X(0,a,b,c...) \rightarrow D°_{(n=2,3,...)} + h\nu_{TES} \qquad\qquad \text{Eq.(A3.2).}$$

The transitions shown in Eq.(A3.2) lie at lower energy than the I_2 line and are called two-electron satellite (TES) of the D°X. Experimentally, one observes that the fundamental D°X recombination I_2 and its TES do no exhibit the same intensity, which can be explained by the fact that:

(*i*) in our excitation regime, D°X states follow a Boltzmann distribution: their fundamental and excited states are therefore not equally populated,

(*ii*) I_2 and TES do not have the same radiative lifetime.

The radiative lifetime of a given transition is indeed proportional to the overlap between the wave functions of its initial and final states. The shape of D°X rotator states wave functions is not trivial and give rise to peculiar selection rules [Gil2007]. In particular, the radiative lifetime of the transition $D°X(a) \rightarrow D°_{2p} + h\nu_{TES}$ is much shorter than that of the transition $D°X(a) \rightarrow D°_{2s} + h\nu_{TES}$. Moreover, these selections rules are altered when the donor nucleus is located in a non-constant potential, as the symmetries of both the D° and the D°X wave functions can change drastically. For instance, when a D° is located close to a surface, its ground state wave function exhibits a *p*-like shape instead of a *s*-like one when located in bulk material [Levine1965]. Although the initial states of the I_2 and TES transitions are not strictly the same as they respectively arise from D°X(0) and D°X(a), these states are in thermal equilibrium. TES and I_2 lines arising from the same D°X population must therefore exhibit the same effective PL decay time τ_{eff} as the D°X population with time is given by

$$n_{D°X}(t) = n_0 Exp[-t(\tau_1 + \tau_2)/\tau_1\tau_2] = n_0 Exp[-t/\tau_{eff}] \qquad \text{Eq.(A3.3)},$$

where τ_1 and τ_2 are the radiative decay times for the processes involving the 1*s* and the 2*s*/2*p* states of the donor, respectively. Although not done here, higher excited states of the neutral donor should of course also be considered as possible final states of the D°X recombination, and Eq.(A3.3) can easily be generalized to that case.

Surprisingly, in our GaN NC, we observe that the decay τ_{PL}(TES) of the TES luminescence is always slower than that of I_2, which we denote $\tau_{PL}(I_2)$. Consequently, the I_2 and the TES PL do not originate from the same population of D°X. We choose to define two

regions: a core and a shell, where the relative radiative decay rates of the I_2 and TES transitions differ substantially. The actual situation is of course more complex, with some progressive variation of properties from the core towards the surface of the NC, together with the presence of a 3 nm thick surface dead layer for free excitons. We should therefore consider the following model as qualitative.

A3.2. A CORE-SHELL MODEL

We write separately the rate equations for D°X populations located in the core and in the shell of the NC. We call α the volume fraction occupied by the bulk-like core (*c*) of the NC, where the D°X → D° recombination is the same as in bulk GaN. On the other hand, we consider that D°X and D° located in a surface shell layer (*s*) of volume fraction $(1 - \alpha)$ are affected by the surface of the NC. In both regions, the time decay of D°X density follows Eq.(A3.3) but with different values of τ_1 and τ_2, for the (*c*) and (*s*) regions. The intensities of I_2 and TES lines for the whole NC are given by the weighted sums of contributions from the core, with weight α, and from the shell, with weight $(1 - \alpha)$. These contributions for each region are given by:

$$
\begin{cases}
I_{I_2(c,s)}(t) \propto \left(\tau_{1(c,s)}\right)^{-1} \exp\left(-t/\tau_{\mathit{eff}\,(c,s)}\right) \\
I_{TES(c,s)}(t) \propto \left(\tau_{2(c,s)}\right)^{-1} \exp\left(-t/\tau_{\mathit{eff}\,(c,s)}\right)
\end{cases}
\qquad \text{Eq.(A3.4).}
$$

In Eq.(A3.4), we take the same decay times τ_{eff} for TES and I_2 transitions originating from the same region of the NC. The instantaneous intensities of these transitions are thus only given by their respective radiative decay times. For bulk GaN, the TES is about 50 times less intense than the I_2 [Paskov2007]. We thus limit the number of adjustable parameters by setting the ratio of radiative lifetimes for the core region to: $\eta = \tau_{2(c)}/\tau_{1(c)} = 50$. Note, however, that the experiments reported in [Paskov2007] have been carried out at 2 K while ours have been obtained at 10 K. The relative occupation of D°X excited states is therefore higher in our case, which should affect the relative probabilities of the different TES contributions and thus the η parameter. Nevertheless, we keep $\eta = 50$ for simplification.

Moreover, the intensity ratio between the I_2 and TES lines is much smaller in NCs than in bulk GaN, suggesting that the TES PL contribution mainly arises from the surface region. Then, the effettive decay rate of the TES line can be approximated by:

$$\tau_{PL}(TES) \approx \tau_{eff(s)} = \tau_{1(s)}\,\tau_{2(s)}\big/\big(\tau_{1(s)} + \tau_{2(s)}\big)$$ Eq.(A3.5).

The initial intensity ratio between the I_2 and TES lines is then given by:

$$\rho = \frac{I_{I_2}(0)}{I_{TES}(0)} \approx \frac{\tau_{2(s)}}{1-\alpha}\left(\frac{\alpha}{\tau_{1(c)}} + \frac{1-\alpha}{\tau_{1(s)}}\right)$$ Eq.(A3.6).

Experimentally, we have access to ρ and to $\tau_{eff(s)}$. The time decay of the I_2 line is slightly nonexponential, but we can measure a time constant at short delay. From these experimental data and using the approximations in Eqs.(A3.5) and (A3.6), we calculate the time evolution of the overall D°X population and of the intensities of I_2 and TES lines. The solution is analytical and both PL decays are bi-exponential:

$$\begin{cases} I_{I_2}(t) = \alpha(\tau_{1(c)})^{-1}Exp(-t/\tau_A) + (1-\alpha)(\tau_{2(c)})^{-1}Exp(-t/\tau_B) \\ I_{TES}(t) = \alpha(\tau_{1(c)})^{-1}Exp(-t/\tau_A) + (1-\alpha)(\tau_{2(s)})^{-1}Exp(-t/\tau_B) \end{cases}$$ Eq.(A3.7),

where the effective decay times τ_A and τ_B in the core and in the shell of the NC are given by:

$$\begin{cases} \tau_A = \left[\frac{\alpha}{1-\alpha}\left(\frac{1}{\tau_{1(c)}} - \frac{1}{\tau_{2(c)}}\right) + \frac{1}{\tau_{2(s)}} + \frac{1}{\tau_{1(s)}}\right]^{-1} \\ \tau_B = \tau_{eff,(s)} = \tau_{1(s)}\,\tau_{2(s)}\big/\big(\tau_{1(s)} + \tau_{2(s)}\big) \end{cases}$$ Eq.(A3.8).

By using Eqs.(A3.7) and (A3.8), we can fit the experimental decays and therefore extract relevant values for parameters of interest, namely: $\tau_{1(c)}$, $\tau_{2(c)}$, $\tau_{1(s)}$, $\tau_{2(s)}$ and α.

REFERENCES

[Gil2007] B. Gil, P. Bigenwald, M. Leroux, P. P. Paskov, and B. Monemar, Phys. Rev. B **75**, 085204 (2007).

[Levine1965] J. D. Levine, Phys. Rev. 140, 586 (1965).

[Paskov2007] P. P. Paskov, B. Monemar, A. Toropov, J. P. Bergman, and A. Usui, Phys. Stat. Sol. (c) **4**, 2601 (2007).

Appendix IV - QW exciton radiative lifetime with temperature in polarization-free quantum wells

In this Appendix, we aim at writing the temperature dependence of the effective lifetime of an exciton confined in a QW. The original demonstrations can be found in papers by [Andreani1991] and [Citrin1993]. We will nevertheless present the most important steps of these calculations, as we believe it to be of importance toward the understanding of the physical phenomena involved.

We will first show how to obtain the radiative lifetime of an exciton confined in a QW and with zero kinetic energy. We will then give the expressions for free and localized QW exciton densities with respect to temperature. From the respective densities and lifetime of free and localized QW excitons, and under the assumption that quasi-thermal equilibrium is reached, we will get the radiative lifetime of the whole exciton population at a given temperature.

We also draw the attention of the reader to the fact that the equations are given in the international system of units. Moreover, while the decay rates Γ correspond to the decay of polarization fields, the decay times τ are attributed to the emission intensity decay. Therefore, in the following, $\tau = 1/(2\Gamma)$.

A4-1. Radiative lifetime of an exciton with zero wave vector.

We consider the radiative recombination of an exciton with polarization $\vec{e}$ confined in a QW into a photon with wave vector $\vec{k}$ and polarization $\vec{\varepsilon}^{(\lambda)}$. We assume the coupling between light and the exciton as a perturbation. The decay rate of an exciton can therefore be

calculated with Fermi's Golden Rule, where the initial and final states $|i\rangle$ and $|f\rangle$ of the transition are:

$|i\rangle$: no photon - an exciton with polarization $\vec{e}$

$|f\rangle$: a photon with wave vector $\vec{k}_0 = (k_{//}, k_z)$ with polarization λ - crystal in its ground state

As thoroughly described in [Andreani1995], the matrix element from $|i\rangle$ to $|f\rangle$ is summed over all allowed photon polarizations and is expressed in terms of exciton oscillator strength:

$$\sum_{\lambda} \left|\langle i|H|f\rangle\right|^2 = \frac{1}{4\pi\varepsilon_0} \frac{\pi}{n^2} \frac{e^2\hbar^2}{m_0 V} \sum_{\lambda} f_{\vec{\varepsilon}} \left|\vec{e}.\vec{\varepsilon}^{(\lambda)}\right|^2 \qquad \text{Eq.(A4.1),}$$

with V the volume of the quantum well, n its refractive index, and $f_{\vec{\varepsilon}}$ quantum well exciton oscillator strength (*see* Chapter I). Assuming that $\vec{k}_{//} = k_x \vec{x}$, one obtains the decay rate Γ for an exciton with wave vector $\vec{k}_{//}$.

$$\Gamma(k_x) = \frac{1}{4\pi\varepsilon_0} \frac{2\pi}{n^2} \frac{e^2\hbar^2}{m_0 V} \sum_{k_z} \sum_{\lambda} f_{\vec{\varepsilon}} \left|\vec{e}.\vec{\varepsilon}^{(\lambda)}\right|^2 \delta(\hbar\omega_k - \frac{\hbar c}{n}\sqrt{k_x^2 - k_z^2}) \qquad \text{Eq.(A4.2).}$$

As the momentum must be conserved, the z-component of the wave vector of the emitted photon is $k_z = \sqrt{k_0^2 - k_x^2}$, with k_0 the total photon wave vector. It can now be shown that the radiative decay rate of an exciton with wave vector $\vec{k}_x$ is

$$\Gamma(k_x) = \frac{1}{4\pi\varepsilon_0} \frac{2\pi}{n} \frac{e^2}{m_0 c} \frac{k_0}{k_z} \sum_{\lambda} \frac{f_{\vec{\varepsilon}}}{S} \left|\vec{e}.\vec{\varepsilon}^{(\lambda)}\right|^2 \theta(k_0 - k_x) \qquad \text{Eq.(A4.3).}$$

$\theta(k)$ is the Heaviside function and is thus zero for $k < 0$. The decay of an exciton with wave vector $k_x > k_0$ is therefore forbidden. When $k_x < k_0$, the exciton can decay into photons with two orthogonal light polarizations respecting $\vec{\varepsilon}.\vec{k} = 0$ (Figure A4.1):

$$\begin{cases} \vec{\varepsilon}^{(1)} = \vec{y} \\ \vec{\varepsilon}^{(2)} = \dfrac{k_z \vec{x} - k_x \vec{z}}{k_0} \end{cases} \qquad\qquad \text{Eq.(A4.4).}$$
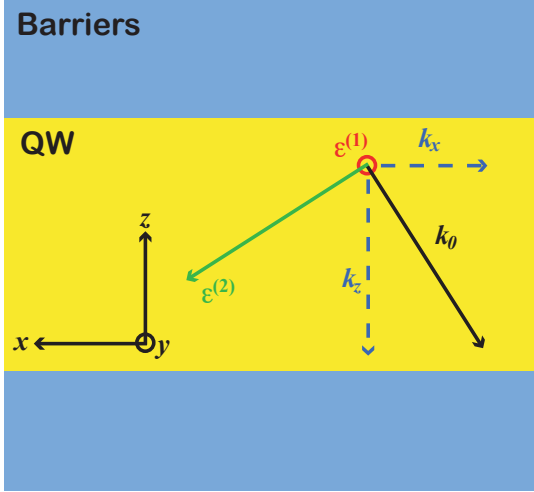

Figure A4.1: The photon emitted after the recombination of a QW exciton has a wave vector $\vec{k}_0$ and a polarization either $\vec{\varepsilon}^{(1)}$ or $\vec{\varepsilon}^{(2)}$. The in-plane wave vector $\vec{k}_{//}$ of the photon is assumed to be along $\vec{x}$. Excitons polarized along $\vec{x}$, $\vec{y}$ or $\vec{z}$ are called L, T and Z excitons, respectively.

Excitons polarized along $\vec{x}$, $\vec{y}$ et $\vec{z}$ are respectively called longitudinal (L), transverse (T), and Z excitons. One then obtains $\vec{e}.\vec{\varepsilon}^{(\lambda)}$ for L, T and Z excitons, and their decay rates are given by:

$$\begin{cases} \Gamma_T(k_x) = \dfrac{1}{2n\varepsilon_0} \dfrac{e^2}{m_0 c} \dfrac{f_{xy}}{S} \dfrac{k_0}{k_z} \\[2mm] \Gamma_L(k_x) = \dfrac{1}{2n\varepsilon_0} \dfrac{e^2}{m_0 c} \dfrac{f_{xy}}{S} \dfrac{k_z}{k_0} \quad , \ k_x \le k_0 \\[2mm] \Gamma_Z(k_x) = \dfrac{1}{2n\varepsilon_0} \dfrac{e^2}{m_0 c} \dfrac{f_z}{S} \dfrac{k_x^2}{k_0 k_z} \end{cases} \qquad \text{Eq.(A4.5).}$$

The photon wave vector along z is $k_z = \sqrt{k_0^2 - k_{//}^2}$. Consequently, for excitons at the center of the Brillouin zone, $k_{//} = 0$ and then $\Gamma_T = \Gamma_L = \Gamma_0 = \dfrac{e^2 f_{xy}}{4\varepsilon_0 n m_0 c S}$. Since the decay time is defined as the reciprocal of two times the decay rate [*see* Citrin1993 and the remark made during the introduction of this Appendix], the radiative decay time for an exciton with $k_{//} = 0$ is $\tau_0 = 1/(2\Gamma_0)$. Note also that sometimes, τ_0 is defined as $1/(2\Gamma_T + 2\Gamma_L)$ [Ciulin2001]. In the

case of polarization free (Al,Ga)N/GaN QWs, one expects $f = 10^{13} / cm^2$, which leads to $\tau_0 =$ 1.2 ps. Such short radiative lifetimes have been measured for the first time in (Al,Ga)As/GaAs by time-resolved PL experiments performed under resonant excitation [Deveaud1991].

A4-2. Quantum well exciton decay time with temperature

A4-2-1 Exciton energy distribution

Although short lifetimes of the order of τ_0 have been measured experimentally under resonant excitation [Deveaud1991], lifetimes measured at 10 K after non-resonant excitation are generally comprised between 100 ps and 1 ns [Damen1990] (as a matter of fact, long lifetimes can also be observed under resonant excitation if the excitation density is too high or if the interfaces of the QW are too rough). Such long lifetimes arise from the fact that:

(*i*) excitons states lying out of the light cone are thermally populated [Andreani1991],

(*ii*) low-temperature PL is generally dominated by excitons loclized along the QW [Weisbuch1981].

QWs exhibit indeed rough interfaces and alloy disorder in the barriers, which both give rise to localized exciton states. For a given structure, these localized states are characterized by their energy depth E_{loc} -the localization energy- and by their density N_D. If we neglect the dissociation of excitons into free electron-hole pairs, the total photogenerated carrier N is equal to $N_{loc} + N_{fr}$, with N_{loc} and N_{fr} the densities of localized and free excitons, respectively [Figure A4.2(a,b)]. Since for a given spin state, the areal density of exciton states is given by $\dfrac{\rho(E)}{S} = \dfrac{M}{2\pi\hbar^2}$, where $M = m_e + m_h = 1.2\ m_0$ is the exciton mass, we obtain that the density of free QW excitons is:
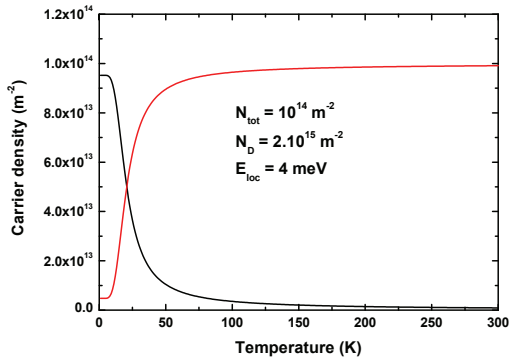
$$N_{fr}(T) \approx \frac{2M}{\pi\hbar^2} \int_{E_X}^{\infty} \frac{1}{1 + Exp\left(\dfrac{E - E_F}{kT}\right)} dE \qquad\qquad \text{Eq.(A4.6),}$$

where we have accounted for the four optically active excitons states. Under non-degenerate excitation conditions, excitons follow a Boltzmann distribution:
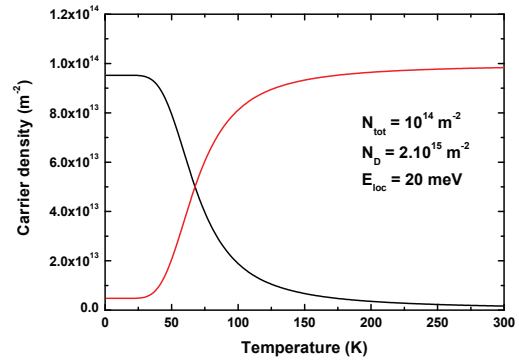
$$N_{fr}(T) \approx \frac{2M}{\pi\hbar^2} \int_{E_X}^{\infty} Exp\left(-\frac{E - E_F}{kT}\right) dE = \frac{2MkT}{\pi\hbar^2} Exp\left(-\frac{E_X(T) - E_F}{kT}\right) \qquad \text{Eq.(A4.7).}$$

Similarly, the density of localized excitons is:

$$N_{loc}(T) \approx N_D Exp\left(-\frac{E_X(T) - E_{loc} - E_F}{kT}\right) \qquad\qquad \text{Eq.(A4.8),}$$
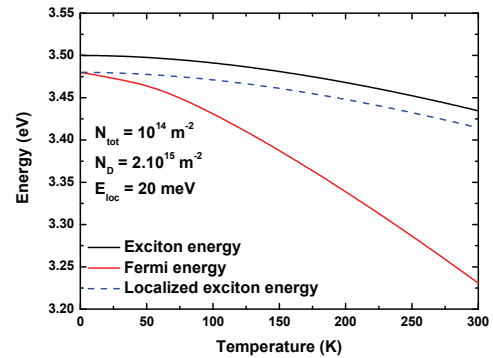
(a)

(b)

Figure A4.2: (a, b) Localized (black) and free exciton (red) densities with respect to T for different localized state densities and localization energies. (c) Exciton Fermi level as a function of T. We used the same parameter as in (b).

(c)

Both $E_X(T)$ (free exciton recombination energy) and E_{loc} can be accessed experimentally. N_D is the density of localized states and is *a priori* unknown. The Fermi level energy E_F for excitons is then given by:

$$E_F(T) = E_X(T) + kT \ln \frac{N}{2\dfrac{MkT}{\pi\hbar^2} + N_D Exp\left(\dfrac{E_{loc}}{kT}\right)}$$
Eq.(A4.9).

As a consequence, we can determine the Fermi level -and therefore free and localized exciton densities- as a function of the single unknown parameter N_D [Figure A4.2(c)].

A4-2-2 Localized and free QW excitons radiative lifetimes

Assuming that the populations of free and bound excitons are in thermal equilibrium at all times (which implies that relaxation processes are much faster than recombinations and that the energy separation between these states is small), the average decay rate for QW excitons is: $\Gamma = (N_{loc}\Gamma_{loc} + N_{fr}\Gamma_{fr})/(N_{loc} + N_{fr}) = 1/\tau_{eff}$. In the previous sections, we have obtained localized and free exciton densities with respect to T, as well as the radiative lifetime of free excitons with zero wave wavector. We still need to express the temperature dependence of localized and free excitons radiative lifetime.

The radiative lifetime of excitons bound to impurities in bulk material has been calculated by [Rashba1962] using the giant oscillator strength method. Their main result is that the oscillator strength of such bound excitons is inversely proportional to their binding energy. [Citrin1993]has extended this theory to the case of QW excitons bound to monolayer width fluctuation of the QW. In agreement to the result of [Rashba1962], and provided the penetration of exciton wavefunction into the barriers is negligible, the larger the spatial extension of the localized state, the smaller the localization energy and the faster the radiative lifetime.

At first sight, the radiative lifetime of localized excitons should not depend on temperature as it is only given by the spatial extension of the localized state. Experimentally, we assume that this radiative lifetime is equal to the QW effective decay time at 10 K. Such

an assumption is justified by the fact that, even for small localization energy, the thermal escape of localized excitons toward the two-dimensional continuum should not be activated at 10 K.
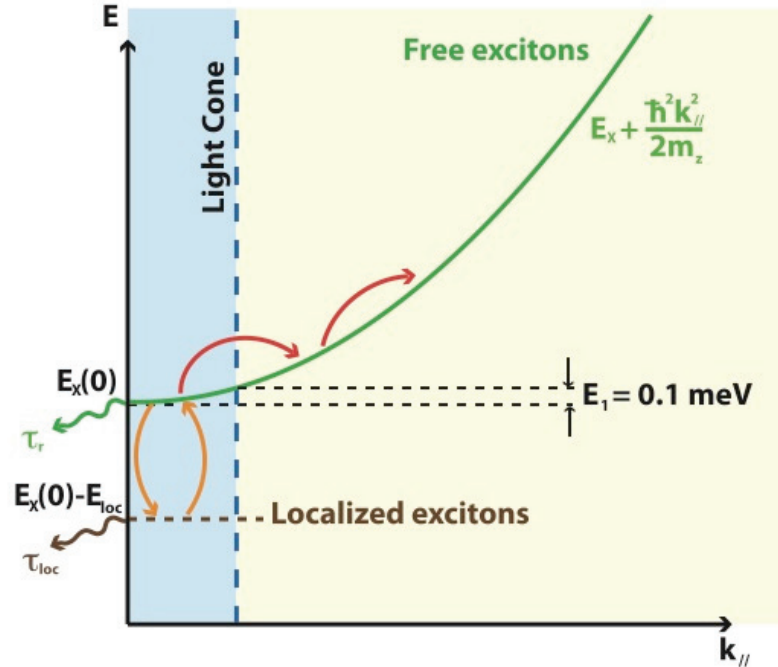

Figure A4.3: Dispersion curves for free and bound QW excitons. Thanks to fast relaxation processes compared to recombination mechanisms, localized and free excitons populations N_{loc} and N_{fr} are in thermal equilibrium. In parallel, free excitons are thermally distributed in k-space and excitons with kinetic energy larger than E_1 lie out of the light cone. For a given excitation density, the relative density of excitons lying out of the light cone increases with temperature and the average QW exciton decay rate decreases.

Concerning free QW excitons, we have already shown that excitons with in-plane wave vector $k_{//} = k_x > k_0 = \sqrt{\dfrac{\varepsilon}{\varepsilon_0} \dfrac{E_X}{\hbar c}}$, *i.e.* excitons with kinetic energy higher than $E_1 = \dfrac{\hbar^2 k_0^2}{2M}$, were dark. In GaN, $E_1 = 1.1$ K. Therefore, only a small fraction of free excitons is radiative when T >> 1 K. As already stated above, we assume that excitons follow a Boltzmann distribution and that L and T modes are equally populated. Thus, averaging $\Gamma_{L,T}(k_x)$ over the Boltzmann distribution, one can show that $\Gamma_T(T) \approx 4\Gamma_0 \alpha$ and $\Gamma_L(T) \approx \dfrac{4}{3}\Gamma_0 \alpha$, with $\alpha = \dfrac{E_1}{k_B T}$

[Andreani1991]. The radiative average decay rate is $\Gamma_r(T) = (\Gamma_L(T) + \Gamma_T(T))/4$, which finally gives the evolution of free exciton radiative lifetime with temperature:

$$\tau_r(T) = \frac{3Mk_BT}{\hbar^2 k_0^2}\tau_0 \qquad\qquad \text{Eq.(A4.10).}$$

In real structures, the situation is more complex as mobile charge carriers can recombine non-radiatively. In general, non-radiative recombination processes are thermally activated with activation energy E_a. We therefore write the free exciton decay rate as $\Gamma_{fr}(T) = \Gamma_r(T) + \Gamma_{nr}(T)$, where Γ_{nr} is the non-radiative decay rate:

$$\tau_{nr}(T) = \Gamma_{nr}(T)^{-1} = \tau_1 Exp\left(-E_a / kT\right) \qquad\qquad \text{Eq.(A4.11).}$$

As a conclusion, the whole temperature dependence of QW PL lifetime can be fitted with only three parameters: N_D, τ_1 and E_a. While N_D is the parameter dominating the low-temperature evolution of the PL lifetime, both τ_1 and E_a can be adjusted to fit the effective decay time in the high-temperature range.

REFERENCES

[Andreani1991] L. C. Andreani, F. Tassone, and F. Bassani, Solid State Comm. **77**, 641 (1991).

[Andreani1995] L. C. Andreani, Optical transitions, excitons, and polaritons in bulk and low-dimensional semiconductor structures. Confined Electrons and Photons: New Physics and Devices, p57, edited by E. Burstein and C. Weisbuch (Plenum, New York, 1995).

[Citrin1993] D. S. Citrin, Phys. Rev. B **47**, 3832 (1993).

[Ciulin2001] V. Ciulin, PhD Thesis, n° 2410, EPFL (2001). *Manuscript available online* (http://library.epfl.ch/theses/?nr=2410).

[Damen1990] T. C. Damen, J. Shah, D. Y. Oberli, D. S. Chemla, J. E. Cunningham, and J. M. Kuo, Phys. Rev. B **42**, 7434 (1990).

[Deveaud1991] B. Deveaud, F. Clérot, N. Roy, K. Satzke, B. Sermage, and D. S. Katzer, Phys. Rev. Lett. **67**, 2355 (1991).

[Rashba1962] E.I. Rashba, and G. E. Gurgenishvili, Soviet Physics - Solid State **4**, 759 (1962) [Fizica Tverdogo Tela **4**, 1029 (1962)].

[Weisbuch1981] C. Weisbuch, R. Dingle, A. C. Gossard, and W. Wiegmann, Solid State Comm. **38**, 709 (1981).

Remerciements

En premier lieu, je tiens à remercier Jean-Daniel Ganière pour avoir supervisé ma thèse durant ces quatre années. Ce fut un réel plaisir de partager tous ces moments au labo avec toi. Tu m'as laissé une très grande et appréciable liberté, et j'ai toujours pu compter sur ton soutien !

Je tiens ensuite à remercier Georges Meylan pour avoir accepter de présider mon jury de thèse. Mes remerciements vont également à Gérald Bastard, Jérôme Faist et Massimo Gurioli pour m'avoir fait l'honneur de juger le travail rapporté dans ce manuscrit.

En plus de Jean-Daniel, ma thèse s'est déroulée sous les yeux bienveillants de Benoît Deveaud-Plédran et de Pierre Lefebvre. Merci tout d'abord à toi Benoît : notre réunion hebdomadaire fut toujours extrêmement enrichissante et amusante ! Quant à toi Pierre, je suis heureux d'avoir passé un an avec toi au labo, et que nous ayons pu continuer à travailler ensemble malgré la distance !

Merci ensuite à mes post-docs successifs, Samuel Sonderegger, Laurent Balet et Jelena Ristić pour m'avoir accompagné lors de cette aventure au quotidien qu'est la cathodoluminescence résolue en temps (aventureuse surtout depuis l'installation du cryostat). De manière plus générale, merci à tous les membres du Laboratoire d'Optoélectronique Quantique pour l'ambiance détendue qui y règne !

Quel bonheur d'avoir pu étudier des échantillons de qualité ! Je remercie donc tout d'abord Amélie Dussaigne, qui a épitaxié la majeure partie des échantillons "de course" étudiés durant ma thèse ! Merci également à Tiankai Zhu, Denis Martin, Enrique Calleja, Eric Feltin, Jean-François Carlin, Henryk Teisseyre et Tadek Suski pour m'avoir fourni les échantillons dont j'ai pu avoir besoin au cours de ces quatre ans !

Pierre CORFDIR ☎ 0041 78 747 60 96
26 years old Nationalities: Swiss and French
Avenue d'Echallens, 8 ✉ pierre.corfdir@epfl.ch
1004 Lausanne - Switzerland

PhD candidate at Ecole Polytechnique Fédérale de Lausanne
Engineer in Materials Science and Nanotechnology

Education

2007-11 (anticipated) *Doctoral school in Physics* at Ecole Polytechnique Fédérale de Lausanne (EPFL) - Switzerland

2006-07 *Master of Research in Physics* at the University of Rennes I - France (obtained with distinction, ranked 1st out of 18)

2004-07 *3rd, 4th and 5th years in Materials Science and Nanotechnology* at the National Institute of Applied Sciences of Rennes (INSA) - France (obtained with distinction)

2002-04 *1st and 2nd preliminary years* at the National Institute of Applied Sciences of Rennes (INSA) - France (obtained with distinction)

2002 *Equivalent of A levels* in maths, physics and chemistry (obtained with distinction)

Computer skills: Mathematica, Matlab, Femlab, Labview, Origin, Microsoft Office, C/C++ and Java programming

Languages: *French* (mother tongue), *English* (very good, quotidian practice at work), *German* (average), *Vietnamese* (beginner)

Work Experience

2007-11 (anticipated) Research assistant and PhD candidate in the Laboratory of Quantum Optoelectronics (EPFL - Switzerland) under the supervision of Dr. J.-D. Ganière, in the group of Prof. B. Deveaud-Plédran.
Thesis title: *Physics of the ultrafast dynamics of excitons in GaN nanostructures.*

2007-10 Teaching assistant in Physics for Prof. A. Pasquarello (EPFL - Switzerland)

2007 Diploma thesis at the Laboratory of Quantum Optoelectronics (EPFL - Switzerland) under the supervision of Dr. J.-D. Ganière, in the group of Prof. B. Deveaud-Plédran.
Diploma title: *Characterization of GaN / AlN quantum dots by time-resolved photoluminescence.*

2006 *11 weeks internship* at the Center of Research on Heteroepitaxy and its Applications (CNRS CRHEA - France) under the supervision of Dr. M. Leroux.
Title: *Reflectivity and photoluminescence experiments and simulations of nitride-based heterostructures.*

References

Dr. Jean-Daniel Ganière (jean-daniel.ganiere@epfl.ch)
Prof. Benoît Deveaud-Plédran (benoit.deveaud-pledran@epfl.ch)
Prof. Nicolas Grandjean (nicolas.grandjean@epfl.ch)
Dr. Pierre Lefebvre (lefebvre@univ-montp2.fr)

List of publications

- ♋ - Selected for publication in the Virtual Journal of Ultrafast Science

- ♍ - Selected for publication in the Virtual Journal of Nanoscale Science & Technology

*12 - **Biexciton-assisted relaxation mechanisms of polaritons in III-nitride-based multi quantum well microcavities**,*

P. Corfdir, J. Levrat, G. Rossbach, R. Butté, E. Feltin, J.-F. Carlin, P. Lefebvre, J.-D. Ganière, N. Grandjean, and B. Deveaud-Plédran, in preparation

*11 - **Carrier thermal escape out of non-polar (Al,Ga)N/GaN quantum wells grown on bulk GaN crystals**,*

P. Corfdir, A. Dussaigne, H. Teisseyre, I. Grzegory, T. Suski, P. Lefebvre, J.-D. Ganière, N. Grandjean, and B. Deveaud-Plédran, in preparation

*10 - **Intrinsic dynamics of weakly and strongly confined excitons in nonpolar nitride-based heterostructures**,*

P. Corfdir, J. Levrat, A. Dussaigne, P. Lefebvre, H. Teisseyre, I. Grzegory, T. Suski, J.-D. Ganière, N. Grandjean, and B. Deveaud-Plédran, accepted for publication in Phys. Rev. B.

*9 - **Biexciton emission and crystalline quality of ZnO nano-objects**,*

P. Corfdir, M. Abid, A. Mouti, P. A. Stadelmann, E. Papa, J.-P. Ansermet, J.-D. Ganière, and B. Deveaud-Plédran, Nanotechnology **22**, 285710 (2011).

*8 - **Time-resolved cathodoluminescence on polychromatic light emitting (In,Ga)N quantum wells grown on (11-22) GaN facets**,*

P. Corfdir, D. Simeonov, E. Feltin, J.-F. Carlin, P. Lefebvre, N. Grandjean, B. Deveaud-Plédran, and J.-D. Ganière, Phys. Stat. Sol. (c) **8**, 1394 (2011).

*7 - **One dimensional exciton luminescence induced by extended defects in GaN/(Al,Ga)N quantum wells**,*

A. Dussaigne, P. Corfdir, J. Levrat, T. Zhu, D. Martin, P. Lefebvre, L. Balet, J.-D. Ganière, R. Butté, N. Grandjean, and B. Deveaud-Plédran, Semicond. Sci. Tech. **26**, 025012 (2011).

6 - **Exciton recombination dynamics in a-plane (Al,Ga)N/GaN quantum wells probed by picosecond photo and cathodoluminescence**,

P. Corfdir, P. Lefebvre, L. Balet, S. Sonderegger, A. Dussaigne, T. Zhu, D. Martin, J.-D. Ganière, N. Grandjean, and B. Deveaud-Plédran, J. Appl. Phys **107**, 043524 (2010).

5 - **Electron localization by a donor in the vicinity of a basal stacking fault in GaN**,

P. Corfdir, P. Lefebvre, J. Ristić, J.-D. Ganière, and B. Deveaud-Plédran, Phys. Rev. B **80**, 153309 (2009).

4 - ☞ - **Low-temperature time-resolved cathodoluminescence study of exciton dynamics involving basal stacking faults in a-plane GaN**,

P. Corfdir, J. Ristić, P. Lefebvre, T. Zhu, D. Martin, A. Dussaigne, J.-D. Ganière, N. Grandjean, and B. Deveaud-Plédran, Appl. Phys. Lett. **94**, 201115 (2009).

3 - **Luminescence and reflectivity characterization of AlGaN/GaN High electron mobility transistors**,

N. Baron, M. Leroux, N. Zeggaoui, P. Corfdir, F. Semond, Z. Bougrioua, M. Azize, Y. Cordier, and J. Massies, Phys. Stat. Sol. C **6**, S715 (2009).

2 - ☞ - **Exciton localization on basal stacking faults in a-plane epitaxial lateral overgrown GaN grown by hydride vapor phase epitaxy**,

P. Corfdir, P. Lefebvre, J. Levrat, A. Dussaigne, J.-D. Ganière, D. Martin, J. Ristić, T. Zhu, N. Grandjean, and B. Deveaud-Plédran, J. Appl. Phys. **105**, 043102 (2009).

1 - ☞ - ♍ - **Time-resolved spectroscopy on GaN nanocolumns grown by plasma assisted molecular beam epitaxy on Si substrates**,

P. Corfdir, P. Lefebvre, J. Ristić, P. Valvin, E. Calleja, A. Trampert, J.-D. Ganière, and B. Deveaud-Plédran, J. Appl. Phys. **105**, 013113 (2009).

Selected conference contributions

2011

Materials Science & Technology - Columbus 2011 (Ohio)

Space- and Time-Resolved Cathodoluminescence to Study ZnO Nanobelts: P. Corfdir, <u>S. Sonderegger</u>, M. Abid, J.-D. Ganière, and B. Deveaud-Plédran (ORAL)

ICNS - Glasgow 2011 (United Kingdom)

Biexciton-assisted relaxation mechanisms in III-nitride based multi-quantum well microcavities: <u>P. Corfdir</u>, J. Levrat, G. Rossbach, R. Butté, E. Feltin, J.-F. Calrin, P. Lefebvre, J.-D. Ganière, N. Grandjean, and B. Deveaud-Plédran. (ORAL)

International Conference on Frontiers of Characterization and Metrology for Nanoelectronics - Grenoble (2011)

Time-resolved cathodoluminescence: <u>J.-D. Ganière</u>, and P. Corfdir. (INVITED)

38th ISCS - Berlin 2011 (Germany)

Direct observation of biexciton localization dynamics in (Al,Ga)N/GaN multi quantum wells: <u>P. Corfdir</u>, J. Levrat, R. Butté, E. Feltin, J.-F. Carlin, P. Lefebvre, J.-D. Ganière, N. Grandjean, and B. Deveaud-Plédran (ORAL)

Is the observation of biexciton luminescence from ZnO nanobelts a reliable optical evidence of high crystalline quality?: <u>P. Corfdir</u>, M. Abid, A. Mouti, P. Stadelmann, J.-D. Ganière, and B. Deveaud-Plédran (ORAL).

2010

IWN 2010 - Tampa (2010)

Distorsion of donor properties in III-nitrides based nano-scale systems: <u>P. Corfdir</u>, P. Lefebvre, J.-D. Ganière, and B. Deveaud-Plédran. (ORAL)

Exciton dynamics in a-plane (Al,Ga)N/GaN single quantum wells grown by molecular beam epitaxy on ELO-GaN: <u>P. Corfdir</u>, P. Lefebvre, A. Dussaigne, L. Balet, S. Sonderegger, T. Zhu, D. Martin, J.-D. Ganière, N. Grandjean, and B. Deveaud-Plédran. (ORAL)

Spatio-time-resolved cathodoluminescence studies on the m-plane $In_{0.05}Ga_{0.95}N$ epilayer grown on a freestanding GaN susbtrate by metalorganic vapor phase epitaxy: <u>M. Kagaya</u>, P. Corfdir, J.-D. Ganière, B. Deveaud-Plédran. N. Grandjean, and S. F. Chichibu. (ORAL)

Microscopy&Microanalysis Society Meeting - Portland (2010)

Novel Picosecond Time-Resolved Cathodoluminescence to probe exciton recombination dynamics in GaN based heterostructures: <u>S. Sonderegger</u>, P. Corfdir, L. Balet, T. Zhu, A. Dussaigne, D. Martin, J. Ristić, P. Lefebvre, J.-D. Ganière, N. Grandjean, and B. Deveaud-Plédran. (INVITED)

GCOE - Kyoto 2009 (Japan)

Picosecond time-resolved cathodoluminescence to study GaN based materials: <u>S. Sonderegger</u>, P. Corfdir, L. Balet J. Ristić, P. Lefebvre, J.-D. Ganière, and B. Deveaud-Plédran. (ORAL)

ICNS - Jeju Island 2009 (Korea)

Low-temperature picosecond time-resolved cathodoluminescence study of exciton localization in *a*-plane GaN: <u>P. Corfdir</u>, P. Lefebvre, J. Ristić, S. Sonderegger, L. Balet, T. Zhu, A. Dussaigne, D. Martin, J.-D. Ganière, N. Grandjean, and B. Deveaud-Plédran. (ORAL)

EMRS Fall Meeting - Warsaw 2009 (Poland)

Study on indium gallium nitride quantum wells: a comparison between MBE grown and MOVPE grown quantum wells: <u>N. A. Kaufmann</u>, A. Dussaigne, P. Corfdir, E. Feltin, D. Martin, J.-D. Ganière, and N. Grandjean. (ORAL)

iNOW - Stockholm & Berlin 2009 (Sweden - Germany)

Comparative study of MOVPE and MBE grown InGaN/GaN quantum wells: <u>N. A. Kaufmann</u>, A. Dussaigne, P. Corfdir, D. Martin, J.-D. Ganière, and N. Grandjean. (POSTER - Best Poster Award)

2008

Swiss Physical Society – Genève 2008

Spectroscopy of GaN nanocolumns grown by molecular beam epitaxy on Si: <u>P. Corfdir</u>, J. Ristić, P. Lefebvre, E. Calleja, J.-D. Ganière, and B. Deveaud-Plédran. (ORAL)

International Workshop on Nitride Semiconductors – Montreux 2008

Time-resolved photoluminescence of GaN nanocolumns grown by molecular beam epitaxy on Si: <u>P. Corfdir</u>, J. Ristić, P. Lefebvre, E. Calleja, J.-D. Ganière, and B. Deveaud-Plédran. (ORAL)

2007

7th International Conference on Nitride Semiconductors – Las Vegas 2007
Luminescence Lifetime in the Vicinity of Threading Dislocations on Bulk GaN Studied by Picosecond Time Resolved Cathodoluminescence (pTRCL): <u>S. Sonderegger</u>, J. Ristic, P. Corfdir, E. Feltin, N. Grandjean, B. Deveaud, J.-D. Ganière. (ORAL)